

THÈSE DE DOCTORAT
DE L'UNIVERSITÉ PSL

Préparée à l'Observatoire de Paris

Contributions to trajectory design in strongly perturbed systems: applications to cislunar space and small bodies

Soutenue par

**Daniel
VILLEGAS PINTO**

Le 16 Septembre 2022

École doctorale n°127

**Astronomie et
Astrophysique
d'Île-de-France**

Préparée à

l'Institut de Mécanique Céleste et
de Calcul des Éphémérides
(IMCCE)

Composition du jury :

Antonella BARUCCI
Professor, Observatoire de Paris

*Présidente du jury
Examinateuse*

Michèle LAVAGNA
Professor, Politecnico de Milano

Rapporteuse

Josep MASDEMONT
Professor, Universitat Politècnica de
Catalunya

Rapporteur

Zubin OLIKARA
Mission Design Engineer, NASA/JPL

Examinateur

Stéphanie LIZY-DESTREZ
Associate Professor, ISAE-SUPAERO

Examinateuse

Daniel HESTROFFER
Astronomer, Observatoire de Paris

Directeur de thèse

Abstract

Keywords : trajectory design, perturbed systems, dynamical systems theory, quasi-periodic, cislunar, small bodies

Acknowledgements

Contents

Abstract	i
Acknowledgements	ii
Contents	iii
List of Figures	v
List of Tables	x
Acronyms	xi
1 Introduction	1
1 Space mission design in perturbed environments	1
2 Research objectives	4
3 Contributions	4
4 Publications	6
4.1 Articles in peer-reviewed journals	6
4.2 Conference Proceedings	6
4.3 Other communications	6
5 Thesis outline	6
2 Background	8
1 Common astrodynamics problems	8
2 Additional perturbations	17
3 Periodic orbits	19
3.1 Numerical continuation	20
4 Stability and hyperbolic invariant manifolds	22
5 Quasi-periodic tori	23
3 Contributions to the numerical computation of quasi-periodic tori	28
1 Initialization of quasi-periodic motion	28
2 The PDE(DFT) algorithm	31
3 The GMOS algorithm	32
4 Additional equations	34
5 Modifications to the algorithms	37
5.1 PDE(DFT)	38
5.2 GMOS	39
6 Comparison	39

7	Applications to trajectory design	42
7.1	The Martian Moon eXploration mission	42
7.2	Torus maps	45
8	Conclusions	48
4	Invariant manifolds in the Augmented Hill Problem for small-body exploration	50
1	Small-body exploration	50
2	Some solutions of the Augmented Hill Problem	52
3	Landing opportunities via the hyperbolic unstable manifolds of periodic terminator orbits	56
4	The hyperbolic manifolds of quasi-periodic terminator orbits	64
5	Conclusions	71
5	The Elliptic-Circular problem and the cislunar environment	72
1	Cislunar space and the Lunar Gateway mission	72
2	Equations of motion	74
3	Numerical continuation	78
3.1	Partial derivatives with respect to continuation parameters	80
3.2	Torus frequencies	81
4	Dynamical solutions	82
4.1	Initial guess generation	83
4.2	Quasi-Periodic Tori Continuation	86
5	Stability analysis	91
6	Torus maps	93
7	Conclusions	96
6	Connections in the cislunar space	97
1	Introduction	97
2	Initialization of hyperbolic manifolds	98
3	Transfers in the Elliptic-Circular	99
4	Translation to ephemeris models	106
5	Transfers in the ephemeris models	109
6	Conclusions	111
7	Conclusions and future work	112
	Bibliography	115

List of Figures

2.1	The rotating reference frame of the CR3BP and its five equilibrium points.	9
2.2	The rotating reference frame of the Hill Problem.	10
2.3	The Earth-Moon's ER3BP viewed from a pseudo-inertial frame.	11
2.4	Representation of the Bicircular problem in its rotating reference frame. The Sun angle σ is measured clockwise from the Earth-Moon line (x -axis).	16
2.5	The family curve of the CR3BP's southern Halo family.	20
2.6	The hyperbolic invariant manifolds of a Lyapunov planar orbit in the Hill Problem.	23
2.7	Example of a two-dimensional torus in \mathbb{T}^2 and the diffeomorphism u that transforms the torus to and back from \mathbb{R}^n . The initial invariant circle is represented in red at $\theta_0 = 0$	24
2.8	Members of a two-dimensional quasi-Halo family (in red) and the periodic Halo orbit (in green) from which the family originates in the Earth-Moon's CR3BP. Plotted in the co-rotating frame centered on the Moon.	25
2.9	L_2 southern quasi-Halo computed for incrementing values of eccentricity in the Earth-Moon ER3BP – (b), (c), (d) – from a periodic Halo of the CR3BP – (a). Plotted in Moon-centered co-rotating frame.	26
3.1	Initial invariant circle about periodic orbit: (a) in \mathbb{T}^2 , plotted on the torus at $\theta_0 = 0$ with the periodic orbit represented by the dotted line and (b) for the surface of section at $\theta_0 = 0$	29
3.2	Sparsity plots for the Jacobian matrices for $(N_0, N_1) = (25, 50)$ and $n = 6$ of (a) the PDE(DFT) method and (b) the GMOS(MS) method.	41
3.3	MMX nominal periodic QSOs around Phobos.	43
3.4	Member of the vertical quasi-periodic QSO tori family (in red): (left) three-dimensional projection with periodic QSO-Lb that it originates from (black dashed line) and a portion of a sample trajectory along the torus' surface (blue); (right) projection over the xz -plane.	45
3.5	Member of the planar quasi-periodic QSO tori family (in red) that originates from the periodic QSO-Lb (black dashed line). A portion of a sample trajectory on the torus' surface is shown in blue.	46
3.6	Example of the operation needed to correctly sample the points at the nodes when using the GMOS algorithm, where the integrated state is rotated back so as to land on the correct nodes.	47
3.8	Torus maps for a member of planar quasi-periodic family QSO-Lb showcasing, as a function of the torus angles, (a) the spacecraft's altitude and (b) its groundspeed with respect to Phobos.	47

3.7	Torus maps for a member of vertical quasi-periodic family QSO-Lb showcasing, as a function of the torus angles, (a) the spacecraft's latitude and (b) its groundspeed with respect to Phobos	48
4.1	The effect of SRP on the equilibrium points of the AHP.	52
4.2	Periodic terminator families: (a) three-dimensional view for two different values of β ; (b) profile view for the family with $\beta = 58.20$	53
4.3	Angle of the complex eigenvalues, $\lambda_i = e^{j\alpha}$, associated with the monodromy matrix of the orbits in the periodic terminator family with $\beta = 92.38$	54
4.4	Evolution of the Sun-side quasi-periodic terminator family for fixed $T = 0.0676560$ with $\beta = 92.38$. The baseline periodic orbit can be seen in green and has $C = 23.472$. Quasi-periodic tori at Jacobi energy values of (a) $C = 23.034$ (b) $C = 21.824$ (c) $C = 20.004$	55
4.5	Evolution of the Sun-side quasi-periodic terminator family for fixed $T = 0.0676560$ with $\beta = 92.38$. The baseline periodic orbit can be seen in green and has $C = 23.472$. Quasi-periodic tori at Jacobi energy values of (a) $C = 23.581$ (b) $C = 23.901$ (c) $C = 24.410$	55
4.6	Evolution of the Sun-side quasi-periodic terminator family for fixed $T = 0.200412$ with $\beta = 92.38$. The baseline periodic orbit can be seen in green and has $C = 36.145$. Quasi-periodic tori at Jacobi energy values of (a) $C = 35.859$ (b) $C = 35.203$ (c) $C = 34.421$	56
4.7	The inner unstable manifold of the L_2 equilibrium point for different values of β at Bennu.	56
4.8	Some of the trajectories for the cubesat lander and asteroid Ryugu. The trajectories in red represent some of trajectories that reach the asteroid surface, while green represents some of the trajectories that escape. The nominal orbit is presented in black and the eclipse shadow is displayed in gray. (a) Full three-dimensional view; (b) zoom-in view.	58
4.9	Some of the landing trajectories for the MASCOT-type lander and asteroid Ryugu. The nominal orbit is presented in black and the eclipse shadow is displayed in gray.	59
4.10	Some of the landing trajectories for the spacecraft-type lander and asteroid Bennu. The nominal orbit is presented in black and the eclipse shadow is displayed in gray.	59
4.11	Times of flight of landing trajectories as a function of initial and landing velocities for cubesat and MASCOT-type landers.	60
4.12	Times of flight of landing trajectories as a function of initial and landing velocities for spacecraft-type lander.	60
4.13	Times of flight of landing trajectories as a function of initial and landing velocities for Landers A and B.	61
4.14	Landing trajectories obtained from the deployment velocity sensitivity analysis with $\sigma = 0.1$ (see Eq. (4.3)) for Lander B and asteroid Bennu. The nominal orbit is presented in black and the eclipse shadow is displayed in gray.	62
4.15	Times of flight of landing trajectories as a function of initial and landing velocities obtained from the deployment velocity sensitivity analysis with $\sigma = 0.1$ (see Eq. (4.3)) for the cubesat, MASCOT-type, and spacecraft-type landers.	62
4.16	Times of flight of landing trajectories as a function of initial and landing velocities obtained from the deployment velocity sensitivity analysis with $\sigma = 0.1$ (see Eq. (4.3)) for the Landers A and B.	62
4.17	Some of the landing trajectories obtained from the deployment velocity sensitivity analysis with $\sigma = 0.5$ (see Eq. (4.3)) for Lander B and asteroid Bennu. The nominal orbit is presented in black and the eclipse shadow is displayed in gray.	63

4.18	Times of flight of landing trajectories as a function of initial and landing velocities obtained from the deployment velocity sensitivity analysis with $\sigma = 0.5$ (see Eq. (4.3)) for the cubesat, MASCOT-type, and spacecraft-type landers.	64
4.19	Times of flight of landing trajectories as a function of initial and landing velocities obtained from the deployment velocity sensitivity analysis with $\sigma = 0.5$ (see Eq. (4.3)) for the Landers A and B.	64
4.20	Landing trajectories for spacecraft ($\beta = 92.38$) and asteroid Bennu from the Sun-side quasi-periodic terminator torus with $C = 34.421$, $T = 0.200412$. The torus is shown in red and the inner unstable manifolds that reach the asteroid in green. A sample trajectory is shown in pink.	65
4.21	The landing locations of the unstable manifold trajectories that intersect the asteroid for spacecraft ($\beta = 92.38$) and asteroid Bennu from the Sun-side quasi-periodic terminator torus with $C = 34.421$, $T = 0.200412$. The landing locations of the periodic terminator's unstable manifolds are also overlayed with a different colormap.	66
4.22	Landing locations at asteroid Bennu from the stable manifolds that intersect the asteroid from the terminator quasi-periodic torus for the cubesat lander ($\beta = 18.86$), with $T = 0.66034$, $C = 16.852$, as a function of the ballistic landing velocity. The landing locations of the periodic terminator orbit for the same lander are overlayed with a different colormap.	66
4.23	Landing locations at asteroid Bennu from the stable manifolds of terminator quasi-periodic tori that intersect the asteroid as a function of the ballistic landing velocity. The landing locations from the periodic terminator orbit for the respective lander are overlayed with a different colormap. (a) MASCOT ($\beta = 58.20$), from torus with $T = 0.28252$, $C = 27.254$; (b) lander A ($\beta = 161.66$), from torus with $T = 0.13169$, $C = 45.526$	67
4.24	Example of an unstable manifold trajectory that does not intersect the asteroid from the quasi-periodic terminator torus associated with the spacecraft ($\beta = 92.38$) at Bennu with $C = 34.421$, $T = 0.200412$	68
4.25	Poincaré map at $x = 0$ of the stable and unstable manifolds associated with spacecraft ($\beta = 92.38$) at Bennu, for the manifolds that don't intersect with the asteroid, from the quasi-periodic terminator torus with $C = 34.421$, $T = 0.200412$	69
4.26	Different homoclinic connections for the quasi-periodic terminator torus associated with the spacecraft ($\beta = 92.38$) with $C = 34.421$, $T = 0.200412$ at Bennu. The outbound or unstable manifold trajectories are shown in green and the return or stable manifold trajectories are shown in dashed pink. The torus is shown in red.	70
5.1	Schematic representation of (a) the Bicircular and of (b) the Elliptic-Circular, in their co-rotating frame centered on the Earth-Moon barycenter. The dashed lines represent the orbits of the primary and secondary as viewed from a pseudo-inertial frame at the moment where the rotating and inertial frames coincide. Note that the eccentricity has been exaggerated and the figures are not to scale.	75
5.2	The 9:2 synodic resonant NRHO under study, shown in the Earth-Moon rotating frame centered on the Moon in dimensional coordinates: (a) the original periodic orbit computed in the CR3BP and (b) the multi-revolution periodic orbit computed in the Bicircular.	84
5.3	The 4:1 synodic resonant NRHO under study, shown in the Earth-Moon rotating frame centered on the Moon in dimensional coordinates: (a) the original periodic orbit computed in the CR3BP and (b) the multi-revolution periodic orbit computed in the Bicircular.	84

5.4	The 4:1 sidereal resonant NRHO under study, shown in the Earth-Moon rotating frame centered on the Moon in dimensional coordinates: (a) the original periodic orbit computed in the CR3BP and (b) the multi-revolution periodic orbit computed in the ER3BP.	85
5.5	(a) The periodic resonant synodic 9:2 NRHO in the Bicircular model and (b) the corresponding quasi-periodic tori of the 9:2 synodic resonant NRHO in the full ECR4BP model for a value of eccentricity $e = 0.0549$	88
5.6	(a) The multi-revolution periodic resonant synodic 4:1 NRHO in the BCR4BP model and (b) the corresponding quasi-periodic tori of the 4:1 synodic resonant NRHO in the full ECR4BP model for a value of eccentricity $e = 0.0549$	89
5.7	(a) The periodic resonant sidereal 4:1 NRHO in the ER3BP model for a value of eccentricity $e = 0.0549$ and (b) the corresponding quasi-periodic tori of the 4:1 sidereal resonant NRHO in the full ECR4BP model for the same value of eccentricity.	89
5.8	The initial invariant circles of the resonant quasi-periodic tori for different family members along the numerical continuation in the ECR4BP, shown in normalized coordinates in co-rotating reference frame centered on the Moon. Initial invariant circles of the (a) 9:2 synodic resonant quasi-periodic NRHO (b) 4:1 synodic resonant quasi-periodic NRHO (c) 4:1 sidereal resonant quasi-periodic NRHO.	90
5.9	The initial invariant circles of quasi-periodic tori for different members along the numerical continuation in the ECR4BP, shown in dimensional coordinates in co-rotating reference frame centered on the Moon. Initial invariant circles of the: (a) 9:2 synodic resonant quasi-periodic NRHO (b) 4:1 synodic resonant quasi-periodic NRHO (c) 4:1 sidereal resonant quasi-periodic NRHO.	90
5.10	Lyapunov exponents plotted against the continuation parameter for each of the quasi-periodic resonant NRHOs during the continuation to the Elliptic-Circular model: (a) 9:2 synodic resonance (b) 4:1 synodic resonance and (c) 4:1 sidereal resonance.	93
5.11	Schematic representation of the conic eclipse model used.	94
5.12	Torus maps for the 9:2 synodic resonant quasi-periodic NRHO: (a) eclipse map showing fraction of Sun disk visible (b) altitude with respect to Moon surface with the eclipses overlayed in bright green.	94
5.13	Torus maps for the 4:1 synodic resonant quasi-periodic NRHO: (a) eclipse map showing fraction of Sun disk visible (b) altitude with respect to Moon surface.	94
5.14	Torus maps for the 4:1 sidereal resonant quasi-periodic NRHO: (a) eclipse map showing fraction of Sun disk visible (b) altitude with respect to Moon surface with the eclipses overlayed in bright green.	95
6.1	Transfers from Earth-vicinity (perigees) to the 9:2 synodic resonant quasi-periodic NRHO.	100
6.2	Transfers from Earth-vicinity (perigees) to the 4:1 synodic resonant quasi-periodic NRHO.	101
6.3	Transfers from Earth-vicinity (perigees) to the 4:1 sidereal resonant quasi-periodic NRHO.	101
6.4	Times of flight versus perigee altitudes for the transfers to the quasi-periodic NRHOs: (a) 9:2 synodic resonance (b) 4:1 synodic resonance (c) 4:1 sidereal resonance.	102

6.5	Times of flight (under 145 days) associated with the transfers to the 9:2 synodic resonant quasi-periodic NRHO as a function of (a) the torus angles (θ_0, θ_1) and (b) mean anomaly per orbital revolution versus θ_1 . Perilunes and apolunes are represented by blue and red vertical lines, respectively.	103
6.6	Times of flight (under 145 days) associated with the transfers to the 4:1 synodic resonant quasi-periodic NRHO as a function of (a) the torus angles (θ_0, θ_1) and (b) mean anomaly per orbital revolution versus θ_1 . Perilunes and apolunes are represented by blue and red vertical lines, respectively.	103
6.7	Times of flight (under 145 days) associated with the transfers to the 4:1 sidereal resonant quasi-periodic NRHO as a function of (a) the torus angles (θ_0, θ_1) and (b) mean anomaly per orbital revolution versus θ_1 . Perilunes and apolunes are represented by blue and red vertical lines, respectively.	104
6.8	Transfer with shortest time of flight from Earth-vicinity (perigee) to the 9:2 synodic resonant quasi-periodic NRHO.	105
6.9	Transfer with shortest time of flight from Earth-vicinity (perigee) to the 4:1 synodic resonant quasi-periodic NRHO.	105
6.10	Transfer with shortest time of flight from Earth-vicinity (perigee) to the 4:1 sidereal resonant quasi-periodic NRHO.	105
6.11	Relative geometries of the Earth, Moon, and Sun in the ephemeris files for the year 2026: (a) Sun angle versus date and (b) Sun angle versus Moon true anomaly as function of the date.	106
6.12	Example of transfer trajectory to the 9:2 synodic resonant quasi-periodic NRHO departing from Earth on 11-Apr-2032 13:33:15.93 (TDB) and duration of 88.47 days: (a) shown in Sun-Earth rotating frame; (b) shown in ECLIPJ2000 frame. The converged trajectory entails a total ΔV of 14.75 m/s.	109
6.13	Example of transfer trajectory to the 9:2 synodic resonant quasi-periodic NRHO departing from Earth on 28-Oct-2030 19:02:50.75 (TDB) and duration of 100.61 days: (a) shown in Sun-Earth rotating frame; (b) shown in ECLIPJ2000 frame. The converged trajectory entails a total ΔV of 17.37 m/s.	110

List of Tables

3.1	Analysis of the average runtime (per torus) associated with obtaining the first five elements of quasi-periodic torus family using the PDE(DFT) method, without (non-square DF) and with (square DF) the implementation of unfolding parameters. Obtained using the <i>Spyder</i> profiler on a 2020 MacBook Air 1.1 GHz Quad-Core i5 with 16Gb RAM.	40
3.2	Analysis of the average runtime (per torus) associated with obtaining the first five elements of quasi-periodic torus family using the GMOS multiple shooting method (MS), without (non-square DF) and with (square DF) the implementation of unfolding parameters. Obtained using the <i>Spyder</i> profiler on a 2020 MacBook Air 1.1 GHz Quad-Core i5 with 16Gb RAM.	41
3.3	MMX candidate orbits.	43
4.1	Lander parameters	57
4.2	Percentage of landing trajectories that reach asteroid Bennu, obtained from the deployment velocity sensitivity analysis with $\sigma = 0.5$ (see Eq. (4.3)).	63
5.1	Physical constants and parameters used for the different models. GM refers to the gravitational parameter, R refers to the body's radius, L to the distance or semi-major axis between two bodies. Sources for data: [107, 79, 52].	82

Acronyms

BCR4BP Bicircular Restricted Four-Body Problem

BVP Boundary Value Problem

CR3BP Circular Restricted Three-Body Problem

DFT Discrete Fourier Transform

DST Dynamical Systems Theory

ECR4BP Elliptic-Circular Restricted Four-Body Problem

EHP Elliptic Hill Problem

ER3BP Elliptic Restricted Three-Body Problem

IDFT Inverse Discrete Fourier Transform

JAXA Japan Aerospace eXploration Agency

MMX Martian Moons eXploration

NRHO Near-Rectilinear Halo Orbit

PDE Partial Differential Equation

SRP Solar Radiation Pressure

STM State Transition Matrix

Chapter 1

Introduction

In this chapter, the motivations behind this thesis work are introduced. Limitations arising from common mission design approaches to heavily perturbed systems are presented in Section 1 and used to frame the research goals proposed in this thesis and shown in Section 2. In Section 3, the specific contributions of this thesis are listed; subsequently the publications associated with these contributions are specified in Section 4. Finally, the outline of the thesis is presented in Section 5.

1 Space mission design in perturbed environments

The last three decades have been marked by a growing interest in a more detailed exploration of other bodies in the solar system. As missions grow more ambitious in their goals and targets, the demanding nature of the systems they aim for fosters an increase in the complexity of their mission design. More specifically, many recent and future missions focus on bodies with high scientific value that have nonetheless complex and chaotic environments due to a combination of possible perturbations. In particular, these perturbations can be associated to factors such as the small mass of the body of interest, irregular gravity, the presence of additional bodies, the eccentricity of the bodies' orbits, among others. Examples of such environments can be seen in missions to asteroids (as [JAXA's Hayabusa](#) [109] and [Hayabusa2](#) missions [102] to asteroids Itokawa and Ryugu respectively, [NASA's OSIRIS-REx](#) mission to asteroid Bennu [62], and the currently underway AIDA mission that includes [ESA's Hera](#) [72] and [NASA's DART](#) [89] counterparts to the binary asteroid system Didymos), to comets (such as [ESA's Rosetta](#) [39] or [NASA's Deep Impact](#) [14]), to planetary moons (such as [JAXA's Martian Moons eXploration \(MMX\)](#) mission to study Phobos in detail [59]), and to our own cislunar environment – the subject of numerous future missions as well as [NASA's Artemis](#) program to return humans to the Moon and to set the next space station in Lunar orbit [77, 78]. The common theme running throughout these systems is the presence of additional perturbations that are not commonly included in traditional astrodynamics models. While it is possible to design baseline trajectories for these environments by “over”-simplifying the dynamics, we risk increasing fuel usage to

operationally maintain said trajectories, missing possible optimal design scenarios, and having a lack of insight into the dynamical properties of the system and of the chosen trajectories. Moreover, it can easily reduce the overall design flexibility due to a lack of coherent options and a smaller number of families of solutions. It is therefore in the best interest of mission designers to already include the main perturbations of a mission’s environment in the baseline trajectory design studies. This gives us the flexibility to focus on and maximize the main goal of space exploration missions: the science opportunities.

In this frame, it is important to firstly understand how to model real environments in the context of specific space missions. The aim of this work is thus to model these perturbed environments by depicting the most relevant perturbations of these systems, in such a way that still allows mission designers to find natural families of solutions on which the mission design can be based upon. The difficulty is to avoid both extreme cases: the over-simplification, which would miss the changes to the solution space introduced by these perturbations, as well as the use of only full ephemeris models, where one can often only find solutions to the trajectory design problems by using black-box optimization techniques, therefore losing design flexibility and dynamical insight. In turn, the solutions found by using these perturbed models can be pruned or refined in later stages of the mission design process by using ephemeris models and correction routines that validate and correct the proposed trajectories.

After identifying the relevant perturbations and modeling the mission’s dynamical environment, one must possess the tools to compute and analyze (families of) possible trajectory design solutions. These tools and methods should be able to incorporate the additional system perturbations and produce realistic operational trajectories. Specifically, this thesis work makes use of numerical methods imported from [Dynamical Systems Theory \(DST\)](#) in order to compute and analyze these motions.

The field of [DST](#) is an area of mathematics that deals with the analysis and description of complex dynamical systems. As such, it can provide important insight into the problems commonly analyzed in astrodynamics, as well as valuable tools to find solutions in these systems. Although this thesis does not lie specifically within the field of [DST](#), as it does not try to fully explore and prove the mathematical concepts that it employs, it makes use of numerical procedures and methods that have been derived from it. These are applied in the context of real space missions and explored in a less formal and more application-driven manner so as to produce and analyze mission design solutions. Work based on [DST](#) has already proven to be extremely valuable to space exploration, with several missions having heavily based their trajectory design concepts on it. Examples of this can be seen in missions such as the International Sun Earth Explorer 3 (ISEE-3), the Genesis mission, the James Webb Space Telescope (JSWT), as well as the Herschel, Planck, and Gaia missions, all of which have flown trajectories first computed by the application of [DST](#) to astrodynamics [35, 66, 11, 88, 46].

When considering the chaotic systems described by restricted three- and four-body problems, analytical solutions do not exist, which leads us to studying the dynamical systems and their possible solutions from a [DST](#) perspective. This translates into analyzing dynamical solutions such as equilibrium or libration points, periodic orbits, and quasi-periodic orbits,

which are, respectively, zero-, one-, and two- or higher-dimensional tori. Importantly, these natural structures typically dictate the general motion of particles on the phase space and provide significant insights into the dynamics of the system, such as stability properties, geometry, regions and directions of motion, among others [61, 55]. Evidently, the inclusion of other perturbations in the models affects these dynamical solutions. For instance, constant perturbations may displace the position of equilibrium points, whereas periodic perturbations, such as the inclusion of additional bodies, will cause the equilibrium points to disappear and to generally be replaced by a manifold with a dimension equal to the number of periodic perturbations. In the same way, non-resonant periodic orbits will be replaced by quasi-periodic tori that incorporate the new periodic perturbation. Solutions that are resonant with the period of an added perturbation will retain their dimensionality in the perturbed model but will be isolated solutions in the phase space due to the requirement on the resonance of their period [55].

The important aspect to note in the previous examples is that it is possible to design trajectories while incorporating perturbations into the dynamical models used to describe the environments of space missions. We do this by acknowledging the perturbed nature of a mission's system from the start and designing for it instead of in spite of it. On this point, the higher-dimensionality of quasi-periodic solutions jumps out as clear advantage, as it translates into significantly larger sets of (families of) solutions and a much wider design flexibility that can incorporate the system's perturbations. Whereas periodic orbits may offer advantages with regards to the ease of their computation, they can often be limiting when designing trajectories in perturbed environments, either because they mostly disappear under the presence of a perturbation, or as pointed out by Olikara [82], because their families of solutions do not cover a wide enough range of the phase space when compared to their higher-dimensional quasi-periodic counterparts. This is also relevant when computing transfers to or from hyperbolic tori; the higher-dimensionality of the quasi-periodic solutions translates into higher-dimensional arrays of possible transfers. Nevertheless, the study and use of periodic orbits as intermediate solutions are an important step in designing valuable and realistic trajectories.

Due to their potential for incorporating perturbations into their formulation and the aforementioned advantages associated with their higher-dimensionality, the study of quasi-periodic tori plays a significant role in this thesis. Specifically, we make use of numerical algorithms in order to generate families of quasi-periodic tori. These are mostly based in the formulations developed by Gómez, Modello, Olikara, and Scheeres [42, 83], often known as the GMOS algorithm, which were compiled and compared with other numerical algorithms in [8]. A variety of other formulations exists, which can take analytic or semi-analytic forms, such as those found in [56, 45, 57, 41]. The numerical nature of the methods hereby used also reflects the application-driven scenario behind this thesis work, meaning we do not delve into KAM theory to try and rigorously prove the existence of the tori. Rather, we use formalisms and considerations coming from these fields and generally assume their existence under standard conditions.

In this thesis, the techniques cited above as well as other methodologies are employed in

mainly two contexts of space mission design: small bodies and the cislunar environment. As mentioned, their relevance to the current and future frame of space exploration makes them valuable subjects. Others authors have dedicated considerable research efforts to each of these areas. In particular, and framing the work to be presented in this thesis, one can mention the work by Scheeres and the Colorado Boulder group on orbit design in perturbed environments and around small bodies [95, 94, 92], works on the deployment of landers to small bodies seen in [101, 36, 49], and other studies on the use of quasi-periodic orbits for their exploration in [16, 6, 9], among others. Regarding trajectory design in the cislunar environment, we can point out recent works on the [Near-Rectilinear Halo Orbit \(NRHO\)](#) family by [111, 31], the use of the Bicircular problem model (to be presented) by [43, 58], which include works on periodic and quasi-periodic orbit design [15, 90] as well as transfer trajectories [96, 69]. Other authors have used coupled restricted three-body problems [25] or the the Restricted Hill Four-Body Problem [91, 84] to find connections between different families in the cislunar environment.

Both subjects of study, small-body exploration and the cislunar environment, capture the essence of the goals that drive this work. These goals are formally stated in the following section.

2 Research objectives

Having introduced the context and motivations for this thesis, the objectives of this research can be established. They can be defined as follows:

1. To gain insight into strongly perturbed environments and on how to model those dynamical systems in a sufficiently accurate manner by means of restricted problems.
2. To elaborate on and develop tools for the systematic computation of realistic solutions in said systems.
3. To apply these methodologies to real mission design problems.

3 Contributions

In this section, the main contributions of this thesis are presented and briefly explained. As stated, although theoretical development was also pursued, this thesis work remains practical and application-driven in its nature. Previous knowledge is re-iterated, adapted and improved when possible, then applied to new problems in order to design realistic trajectories for space missions. The contributions can be divided as follows:

Contributions to the numerical computation of quasi-periodic tori: A study on numerical methods for computing families of quasi-periodic tori has been undertaken. In addition to presenting the two methods considered in this work, the GMOS and PDE(DFT) algorithms [8], we formulate homotopy continuation as a means to introduce periodic perturbations into the computation of quasi-periodic tori, generalize the notions for the number of equations and parameters needed in the computation of quasi-periodic tori, and implement a modification to

the [Discrete Fourier Transform \(DFT\)](#) formulation typically used to compute partial derivatives in these methods. Additionally, modifications are made to the two numerical algorithms, in order to improve the computational aspects of their implementation and their robustness. Specifically, we implement the use of unfolding parameters to the PDE(DFT) formulation and introduce the integration of all the trajectories simultaneously in the Boundary Value Problem formulation of the GMOS method to allow for integral-type constraint equations and a more coherent error control between the integrated trajectories. The formulations are applied to the case of Mars' moon, Phobos, in the frame of [JAXA's Martian Moons eXploration \(MMX\)](#) mission as a short example.

Invariant manifolds in the Augmented Hill Problem: In order to demonstrate some of the presented dynamical tools in the context of small-body exploration, we present a study on the invariant manifolds of the L₂ point and those of periodic orbit families emanating from it under the hypothesis of the [Augmented Hill Problem \(AHP\)](#). Focusing on a particular type of family that is equivalent to the [Circular Restricted Three-Body Problem \(CR3BP\)](#)'s Halo family, and which has interesting properties for small-body exploration, we present baseline low-energy trajectories to land on asteroids or comets for landers with different mass-to-area ratios from both periodic and quasi-periodic trajectories. Furthermore, we demonstrate how the quasi-periodic tori considered can be employed in designing science trajectories that have excursions around the small body before returning to the quasi-periodic torus by computing homoclinic connections, which we show can be easily calculated due to the families' geometric and dynamical properties.

The Elliptic-Circular Restricted Four-Body Problem: A significant result of this thesis is the formulation of what we define as the Elliptic-Circular Restricted Four-Body Problem ([ECR4BP](#)) and its application to trajectory design in the cis-lunar environment. The model was only once before mentioned in literature under the name of the Circular-Elliptic model, albeit not formulated or formally introduced, by Castellà and Jorba in [27], to study the practical stability of the Earth-Moon's L₄ and L₅ equilibrium points. In this thesis, the equations of motion of the problem are derived, and the previously introduced methods for computing quasi-periodic motion in perturbed systems are applied to the case of the Earth-Moon-Sun system. Specifically, we compute the dynamical equivalents of the [CR3BP](#)'s synodic and sidereal resonant Near-Rectilinear Halo Orbits ([NRHO](#)) [51], which are studied in the context of [NASA's Lunar Gateway](#) mission.

Transfers in the cis-lunar environment: Using the formulation of the Elliptic-Circular model, we compute transfers from Earth-vicinity to the aforementioned resonant quasi-periodic [NRHOs](#). These are obtained from the stable hyperbolic manifolds of the tori, also known as their whiskers. These transfers are analyzed and a simple algorithm is presented that allows for their transformation to a real-ephemeris model, where they can be used as initial guesses in multiple shooting optimization algorithms to find the real transfer trajectories.

4 Publications

The journal articles, conference proceedings papers, and other communications published or presented during this thesis are listed in what follows.

4.1 Articles in peer-reviewed journals

- D. Villegas-Pinto, N. Baresi, S. Locoche, D. Hestroffer, “Resonant quasi-periodic near-rectilinear Halo orbits in the Elliptic-Circular Earth-Moon-Sun Problem”, Advances in Space Research, 2022, [*In Press*].

4.2 Conference Proceedings

- D. Villegas-Pinto, N. Baresi, S. Locoche, D. Hestroffer, “Transfers to resonant quasi-periodic Near-Rectilinear Halo Orbits in the Earth-Moon-Sun Elliptic-Circular problem”, International Astronautical Congress, 2022, Paris, France;
- D. Villegas-Pinto, N. Baresi, S. Locoche, D. Hestroffer, “Quasi-Periodic Near-Rectilinear Halo Orbits in the Circular-Elliptic Restricted Four-Body Problem”, AAS/AIAA Astrodynamics Specialist Conference , 2021, Online;
- D. Villegas-Pinto, N. Baresi, D. Hestroffer, E. Canalias, “On the numerical computation of quasi-periodic families and applications to the Martian Moons eXploration mission”, ESA Guidance Navigation and Control & International Conference on Astrodynamics Tools and Techniques (GNC & ICATT), 2021, Online;
- D. Villegas-Pinto, D. Hestroffer, E. Canalias, F. Capolupo, “Deployment of small-body landers from terminator orbits in perturbed environments”, AAS/AIAA Astrodynamics Specialist Conference, 2020, Online;
- D. Villegas-Pinto, S. Soldini, Y. Tsuda, J. Heiligers, “Temporary Capture of Asteroid Ejecta into Periodic Orbits: Application to JAXA’s Hayabusa2 Impact Event”, AIAA Scitech Forum, 2020, Orlando, USA; <https://doi.org/10.2514/6.2020-0221>.

4.3 Other communications

- D. Villegas-Pinto, “Trajectory design in strongly perturbed three-body problems”, Journées CNES Jeunes Chercheurs (JC2), 2021, Toulouse, France;
- N. Baresi, D. Villegas-Pinto, “Quasi-Periodic Orbits for the Exploration of Small Irregular Moons ”, 2021 SIAM Conference on Dynamical Systems, 2021, Online.

5 Thesis outline

This thesis is organized in the following manner. Chapter 2 presents the background knowledge and the theoretical preliminaries necessary for the development of the present work. Then,

in Chapter 3, this thesis’ contributions to the numerical computation of quasi-periodic tori are presented; modifications to two established algorithms are developed and tested against their standard formulation. Chapter 4 then studies the subject of small-body exploration in the context of the AHP, which includes Solar Radiation Pressure (SRP) and eclipses. Baseline landing trajectories from periodic and quasi-periodic solutions are computed, as well as homoclinic connections for the quasi-periodic orbits. Following this, the topic of the cislunar environment is introduced in Chapter 5, where a novel dynamical model that includes the Sun’s gravitational force and the Moon’s eccentricity is presented and analyzed in the context of NASA’s future Lunar Gateway mission. Specifically, we study the dynamical equivalents of the Gateway’s planned orbits in this formulation, which are resonant quasi-periodic tori. Chapter 6 leverages this knowledge to compute transfers between Earth-vicinity and these quasi-periodic tori, which are analyzed and transformed to full-ephemeris coordinates to be used as initial guesses in optimization and shooting algorithms. This is followed by the general conclusions of the thesis and recommendations for future work in Chapter 7.

Chapter 2

Background

In this chapter, the main theoretical background necessary for the development of this thesis is presented. In Section 1, different restricted three- and four-body astrodynamics problems are introduced. These represent the framework for the dynamical models in which a massless particle moves. Then, in Section 2, common perturbations that can be added to these astrodynamics problems are discussed. Section 3 presents periodic orbits as a dynamical solution of the presented models, as well as a numerical technique used to compute families of these solutions. Section 4 discusses stability and hyperbolic invariant manifolds, analyzing how these manifolds can be computed from hyperbolic tori such as periodic orbits. Finally, Section 5 introduces quasi-periodic motion, which is organized in dynamical solutions commonly known as quasi-periodic tori.

1 Common astrodynamics problems

In order to describe the motion of a spacecraft in different types of environments, one can make use of different dynamical models from astrodynamics. These models, usually referred to as problems, consider that a particle or a spacecraft has negligible mass (i.e. restricted problems), which is under the gravitational influence of one or more bodies. Due to the type of space missions addressed in this work, we always consider at least two bodies in addition to the spacecraft. Specifically, we focus on restricted three- and four-body problems. These problems can be written as a system of first order differential equations of the type

$$\dot{\mathbf{X}} = \mathbf{f}(\mathbf{X}, \boldsymbol{\xi}, t) \quad (2.1)$$

where typically $\mathbf{X} = [x, y, z, \dot{x}, \dot{y}, \dot{z}]^T$, t represents the time variable, $\boldsymbol{\xi}$ is a vector of possible external parameters of dimension k , and \mathbf{f} is a smooth vector field $\mathbf{f} : \mathbb{R}^n \times \mathbb{R}^k \times \mathbb{R} \rightarrow \mathbb{R}^n$, with $n = 6$ in this particular case. Using this notation, we can define a few common astrodynamics problems on which we can base our dynamical systems, to be extended with the addition of one or more perturbations. A short list can be seen below, starting with one of the most used models in astrodynamics, the [Circular Restricted Three-Body Problem \(CR3BP\)](#), followed by

a specific case of the CR3BP, as well as extensions of the model to include the perturbations posed by the eccentricity of the primaries' orbits or an additional body.

Circular Restricted Three-Body Problem: The CR3BP has been extensively studied and constitutes the basis of many models and studies found in literature. It describes the case where two bodies – the primary, which is more massive, and the secondary – move about each other in circular orbits. A rotating reference frame centered on the barycenter of the system is used, with the x -axis pointing from the primary to the secondary, the z -axis pointing along their orbits' angular momentum vector, and the y -axis completing the orthogonal frame. We can write the equations of motion of the CR3BP in dimensionless form taking as units of length, time, and mass, the distance between the two bodies [LU] = l (which is constant in the CR3BP), the inverse of the mean motion [TU] = $1/n$, and the sum of their masses [MU] = $m_1 + m_2 = M$, respectively. The primary is placed at $x_1 = -\mu$ along the x -axis and the secondary at $x_2 = 1 - \mu$ with $\mu = \frac{m_2}{m_1+m_2}$. A representation of the rotating frame with the two primaries and the problem's five equilibrium points, L_i , can be seen in Figure 2.1. The study of these libration points, as they are also known, offers important insights into the dynamics of the problem, as their dynamical properties can be leveraged to construct families of solutions, to analyze stability, among others [25].

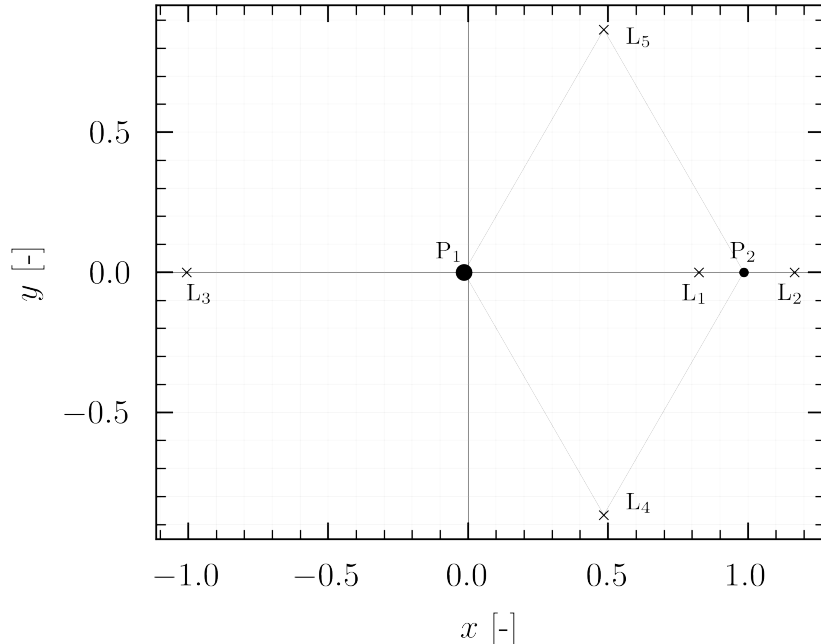


Figure 2.1: The rotating reference frame of the CR3BP and its five equilibrium points.

As defined in [100], and using the aforementioned normalized units, we can write the

normalized equations of motion of the CR3BP as

$$\ddot{x} - 2\dot{y} = \frac{\partial \Omega}{\partial x}, \quad (2.2a)$$

$$\ddot{y} + 2\dot{x} = \frac{\partial \Omega}{\partial y}, \quad (2.2b)$$

$$\ddot{z} = \frac{\partial \Omega}{\partial z}, \quad (2.2c)$$

where Ω is the effective potential

$$\Omega = \frac{1}{2} (x^2 + y^2) + \frac{1-\mu}{r_1} + \frac{\mu}{r_2} = \frac{1}{2} (x^2 + y^2) + U \quad (2.3)$$

and $r_1 = \sqrt{(x+\mu)^2 + y^2 + z^2}$, $r_2 = \sqrt{(x-(1-\mu))^2 + y^2 + z^2}$. As seen in Eq. (2.3), the traditional CR3BP treats the primary and secondary as point masses. However, it is common to represent their gravitational potential as U , which makes it simple to replace the gravity models of the bodies. Because the problem is time-invariant or time-independent, as can be seen in the equations of motion, it admits an integral of motion or an energy integral, called the Jacobi constant, C . As the name indicates, C is constant for a particular solution or trajectory of the problem, and it is only a function of the position and velocity of a particle:

$$C = 2\Omega - v^2 = (x^2 + y^2) + 2U - (\dot{x}^2 + \dot{y}^2 + \dot{z}^2), \quad (2.4)$$

where v is the velocity.

Hill Problem: The Hill Problem is a specific case of the CR3BP, where we approximate the dynamics to the vicinity of the secondary such that $\frac{r}{d} \ll 1$, where r is the distance from the particle to the secondary and d is the distance from the secondary to the primary, and where $\frac{m_2}{m_1} \ll 1$. As with the CR3BP, a rotating reference frame is used, only that for the Hill Problem it is centered on the secondary instead of the primary, as shown in Figure 2.2. The reference frame is defined by the x -axis pointing away from the primary body, the z -axis pointing in the direction of the orbit's angular momentum vector, and the y -axis completing the orthogonal frame. Because the equations of motion are approximated to the vicinity of

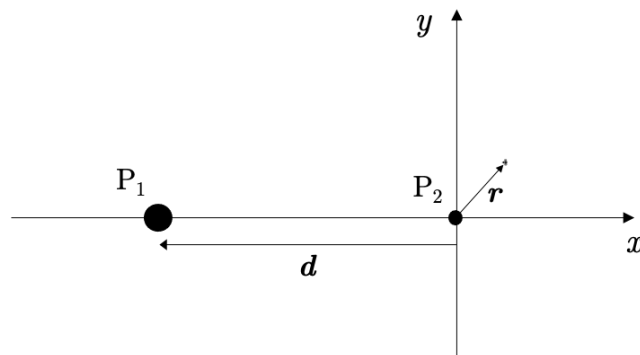


Figure 2.2: The rotating reference frame of the Hill Problem.

the secondary, the Hill Problem considers the relative acceleration posed by the primary body instead of the absolute acceleration [95]. This is often also called the third-body effect. Using as length and time units $[LU] = (\mu_2/n^2)^{1/3}$ and $[TU] = 1/n$, respectively, we can write the normalized equations of motion for the Hill Problem as

$$\ddot{x} - 2\dot{y} = -\frac{x}{r^3} + 3x, \quad (2.5a)$$

$$\ddot{y} + 2\dot{x} = -\frac{y}{r^3}, \quad (2.5b)$$

$$\ddot{z} = -\frac{z}{r^3} - z. \quad (2.5c)$$

Like the CR3BP, the system is autonomous and admits an energy integral, also known as the Jacobi constant

$$C = 2\Omega_H - v^2 = 3x^2 - z^2 + \frac{2}{r} - (\dot{x}^2 + \dot{y}^2 + \dot{z}^2). \quad (2.6)$$

The Hill Problem is particularly used to analyze the dynamics about small bodies such as asteroids or comets due to their small mass and to the fact that the distance to the Sun is much greater than that from the spacecraft or particle to the small body.

Elliptic Restricted Three-Body Problem: The Elliptic Restricted Three-Body Problem (ER3BP) is a generalization of the CR3BP that describes the case where the bodies revolve about their barycenter in elliptical orbits, i.e. the distance between the primary and secondary is not constant. Figure 2.3 displays the geometry of the problem viewed from a pseudo-inertial frame and applied to the Earth-Moon system. When the eccentricity of their orbits is set

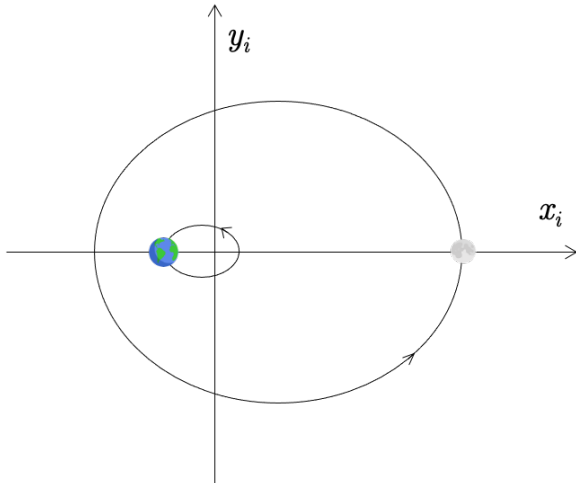


Figure 2.3: The Earth-Moon's ER3BP viewed from a pseudo-inertial frame.

to zero, the problem simplifies into the classical CR3BP. As such, it can also be seen as the addition of a periodic perturbation to the autonomous CR3BP system (which will be discussed in the next section). The axis are the same as in the CR3BP, i.e. a co-rotating reference frame centered at the barycenter of the primaries is used. However, due to the ellipticity of the

primaries' orbits in the ER3BP, which causes the distance between them to be time-dependent, the normalization of the equations is not as simple. Because the three-dimensional ER3BP is not nearly as common as the CR3BP in literature and because it will be used later on in this thesis, let us derive its equations more thoroughly. Considering an inertial frame and a rotating frame that rotates about the same origin with an angular velocity $\dot{\nu} = \frac{d\nu}{dt}$, we can write the acceleration in dimensional coordinates in the inertial frame as

$$\ddot{\mathbf{r}}_I^* = \ddot{\mathbf{r}}^* + 2\dot{\nu} \times \dot{\mathbf{r}}^* + \dot{\nu} \times (\dot{\nu} \times \mathbf{r}^*) + \ddot{\nu} \times \mathbf{r}^*, \quad (2.7)$$

where \mathbf{r}_I^* is the position vector in the inertial frame and \mathbf{r}^* is the position vector in the rotating frame. The superscript \square^* represents dimensional coordinates. Note that since for the elliptical case the angular velocity of the primaries is not constant, we cannot omit $\ddot{\nu}$. Of course, the acceleration in the inertial frame is simply $\ddot{\mathbf{r}}_I^* = -\frac{Gm_1}{r_1^{*3}}(\mathbf{r}^* - \mathbf{r}_1^*) - \frac{Gm_2}{r_2^{*3}}(\mathbf{r}^* - \mathbf{r}_2^*)$, where \mathbf{r}_1^* and \mathbf{r}_2^* are the positions of the primary and secondary in the rotating reference frame, respectively. Simplifying Eq. (2.7) we arrive at

$$\begin{bmatrix} \ddot{x}^* \\ \ddot{y}^* \\ \ddot{z}^* \end{bmatrix} + 2\dot{\nu} \begin{bmatrix} -\dot{y}^* \\ \dot{x}^* \\ 0 \end{bmatrix} - \dot{\nu}^2 \begin{bmatrix} -x^* \\ y^* \\ 0 \end{bmatrix} + \ddot{\nu} \begin{bmatrix} -y^* \\ x^* \\ 0 \end{bmatrix} = -\frac{Gm_1}{r_1^{*3}} \begin{bmatrix} x^* - x_1^* \\ y^* \\ z^* \end{bmatrix} - \frac{Gm_2}{r_2^{*3}} \begin{bmatrix} x^* - x_2^* \\ y^* \\ z^* \end{bmatrix}. \quad (2.8)$$

The system represented in Eq. (2.8) is dependent on time, i.e. it represents a non-autonomous Hamiltonian. However, we can transform the problem by using the true anomaly ν as a free variable, instead of time, and normalizing the equations by the variable distance between the two primaries, l . This distance is given by

$$l = \frac{a(1-e^2)}{1+e\cos\nu}, \quad (2.9)$$

which is a function of the true anomaly and describes the Two-Body Problem (2BP) [100]. Recalling the conservation of angular momentum $\dot{\nu}l^2 = h = \sqrt{GMa(1-e^2)}$, where a and e are the semi-major axis and the eccentricity of either primary around the other, we can write

$$\dot{\nu} = \frac{d\nu}{dt} = \frac{(GM)^{1/2}(1+e\cos\nu)^2}{a^{3/2}(1-e^2)^{3/2}}. \quad (2.10)$$

We can now use the distance between the two primaries, l , the time derivative of the true anomaly, $\dot{\nu}$, and the sum of the masses of the primaries, M , to define the units of length, time, and mass as $[LU] = l$, $[TU] = 1/\dot{\nu}$, $[MU] = m_1 + m_2$, respectively.

To completely transform the equations of motion we need also the following simplifications. From the conservation of angular momentum in the 2BP

$$\left(l^2 \left(\frac{d\nu}{dt}\right)\right)^2 = h^2 = a(1-e^2)GM, \quad (2.11)$$

and, because the angular momentum is constant, i.e. $\frac{d}{dt} \left(l^2 \frac{d\nu}{dt} \right) = 0$

$$l \frac{d^2\nu}{dt^2} + 2 \frac{dl}{dt} \frac{d\nu}{dt} = 0. \quad (2.12)$$

The final simplification comes from vector calculus. Taking \mathbf{l} in the 2BP as the radial vector, and $\boldsymbol{\nu}$ as the true anomaly vector, $\mathbf{l} = l \hat{\mathbf{l}} = l(\cos \nu, \sin \nu)$ and $\hat{\boldsymbol{\nu}} = (-\sin \nu, \cos \nu)$, normal to $\hat{\mathbf{l}}$. Note that the superscript $\hat{\square}$ represents a unit vector. Differentiating \mathbf{l} with respect to time

$$\frac{d\mathbf{l}}{dt} = \frac{dl}{dt} (\cos \nu, \sin \nu) + l \frac{d\nu}{dt} (-\sin \nu, \cos \nu) = \frac{dl}{dt} \hat{\mathbf{l}} + l \frac{d\nu}{dt} \hat{\boldsymbol{\nu}}. \quad (2.13)$$

In the same way, we reach

$$\frac{d^2\mathbf{l}}{dt^2} = \left(\frac{d^2l}{dt^2} - l \left(\frac{d\nu}{dt} \right)^2 \right) \hat{\mathbf{l}} + \left(2 \frac{dl}{dt} \frac{d\nu}{dt} + l \frac{d^2\nu}{dt^2} \right) \hat{\boldsymbol{\nu}}. \quad (2.14)$$

However, from the 2BP, we know that the acceleration only has a radial component

$$\frac{d^2\mathbf{l}}{dt^2} = -\frac{GM}{l^2} \hat{\mathbf{l}}, \quad (2.15)$$

and therefore

$$\frac{d^2l}{dt^2} - l \left(\frac{d\nu}{dt} \right)^2 = -\frac{GM}{l^2}. \quad (2.16)$$

Using $\frac{d}{dt} = \frac{d\nu}{dt} \frac{d}{d\nu}$ and $\mathbf{r} = \frac{\mathbf{r}^*}{l}$, we can now transform the terms in Eq. (2.8). Taking the first term of the left-hand side

$$\frac{d^2r^*}{dt^2} = \frac{d}{dt} \left(\frac{d}{dt} (\mathbf{r} \cdot \mathbf{l}) \right) = l \frac{d^2r}{dt^2} + 2 \frac{dl}{dt} \frac{dr}{dt} + r \frac{d^2l}{dt^2} = l \left[\frac{dr}{dt} \frac{d^2\nu}{dt^2} + \frac{d^2r}{df^2} \left(\frac{d\nu}{dt} \right)^2 \right] + 2 \frac{dl}{dt} \frac{dr}{d\nu} \frac{d\nu}{dt} + r \frac{d^2l}{dt^2}. \quad (2.17)$$

The second term becomes

$$2 \frac{df}{dt} \begin{bmatrix} -\frac{d(y \cdot l)}{dt} \\ \frac{d(x \cdot l)}{dt} \\ 0 \end{bmatrix} = 2 \frac{df}{dt} \begin{bmatrix} -y \frac{dl}{dt} - l \frac{d\nu}{dt} \frac{dy}{dt} \\ x \frac{dl}{dt} + l \frac{d\nu}{dt} \frac{dx}{dt} \\ 0 \end{bmatrix}. \quad (2.18)$$

The third and fourth terms become $-l (d\nu/dt)^2 [x, y, 0]^T$ and $l (d^2f/dt^2) [-y, x, 0]^T$, respectively. The right-hand side of Eq. (2.8) becomes

$$-\frac{GM}{l^2} \left(\frac{1-\mu}{r_1^3} \begin{bmatrix} x+\mu \\ y \\ z \end{bmatrix} + \frac{\mu}{r_2^3} \begin{bmatrix} x-(1-\mu) \\ y \\ z \end{bmatrix} \right), \quad (2.19)$$

where, again, $\mu = m_2 / (m_1 + m_2)$ and $r_1 = \sqrt{(x + \mu)^2 + y^2 + z^2}$, $r_2 = \sqrt{(x - (1 - \mu))^2 + y^2 + z^2}$. Combining Eqs. (2.17) to (2.19), we can then write, for the \hat{x} -direction

$$l \left(\frac{d\nu}{dt} \right)^2 \left(\frac{d^2x}{d\nu^2} - 2 \frac{dy}{d\nu} \right) + \left(\frac{dx}{d\nu} - y \right) \left(l \frac{d^2\nu}{dt^2} + 2 \frac{d\nu}{dt} \frac{dl}{dt} \right) + x \left(\frac{d^2l}{dt^2} - l \left(\frac{d\nu}{dt} \right)^2 \right) = \frac{GM}{l^2} \left(-\frac{x + \mu}{r_1^3} (1 - \mu) - \frac{x - (1 - \mu)}{r_2^3} \mu \right). \quad (2.20)$$

Recalling the simplifications calculated in Eqs. (2.11), (2.12), and (2.14), we can arrive at the dimensionless equation of motion in the x -direction

$$x'' - 2y' = \frac{1}{1 + e \cos \nu} \left(x - \frac{x + \mu}{r_1^3} (1 - \mu) - \frac{x - (1 - \mu)}{r_2^3} \mu \right), \quad (2.21)$$

where $\square' = \frac{d\square}{d\nu}$ is the differentiation with respect to the true anomaly. Applying the same process in the y - and z -directions, we arrive at the dimensionless equations of motion for these directions, respectively

$$y'' + 2x' = \frac{1}{1 + e \cos \nu} \left(y - \frac{y}{r_1^3} (1 - \mu) - \frac{y}{r_2^3} \mu \right), \quad (2.22)$$

$$z'' + z = \frac{1}{1 + e \cos \nu} \left(z - \frac{z}{r_1^3} (1 - \mu) - \frac{z}{r_2^3} \mu \right). \quad (2.23)$$

We can also write

$$x'' - 2y' = \frac{\partial \omega}{\partial x}, \quad (2.24a)$$

$$y'' + 2x' = \frac{\partial \omega}{\partial y}, \quad (2.24b)$$

$$z'' + z = \frac{\partial \omega}{\partial z}, \quad (2.24c)$$

with

$$\omega = \frac{1}{1 + e \cos \nu} \left(\frac{1}{2} (x^2 + y^2 + z^2) + \frac{1 - \mu}{r_1} + \frac{\mu}{r_2} \right). \quad (2.25)$$

An alternative formulation proposed in [67] that is closer to the form of the equations for the CR3BP is

$$x'' - 2y' = \frac{\partial \psi}{\partial x}, \quad (2.26a)$$

$$y'' + 2x' = \frac{\partial \psi}{\partial y}, \quad (2.26b)$$

$$z'' = \frac{\partial \psi}{\partial z}, \quad (2.26c)$$

with

$$\psi = \frac{1}{1+e\cos\nu} \left(\frac{1}{2} (x^2 + y^2 - ez^2 \cos\nu) + \frac{1-\mu}{r_1} + \frac{\mu}{r_2} \right). \quad (2.27)$$

Finally, note that because the system is non-autonomous, it no longer possesses an integral of motion. One can, nevertheless, analyze pulsating subregions of motions and perform transformations to yield equivalents of an energy constant [21, 67].

Elliptic Hill Problem: As the name suggests, the Elliptic Hill Problem (EHP) is an extension of the Hill Problem, or, in the same way, a specific case of the ER3BP. The equations of motion are derived directly from the ER3BP by taking the same approximations that are taken for the Hill Problem, where the motion is approximated to the vicinity of the secondary body, with $\frac{m_2}{m_1} \ll 1$. We can write the dimensionless equations of motion of the EHP from Eq. (2.8) using

$$[\text{LU}] = \left(\frac{\mu_2}{\dot{\nu}^2} \right)^{1/3} = \left(\frac{\mu_2}{\mu_1} \right)^{1/3} l, \quad (2.28a)$$

$$[\text{TU}] = 1/\dot{\nu}, \quad (2.28b)$$

where l and $\dot{\nu}$ are the same as for the ER3BP, defined in Eqs. (5.1) and (5.2), respectively. The dimensionless equations of motion then become

$$x'' - 2y' = \frac{1}{1+e\cos\nu} \left(3x - \frac{x}{r^3} \right), \quad (2.29a)$$

$$y' + 2x' = \frac{1}{1+e\cos\nu} \left(-\frac{y}{r^3} \right), \quad (2.29b)$$

$$z'' = \frac{1}{1+e\cos\nu} \left(-z - \frac{z}{r^3} \right), \quad (2.29c)$$

where again the superscript $\square' = d/d\nu$ represents differentiation with respect to the true anomaly ν .

Bicircular Restricted Four-Body Problem: Taking the CR3BP as a starting point, one can arrive at the so-called Bicircular Restricted Four-Body Problem (BCR4BP), or simply the Bicircular problem for short, by adding the perturbation of a third body that moves in a circular orbit about the barycenter of the primary and secondary. Although the model is not coherent, i.e. the motion of the three-bodies does not describe a solution of the three-body problem as the effect of the third body's gravity on the other two bodies is neglected, it can be a good approximation of the dynamics as a simplified restricted four-body model. It is often applied in the context of the Earth-Moon-Sun system in order to include both the Earth-Moon and the Earth-Sun dynamics [26, 58]. A schematic representation of the problem's geometry applied to the Earth-Moon-Sun case can be seen in Figure 2.4, viewed from the co-rotating or *synodic* reference frame (which rotates with the Earth and Moon) centered on the Earth-Moon barycenter.

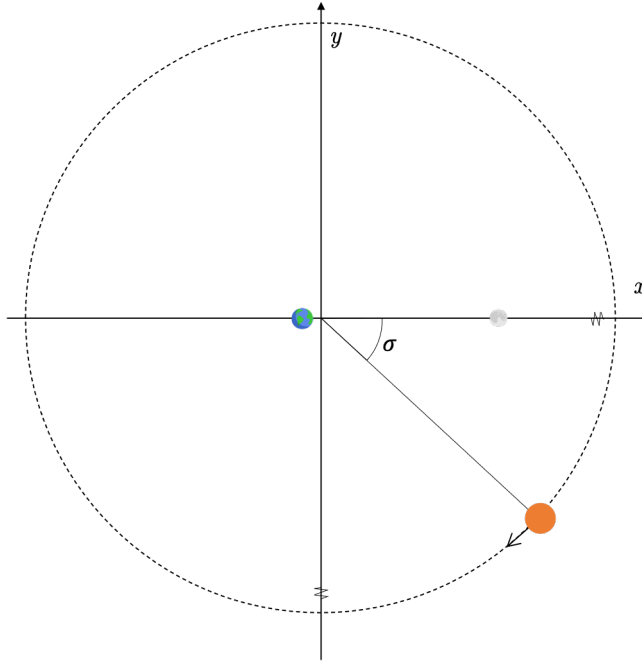


Figure 2.4: Representation of the Bicircular problem in its rotating reference frame. The Sun angle σ is measured clockwise from the Earth-Moon line (x -axis).

The Bicircular problem represents a periodic system, characterized by its synodic frequency or period, i.e. the rate at which the relative positions of the three primary bodies repeat, which is given by $\Omega_3 = n - n_3$, where n is the mean motion of the primary and secondary and n_3 is the third body's mean motion. In addition to using the same rotating frame as the CR3BP, the Bicircular problem uses the same the same length, time, and mass units. Following [43], we can write the normalized equations of motion as

$$x'' - 2y' = \frac{\partial\psi}{\partial x}, \quad (2.30a)$$

$$y'' + 2x' = \frac{\partial\psi}{\partial y}, \quad (2.30b)$$

$$z'' = \frac{\partial\psi}{\partial z}, \quad (2.30c)$$

with

$$\psi = \frac{1}{2} (x^2 + y^2) + \frac{1-\mu}{r_1} + \frac{\mu}{r_2} + \frac{\mu_3}{r_3} - \frac{\mu_3}{a_3^3} (x_3 x + y_3 y + z_3 z), \quad (2.31)$$

where $\mu_3 = \frac{m_3}{m_1+m_2}$ is the normalized Sun mass, a_3 is the normalized semi-major axis of the third body's orbit, $[x_3, y_3, z_3]^T$ is the position vector of the third body in the rotating frame, and $r_3 = \sqrt{(x - x_3)^2 + (y - y_3)^2 + (z - z_3)^2}$ is the distance between the spacecraft and the third body. The other variables, r_1 , r_2 , and μ , are defined as for the CR3BP case. To compute the

position of the third body in the pulsating frame we use

$$\begin{cases} x_3 = a_3 \cos \sigma, \\ y_3 = -a_3 \sin \sigma, \\ z_3 = 0, \end{cases} \quad (2.32)$$

where σ is the angular position of the third body in the rotating frame, as shown in Figure 2.4, noting the minus sign for y_3 as the third body moves in a clockwise direction around the primary-secondary barycenter. Alternatively, the minus sign for y_3 can be omitted and added in the body's angular velocity. Because the third body's orbit is circular, it moves at a constant angular rate, Ω_3 , which can be written in normalized coordinates as

$$\dot{\sigma} = \frac{n - n_3}{n} \quad (2.33)$$

recalling that the time unit is $[\text{TU}] = 1/n$. Note that although we can simply integrate the equations of motion as is by writing $\sigma(t) = \sigma_0 + \dot{\sigma}t$, it may be beneficial for the convergence of some numerical algorithms to integrate the *sine* and *cosine* components of σ . That is, we can write $c = \cos \sigma$ and $s = \sin \sigma$ and append c and s to our state-vector, integrating the new variables as

$$\frac{dc}{dt} = -s \dot{\sigma}, \quad (2.34a)$$

$$\frac{ds}{dt} = c \dot{\sigma}. \quad (2.34b)$$

Once again, since the system is non-autonomous, it does not have an integral of motion, as was the case with the other periodic systems presented.

2 Additional perturbations

Different perturbations can be considered in order to render simplified astrodynamics problems closer to the real dynamics while maintaining a degree of simplicity that allows for the systematic computation of families of dynamical solutions. It should be noted that all the perturbations hereby addressed are framed in either the context of a constant perturbation or (a combination of) periodic perturbations. This allows us to construct periodic or quasi-periodic dynamical systems that admit natural dynamical solutions such as quasi-periodic tori. The inclusion of non-periodic perturbations, such as the use of a pre-computed ephemeris position for a perturbing body, would disrupt this possibility.

The eccentricity of the primaries' orbits is one possible perturbation, addressed in the previous section under the formulation of elliptical problems ([ER3BP](#), [EHP](#)). As with all other perturbations, its inclusion in the dynamical model depends on the relative significance it poses with respect to the other perturbations of the system. The perturbation is periodic since it makes the distance between the two primaries vary as a function of their true anomaly, which

makes the system time-dependent.

Additionally, one can include different gravity potential models for the primary bodies. Note that in Section 1 only standard point-mass gravity potentials were considered for describing the bodies, although different models can easily be used instead. Examples of different gravity potential models include the spherical harmonics model [95], the constant density triaxial ellipsoidal model [95], and the constant density polyhedron model [106]. Depending on the type of trajectories being considered, as well as the mission design phase, different models can be considered. The work developed in [101] shows examples of mission design considering only one massive body, usually an asteroid or a comet, where high-fidelity gravity modeling is implemented in the context of the deployment of scientific packages to the surfaces of these bodies. We note that although high-fidelity gravity modeling is not used in this thesis, it could easily be implemented and treated as a periodic perturbation to the system, in the same way as the other perturbations addressed in this thesis. In that case, the period of the perturbation would correspond to the body's spin period.

Another common perturbation, which is especially significant when considering the dynamics about asteroids and comets, is that posed by [Solar Radiation Pressure \(SRP\)](#). Due to the small mass of these bodies, the acceleration imparted by SRP can significantly affect the dynamics. In the same way, eclipses also become important to consider. These factors can significantly alter the geometry of periodic orbits [37], as well as their stability [104]. We can write the acceleration caused by SRP on a body as [70]

$$\mathbf{a}_{SRP} = -\frac{C_r W_E R_{AU}^2}{B c d_S^2} \cos^2 \alpha \hat{\mathbf{n}}, \quad (2.35)$$

where C_r is the reflectivity coefficient, $W_E = 1368 \text{ J s}^{-1}\text{m}^{-2}$ is the solar irradiance, R_{AU} is the distance of 1 AU, B is the mass-to-area ratio of the body under the influence of SRP, c is the speed of light, \mathbf{d}_S is the vector from the Sun to the body, α is the angle between the incident radiation and the surface normal, and $\hat{\mathbf{n}}$ is the surface normal. A common approximation when modeling spacecraft is to use a *cannonball* model, i.e. to assume that the body is spherical. This gets rid of the need to track the spacecraft's attitude and simply assumes an average mass-to-area ratio over the whole body. Eq. (2.35) then simplifies to

$$\mathbf{a}_{SRP} = \frac{C_r W_E R_{AU}^2}{B c} \frac{\mathbf{d}_S}{d_S^3}. \quad (2.36)$$

Depending on the problem used and whether the Sun is the primary body or not, the perturbation posed by the SRP can be considered to be constant, e.g. for the case of the Hill Problem applied to an asteroid orbiter with SRP, also known as the [Augmented Hill Problem \(AHP\)](#), or position/time dependent (considering the Sun as a non-central body, the SRP would act along the same vector as the Sun's gravitational acceleration but with opposite sign).

Finally, one can also consider the presence of additional bodies in the dynamical system. A common example that was previously presented and will be addressed again later in this thesis is that of the cislunar environment. Indeed, as was seen, one way of modeling the cislunar

environment is to use the Bicircular model and include the Sun as the third body. Other such models exist where additional bodies are added as a perturbation to the dynamics. An example is the Hill Four-Body Problem [95, 82], where the Hill Problem is used as a starting point and an additional body is then introduced to the model.

To sum up, the perturbations to be considered in this thesis can be modeled, in general, using the formulation

$$\mathbf{f}(\mathbf{X}, t) = \mathbf{f}_0(\mathbf{X}, t) + \mathbf{f}_c + \mathbf{f}_p(\mathbf{X}, t), \quad (2.37)$$

where \mathbf{f}_0 represents the base model or problem, \mathbf{f}_c are possible constant perturbations, and \mathbf{f}_p represents possible periodic perturbations.

3 Periodic orbits

The definition of a periodic orbit can be written as follows:

$$\mathbf{X}_t = \varphi(\mathbf{X}_t, t + T), \quad (2.38)$$

where T is the smallest period that verifies equation and \mathbf{X}_t is a state along the periodic orbit at some time t . When considering time-independent autonomous systems, such as the CR3BP or the Hill Problem, periodic orbits can be found in one-parameter families. That is, one parameter can be used to describe the family along its family curve. As an example, one can consider the (southern) Halo family of the CR3BP [50]. Its family curve can be plotted using, for instance, the period and the Jacobi constant of each orbit along the family, as seen in Figure 2.5, where the period is given in normalized coordinates. Note that this defines a one-dimensional curve, which can be described by a single parameter along the family. This parameter can sometimes be the orbit period, but since we can have inflection points along the family's orbital parameters, it is more common and accurate to use the *pseudo-arclength* parameter [97], which will be defined in what follows.

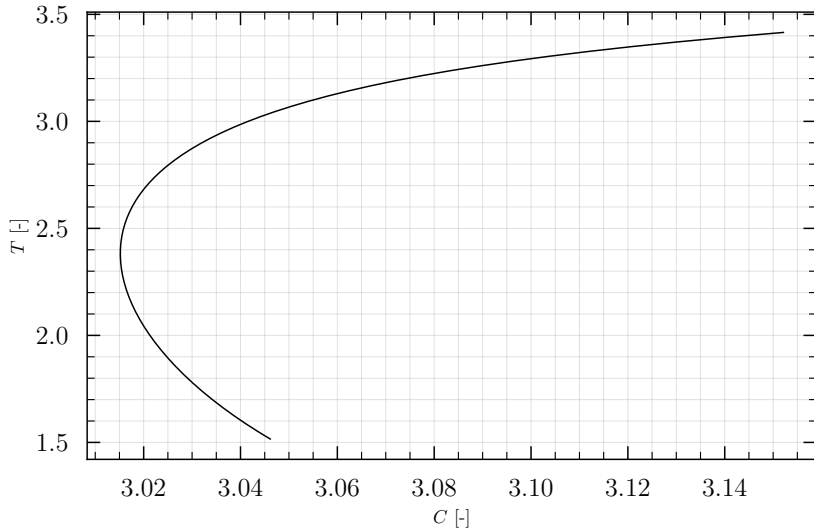


Figure 2.5: The family curve of the CR3BP’s southern Halo family.

Additionally, if the system admits an integral of motion, such as the CR3BP, periodic orbit families can be initialized from the eigenspace of equilibrium points that admit a purely imaginary eigenvalue pair via the Lyapunov Theorem [71] with a period of $T = 2\pi/b$, where b is the imaginary part of said eigenvalue pair.

3.1 Numerical continuation

In this thesis, different numerical methods arising from the field of DST are leveraged to compute natural solutions and to build dynamical models that are closer to reality. One such tool is the numerical continuation of solutions by means of predictor-corrector algorithms. Specifically, we can make use of Ordinary Differential Equations (ODEs) to integrate predicted solutions and then correct these guesses using the Newton-Raphson method, also known as Newton’s method. The work by Doedel et al. [32, 33] uses these formulations in their numerical continuation software AUTO to perform detailed studies of periodic orbits in Hamiltonian systems. In this line, one way of computing families of periodic orbits is to solve the Boundary Value Problem (BVP) associated with Eq. (2.38) under the equations of motion defined by the system in Eq. (2.1) as

$$\mathbf{g}(\mathbf{X}_0, T) = \varphi_T(\mathbf{X}_0) - \mathbf{X}_0 = \mathbf{0}, \quad (2.39)$$

where φ_T is the solution flow after T and $\mathbf{g} : \mathbb{R}^n \times \mathbb{R} \rightarrow \mathbb{R}^n$, assuming that any external parameters are known. It is common to normalize the equations with respect to the period such that $\tau = Tt$, where $\tau \in [0, 1]$, as it allows for the unknown T to appear explicitly in the equations of motion as

$$\mathbf{X}' = \frac{d\mathbf{X}}{d\tau} = T\mathbf{f}(\mathbf{X}). \quad (2.40)$$

In addition to Eq. (2.39), we need two more equations in order to solve the **BVP**; one is necessary because the period is not known, meaning we have n equations but $n + 1$ unknowns, while the other is necessary to fix the initial point or phase along the periodic orbit and is commonly known as a phase condition. One possible formulation for the phase condition is the classical Poincaré phase condition [32]:

$$p(\mathbf{X}_0) = \mathbf{f}(\tilde{\mathbf{X}})^T (\mathbf{X}_0 - \tilde{\mathbf{X}}_0), \quad (2.41)$$

where $\tilde{\mathbf{X}}$ is a previously known solution (or an approximation of a solution). The last equation to be added is known as the pseudo-arclength continuation equation [97], which makes use of the family curve to compute different members along the family, separated by a user-defined step size:

$$q(\mathbf{X}_0, T) = (\mathbf{X}_0 - \tilde{\mathbf{X}}_0)^T \frac{\partial \tilde{\mathbf{X}}_0}{\partial h} + (T - \tilde{T}) \frac{\partial \tilde{T}}{\partial h} - \delta s, \quad (2.42)$$

where h is the arclength parameter that steps along the family curve, $\partial \tilde{\mathbf{z}} / \partial h$ is the family tangent at the known solution, with $\tilde{\mathbf{z}} = [\tilde{\mathbf{X}}_0; \tilde{T}]^T$, and δs is the user-defined stepsize along the family. In order to compute the family tangent we can compute the null space of Jacobian $D\mathbf{H}$ at the known solution $\tilde{\mathbf{z}}$, where \mathbf{H} is the reduced matrix of the **BVP** system:

$$\mathbf{H}(\tilde{\mathbf{z}}) = \begin{bmatrix} \mathbf{g}(\tilde{\mathbf{z}}) \\ p(\tilde{\mathbf{z}}) \end{bmatrix} = \mathbf{0}. \quad (2.43)$$

Assuming that \mathbf{H} depends implicitly on the arclength parameter, h , we can find $\partial \tilde{\mathbf{z}} / \partial h$ from the null space of $D\mathbf{H}$ via the chain rule as

$$\frac{\partial \mathbf{H}}{\partial h} = \frac{\partial \mathbf{H}}{\partial \tilde{\mathbf{z}}} \frac{\partial \tilde{\mathbf{z}}}{\partial h} = D\mathbf{H}(\tilde{\mathbf{z}}) \frac{\partial \tilde{\mathbf{z}}}{\partial h} = \mathbf{0}. \quad (2.44)$$

Then, the full **BVP** can be formed as

$$\mathbf{F}(\mathbf{z}) = \begin{bmatrix} \mathbf{g}(\mathbf{z}) \\ p(\mathbf{z}) \\ q(\mathbf{z}) \end{bmatrix}. \quad (2.45)$$

The problem is then corrected iteratively until $\|\mathbf{F}\| < \epsilon$, where ϵ is an user-defined error tolerance, via Newton's method

$$\delta \mathbf{z} D\mathbf{F}(\mathbf{z}) = -\mathbf{F}(\mathbf{z}), \quad (2.46)$$

where $\delta \mathbf{z}$ is the correction to be applied, and for which Eq. (2.46) is solved for. Once a solution is found, a new guess along the family can be found as

$$\mathbf{z}^{k+1} = \mathbf{z}^k + \frac{\partial \mathbf{z}^k}{\partial h} \delta s, \quad (2.47)$$

where \mathbf{z}^k is the newly found solution. A simple check can also be made to ensure that the family tangent, $\frac{\partial \mathbf{z}^k}{\partial h}$, points in the desired direction along the family curve:

$$d = \text{sign}\left\{ \langle \mathbf{z}^k - \mathbf{z}^{k-1}, \frac{\partial \mathbf{z}^k}{\partial h} \rangle \right\}. \quad (2.48)$$

4 Stability and hyperbolic invariant manifolds

When analyzing periodic orbits, it is often valuable to study their stability. It is possible to do so by analyzing their [State Transition Matrix \(STM\)](#), $\Phi(t)$, defined as [73]

$$\Phi(t) = \frac{d\varphi_t(\mathbf{X}_0)}{d\mathbf{X}_0}, \quad (2.49)$$

which maps the variations with respect to the initial \mathbf{X}_0 forward in time along the orbit. The stability information is obtained when the [STM](#) is integrated over one full period of the periodic orbit defined by (\mathbf{X}_0, T) , at which point we obtain what is called the Monodromy matrix, $\mathbf{M} = \Phi(T)$. Starting from Eq. (2.49), the Monodromy matrix can be computed by integrating the following ordinary differential equation

$$\dot{\Phi}(t) = \mathbf{A}(t)\Phi(t), \quad (2.50)$$

where \mathbf{A} is the Jacobian of the equations of motion at some time t

$$\mathbf{A}(t) = \frac{\partial \mathbf{f}(\mathbf{X}, t)}{\partial \mathbf{X}}. \quad (2.51)$$

Knowing that $\Phi(t_0) = \mathbf{I}_n$, the identity matrix, Eq. (2.49) can be integrated from t_0 to T to obtain \mathbf{M} . For the Hamiltonian systems considered in this thesis, all the eigenvalues of M occur in reciprocal pairs of the type $(\lambda, 1/\lambda)$ [95]. Because linear stability is attained only for $||\lambda_i|| \leq 1$, all the eigenvalues must be on the unit circle for a periodic orbit to be considered linearly stable. Additionally, for autonomous Hamiltonian systems as the [CR3BP](#) or the Hill Problem, which permit a time-invariant integral of motion, there always exists a unity eigenvalue pair [18].

When considering unstable periodic orbits, non-unity eigenvalue pairs define hyperbolic directions that can be used to compute hyperbolic stable – associated with an eigenvalue smaller than unity – and unstable – associated with an eigenvalue larger than unity – invariant manifolds [60]. These trajectories depart or arrive at the orbit along the local hyperbolic eigenvector direction as $t \rightarrow \infty$ when an infinitesimal perturbation ε is applied in said directions. In theory this establishes a way of arriving to or departing from a periodic orbit without using any fuel. Although in practice some correction maneuvers are necessary, they are typically very small when compared to traditional transfer maneuvers. Previous missions, such as the Genesis mission [66] and others [23] have taken advantage of this dynamical system property to design cheap transfer trajectories. The eigenvectors associated with the stable and unstable directions of an hyperbolic eigenvalue pair, \mathbf{v}^S , \mathbf{v}^U , respectively, can be propagated along the periodic

orbit to any point $t = t_i$ using the STM as [60]

$$\mathbf{v}^{S,U}(t_i) = \Phi(t_i)\mathbf{v}^{S,U}. \quad (2.52)$$

Then, the linearly approximated initial conditions for the hyperbolic manifolds from a point $\mathbf{X}_i = \varphi_{t_i}(\mathbf{X}_0)$ along the orbit become

$$\mathbf{X}_i^{S,U} = \mathbf{X}_i \pm \varepsilon \frac{\mathbf{v}_i^{S,U}}{\|\mathbf{v}_i^{S,U}\|}. \quad (2.53)$$

where ε is a small perturbation. With this formulation, we can integrate the initial conditions of the stable and unstable manifolds backwards and forwards in time, respectively, to yield the hyperbolic manifolds of unstable periodic orbits, such as the ones seen in Figure 2.6 for the case of a Lyapunov planar orbit in the context of the Hill Problem.

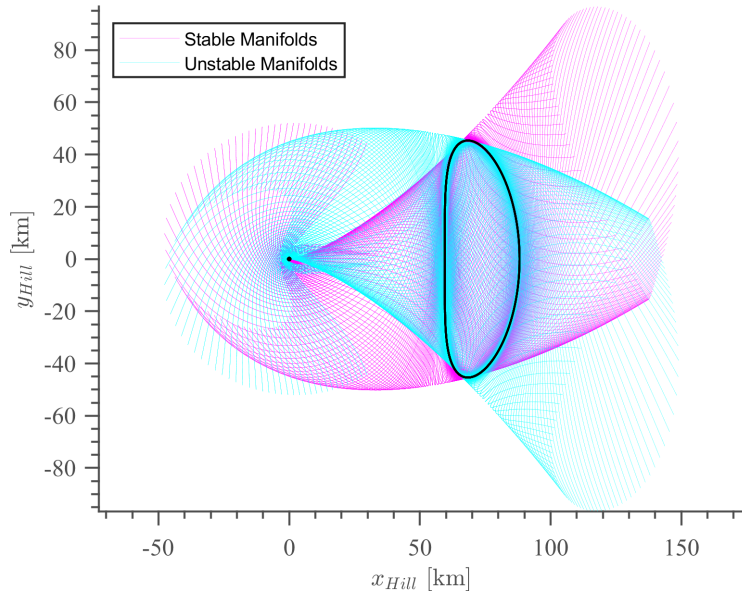


Figure 2.6: The hyperbolic invariant manifolds of a Lyapunov planar orbit in the Hill Problem.

5 Quasi-periodic tori

Quasi-periodic trajectories can be described by the motion that covers a two- or higher-dimensional invariant torus as time tends to infinity. This torus exists in phase space \mathbb{T}^d , where d is the dimension of the torus. In fact, there exists a diffeomorphism $\mathbf{u}(\boldsymbol{\theta}) : \mathbb{T}^d \rightarrow \mathbb{R}^n$ that maps points from the surface of the d -dimensional torus to states in the n -dimensional phase space of our dynamical system, and vice-versa. A representation of this diffeomorphism can be seen in Figure 2.7, where this mapping is represented. Computing a quasi-periodic torus is equivalent to finding the diffeomorphism \mathbf{u} and the torus frequencies that characterize it. The angular coordinates $\boldsymbol{\theta} = \{\theta_0, \dots, \theta_{d-1}\}$ parametrize the torus in each of its d dimensions and have

modulus 2π under \mathbf{u} , such that

$$\mathbf{u}(\theta_i, \cdot) = \mathbf{u}(\theta_i + 2\pi, \cdot), \quad (2.54)$$

where θ_i represents one of the torus angles and the others remain unchanged. The frequencies $\boldsymbol{\omega} = \dot{\boldsymbol{\theta}}$ represent the incommensurate constant torus frequencies that uniquely identify the quasi-periodic solution among different quasi-periodic candidates. A periodic orbit is a one-dimensional torus ($d = 1$), where $\boldsymbol{\theta} = \theta_0$ represents the longitudinal angle along the curve and $\omega_0 = 2\pi/T$ is equivalent to the orbit's mean motion, where T is the orbit's period. Similarly, an equilibrium point is a zero-dimensional torus. A two-dimensional torus, such as the one

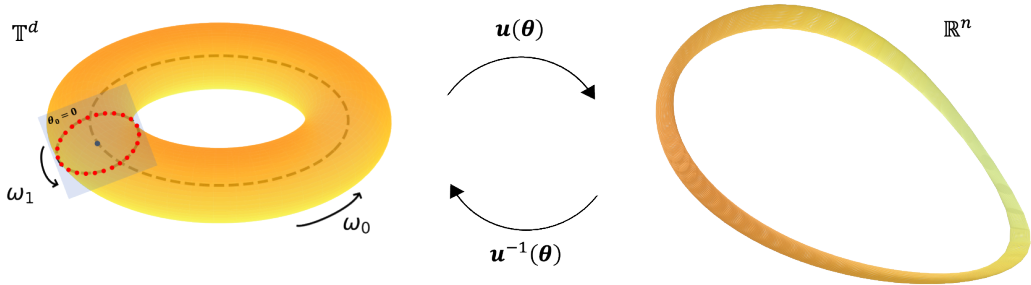


Figure 2.7: Example of a two-dimensional torus in \mathbb{T}^2 and the diffeomorphism \mathbf{u} that transforms the torus to and back from \mathbb{R}^n . The initial invariant circle is represented in red at $\theta_0 = 0$.

in Figure 2.7, is then described by two angular directions. Each torus frequency gives us the rotation of their respective angle as a function of time. Note that in this thesis we focus only on torus frequencies that are incommensurate so as to preserve the d -dimensional quasi-periodic motion, and assume that the more rigorous conditions of non-degeneracy and analyticity are preserved [55]. Because the frequencies are incommensurate, a trajectory on the surface of a quasi-periodic torus will cover its surface completely as time tends to infinity. A full $\Delta\theta_0 = 2\pi$ rotation along the ω_0 direction takes a time $T = 2\pi/\omega_0$; we can then verify that after T , the angle θ_1 will have rotated by $\rho_1 = \omega_1 T = \omega_1 2\pi/\omega_0$, where $\boldsymbol{\rho} = \{\rho_1, \dots, \rho_{d-1}\} = \{\omega_1 T, \dots, \omega_{d-1} T\}$ is usually referred to as the rotation vector. Since ρ_1 is not a rational number, the value of θ_1 after any number of revolutions $\Delta\theta_0 = 2\pi$ will never repeat. When considering two-dimensional tori it is common to refer to $\boldsymbol{\rho}$ as the rotation number instead of rotation vector, as $\boldsymbol{\rho} = \rho_1 = \rho$.

Quasi-periodic tori can be computed from different settings. One possibility is that they emanate from the center manifolds of periodic orbits or equilibrium points, which are defined by unitary complex eigenvalue pairs. Considering that quasi-periodic tori are of dimension two or higher, a periodic orbit with one center eigenvalue pair will generate a family of two-dimensional quasi-periodic tori, while a periodic orbit with two center eigenvalue pairs will generate a family of three-dimensional tori. Likewise, since an equilibrium point is a zero-dimensional torus, two center eigenvalue pairs are required to generate a two-dimensional quasi-periodic tori family from it. In the example of a periodic orbit with a single unitary complex eigenvalue pair, a quasi-

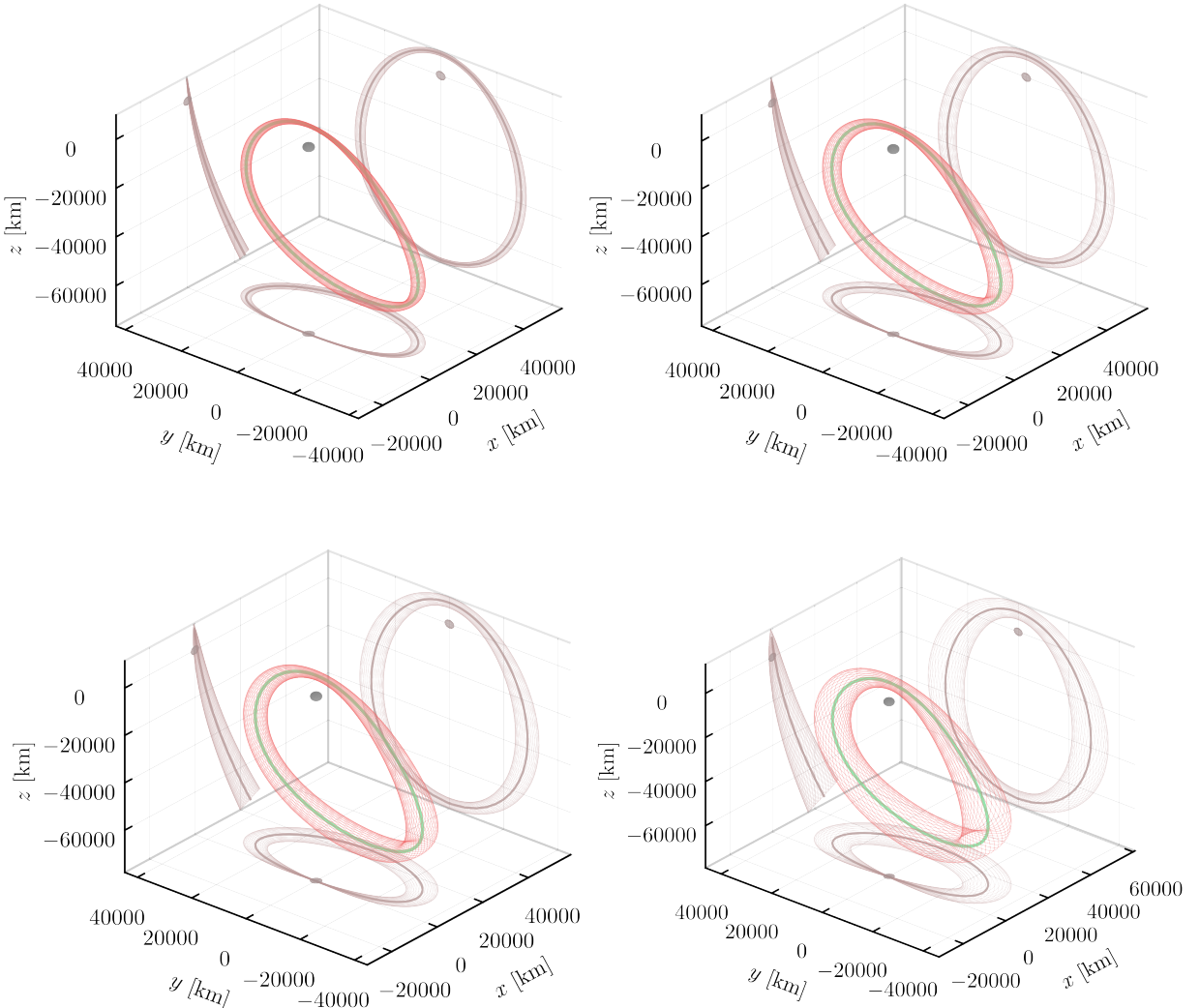


Figure 2.8: Members of a two-dimensional quasi-Halo family (in red) and the periodic Halo orbit (in green) from which the family originates in the Earth-Moon’s CR3BP. Plotted in the co-rotating frame centered on the Moon.

periodic tori family can be generated by initializing the first family member’s fundamental or longitudinal period equal to that of the periodic orbit and the second torus frequency given as a function of the angle of the complex number [81, 5] (a more detailed explanation on the initialization of quasi-periodic motion will be given in Chapter 3). An example of a few members of a two-dimensional quasi-Halo family can be seen together with the periodic Halo orbit from which the family originates in Figure 2.8, which were computed in the Earth-Moon’s CR3BP and are plotted in the co-rotating reference frame centered on the Moon.

Additionally, a d -dimensional quasi-periodic torus can also be obtained when adding a periodic perturbation to a dynamical system that admits a $(d - 1)$ -dimensional manifold. In this case, a new d -dimensional torus can generally be formed and the new torus frequency will be commensurate to that of the periodic perturbation [55], assuming that the period of the original periodic orbit is incommensurate with that of the perturbation. A simple example is the computation of a two-dimensional quasi-periodic torus in the ER3BP from a periodic orbit

of the CR3BP. In this case, the torus will be defined by two frequencies, the first associated with the periodic orbit's original period and the second with the period of the ER3BP. An example of such a case, for an L₂ southern Halo orbit in the Earth-Moon's CR3BP and its corresponding quasi-periodic tori in ER3BP for different values of eccentricity can be seen in Figure 2.9.

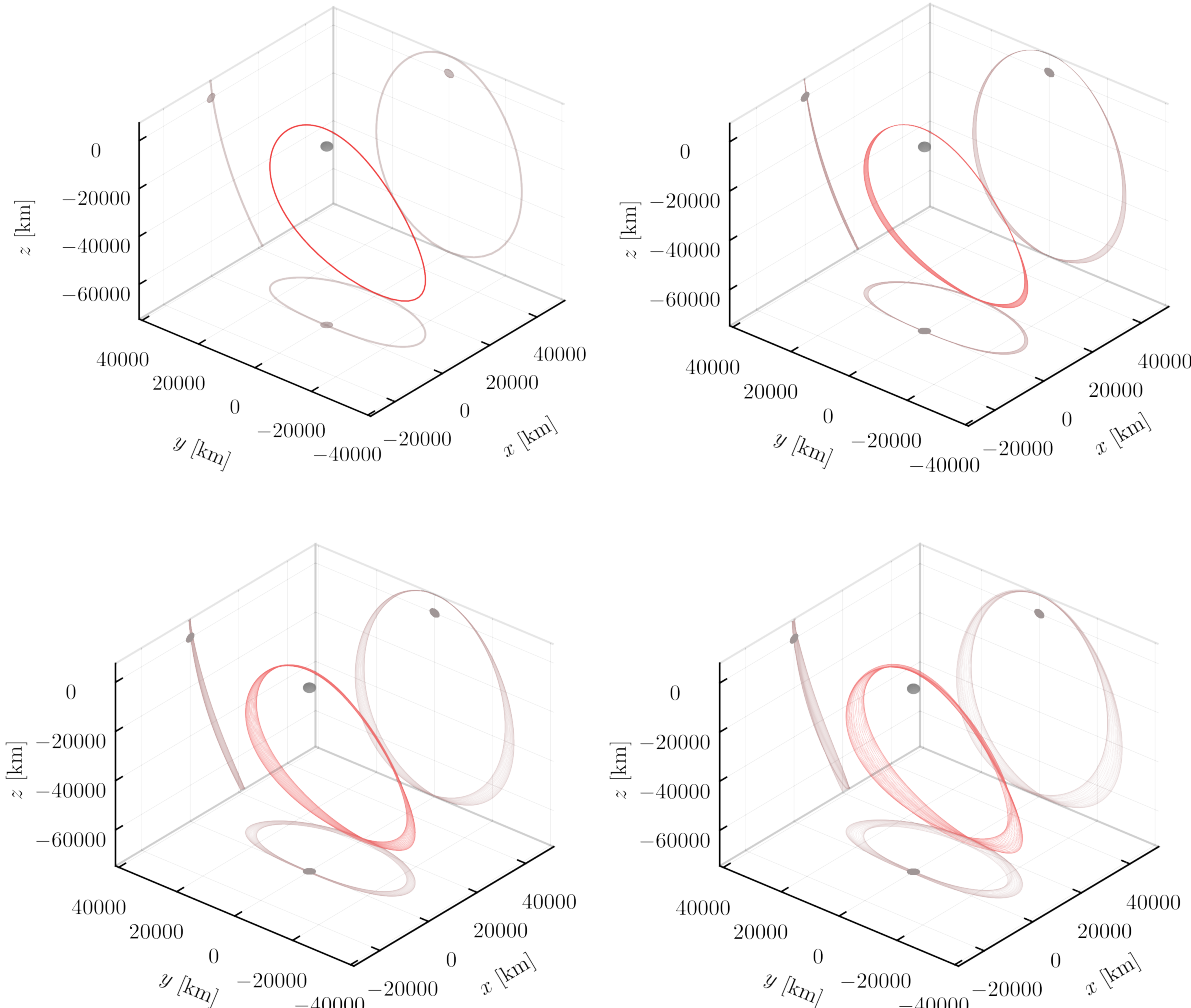


Figure 2.9: L₂ southern quasi-Halo computed for incrementing values of eccentricity in the Earth-Moon ER3BP – (b), (c), (d) – from a periodic Halo of the CR3BP – (a). Plotted in Moon-centered co-rotating frame.

Although both presented formulations for the initialization of quasi-periodic tori are addressed in this thesis, it is the latter formulation that truly encompasses the advantage of periodic orbits for trajectory design in perturbed environments. The ability to incorporate perturbations into the formulation of our trajectories allows us to describe and predict the motion of spacecraft more accurately and with more possibilities for mission design. This property is leveraged later in this thesis for applications in the cis-lunar environment.

Finally, it is important to mention after this introduction to quasi-periodic motion, that we do not attempt to rigorously prove the existence of the quasi-periodic tori computed and studied in this thesis under the principles and standards of KAM theory [65]. This would require a deeper

analysis and understanding of the underlying mathematical and dynamical structures of these Hamiltonian systems. Because the aim of this thesis is its applicability to real missions rather than fundamental research, the knowledge and methods borrowed from DST remain numerical and practical in their nature, serving the goal proposed.

Chapter 3

Contributions to the numerical computation of quasi-periodic tori

In this chapter, contributions to two numerical methods used to compute quasi-periodic tori are presented; namely, to a method based on [Partial Differential Equation \(PDE\)](#) and the [Discrete Fourier Transform \(DFT\)](#), known as [PDE\(DFT\)](#) [8], and to another based on the stroboscopic mapping of invariant curves via a [Boundary Value Problem \(BVP\)](#) formulation, known as GMOS after its creators [42, 83]. We begin by describing the two possible initialization schemes for quasi-periodic motion in Section 1, which is followed by the core formulation of the PDE(DFT) and GMOS methods in their standard forms in Sections 2 and 3, respectively. Then, in Section 4 the typical additional equations that must be added to the formulation of either algorithm are introduced. Section 5 presents the modifications to the two base algorithms implemented in this thesis, followed by an analysis on their computational performance with and without the modifications in Section 6. Later, in Section 7, we open the door to possible applications of these algorithms in astrodynamics, where we explore a short example for Phobos' exploration in the context of the [Martian Moons eXploration \(MMX\)](#) mission. Lastly, Section 8 presents the conclusions of this chapter and sums up its main results.

1 Initialization of quasi-periodic motion

As mentioned in Chapter 2, quasi-periodic motion can originate either from a center manifold or from the forcing of a periodic perturbation to a lower dimensional torus, such as a periodic orbit, which generally increases the dimension of said torus and forces one of the quasi-periodic torus' frequencies to be that of the perturbation [55].

For the first case, one can extract quasi-periodic motion from the center eigenspace of an elliptic manifold, i.e. the complex unitary eigenvalue pair of an equilibrium point or periodic orbit. Let us recall the formalism $\mathbf{u}(\boldsymbol{\theta}) : \mathbb{T}^d \rightarrow \mathbb{R}^n$ that defines the diffeomorphism and the constant incommensurate angular frequencies $\boldsymbol{\omega} = \dot{\boldsymbol{\theta}}$ that uniquely identify the torus. Likewise, $\boldsymbol{\rho} = \{\omega_1 T, \dots, \omega_{d-1} T\}$ is the rotation vector. Then, considering a periodic orbit with period T ,

let $\tilde{\mathbf{v}}$ be the eigenvector associated with a pair of complex unitary eigenvalues, $\tilde{\lambda}_0, \tilde{\lambda}_1$, such that $\tilde{\lambda}_0, \tilde{\lambda}_1 = e^{\pm j\alpha}$, where α is the phase angle of the eigenvalues and j is the imaginary number. We can then approximate the invariant curve, $\psi(\theta_1)$,

$$\psi(\theta_1) = \cos(\theta_1) \operatorname{Re}(\tilde{\mathbf{v}}) - \sin(\theta_1) \operatorname{Im}(\tilde{\mathbf{v}}), \quad (3.1)$$

which defines the quasi-periodic directions/circle with respect to the initial state of the periodic orbit, i.e. at $\theta_0 = 0$, towards the linear approximation of the torus' surface [8, 82]. A representation of a quasi-periodic torus and its initial invariant circle about a periodic orbit in \mathbb{T}^2 can be seen in Figure 3.1.

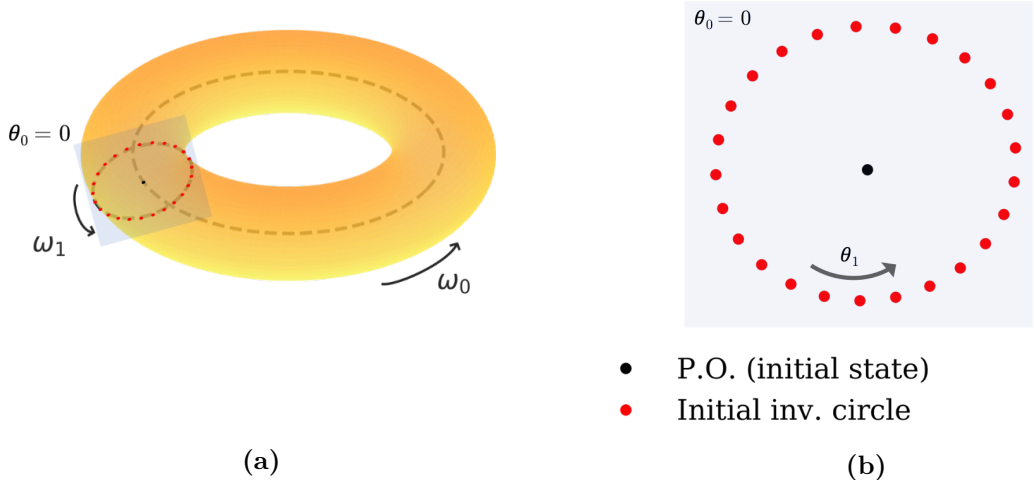


Figure 3.1: Initial invariant circle about periodic orbit: (a) in \mathbb{T}^2 , plotted on the torus at $\theta_0 = 0$ with the periodic orbit represented by the dotted line and (b) for the surface of section at $\theta_0 = 0$.

For the initialization of the **PDE(DFT)** algorithm we actually need to obtain invariant circles at different values of θ_0 . In that case, it suffices to propagate the eigenvector $\tilde{\mathbf{v}}$ throughout the orbit by means of the **STM**. However, note that the invariant circle rotates at a rate of ω_1 , such that

$$\varphi_t(\mathbf{u}(\theta_0(0), \theta_1)) = \mathbf{u}(\theta_0(t), \theta_1 + \omega_1 t), \quad (3.2)$$

under the influence of the torus' actions. We can remove the rotation so that all discretized invariant circles computed at different values of θ_0 land on a orthogonal regular grid by propagating the unitary eigenvector while undoing the rotation as

$$\tilde{\mathbf{v}}_k = e^{-j\omega_1 t_k} \Phi(t_k) \tilde{\mathbf{v}}, \quad (3.3)$$

where $t_k = kT/N_0$, with $k = \{0, 1, \dots, N_0 - 1\}$, and $e^{-j\omega_1 t_k}$ is the unwinding factor. We can then replace \mathbf{v} by \mathbf{v}_k in Eq. (3.1) to obtain $\psi_k(\theta_1)$. To initialize the invariant circle(s), we normalize

ψ_k and add it to a state along the periodic orbit, \mathbf{X}_k , multiplied by a step size δs as

$$\mathbf{u}_k(\theta_1) = \mathbf{X}_k + \delta s \psi_k(\theta_1)/\|\psi_k(\theta_1)\|. \quad (3.4)$$

These initial approximations and variations are used later to generate the guess for the next member of the quasi-periodic tori family and can also be employed in approximating the family tangent by means of the difference between consecutive tori. Using the aforementioned notation, the torus frequencies are initialized as

$$\omega_0 = 2\pi/T, \quad (3.5a)$$

$$\omega_1 = \alpha/T, \quad (3.5b)$$

which means that the rotation number will be initialized as $\rho = T\omega_1 = \alpha$.

In the case that a quasi-periodic tori does not originate from a center manifold but rather from the forcing of an external periodic perturbation, the initialization procedure is even simpler than for the previous case. When adding a periodic perturbation to a system we make use of what is known as homotopy continuation. By making use of this method, the procedure is organized into families of problems and solutions that depend on an artificial homotopy continuation parameter, ϵ . This parameter is tracked from the initial point, which represents the original unperturbed system, to the final point, which represents the perturbed system for which a solution is required [99]. Typically, the perturbation is added gradually to the system via said homotopy parameter, such that ϵ varies from zero to one as

$$\tilde{\mathbf{f}}(\epsilon) = (1 - \epsilon)\mathbf{f}_0 + \epsilon\mathbf{f}_p, \quad (3.6)$$

where \mathbf{f}_0 represents the original system and \mathbf{f}_p is the perturbed system. Note that for the cases explored in this thesis, \mathbf{f}_0 and \mathbf{f}_p typically have common terms, which means Eq. (3.6) can be simplified. Since $\epsilon \in [0, 1]$, the solution of the quasi-periodic torus that corresponds to $\tilde{\mathbf{f}}(0)$ will correspond to whatever lower-dimensional torus is used as a starting point. If, following the previous example, a discretized periodic orbit, X_k , is used as the one-dimensional manifold solution of the \mathbf{f}_0 system, the initial guess for the invariant circle(s) can simply be \mathbf{X}_k , repeated N_1 times for the number of discretization points used along the θ_1 direction. After the first iteration, the invariant circle(s) will naturally start deviating from \mathbf{X}_k as a function of ϵ , forming an invariant curve around the periodic orbit. For the torus frequencies, the fundamental or longitudinal frequency will be the same as before, whereas ω_1 will reflect the periodic perturbation of \mathbf{f}_p , as

$$\omega_0 = 2\pi/T, \quad (3.7a)$$

$$\omega_1 = 2\pi/T_p, \quad (3.7b)$$

where T_p is the period of the perturbation.

2 The PDE(DFT) algorithm

As indicated by its name, the **PDE(DFT)** finds the diffeomorphism \mathbf{u} and the torus frequencies $\boldsymbol{\omega}$ by employing Partial Differential Equations (**PDEs**). In turn, the **Discrete Fourier Transform (DFT)** is employed in order to compute the derivatives associated with some of these equations. Let us first assume a generic vector field $\mathbf{f}(\mathbf{X}, \boldsymbol{\xi}, t) = \dot{\mathbf{X}}$, where again $\boldsymbol{\xi}$ is some vector of additional parameters that we will ignore for now, and t represents a possible time variable. Note that in the following, we make no assumptions as to the time-dependence of the system. The methodology applies to both time-dependent and time-independent systems, where only the explicit computation of some partial derivatives changes. Replacing the state-vector \mathbf{X} with the torus \mathbf{u} in the system \mathbf{f} and applying the chain rule, we arrive at

$$\mathbf{f}(\mathbf{u}(\boldsymbol{\theta}), t) = \sum_{i=0}^{d-1} \frac{\partial \mathbf{u}}{\partial \theta_i} \frac{d\theta_i}{dt} = \sum_{i=0}^{d-1} \frac{\partial \mathbf{u}}{\partial \theta_i} \omega_i, \quad (3.8)$$

where d is the dimension of the torus. Eq. (3.8) defines the invariance equation of the quasi-periodic torus, which forms the basis of the **PDE(DFT)** method. We can then discretize the torus \mathbf{u} in $N = N_0 \times \dots \times N_{d-1}$ points, as $\mathbf{U}(\boldsymbol{\theta})$, by selecting a number of nodes N_i in each θ_i direction, e.g. $\theta_{0,n_0} = 2\pi n_0 / N_0$ for $n_0 = \{0, \dots, N_0 - 1\}$ and likewise for the other dimensions. We can then formulate the problem as

$$\mathbf{G}(\mathbf{z}) = \sum_{i=0}^{d-1} \frac{\partial \mathbf{U}}{\partial \theta_i} \omega_i - \mathbf{f}(\mathbf{U}) = \mathbf{0}, \quad (3.9)$$

where $\mathbf{z} = [\mathbf{U}, \boldsymbol{\omega}]^T$, $\boldsymbol{\omega} = \{\omega_0, \dots, \omega_{d-1}\}$. Different methods to compute the partial derivatives in Eq. (3.9) could be used; in this research, we consider the **DFT**, as advocated in [83, 8]. We can write the d -dimensional DFT as

$$\hat{\mathbf{U}}[\mathbf{k}] = \sum_{n_0=0}^{N_0-1} \dots \sum_{n_{d-1}=0}^{N_{d-1}-1} \mathbf{U}\left(\frac{2\pi\mathbf{n}}{N}\right) e^{-2\pi j(\mathbf{n} \cdot \mathbf{k}/N)}, \quad (3.10)$$

where $(\mathbf{n} \cdot \mathbf{k}/N) = (n_0 k_0 / N_0 + \dots + n_{d-1} k_{d-1} / N_{d-1})$. The **Inverse Discrete Fourier Transform (IDFT)** is then

$$\mathbf{U}(\boldsymbol{\theta}) = \frac{1}{N} \sum_{k_0=0}^{N_0-1} \dots \sum_{k_{d-1}=0}^{N_{d-1}-1} \hat{\mathbf{U}}[\mathbf{k}] e^{(\boldsymbol{\theta} \cdot \gamma(\mathbf{k}))}, \quad (3.11)$$

where $\gamma_i(k_i)$ is given by

$$\gamma_i(k_i) = \begin{cases} jk_i & \text{if } 0 \leq k_i < N_i/2, \\ j(k_i - N_i) & \text{if } N_i/2 < k_i < N_i, \\ 0 & \text{if } k_i = N_i/2, \end{cases} \quad (3.12)$$

for $i = \{0, \dots, d - 1\}$. Note that we use a different formulation of the **DFT** to that employed in [8]. This comes from the trigonometric interpolation implementation of the Fourier transform that minimizes the oscillation related to aliasing (see [54] for details) and makes the transform well-defined between the nodes, independently of whether the number of nodes is even or odd, which is not the case for previous formulations of the algorithm.

Using this formulation, we can directly take the partial derivatives with respect to θ_i from Eq. (3.11) by simply multiplying the Fourier coefficients by γ_i . However, it is not efficient to transform our function each time we wish to take the partial derivatives. Instead, note that these operations can be grouped and later multiplied directly by $U(\boldsymbol{\theta})$. Writing the transforms as separate matrix blocks, we can define the operand to obtain the partial derivative with respect to θ_i as

$$[D\theta_i] = [D^{-1}][\gamma_i][D], \quad (3.13)$$

where $[D]$ and $[D^{-1}]$ represent the **DFT** and **IDFT** matrix operations respectively. Additionally, note that we do not necessarily need to use the d -dimensional **DFT**, since we are only taking first order partial derivatives in one direction at a time. Nevertheless, the operand $[D\theta_i]$ can be pre-computed and multiplied by $U(\boldsymbol{\theta})$ to produce the relevant partial derivatives as $\partial U(\boldsymbol{\theta})/\partial\theta_i = [D\theta_i] U(\boldsymbol{\theta})$. This also makes the computation of the Jacobian matrix simpler, since we can directly take the partial with respect to U . Rewriting the invariance condition in Eq. (3.9) we arrive at

$$\mathbf{G}(\mathbf{z}) = \sum_{i=0}^{d-1} [D\theta_i] U(\boldsymbol{\theta}) \omega_i - \mathbf{f}(U) = \mathbf{0}. \quad (3.14)$$

Finally, note that when the system is time-dependent, it can occur that one of the partial derivatives $\partial \mathbf{u}/\partial\theta_i$ can either be taken explicitly (if one of the angles appears in the state-vector), or might be explicitly related to \mathbf{f} . For the latter, an example is the **ER3BP**, where the normalized system uses the true anomaly, ν , as the time variable, such that $\mathbf{f}(\mathbf{u}, \nu) = \mathbf{u}' = d\mathbf{u}/d\nu|_\nu$.

3 The GMOS algorithm

The GMOS algorithm, named after Goméz, Mondelo, Olikara, and Scheeres [42, 81], allows us to find the diffeomorphism \mathbf{u} by mapping the stroboscopic image of an invariant curve, or, in other words, by integrating an initial invariant circle (at some initial θ_0) over the stroboscopic time T , for which we then revert the rotation ρ over its other angles. It is therefore framed as **Boundary Value Problem (BVP)**, and it can take a single-shooting formulation, where the initial invariant circle is integrated up to T , or a multiple-shooting formulation, where the integration arcs are subdivided in N_0 nodes. In what follows, the core formulation of GMOS is described without making assumptions with regards to the single- versus multiple-shooting implementation, nor the time-dependence or time-independence of the system.

Integrating the initial invariant circle under the flow of the system over a time T , or, alternatively, after $\Delta\theta_0 = 2\pi$, the other angles θ_i will have rotated by $\rho_i = \omega_i T = \omega_i 2\pi/\omega_0$. We can then write

$$\varphi_T(\mathbf{u}(\theta_0, \theta_1, \dots, \theta_{d-1})) = \mathbf{u}(\theta_0, \theta_1 + \rho_1, \dots, \theta_{d-1} + \rho_{d-1}), \quad (3.15)$$

since we have the boundary conditions $\mathbf{u}(\theta_i + 2\pi, \cdot) = \mathbf{u}(\theta_i, \cdot)$, and φ_T represents the flow after a time T . Note that $\varphi_T(\mathbf{u}(\boldsymbol{\theta}))$ is the image of our stroboscopic map \mathbf{u} under a rotation along θ_0 equal to $\Delta\theta_0 = 2\pi = \omega_0 T$. As with the case of the [BVP](#) for computing periodic orbits presented in Section 3 of Chapter 2, it is common to rescale the time as $\tau = Tt$, such that $d\mathbf{u}/d\tau = T\mathbf{f}(\mathbf{u}, \tau)$ and $\tau \in [0, 1]$ [82]. We neglect this notation in the following equations for clarity, but adopt this convention in the implementation of the algorithm. We define a rotation operator $R_{-\boldsymbol{\rho}}$ that undoes the rotation along the other angular directions such that $R_{-\rho_i}(\mathbf{u}(\cdot, \theta_i + \rho_i)) = \mathbf{u}(\cdot, \theta_i)$. We can then write the invariance condition for the GMOS algorithm

$$R_{-\boldsymbol{\rho}}(\varphi_T(\mathbf{u})) - \mathbf{u} = \mathbf{0}. \quad (3.16)$$

The rotation operator can be written by means of the [DFT](#), noting that the rotations needs only be undone in the angular directions ranging from θ_1 to θ_{d-1} . Then, the [DFT](#) of the discretized invariant circle $\mathbf{X}_T(\theta_1, \dots, \theta_{d-1}) = \mathbf{X}_T(\bar{\boldsymbol{\theta}}) = \varphi_T(\mathbf{u}(\boldsymbol{\theta}))$ can be written as before

$$\hat{\mathbf{X}}_T[\mathbf{k}] = \sum_{n_1=0}^{N_1-1} \dots \sum_{n_{d-1}=0}^{N_{d-1}-1} \mathbf{X}_T\left(\frac{2\pi n}{N}\right) e^{-2\pi j(\mathbf{n} \cdot \mathbf{k} / N)}, \quad (3.17)$$

where in this case $\mathbf{n} = \{n_1, \dots, n_{d-1}\}$, $\mathbf{k} = \{k_1, \dots, k_{d-1}\}$, $\mathbf{N} = \{N_1, \dots, N_{d-1}\}$. The rotation can then be included in the inverse transform as

$$R_{-\boldsymbol{\rho}}(\mathbf{X}_T(\bar{\boldsymbol{\theta}})) = \frac{1}{N_1} \dots \frac{1}{N_{d-1}} \sum_{k_1=0}^{N_1-1} \dots \sum_{k_{d-1}=0}^{N_{d-1}-1} \hat{\mathbf{X}}_T[\mathbf{k}] e^{(\bar{\boldsymbol{\theta}} - \boldsymbol{\rho}) \cdot \boldsymbol{\gamma}(\mathbf{k})}, \quad (3.18)$$

where $\boldsymbol{\gamma}$ is defined as in Eq. (3.12) for $i = \{1, \dots, d-1\}$. Again, we can write these operations in matrix blocks as

$$[R_{-\boldsymbol{\rho}}] = [D^{-1}][Q_{-\boldsymbol{\rho}}][D], \quad (3.19)$$

where $[Q_{-\boldsymbol{\rho}}]$ is the diagonal matrix that rotates the Fourier coefficients by $e^{j(-\boldsymbol{\rho} \cdot \mathbf{k})}$. This yields our final invariance condition

$$\mathbf{G}(\mathbf{z}) = [R_{-\boldsymbol{\rho}}]\mathbf{X}_T - \mathbf{X}_0 = \mathbf{0}, \quad (3.20)$$

where \mathbf{X}_0 represents the initial invariant circle for some θ_0 and $\mathbf{z} = [\mathbf{u}; T; \boldsymbol{\rho}]^T$. Finally, we note that when using the multiple-shooting implementation of GMOS, also referred to as GMOS(MS),

we can write \mathbf{G} as

$$\mathbf{G} = \begin{bmatrix} \mathbf{m}^0 \\ \vdots \\ \mathbf{m}^{N_0-2} \\ \mathbf{g} \end{bmatrix} = \mathbf{0}, \quad (3.21)$$

with \mathbf{g} taking the same form as the single-shooting invariance condition of Eq. (3.20) but between the last and first nodes as $\mathbf{g} = [R_{-\rho}] \mathbf{X}_\tau^{N_0-1} - \mathbf{X}_0^0$ and where \mathbf{m}^i represents the continuity at the nodes [13] as

$$\mathbf{m}^i(\mathbf{X}) = \varphi_\tau(\mathbf{X}^i, t^i) - \mathbf{X}^{i+1} = \mathbf{X}_\tau^i - \mathbf{X}_0^{i+1}, \quad (3.22)$$

where $i = \{0, 1, \dots, N_0 - 2\}$, N_0 is the number of multiple shooting nodes, and $\varphi_\tau(\mathbf{X}^i, t^i)$ is the flow integrated from the initial conditions (\mathbf{X}^i, t^i) after some time $\tau = T/N_0$.

4 Additional equations

Note that up to now we have $N = N_0 \times \dots \times N_{d-1}$ equations for the PDE(DFT) algorithm and $N = N_1 \times \dots \times N_{d-1}$ or $N = N_0 \times \dots \times N_{d-1}$ for the GMOS algorithm (depending whether the single- or multiple-shooting implementation is used). However, the total number of equations needed actually depends on the number of parameters that describe the family and the number of external parameters of the system. As a note, in the following we tacitly assume that the necessary conditions for the persistence of quasi-periodic motion are maintained, such as non-resonance and non-degeneracy [55].

As hinted at in Chapter 2, d -dimensional families that are dependent on k external parameters typically live in $(d - k)$ -parameter families. This goes in line with the formulations stated by Olikara in [82], regarding the number of parameters and equations needed to compute tori in autonomous, periodically forced, and quasi-periodically forced systems, and by Baresi in [8], regarding the number of parameters that describe the families in autonomous systems, i.e. where the families are independent of external parameters. Jorba and Villanueva [55] also analyze these dependences to arrive at similar and more detailed conclusions. As indicated by Olikara, external forcing parameters are usually translated into an equivalent of one of the torus angles, θ_i , appearing in the equations of motion. However, this assumes that the external parameters are fixed and not part of the continuation process. In reality, we can either be computing a quasi-periodic solution from scratch in a time-dependent system, where indeed the external forcing parameters will be fixed, or making use of homotopy continuation to continue a solution into a time-dependent system, as shown in Eq. (3.6), where these parameters will vary along the continuation process.

For the first case, when we have k external *fixed* parameters, d -dimensional tori do indeed tend to inhabit $(d - k)$ -parameter families, which means we have $(N + d - k)$ unknowns, and we usually need $(d - k)$ phase conditions and $(d - k)$ parametrizing conditions (to be defined).

These are, similarly to the periodic orbit case of Chapter 2, used to fix the relative phase of the solutions and to select a specific solution among the family, respectively. As an example, one can think of computing a family of two-dimensional quasi-periodic tori in the **BCR4BP** from a previously known two-dimensional torus. In this case, $d = 2$ and $k = 1$, and one of the torus' angles will be represented in the equations of motion by the Sun angle. As such, one of the torus frequencies will be known *a-priori* as it corresponds to the Sun's angular velocity in the **BCR4BP** frame. We will then have a one-parameter family of two-dimensional tori, described by the other torus frequency or, equivalently, the fundamental period, which will be used to step along the family (assuming we step over resonances), and we will require only one phase and one parametrizing conditions.

For the second case, when we compute a torus solution from the introduction of a periodic perturbation to a system via homotopy continuation, the homotopy continuation parameter will actually become a variable in the **BVP** equations. This means that, even though one of the torus frequencies will be fixed to that of the new perturbation, the homotopy parameter will be used to step along the artificial family formed by the d -dimensional manifold at different values of ϵ . A more generic formulation for the number of parameters needed to describe the family can then be given as follows. Let us assume k to be the number of forced perturbations, i.e. for which we either don't make use of homotopy continuation or for which the "full" value of the perturbation has already been attained ($\epsilon = 1$) and is therefore fixed, and k_p to be the number of *variable* perturbations along which the homotopy continuation can be performed. Then, a d -dimensional manifold will typically inhabit a $(d - k)$ -parameter family. We will have $(N + d - k)$ unknowns (in which we include the k_p homotopy parameters), and we will need to include $(d - k - k_p)$ phase conditions and $(d - k)$ parametrizing conditions. As an example, consider continuing a periodic orbit of the **CR3BP** into a two-dimensional quasi-periodic tori family of the time-dependent **ER3BP**. In this case, we will have $d = 2$, $k = 0$, and $k_p = 1$. Similarly to the previous example, one of the torus frequencies will be known and fixed to the angular rate of the primaries' true anomaly. However, we will have ϵ as a new variable representing the introduction of the primaries' eccentricity, and two possible continuation directions: T and ϵ . In this case, we would then tend to have a two-parameter family of two-dimensional tori, and require one phase condition and two parametrizing conditions.

It should be noted , however, that these formulations depend on how the tori are parametrized. If we fix T until we achieve the desired value of eccentricity, we could effectively remove it from the vector of unknowns and we would require one less parametrizing equation. Nevertheless, this last formulation allows us to be more general and retain applicability for all cases. Finally, it is worth mentioning that an improvement in numerical convergence has sometimes been verified by maintaining a phase condition for the direction of a known torus frequency in quasi-periodic systems.

Now that the number of equations, parameters, and unknowns needed to compute families of quasi-periodic tori have been discussed, we can focus on the form of the additional equations. As mentioned, we may require phase conditions and parametrizing conditions. The phase condition

for i th angular direction can be written as [82, 8]

$$p_i(\mathbf{u}) = \langle \mathbf{u} - \tilde{\mathbf{u}}, \frac{\partial \tilde{\mathbf{u}}}{\partial \theta_i} \rangle = \frac{1}{N} \sum_{i=1}^{N_0-1} \dots \sum_{i=1}^{N_{d-1}-1} (\mathbf{u} - \tilde{\mathbf{u}})^T \frac{\partial \tilde{\mathbf{u}}}{\partial \theta_i} = 0, \quad (3.23)$$

where $\tilde{\mathbf{u}}$ is a previously known torus of the same family. To compute the partials with respect to θ_i we can use the DFT as described in Eq. (3.13) for both algorithms. Specifically for the GMOS algorithm, we can approximate the partial along the θ_0 direction from Eq. (3.8) by substituting the partials that were obtained from the DFT method

$$\frac{\partial \mathbf{u}}{\partial \theta_0} = \frac{1}{\omega_0} \left[\mathbf{f}(\mathbf{u}) - \sum_{i=1}^{d-1} \frac{\partial \mathbf{u}}{\partial \theta_i} \omega_i \right]. \quad (3.24)$$

The first parametrizing equation is usually set to either a specific energy level \bar{C} , when the system is autonomous

$$q_0(\mathbf{u}) = \frac{1}{N} \sum_{i=1}^{N_0-1} \dots \sum_{i=1}^{N_{d-1}-1} C(\mathbf{u}) - \bar{C} = 0, \quad (3.25)$$

or a specific period \bar{T}

$$q_0(T) = T - \bar{T} = 0, \quad (3.26)$$

although in theory we could fix any other torus frequency this way. Note, of course, that since $T = 2\pi/\omega_0$, it is equivalent to say we fix the period or the fundamental frequency of the torus. Similarly to the numerical continuation of periodic orbits, the remaining equations are usually covered by the pseudo-arclength continuation [97]. For a two-dimensional quasi-periodic tori family in an autonomous system, the equation takes the form

$$q_1(\mathbf{z}) = \langle \mathbf{z} - \tilde{\mathbf{z}}, \frac{\partial \tilde{\mathbf{z}}}{\partial h} \rangle - \delta h = \frac{1}{N} \sum_{i=1}^{N_0-1} \sum_{j=1}^{N_1-1} (\mathbf{u} - \tilde{\mathbf{u}})^T \frac{\partial \tilde{\mathbf{u}}}{\partial h} + (T - \bar{T}) \frac{\partial \tilde{T}}{\partial h} + (\rho - \tilde{\rho}) \frac{\partial \tilde{\rho}}{\partial h} - \delta h = 0, \quad (3.27)$$

where $\partial \tilde{\mathbf{z}} / \partial h$ is the family tangent at the previously known solution, which characterizes the relative variation of the torus variables with respect to the pseudo-arclength parameter h , and δh is the step size. For higher-dimensional tori, a multiple-parameter continuation method must be implemented instead [47, 84]. The family tangent can be approximated as the difference between the last two known solutions or, as for the periodic orbit case of Chapter 2, from the null space of the Jacobian of \mathbf{G} appended with the additional equations up to and excluding equation q_1 . Although different formulations are possible, the factor used to normalize the family tangent must be such that

$$\langle \frac{\partial \mathbf{z}}{\partial h}, \frac{\partial \mathbf{z}}{\partial h} \rangle = 1, \quad (3.28)$$

for a known solution $\mathbf{z}(h)$. This comes from approximating the next solution to first order by

taking a step δh from $\mathbf{z}(h)$ as

$$\mathbf{z}(h + \delta h) = \mathbf{z}(h) + \frac{\partial \mathbf{z}}{\partial h} \delta h, \quad (3.29)$$

and substituting into equation (3.27). With these additional equations we can now build the complete error vector \mathbf{F}

$$\mathbf{F}(\mathbf{z}) = \begin{bmatrix} \mathbf{G}(\mathbf{z}) \\ \mathbf{p}(\mathbf{z}) \\ \mathbf{q}(\mathbf{z}) \end{bmatrix} = \mathbf{0}, \quad (3.30)$$

for which a solution can be found iteratively using

$$D\mathbf{F}(\mathbf{z})\delta\mathbf{z} = -\mathbf{F}(\mathbf{z}), \quad (3.31)$$

where $D\mathbf{F}$ is the Jacobian matrix of \mathbf{F} [83]. Then, as for the periodic orbit case, the next family member is initialized as

$$\mathbf{z}^{m+1} = \mathbf{z}^m + \frac{\partial \mathbf{z}^m}{\partial h} \delta h. \quad (3.32)$$

Finally, note that, starting from a known solution or good enough initial guess $\mathbf{z} = (\tilde{\mathbf{X}}_0, \tilde{\boldsymbol{\xi}})$, where $\tilde{\boldsymbol{\xi}}$ are any additional parameters, we have that $\mathbf{G}(\tilde{\mathbf{X}}_0, \tilde{\boldsymbol{\xi}}) = \mathbf{0}$. Then, by the Implicit Function Theorem, if

- $\mathbf{G}_X(\tilde{\mathbf{X}}_0, \tilde{\boldsymbol{\xi}}) \in \mathbb{R}^N \times \mathbb{R}^N$ is non-singular
- and \mathbf{G} and \mathbf{G}_X are smooth near $(\tilde{\mathbf{X}}_0, \tilde{\boldsymbol{\xi}})$,

then there exists a unique continuous family $(\mathbf{X}_0(h), \boldsymbol{\xi}(h))$, along the continuation parameter h , which may be one of the parameters in $\boldsymbol{\xi}$, such that

- $(\mathbf{X}_0(h_0), \boldsymbol{\xi}(h_0)) = (\tilde{\mathbf{X}}_0, \tilde{\boldsymbol{\xi}})$,
- $\mathbf{G}(\mathbf{X}_0(h), \boldsymbol{\xi}(h)) = \mathbf{0}$ for h near h_0 .

This allows us to justify the existence of a family and use the aforementioned numerical continuation formulations.

5 Modifications to the algorithms

In addition to the changes in the implementation of the DFT routine used in both algorithms, the formulation of the homotopy continuation procedure, and the reinterpretation of the number of equations, parameters, and unknowns for the different types of problems, a few algorithm-specific modifications have also been implemented. Specifically, we implement the use of unfolding parameters in the PDE(DFT) algorithm to square the Jacobian matrix, and integrate all

trajectories simultaneously in the GMOS algorithm by extending the state-vector and the vector-field. Although unfolding parameters have been implemented before for GMOS [82] and advocated in general for BVPs, they have not been used for PDE-type approaches. These modifications are detailed below.

5.1 PDE(DFT)

Although we have so far added all the equations needed in order to compute families of quasi-periodic tori, one may note that the Jacobian matrix $D\mathbf{F}$ is often not square. Indeed, using the formulation introduced in Section 4, note that we will usually have $(d - k - k_p)$ more equations than unknowns. This means that one has to solve Eq. (3.31) using algorithms such as QR factorization for a non-square matrix, which represents a significant hurdle in terms of computational time and is prone to numerical errors. This is particularly significant for the PDE(DFT) method, as N is typically larger due the larger number of discretization points needed (which yields Jacobian matrices generally in the order of at least 7500^2 entries and larger). We can minimize this by squaring the $D\mathbf{F}$ matrix with the introduction of unfolding parameters. Specifically, we add $(d - k - k_p)$ unfolding parameters, λ_i . These parameters embed the Hamiltonian system augmenting the vector field in such a way that a solution is only found for $\boldsymbol{\lambda} = \mathbf{0}$, and are commonly implemented in continuation routines for periodic orbit families [32, 75]. The use of unfolding parameters also has the significant advantage of making the continuation algorithms more robust and less prone to dynamical and numerical instabilities. In order to extend the vector field we use the approach introduced in [82], which makes use of the partial derivatives with respect to the action angles, \mathbf{I} , of the torus

$$\mathbf{f}(\mathbf{X}) := \mathbf{f}_0(\mathbf{X}) + \sum_{i=0}^{d-1} \lambda_i \frac{\partial I_i}{\partial \mathbf{X}}(\mathbf{X}), \quad (3.33)$$

which matches the original vector field \mathbf{f}_0 only for $\boldsymbol{\lambda} = \mathbf{0}$. Locally, the torus actions behave similarly to an integral of motion, with the advantage that we have the same number of torus actions as independent angle coordinates. Moreover, we do not need to compute the torus actions explicitly, as we can directly obtain the relevant partial derivatives from [82]:

$$\frac{\partial I_i}{\partial \mathbf{X}} = -\frac{\partial \mathbf{y}}{\partial \mathbf{X}}^T \mathbf{J} \frac{\partial \mathbf{y}}{\partial \mathbf{X}} \frac{\partial \mathbf{u}}{\partial \theta_i}, \quad (3.34)$$

where \mathbf{y} is the transformation to canonical coordinates $\mathbf{y}(\mathbf{X}) := (\mathbf{q}, \mathbf{p})(\mathbf{X}) \in \mathbb{R}^{n/2} \times \mathbb{R}^{n/2}$, and \mathbf{q}, \mathbf{p} are the generalized coordinates and momenta, respectively. The matrix \mathbf{J} is $n \times n$ and defined as

$$\mathbf{J} = \begin{bmatrix} \mathbf{0} & +\mathbf{I}_{n/2} \\ -\mathbf{I}_{n/2} & \mathbf{0} \end{bmatrix}, \quad (3.35)$$

where $\mathbf{I}_{n/2}$ is the identity matrix.

5.2 GMOS

The GMOS algorithm requires us to integrate N trajectories, which can result in a significant computational cost. We avoid this by introducing the improvement of integrating all the trajectories simultaneously, therefore extending the state-vector. This not only has the benefit of reducing the computational time (which could also be obtained by parallelizing the integration), but as mentioned by Betts in [13] (see chapter 3.9.3), it plays an important role on the consistency of our approximations. Indeed, by constructing an augmented system where all the trajectories are integrated together, we guarantee that they will have the same number of integration steps, which translates into a more consistent approximation among all the solutions and for further operations using said solutions. The error differences that result from different numbers of integration steps can be further accentuated by numerical differentiation schemes used after the integration routine, such as computing partial derivatives with, in our case, the [DFT](#). Although the trajectories might remain under the error tolerance stipulated by the integration routine, they will often require vastly different numbers of steps to do so and might not yield consistent approximations. Integrating all the trajectories simultaneously allows us to not require such low tolerance errors and maintain consistency among all trajectories, with the addition of significantly reducing the computation time.

Another important benefit associated with integrating all trajectories simultaneously is that it allows us to use variational equations that involve interdependence between the θ_0 direction and the other angular directions. That is, we can integrate, along the θ_0 direction, quantities that vary with the whole invariant circle that is being integrated. This enables the use of integral constraints in place of the discrete constraints exemplified in Section 4 for the phase conditions, which are said to be more robust and efficient [32].

6 Comparison

Having detailed the algorithms in the previous sections, we can now compare their numerical efficiency, as well as the improvements being introduced. Firstly, it is important to discuss the bottlenecks of each algorithm in terms of computational time. Since the [PDE\(DFT\)](#) algorithm does not require integration, its bottleneck is clearly the computation of Newton's method in Eq. (3.31), which requires solving a linear problem of the type $Ax = b$ for potentially a very large matrix A (see Figure 3.2a as an example). For a non-square matrix this requires using methods such as QR factorization, which are computationally demanding. As mentioned, in order to address this we have implemented unfolding parameters, which square the Jacobian matrix and significantly decrease the computational time of the operation. An example of the reduction in computational time achieved by this, when compared to the [PDE\(DFT\)](#) implementation without unfolding parameters, can be seen in Table 3.1 for a two-dimensional torus and different numbers of nodes. It should be noted that the running times were obtained using the *Spyder* profiler for *Python* and that they can vary slightly for different runs as they also depend on parameters external to the program. Nonetheless, it is clear that the introduction of unfolding parameters improves the computational efficiency of the algorithm significantly, producing a decrease of

about 80% in runtime.

Table 3.1: Analysis of the average runtime (per torus) associated with obtaining the first five elements of quasi-periodic torus family using the PDE(DFT) method, without (non-square DF) and with (square DF) the implementation of unfolding parameters. Obtained using the *Spyder* profiler on a 2020 MacBook Air 1.1 GHz Quad-Core i5 with 16Gb RAM.

Average runtime - PDE(DFT)		
(N_0, N_1)	(25, 50)	(50, 50)
Newton method, non-square DF [s]	43.19 s	357.42 s
Newton method, square DF [s]	8.68 s	53.55 s
Time reduction in Newton method [%]	79.93 %	85.02 %
To find individual torus, non-square DF [s]	87.2 s	756.1 s
To find individual torus, square DF [s]	17.02 s	148.02 s
Time reduction to find individual torus [%]	80.37 %	80.42 %

When using a single shooting approach for the GMOS algorithm, i.e. all trajectories are integrated for a time T , the computational bottleneck of the algorithm is typically not in solving Newton's method but rather in the integration routine (the computational time for Newton's method in the single shooting method is typically two to three orders of magnitude below the integration time). However, there are situations where, due to numerical or dynamical instabilities, we must use a multiple shooting implementation, i.e. splitting each trajectory into N_0 sections and integrating each for T/N_0 . In these situations, solving Newton's method becomes more significant in terms of computational expense, as the number of entries of the Jacobian matrix increases by a factor of N_0^2 . The multiple shooting implementation of GMOS will then benefit more from the implementation of the unfolding parameters than the single shooting implementation. That being said, the unfolding parameters should still be used for the single shooting version of GMOS, as they provide more robustness to the algorithm. An analysis of the average runtime needed to solve Newton's method and to arrive at an individual torus solution when using the GMOS multiple shooting algorithm can be seen in Table 3.2, which are obtained from using the same conditions as in Table 3.1 only for the GMOS algorithm. Note that we are using the GMOS implementation with the modifications described in section 5, integrating all the trajectories simultaneously by appending them to the state-vector; in Table 3.2 we simply compare the performance of the algorithm with and without unfolding parameters. It is clear that as we increase the number of nodes, the unfolding parameters have a greater impact on the computational time. In fact, as the total number of nodes, N , grows, the computation time needed to solve Newton's method grows faster than the computation time needed to integrate all the trajectories, eventually becoming more computationally demanding than the integration routine, which is why the squaring of the Jacobian matrix via the use of unfolding parameters becomes so crucial.

An important difference with respect to the PDE(DFT) algorithm is that, even when faced with numerical or dynamical instabilities, the GMOS multiple shooting algorithm does not typically require as many nodes in the θ_0 direction, i.e. N_0 can usually be significantly smaller¹

¹The large number of N_0 nodes ($N_0 = 50$) seen in Table 3.2 is shown merely for demonstration purposes so it

Table 3.2: Analysis of the average runtime (per torus) associated with obtaining the first five elements of quasi-periodic torus family using the GMOS multiple shooting method (MS), without (non-square DF) and with (square DF) the implementation of unfolding parameters. Obtained using the *Spyder* profiler on a 2020 MacBook Air 1.1 GHz Quad-Core i5 with 16Gb RAM.

Average runtime - GMOS(MS)				
(N_0, N_1)	(5, 50)	(10, 50)	(25, 50)	(50, 50)
Newton method, non-square DF [s]	0.32 s	2.21 s	36.6 s	237.8 s
Newton method, square DF [s]	0.1 s	0.53 s	6.26 s	44.03 s
Time reduction in Newton method [%]	68.58 %	76.17 %	82.9 %	81.49 %
To find individual torus, non-square DF [s]	3.6 s	7.9 s	75.42 s	446.4 s
To find individual torus, square DF [s]	3.23 s	4.26 s	17.34 s	78 s
Time reduction to find individual torus [%]	10.29 %	46.1 %	77.01 %	82.53 %

(most of the time it can actually be set to zero, reverting into the single shooting implementation). This is due to the fact that we are still integrating the trajectories within the vector field, whereas the **PDE(DFT)** algorithm needs to find points that are consistent with the vector field. The upsides to this are that the **PDE(DFT)** method does not require integration, which means we do not carry over the numerical errors nor the computational time associated with it, and that a discretized solution of the full torus is available after convergence at a regular grid (unaffected by the rotation number), and specific points on the torus can be found via numerical interpolation. However, as mentioned, this seems to come at the expense of a longer computational time, due to the larger number of points required to accurately represent the torus and the associated large algebraic operations.

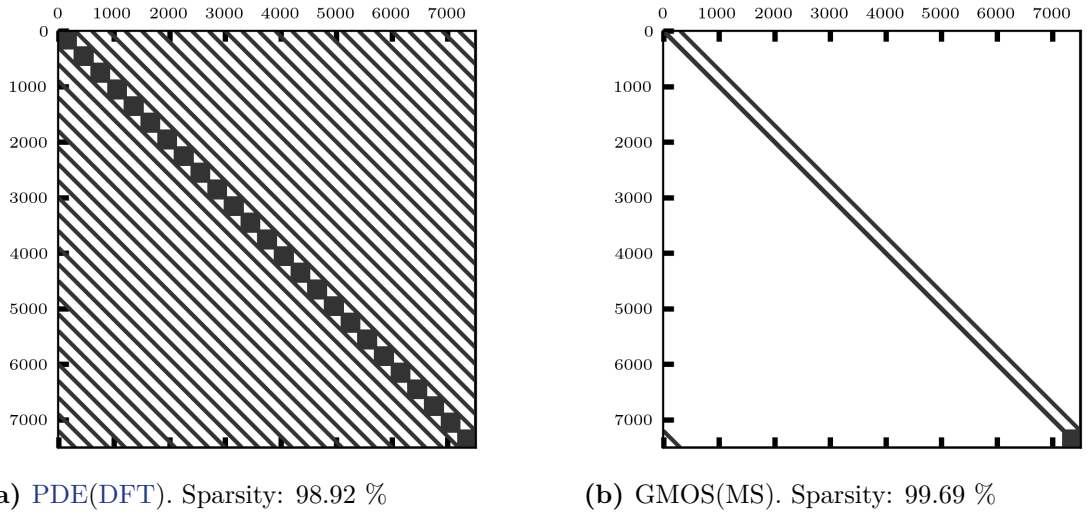


Figure 3.2: Sparsity plots for the Jacobian matrices for $(N_0, N_1) = (25, 50)$ and $n = 6$ of (a) the **PDE(DFT)** method and (b) the **GMOS(MS)** method.

Additionally, one might notice that even when using the same number of nodes for each can be compared fairly with the **PDE(DFT)** algorithm; usually we want to keep this number as low as possible in order to reduce the computation time.

angular direction, Tables 3.1 and 3.2 show that the GMOS multiple shooting algorithm outperforms the PDE(DFT) for the time needed to solve Newton’s method equation, even when using unfolding parameters. This is likely due to a “better-behaved” configuration of GMOS’s Jacobian matrix, in terms of sparsity configuration. The sparsity plot of the Jacobian matrix $D\mathbf{F}$ for each method can be seen in Figure 3.2. Note that the non-zero terms of the GMOS matrix are mostly placed along the diagonal, whereas the PDE(DFT) presents diagonal entries along the whole matrix. Sparse Jacobian matrices whose entries are placed mostly along the diagonal are generally faster to invert, or to solve Newton’s method equation with [13], which might make the operation faster for the GMOS algorithm when using large numbers of nodes. Additionally, it is worth noting that this sparse configuration could open the door for a faster implementation of the two methods if numerical libraries based on sparse matrices are used for the algorithms. Furthermore, we can see that for the largest number of nodes along θ_0 , the average runtime of the GMOS(MS) necessary to find one quasi-periodic torus is smaller than that of the PDE(DFT) method (78s for GMOS compared to around 150s for PDE(DFT)), even though the GMOS requires numerical integration. This might be related to the fact that the PDE(DFT) method requires a larger number of algebraic operations involving very large matrices, which are significantly slow, although the integration time associated with GMOS can vary depending on the initial conditions and dynamics. Nevertheless, we find that in general, the GMOS algorithm outperforms PDE(DFT) and as such should be preferred for most applications. The same conclusion was also put forward in [5].

7 Applications to trajectory design

Having introduced the methods and equations necessary for the computation of families of quasi-periodic tori, we can now find quasi-periodic motion in the frame of specific missions, focusing on the applications and possibilities that said trajectories enable. In Section 7.1, we discuss the Martian Moons eXploration (MMX) mission by JAXA, the extensions of its candidate periodic orbits to quasi-periodic tori families, and applications to its mission design. In Section 7.2, we present a powerful tool to visualize the trajectories that move along the surface of quasi-periodic tori, and demonstrate its uses to plot relevant quantities in the frame of the MMX mission.

7.1 The Martian Moon eXploration mission

The MMX mission by JAXA will attempt to answer the questions surrounding the origin of the Martian Moons, Phobos and Deimos, with plans to return a sample from Phobos’ surface to Earth and to perform extensive scientific observations on and around Phobos [59]. To be launched in 2024, MMX will orbit Phobos on a orbit family called Quasi-Satellite Orbit (QSO), also known as Distant-Retrograde Orbit (DRO). Due to their attractive linear stability and dynamical properties, five nominal QSOs have been selected, categorized by different altitude values as low (QSO-La, QSO-Lb, QSO-Lc), medium (QSO-M), and high altitude (QSO-H) [24].

These nominal trajectories², which are, as the rest of the QSO family, equatorial, can be seen in Figure 3.3, with some of their physical features presented in Table 3.3. As observed in [7], these

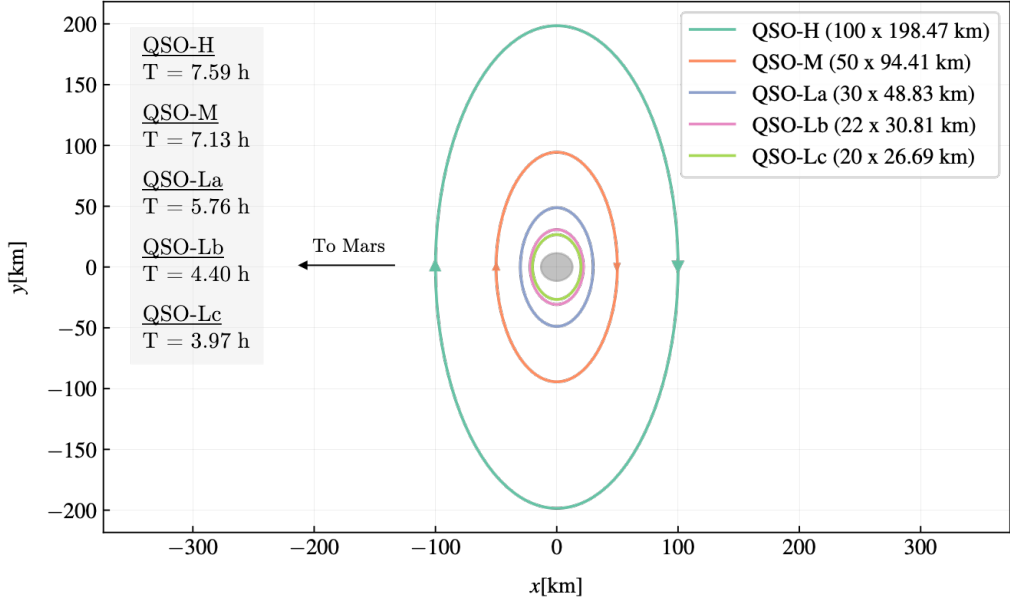


Figure 3.3: MMX nominal periodic QSOs around Phobos.

Table 3.3: MMX candidate orbits.

Name	$X \times Y$ (km)	$\dot{X} \times \dot{Y}$ (m/s)	T (hrs)
QSO-H	100×198.47	22.95×45.74	7.59
QSO-M	50×94.41	12.04×23.41	7.13
QSO-La	30×48.83	8.68×15.31	5.76
QSO-Lb	22×30.81	8.25×12.79	4.40
QSO-Lc	20×26.69	8.31×12.31	3.97

five periodic orbits are surrounded by areas of regular motion that make them desirable for the MMX mission. Moreover, their center manifolds include both in-plane and out-of-plane motion that give way to two families of two-dimensional quasi-periodic tori (or one family of three-dimensional tori). These quasi-periodic extensions of the QSO orbits, where the in-plane or planar quasi-periodic families are sometimes referred to as Swing QSOs and the out-of-plane or vertical as 3D QSOs, offer significant advantages in terms of scientific observations and mission design.

In order to further analyze and exemplify the applications of the quasi-periodic tori for the MMX mission, let us define a dynamical model for the Mars-Phobos system. We use the Hill Problem model, as described in Chapter 2. We model the gravity of Phobos using a constant density tri-axial ellipsoid model [95]. Note that because Phobos is tidally locked with Mars we can express the equations of motion in a rotating reference frame centered on Phobos where the

²We note that the official amplitude of QSO-La changed from $X = 30$ km to $X = 33$ km in Spring 2022. The values hereby presented reflect the official orbits before this change.

x -axis points at all times in the anti-Mars direction and is always aligned with Phobos' largest ellipsoidal axis. The z -axis points in the direction of Mars-Phobos' orbital angular momentum vector and the y -axis completes the orthonormal frame. The dimensionless equations of motion can be written as

$$\ddot{x} - 2\dot{y} = \frac{\partial g}{\partial x} + 3x \quad (3.36a)$$

$$\ddot{y} + 2\dot{x} = \frac{\partial g}{\partial y} \quad (3.36b)$$

$$\ddot{z} = \frac{\partial g}{\partial y} - z \quad (3.36c)$$

where the length and time units are $[LU] = (\mu_2/n^2)^{1/3}$ and $[TU] = 1/n$, respectively, μ_2 is Phobos' gravitational parameter, n is Phobos' mean motion about Mars, and g is the gravity potential of the constant density ellipsoid, as defined in [7, 95].

Having defined our vector field, we are now in a position to apply the methods described in the previous sections in order to obtain quasi-periodic tori around QSOs. Note that the choice of in-plane vs out-of-plane quasi-periodic tori comes from the choice of the center eigenvalues and associated eigenvectors of the periodic orbit. Since QSOs possess two unitary complex eigenvalues we can choose either to obtain our in-plane or out-of-plane quasi-periodic motion. Focusing on the Lb-QSO, we can then produce its associated quasi-periodic vertical QSO by choosing an eigenvalue whose eigenvector has an out-of-plane component. Implementing the family continuation routine associated with either algorithm, we can obtain a family of vertical quasi-periodic QSOs. In Figure 3.4, we can see a member of the family, together with the nominal periodic QSO-Lb (in a dashed black line) and a portion of a sample quasi-periodic trajectory on the surface of the torus in blue.

We can proceed equivalently in order to obtain planar quasi-periodic QSOs, such as the quasi-periodic torus seen in Figure 3.5, obtained also from the periodic QSO-Lb.

Just by analyzing Figures 3.4 and 3.5, it is clear that the quasi-periodic trajectories offer new opportunities for mission design when compared to the periodic orbits. In fact, we can see that in terms of science possibilities, the quasi-periodic tori give us significantly wider ranges of observation scenarios and conditions. Specifically, we can see that the vertical quasi-periodic torus of QSO-Lb shown in Figure 3.4 allows us to reach significantly higher latitudes (around 30° for the QSO-Lb, higher for the larger QSOs), which would otherwise be impossible given that periodic QSOs are equatorial. Alternatively, for the planar quasi-periodic QSO-Lb family, we can see that in the same revolution the trajectory's altitude varies significantly more than for the periodic orbit. In the same orbital revolution, the spacecraft reaches significantly lower and higher altitudes than those of the periodic orbit.

These characteristics in turn enable the possibility of obtaining better resolution measurements and performing different scientific observations, which would allow us to obtain relevant data in areas such as spectroscopy, gravity measurement, remote sensing, and others. Additionally, these quasi-periodic trajectories could enable an easier access to land on Phobos, as they give us a significantly wider array of initial conditions from which to deploy a lander or

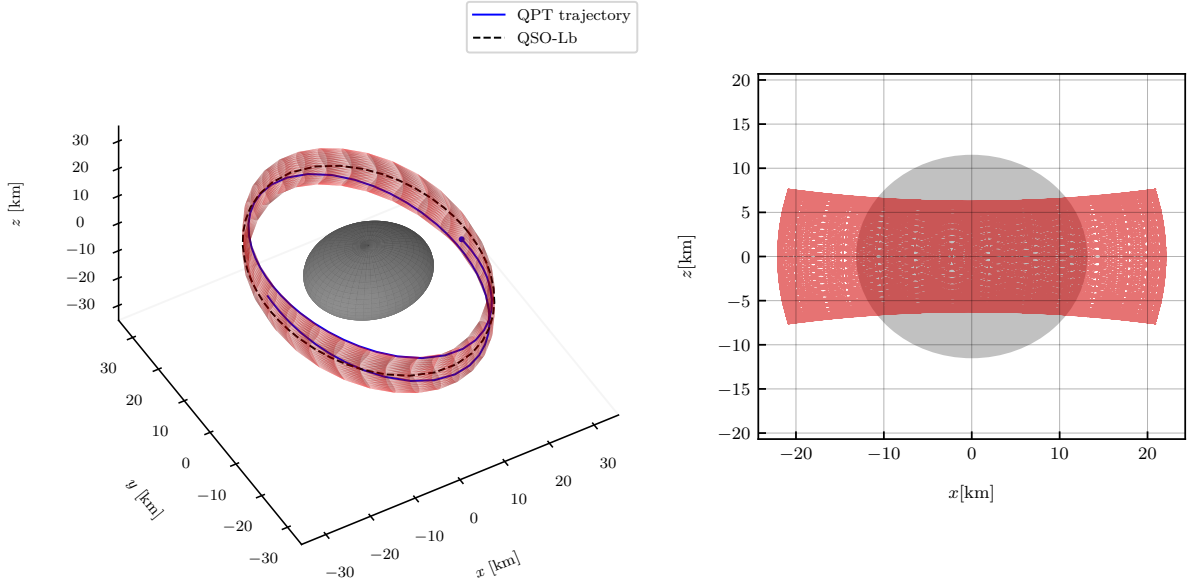


Figure 3.4: Member of the vertical quasi-periodic QSO tori family (in red): (left) three-dimensional projection with periodic QSO-Lb that it originates from (black dashed line) and a portion of a sample trajectory along the torus' surface (blue); (right) projection over the xz -plane.

execute a maneuver to commence a landing trajectory. Furthermore, even when the quasi-periodic trajectories significantly depart from the nominal periodic orbit from which they originate, they move on a surface – a two-dimensional manifold – that grants mission designers higher flexibility in terms of maneuvers and trajectory optimization, as well as with regards to orbit maintenance [6].

7.2 Torus maps

Another advantage of using quasi-periodic tori is that we are able to better quantify and monitor physical parameters, such as the aforementioned (altitude, latitude, among others) by means of torus maps. As mentioned in Section 1 of this chapter, quasi-periodic tori are characterized by their incommensurate frequencies. As such, we can fully describe the variation of the torus angles θ_i as a function of time. For the two-dimensional tori we are currently analyzing, we can then write

$$\begin{cases} \theta_0(t) = \theta_0(t_0) + \omega_0(t - t_0) \\ \theta_1(t) = \theta_1(t_0) + \omega_1(t - t_0) \end{cases} \quad (3.37)$$

for some initial time t_0 and initial angles $\theta_i(t_0)$. This parametrization allows us to describe, based on the initial angle coordinates, how a trajectory will move on the surface of a quasi-periodic torus. That is, it allows to map our states from \mathbb{T}^2 to \mathbb{R}^6 and vice-versa. While simple, this tool can be very powerful; it means, for instance, we can directly select an injection point described by the torus angles and obtain its corresponding state-vector in \mathbb{R}^6 , or, based on an

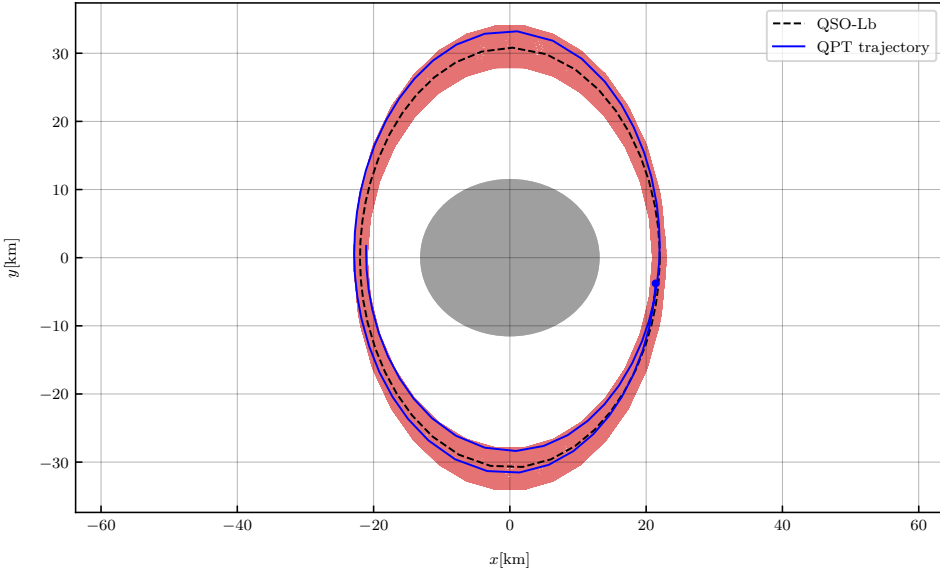


Figure 3.5: Member of the planar quasi-periodic **QSO** tori family (in red) that originates from the periodic **QSO**-Lb (black dashed line). A portion of a sample trajectory on the torus' surface is shown in blue.

initialized trajectory on the torus' surface in \mathbb{R}^6 , we can study its variation as a function of time without the need for numerical integration. In order to do so, we need only the state-vectors in \mathbb{R}^6 that describe the invariant torus on a regular grid over the angle coordinates. That is, we need the torus function $\mathbf{u}(\theta)$ defined at a regular grid over θ . At this point, one may notice that this discretization is directly available from the PDE(DFT) method, as that is how the torus is discretized and stored in order to satisfy the invariant condition of the algorithm (Eq. (3.8)). However, this is not the case for the GMOS method. Even if we store the integrated trajectories at a regularly spaced grid, a trajectory on the torus' surface that has as an initial condition $\theta_0 = 0$ and $\theta_1 = 0$ with $t_0 = 0$, will, after some time t , have $\theta_0 = \omega_0 t$ and $\theta_1 = \omega_1 t$, because θ_1 varies over the θ_0 direction. To obtain the value of \mathbf{u} on a regularly space grid, we require, for each “row” of θ_0 , a constant value of θ_1 . As such, we need to rotate back θ_1 by an amount $-\omega_1 t$. A visual example of why we need to perform this rotation for the GMOS algorithm can be seen in Figure 3.6, where we can see the flow of the integrate trajectory on the map and the required rotation to land on the correct node. We perform this rotation exactly in the same way as described in Eq. (3.19), only now the angle to be rotated will be $-\omega_1 t$ instead of $-\rho$. However, note that when t reaches $t = T$, the operation will be exactly the same, since $\rho = \omega_1 T$.

Using this information, we can now directly apply the torus maps in order to plot specific physical quantities over quasi-periodic trajectories that move along the torus' surface. We can see how, for instance, the altitude of our spacecraft evolves as a function of time when initialized with specific angle coordinates on the torus, without needing to integrate the trajectory. We find pertinent examples of this in Figures 3.7 and 3.8, where we plot different quantities over the torus maps for both the planar and vertical quasi-periodic **QSO**-Lb tori shown before in Figures

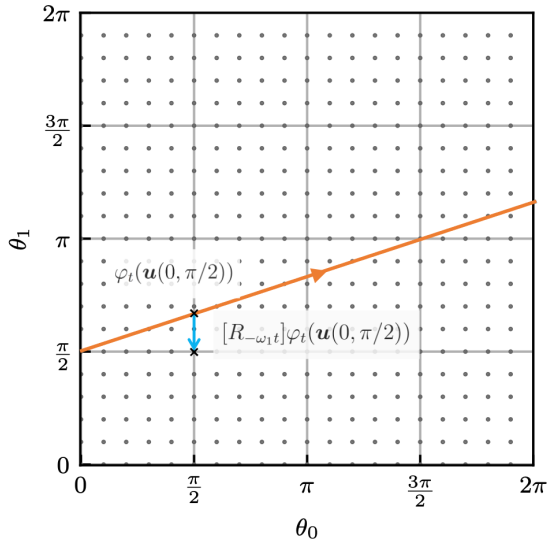


Figure 3.6: Example of the operation needed to correctly sample the points at the nodes when using the GMOS algorithm, where the integrated state is rotated back so as to land on the correct nodes.

3.4 and 3.5. In Figures 3.7a and 3.7b we plot, respectively, the latitude and groundspeed of the spacecraft with respect to Phobos when moving along the vertical quasi-periodic QSO-Lb torus. We can observe the high latitudes reached and how they vary with the quasi-periodic motion, as well as the differences in groundspeed along the torus' surface.

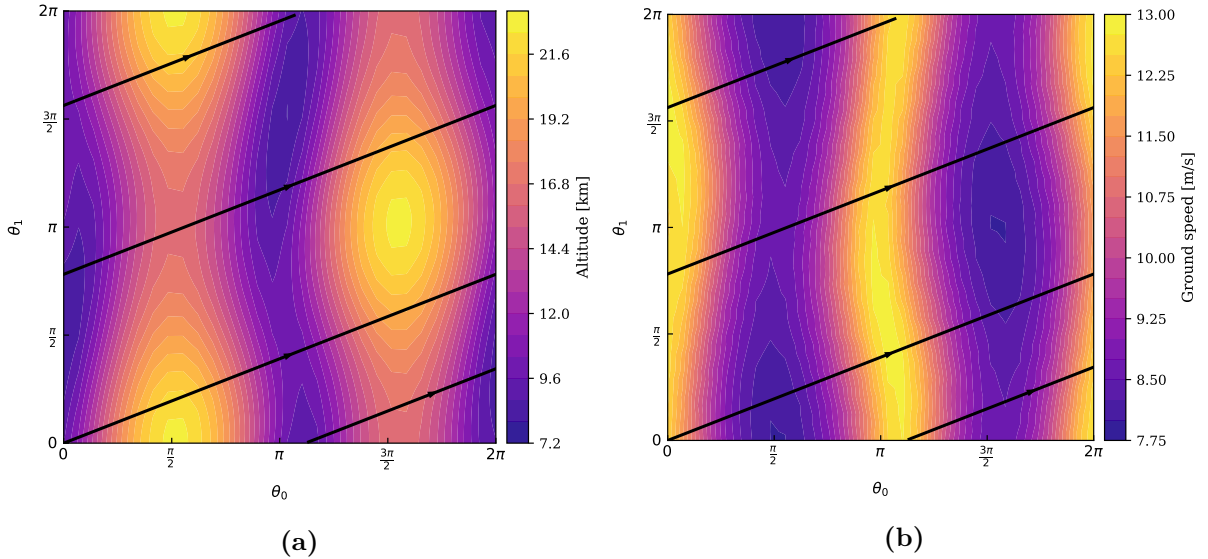


Figure 3.8: Torus maps for a member of planar quasi-periodic family QSO-Lb showcasing, as a function of the torus angles, (a) the spacecraft's altitude and (b) its groundspeed with respect to Phobos.

In Figures 3.8a and 3.8b we can see, respectively, the altitude and groundspeed of the spacecraft with respect to Phobos when moving along the planar quasi-periodic QSO-Lb torus.

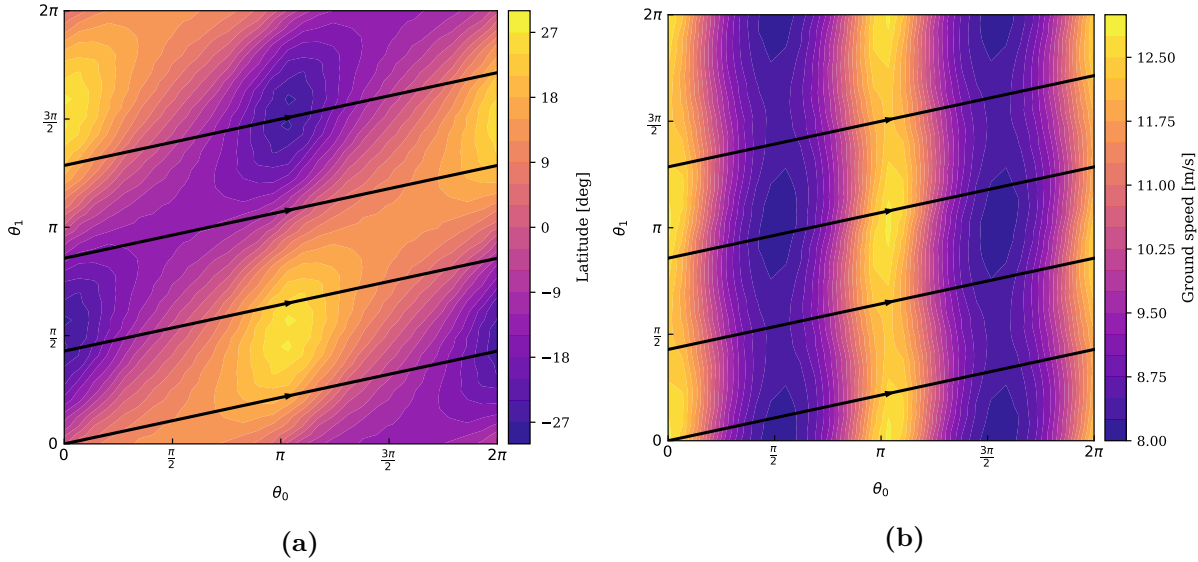


Figure 3.7: Torus maps for a member of vertical quasi-periodic family [QSO-Lb](#) showcasing, as a function of the torus angles, (a) the spacecraft's latitude and (b) its groundspeed with respect to Phobos.

It is interesting to compare these values with those for the vertical quasi-periodic trajectory, and how different scientific objectives can make use of both scenarios.

Using these torus maps, we could for instance select an injection point on the quasi-periodic torus that would lead the spacecraft to pass over a specific area of Phobos after a predetermined time, or rather aim for a specific groundspeed over such an area, among many other possibilities. Using torus maps gives the design of these quasi-periodic trajectories a lot of flexibility in order to accommodate scientific requirements and other constraints.

8 Conclusions

This chapter has detailed contributions to two numerical methods used to compute families of quasi-periodic tori. Specifically, the [PDE\(DFT\)](#) and GMOS methods have been addressed. In addition to the initialization and core formulation of the methods, we have introduced some modifications to improve each algorithm. The notion of homotopy continuation was applied to the computation of families of quasi-periodic tori solutions in the perturbed dynamical systems addressed in this thesis, which will be used in later chapters. We have adopted a different formulation with respect to previous works, to allow for a more general understanding on the number of parameters that describes each family of solutions, as well as the number of equations needed and the associated unknowns. The inclusion of unfolding parameters and the integration of all trajectories simultaneously allows for a more robust and computationally efficient implementation of the [PDE\(DFT\)](#) and GMOS algorithms, respectively. An example of the application of these methods to [JAXA's MMX](#) mission has shown the value and flexibility that these tools can have in mission design, where we have also used a dynamical tool known as *torus maps*, which allows for a powerful visualization of quasi-periodic trajectories with respect

to physical properties of interest.

In the following chapters we apply these methodologies to other missions and dynamical environments, with the goal of better characterizing perturbed dynamics and finding interesting and realistic orbit solutions.

Chapter 4

Invariant manifolds in the Augmented Hill Problem for small-body exploration

In this chapter, the theoretical background and methodologies previously introduced are leveraged to exemplify possible applications for small-body exploration. Particularly, we focus on the [Augmented Hill Problem \(AHP\)](#), a formulation of the Hill Problem that includes [Solar Radiation Pressure \(SRP\)](#) and eclipses that is often a good approximation for the dynamics about small bodies. In Section 1, the context of this study is presented with a small introduction to small-body exploration. This is followed by a presentation of some of the dynamical solutions of the [AHP](#) model in Section 2, which focuses particularly on the periodic and quasi-periodic solutions to be studied in this chapter. Section 3 then analyzes landing trajectories from some of the considered periodic orbits via their hyperbolic invariant manifolds. This is followed by an analysis into the hyperbolic manifolds of the quasi-periodic trajectories in Section 4, both as possible baseline landing trajectories and as homoclinic connections that can be useful to science operations. Finally, Section 5 resumes the findings of this chapter, demonstrating the value of dynamical systems tools to designing trajectories for small-body exploration.

1 Small-body exploration

The scientific exploration of asteroids and comets, besides being a great testament to the development of space exploration, may allow us to attain an unprecedented degree of knowledge about the origins of our solar system. These small bodies are said to contain remnants of the beginning of the solar system, and key-information about its formation and history. The scientific data from the sample-return Hayabusa2 mission by JAXA and the sample-return OSIRIS-REx mission by NASA is yet to be completely analyzed, and even so they have already contributed to many scientific discoveries [74, 63]. Additionally, as is the case with ESA's Hera and NASA's DART counterpart missions to the binary asteroid Didymos, the study of these near-Earth objects can be very relevant to the topics of planetary protection and space situational awareness. DART was launched in the end of 2021 and should impact the smaller body, Dimorphos, on

September 26, 2022, at a relative velocity of around 6 km/s [89], whereas Hera will arrive a few years later to the binary system to analyze the aftermath of DART’s impact to Dimorphos [72]. Other small-body missions include two of NASA’s Discovery program missions: Lucy, which was launched in the end of 2021 and which will investigate seven Trojan asteroids [64], and Psyche, which will rendezvous with and study the largest known metal asteroid in the solar system [80]. Additionally, the planned Janus mission consists of a twin spacecraft design that will fly-by near-Earth objects of interest and will be launched together with Psyche as part of the NASA SIMPLEx’s program [93].

The relevance of small-body missions in the current era of space exploration raises the importance of the study and modeling of the environments about these bodies. As it has already been said, their small gravity amplifies the significance of additional perturbations, such as that posed by **Solar Radiation Pressure (SRP)**. It is common to model these environments using adaptions of the Hill problem detailed in Chapter 2. In this chapter we make use of what is sometimes referred to as the **Augmented Hill Problem (AHP)**, where the Hill approximation is used to include the **SRP** acceleration to the dynamics, which is assumed to be constant and parallel to the x -axis of the Hill Problem’s rotating frame (see Figure 2.2 of Chapter 2). This comes from the approximation to the vicinity of the small body, where we assume that the distance to the Sun is approximately constant. Additionally, although it is often not included in the problem’s formulation, we include eclipses caused by the small body. A simple cylindrical eclipse model is used for this due to the distance and the relative size of the small body with respect to the Sun, which make the differences to a more complex model, such as the conic eclipse model, negligible [108].

As indicated, we adopt the same orthogonal rotating reference frame of the Hill Problem, centered on the secondary body, where the x -axis points in the anti-Sun at all times and the z -axis points in the direction of the angular momentum vector of the secondary’s orbit about the Sun. The length and time units also remain the same, $[LU] = (\mu/n^2)^{1/3}$ and $[TU] = 1/n$, respectively, where μ is the secondary’s gravitational parameter and n is its mean motion about the Sun. The normalized equations of motion are

$$\ddot{x} - 2\dot{y} = -\frac{x}{r^3} + 3x + \beta \quad (4.1a)$$

$$\ddot{y} + 2\dot{x} = -\frac{y}{r^3} \quad (4.1b)$$

$$\ddot{z} = -\frac{z}{r^3} - z \quad (4.1c)$$

where $r = \sqrt{x^2 + y^2 + z^2}$ and β is the normalized **SRP** acceleration. The normalized **SRP** can be expressed as a ratio between the dimensional **SRP** acceleration and the secondary’s mass parameter, as

$$\beta = \frac{(1 + C_R)P_0}{m/A \mu^{1/3} \mu_S^{2/3}} \quad (4.2)$$

where C_R is the reflectivity coefficient or albedo, $P_0 \approx 1.02 \times 10^{17} \text{ kg m s}^{-2}$ is the solar constant,

m/A is the mass-to-area ratio, and μ_S is the gravitational parameter of the Sun. Since the non-dimensional SRP acceleration is normalized using the gravitational constants of the primaries, it can be directly compared for different sets of primaries. This provides a clear measure of how significant the SRP is in a particular environment, depending on the mass-to-area ratio considered. Additionally, for the eclipse model, the cylindrical model simply sets the value of β to zero when in the shadow region. A sigmoid step function is also used to simulate a fast but continuous transition between light and shadow.

2 Some solutions of the Augmented Hill Problem

While the Hill Problem has two equilibrium points, L_1 and L_2 , situated along the x -axis at $x = \pm(1/3)^{1/3}$, the increase of the relative value of SRP acceleration, or β , causes the L_1 point to move very abruptly in the Sun direction, and draws the L_2 asymptotically towards the small body. This can be seen in Figure 4.1, which shows the position of each equilibrium point versus the normalized value of the SRP acceleration. To exemplify the applications to

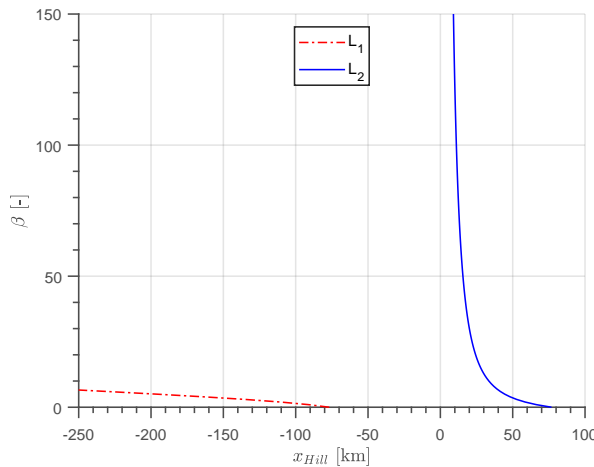


Figure 4.1: The effect of SRP on the equilibrium points of the AHP.

trajectory design in the environments around small bodies, we focus on analyzing trajectories originating from the equivalent of CR3BP's Halo orbits, which are sometimes called terminator orbits in the context of the AHP, and which, like their CR3BP equivalents, originate from the L_2 equilibrium point. Due to this latter fact, said families of periodic orbit experience a similar behavior to the L_2 point in response to an increase in β , moving progressively closer to the small body. Additionally, they gradually approximate the direction perpendicular to the Sun's direction as β increases. This can be more easily visualized in Figure 4.2, which displays two periodic terminator families for different values of β in Figure 4.2a in a three-dimensional view, and a profile view of one of the families in Figure 4.2b. The geometry characteristic to this type of orbit often presents advantages as a spacecraft traveling along one does not cross the eclipse region. Additionally, the orbits are robust to large SRP acceleration values and the ones closer to the primary are actually stable (see [104, 17] for more details). A distinction in nomenclature

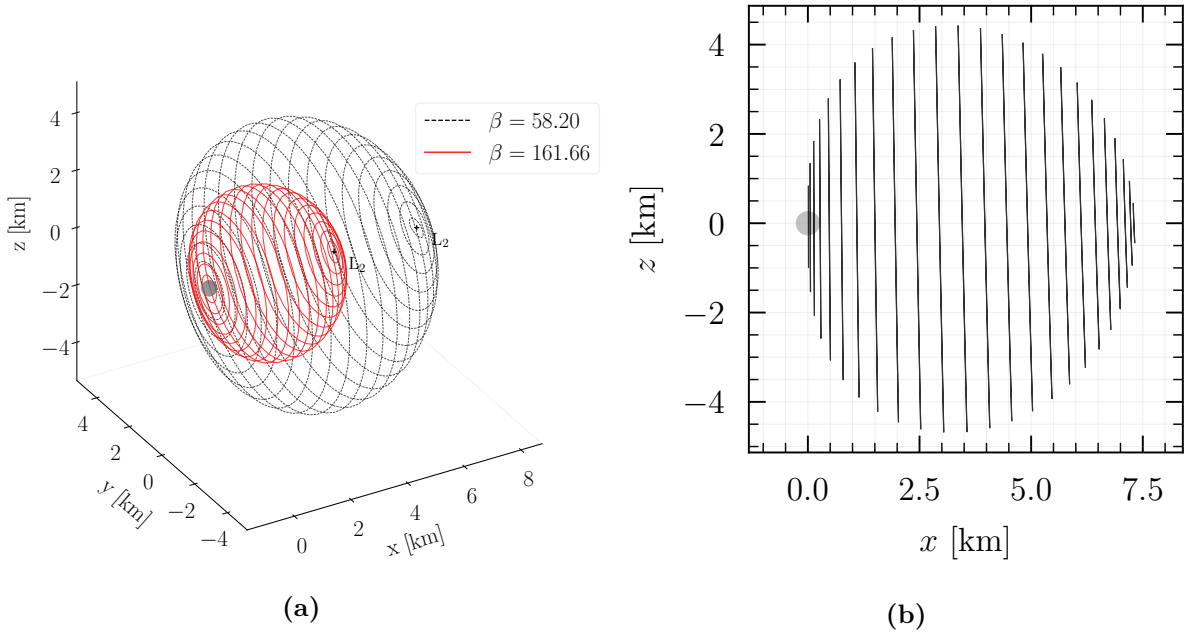


Figure 4.2: Periodic terminator families: (a) three-dimensional view for two different values of β ; (b) profile view for the family with $\beta = 58.20$.

should, however, be made with respect to the orbits that have been used for the OSIRIS-REx mission [94] and that are planned for one of the cubesats in the Hera mission [40]. For the former, these trajectories are also referred to as terminator orbits and, for the latter, they are referred to as Self-Stabilizing Terminator Orbits (SSTO). Although these trajectories are similar in nature to the periodic terminator orbits we've just presented, they do not belong to the same family and are computed differently, where the SSTOs originate from a formulation using averaged orbit elements. Nevertheless, their similar geometry and stability properties translates into interesting mission design options for either types of orbit. In this work, we use the term terminator orbits to refer to the CR3BP's analogous of the Halo orbit family in the AHP model. Additionally, note that due to the z -axis symmetry associated with the CR3BP and the AHP, we can compute both the northern or southern versions of these families by simply mirroring the z -component. Although omitted for succinctness, we showcase the southern version of these families in this chapter.

Because periodic terminator families have complex unitary eigenvalues associated with their monodromy matrix – as can be seen in Figure 4.3, where the angle of the complex unitary values, $\lambda_i = e^{j\alpha}$, is plotted against the initial x coordinate – we can employ the methods presented in Chapter 3 to compute quasi-periodic tori from these periodic orbits. The work by Broschart et al. in [16] showcases examples of quasi-periodic extensions of these terminator orbits, as well as examples of resonant multi-revolution terminator orbits that are found for commensurate torus frequencies. Note that, as seen in Figure 4.3, the portion of the family closer to the body contains a two-dimensional center manifold, or equivalently, two one-dimensional center manifold directions, dictated by the two complex unitary eigenvalues pairs. As explained in previous chapters, these can define a three-dimensional torus family or two two-dimensional

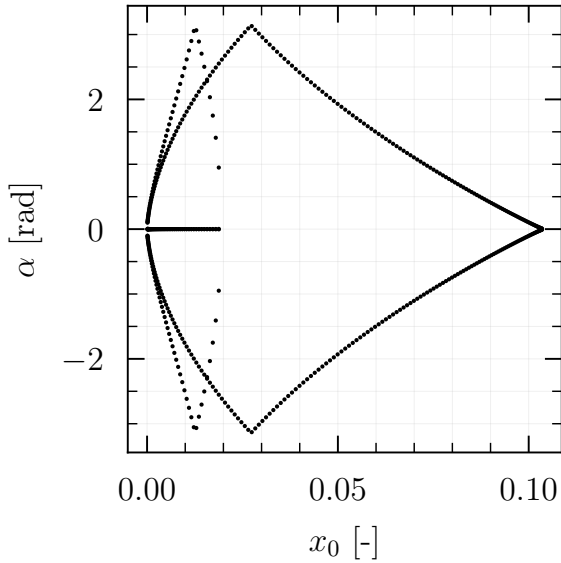


Figure 4.3: Angle of the complex eigenvalues, $\lambda_i = e^{j\alpha}$, associated with the monodromy matrix of the orbits in the periodic terminator family with $\beta = 92.38$.

torus families, respectively. This eigenstructure behavior remains consistent for the different values of β . Broschart et al. [16] compute two families of two-dimensional tori, and call the families associated with center manifold direction that exists only closer to the small body as the dark-side families, since their quasi-periodic tori typically extend in the anti-Sun direction. The families associated with the center direction that persists throughout the whole periodic family are called the Sun-side families, since the tori extend in the Sun's direction. The same authors focus on computing tori for fixed values of Jacobi constant. In this thesis, in order to complete the pre-established work on these families of quasi-periodic terminator families and to provide examples of the wide applications of dynamical systems theory to mission design in these perturbed environments, we study some of these quasi-periodic families for fixed T values. Because the families present similar behavior for different values of β , we present results for values representative of a spacecraft (such as Hayabusa2 or OSIRIS-REx) at a body such as asteroid Bennu, which translates into $\beta = 92.38$.

Figures 4.4 and 4.5 display examples of quasi-periodic terminator tori for both the Sun-side and dark-side families, respectively, at different family members along the tori family continuation, and using the same baseline periodic orbit as a starting point (with $T = 0.067656$ in normalized units). Figure 4.6 shows the quasi-periodic family evolution for the Sun-side family from a baseline periodic orbit close to the L₂ point (at $T = 0.200412$), for which the center eigenspace of the periodic terminator orbit is only one-dimensional, meaning only the Sun-side quasi-periodic families exist. It is interesting to note how the Sun-side and dark-side tori generated from the periodic orbit closest to the body cover the asteroid as we move further along each family. Conversely, the quasi-periodic family closest to the L₂ extends around the nominal periodic orbit while remaining at approximately the same distance from the asteroid. Additionally, as expected from the plot of Figure 4.3, the portion of the periodic family with

only a one-dimensional center manifold is unstable, as are the quasi-periodic tori emanating from said orbits, whose stability values seem to remain approximately constant throughout the continuation procedure. The portion with a two-dimensional center manifold is, however, stable, and this is also reflected in the stability of the quasi-periodic tori, which remain close to the linear stability limit throughout the family continuation.

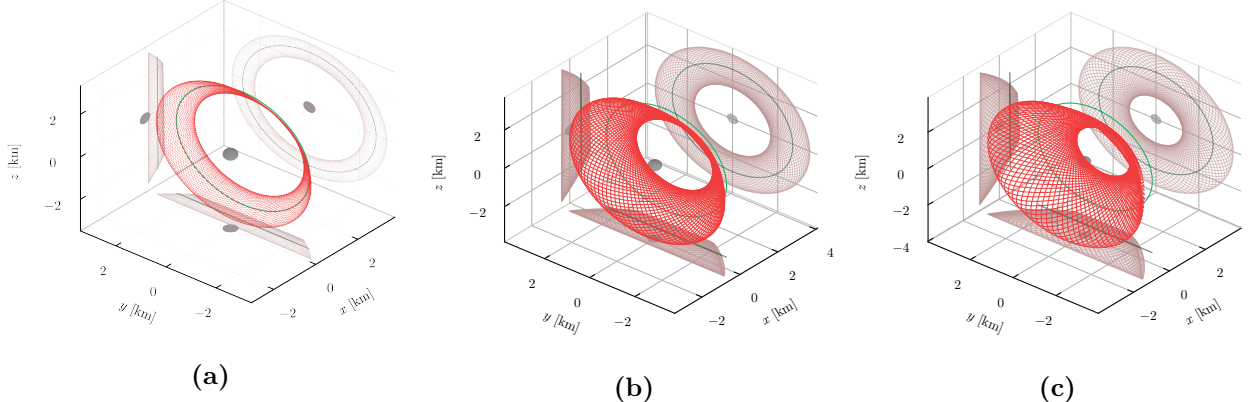


Figure 4.4: Evolution of the Sun-side quasi-periodic terminator family for fixed $T = 0.0676560$ with $\beta = 92.38$. The baseline periodic orbit can be seen in green and has $C = 23.472$. Quasi-periodic tori at Jacobi energy values of (a) $C = 23.034$ (b) $C = 21.824$ (c) $C = 20.004$.

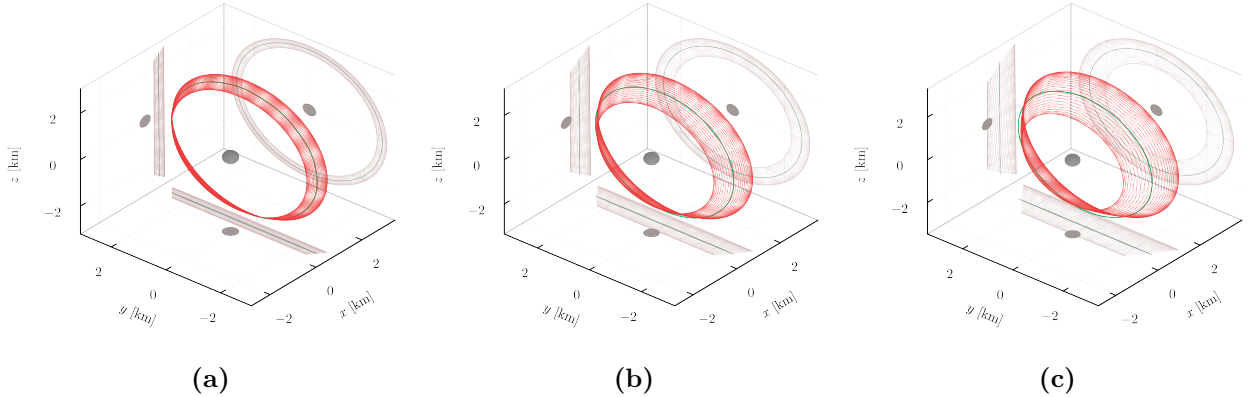


Figure 4.5: Evolution of the Sun-side quasi-periodic terminator family for fixed $T = 0.0676560$ with $\beta = 92.38$. The baseline periodic orbit can be seen in green and has $C = 23.472$. Quasi-periodic tori at Jacobi energy values of (a) $C = 23.581$ (b) $C = 23.901$ (c) $C = 24.410$.

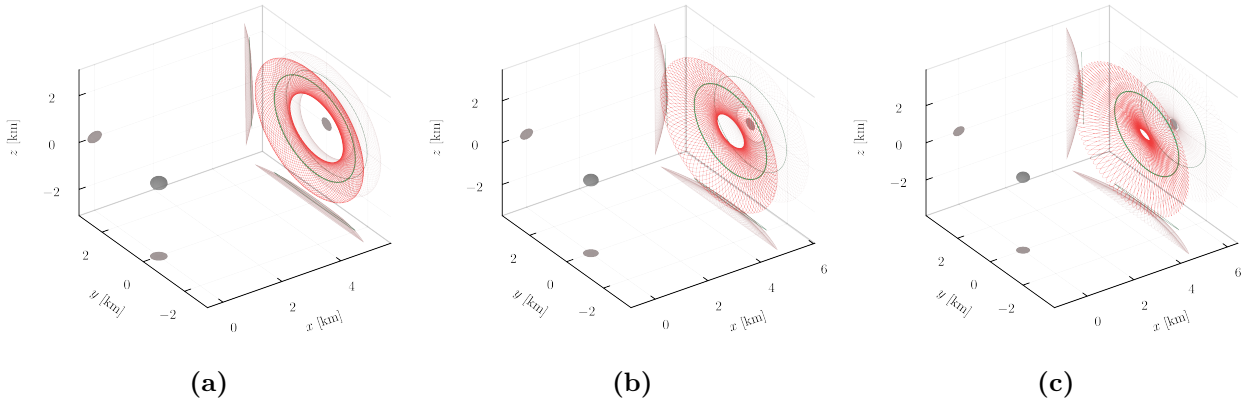


Figure 4.6: Evolution of the Sun-side quasi-periodic terminator family for fixed $T = 0.200412$ with $\beta = 92.38$. The baseline periodic orbit can be seen in green and has $C = 36.145$. Quasi-periodic tori at Jacobi energy values of (a) $C = 35.859$ (b) $C = 35.203$ (c) $C = 34.421$.

3 Landing opportunities via the hyperbolic unstable manifolds of periodic terminator orbits

An important property of the AHP is that the direction of the L₂ hyperbolic manifolds changes with increasing values of SRP acceleration, as the L₂ point gets closer to the asteroid. Indeed, as seen in Figure 4.7, the inner unstable manifold of the L₂ point gets closer to the x -axis, i.e. the Sun-asteroid line, and, for large enough¹ values of β , it actually intersects the secondary, which is represented by asteroid Bennu in this case. Note that since the terminator family is an

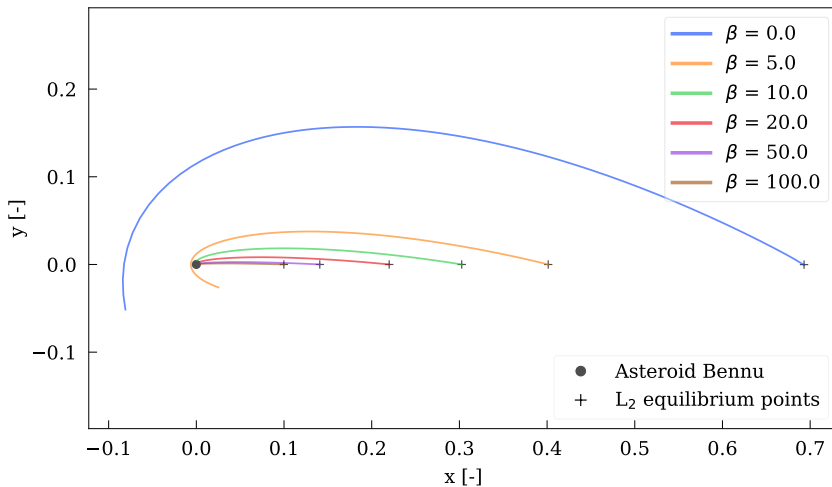


Figure 4.7: The inner unstable manifold of the L₂ equilibrium point for different values of β at Bennu.

L_2 family, the general direction and shape of its manifolds will also be dictated by that of the L_2 equilibrium point's manifolds, even more so for orbits close to it, where the effect will be more significant. This dynamical property can be used to the advantage of mission designers hoping

¹The exact threshold depends on the radius of the asteroid but seems to be between $\beta = 5$ and $\beta = 15$.

to generate baseline landing trajectories to the surface of small bodies. Whether it be larger spacecraft, cubesats, or rovers, the deployment and landing of these structures is extremely challenging due to weak gravity, the small sphere of influence, and the generally perturbed dynamics that most small bodies such as asteroids and small comets possess. Previous works have studied landing trajectories onto small bodies [101, 36, 49], but these do not usually take a baseline orbit or trajectory into account, and rather focus on initial conditions of the lander's trajectory as opposed to assuming that the mothercraft is in a particular orbit. A study that does, however, take this into account is presented in [28], where baseline periodic orbits are divided into various nodes, from which departure Delta-V's are applied. The approach taken in this section follows a similar direction, diverging on the family of orbits used and on the method used to obtain the deployment conditions. Here, we make use of the direction of the unstable manifolds of the terminator orbits closest to L_2 to generate these landing trajectories. In this section we focus only on the periodic terminator orbits.

Different types of landing probes have been considered in this study. Namely, as specified in Table 4.1, we have considered lander-types that resemble a spacecraft, a cubesat, a MASCOT-type lander [103], and two additional ones – with smaller mass-to-area ratio – named lander A and B. Note that for the cubesat we consider an effective area of 0.023 m^2 and mass of 4 kg [19], and for the MASCOT-type lander [103] we consider an effective area of 0.072 m^2 and a mass of 10 kg . A general reflectivity coefficient of $C_R = 0.4$ is considered for all the landers. Lastly, we

Table 4.1: Lander parameters

Lander	$m/A [\text{kg/m}^2]$	β at Bennu	β at Ryugu
Cubesat	171.43	18.86	10.08
MASCOT	55.56	58.20	31.12
Spacecraft	35.00	92.38	49.40
Lander A	20.00	161.66	86.44
Lander B	10.00	323.31	172.88

consider that asteroids Bennu and Ryugu are spherical bodies with radii of 252.78 m and 446.5 m , respectively, and gravitational constants of $4.892 \text{ m}^3 \text{ s}^{-2}$ and $32.0 \text{ m}^3 \text{ s}^{-2}$, respectively [63, 10, 98].

To simulate the landing trajectories from the terminator orbits, we select 160 equidistant nodes along each orbit and compute its inner unstable manifolds. We find that, excluding the cubesat lander, 100 % of the trajectories reach the asteroid surface. For the cubesat, 80 % reach Ryugu and 100 % reach Bennu. Given the large mass-to-area ratio considered for the cubesat, and therefore its small value of β (see Table 4.1), it was expected that some of the trajectories would not intersect the asteroid surface. For such low β values, the effect of the L_2 manifold is sometimes not sufficient to guide all the trajectories directly to the small-body. As can be seen in Figure 4.8 for the case of the cubesat at Ryugu, some of the manifolds miss the asteroid on a first pass and either escape or impact later.

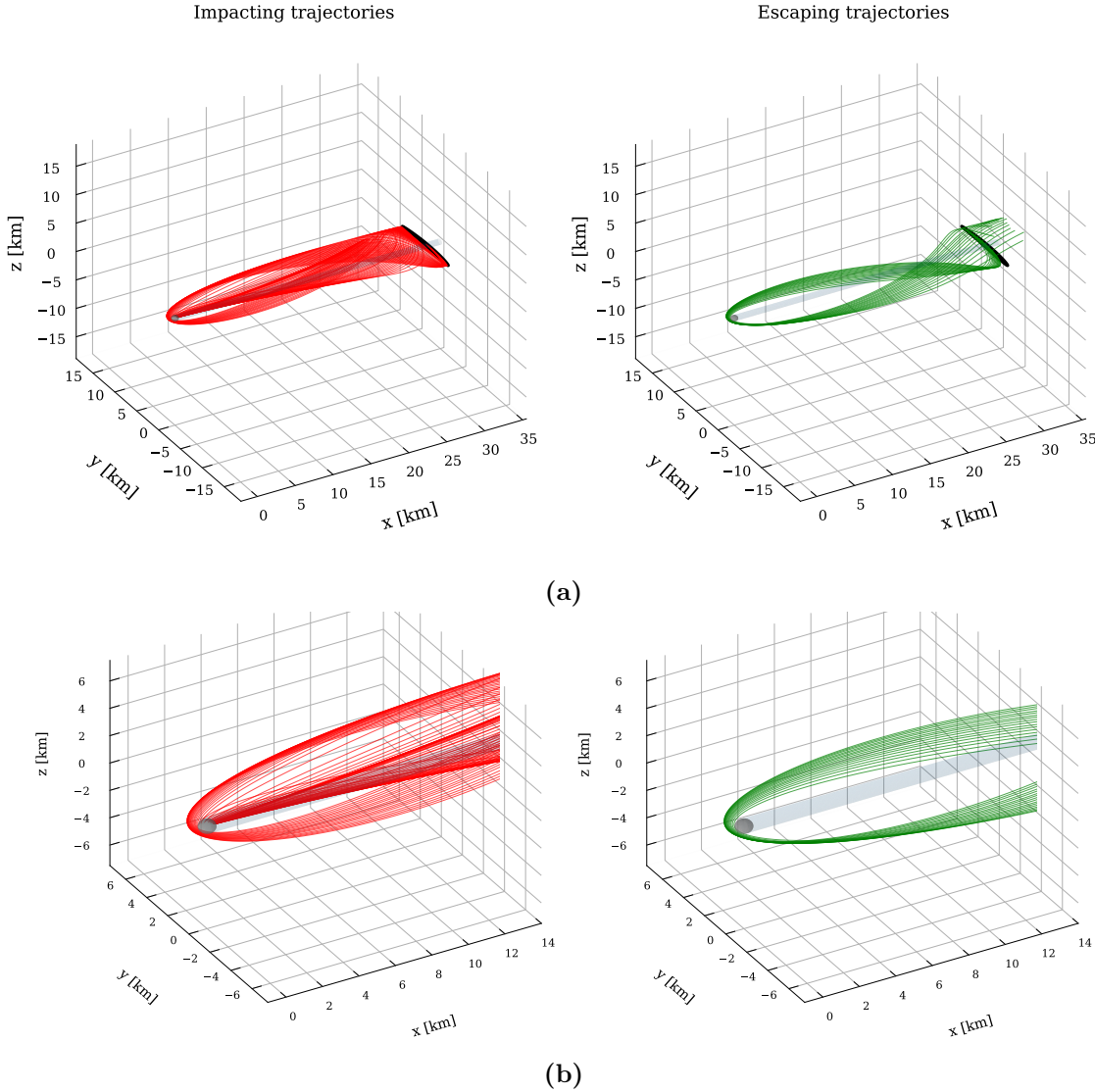


Figure 4.8: Some of the trajectories for the cubesat lander and asteroid Ryugu. The trajectories in red represent some of the trajectories that reach the asteroid surface, while green represents some of the trajectories that escape. The nominal orbit is presented in black and the eclipse shadow is displayed in gray. (a) Full three-dimensional view; (b) zoom-in view.

Contrary to the trajectories of the cubesat, we see that the other landers have very direct trajectories and land with angles close to the surface normal, on average with an angle of 10° from it. Examples of this can be seen in Figures 4.9 and 4.10, which show the unstable manifolds' landing trajectories for the cases of the MASCOT-type and the spacecraft-type landers, which shows how the trajectories become more direct for increasing values of β . The remaining trajectories for the other landers all present these characteristics.

Figures 4.11 to 4.13 show the of flight of the landing trajectories together with the initial and landing velocities of the different landers. A few points become clear by analyzing these figures. Firstly, we see that although not significantly smaller, all the landing velocities are below the two-body escape velocity, which are $v_{esc}^{Bennu} = 19.67$ cm/s and $v_{esc}^{Ryugu} = 37.86$ cm/s, for Bennu and Ryugu, respectively. While this does not necessarily guarantee that a ballistic landing would

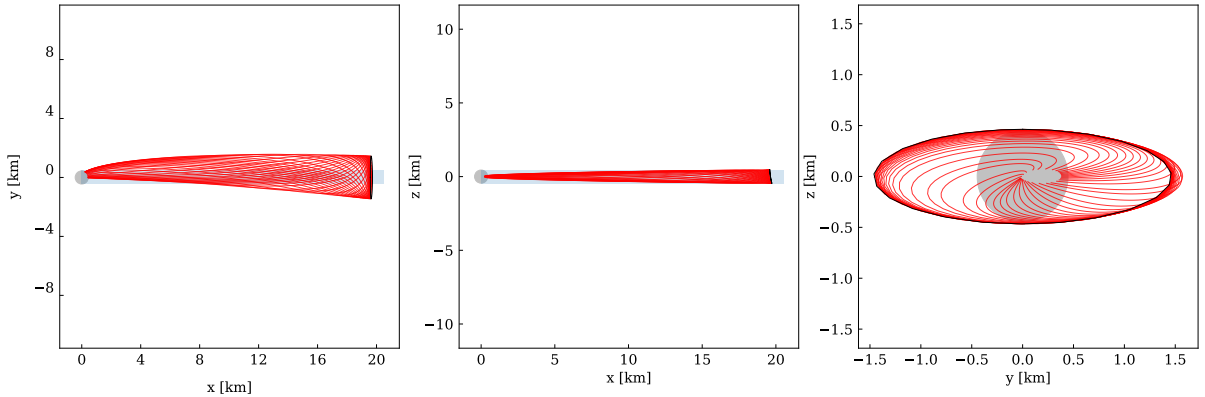


Figure 4.9: Some of the landing trajectories for the MASCOT-type lander and asteroid Ryugu. The nominal orbit is presented in black and the eclipse shadow is displayed in gray.

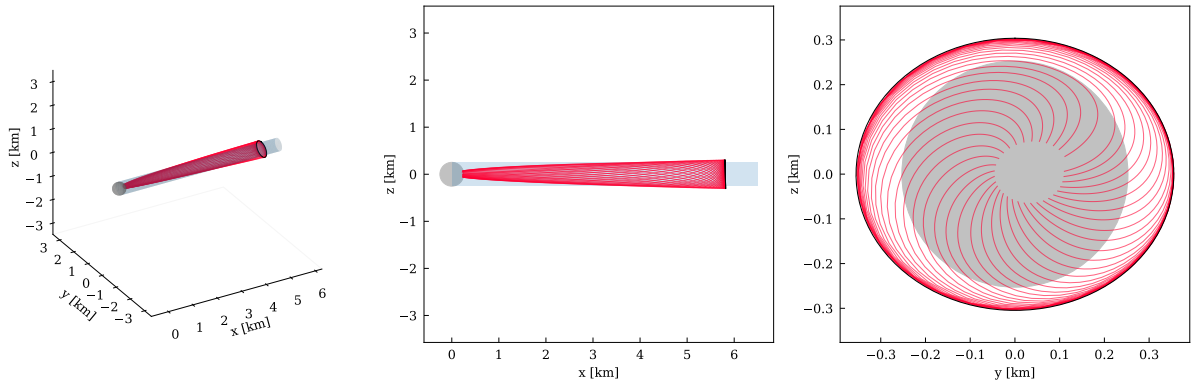


Figure 4.10: Some of the landing trajectories for the spacecraft-type lander and asteroid Bennu. The nominal orbit is presented in black and the eclipse shadow is displayed in gray.

not escape after bouncing – a more detailed analysis considering surface characteristics, among others, would be necessary – it is a good indication for any landing trajectory, particularly when considering these as simply baseline trajectories to be followed via active control. Moreover, we see that the landing velocities decrease for larger β values.

Finally, analyzing the times of flight of the trajectories, we find that although they are quite long – a characteristic of these low-energy trajectories that start far from the small body – they decrease significantly for larger β values. As β increases, the L₂ point draws closer to the secondary, which increases the deployment velocity and shortens the distance from the deployment position to the small body. This translates into times of flight in the order of several weeks down to a few days, depending on the mass-to-area ratio of the lander considered. Furthermore, we see that the same landers have longer times of flight for Ryugu than for Bennu, due to the fact that Ryugu’s gravitational parameter is larger, and thus, the same lander will have a smaller β value in Ryugu than in Bennu (see Eq. (4.2)). The times of flight for the cubesat landings in Ryugu vary significantly because the low β value makes many of the trajectories miss the asteroid on the first pass, as seen in Figure 4.8. Nevertheless, as mentioned, these trajectories are mainly computed with the goal of being used simply as a baseline that guides spacecraft

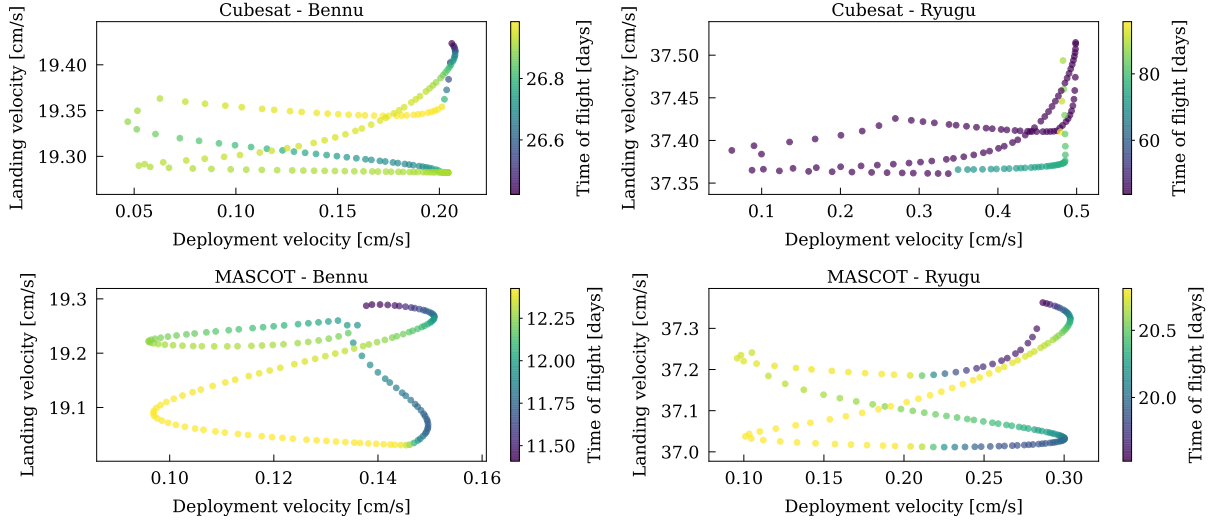


Figure 4.11: Times of flight of landing trajectories as a function of initial and landing velocities for cubesat and MASCOT-type landers.

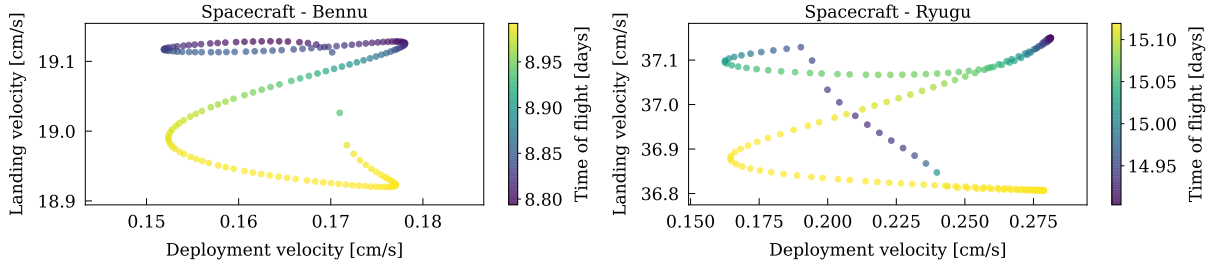


Figure 4.12: Times of flight of landing trajectories as a function of initial and landing velocities for spacecraft-type lander.

to the surface of the body (and for which the spacecraft can be inserted at any point along the baseline landing trajectory), which means that the magnitude of the times of flight is not necessarily relevant.

One could, however, envision situations where only weak guidance capabilities are available or that might need to deal with errors in deployment velocity or position, which could be particularly relevant for small landers with limited control. In this frame, in order to quantify the robustness of the landing trajectories presented, a sensitivity analysis is undertaken. Given that, when using non-dimensional coordinates, the impact of using different primaries is only reflected on their radius, for the sake of simplicity and conciseness, we present only the results of the sensitivity analysis for Bennu.

To introduce errors into the deployment velocity we make use of a normal distribution along each of the x -, y -, and z -directions of said velocity. This introduces a relative error on the magnitude of each individual velocity component and is given by

$$v_i = v_i^* + v_i^* \phi(\sigma) , \quad i = \{x, y, z\} \quad (4.3)$$

where v_i^* is the nominal deployment velocity component and $\phi(\sigma)$ is a normal distribution

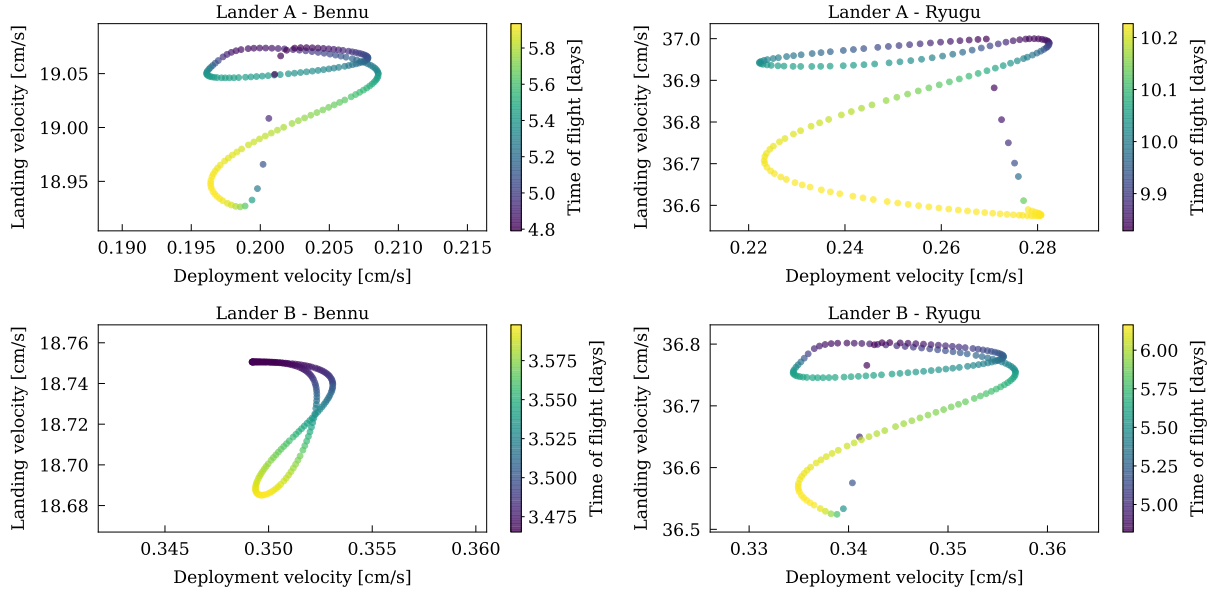


Figure 4.13: Times of flight of landing trajectories as a function of initial and landing velocities for Landers A and B.

centered in zero with a standard deviation of σ along each direction. We select a standard deviation of $\sigma = 0.1$, which translates into a mean angle error around 7° and a mean velocity magnitude error around 2 %. As mentioned before, the nominal deployment conditions are computed by obtaining the unstable manifolds at equidistant nodes along a baseline terminator orbit. When introducing the velocity errors, we compute, at each node, $N = 10$ velocity vectors from the normal distribution, i.e. for each node, we obtain $N = 10$ deployment state-vectors, which have the same position but different deployment velocities. We use 32 equidistant nodes along the nominal orbit of each lander, which accounts to 320 trajectories per lander.

We find that despite the errors introduced, all the trajectories still reach the asteroid. In fact, the trajectories present only minor deviations from the nominal landing trajectories. The main digressions from the nominal trajectories occur in the beginning of the trajectory, but soon return to the nominal trajectories with minor deviations. An example of this, which shows the most significant deviations out of all the landers, can be seen in Figure 4.14. This presents the trajectories for Lander B, which, despite the initial deviations, all reach the asteroid surface and land, on average, around the same locations. Additionally, we find that the landing velocities remain approximately the same, showing only minor increases in some of the maximum landing velocities, as well as slightly lower minimum landing velocities. Interestingly, although the maximum times of flight increase due to the errors introduced, as seen in Figures 4.15 and 4.16, the minimum times of flight actually decrease when compared to those of the nominal landing trajectories (see Figures 4.11 to 4.13 for Bennu). These minima seem to exist for trajectories that enter the eclipse region immediately after deployment, and are typically shown as approximately horizontal lines in the scatter plots.

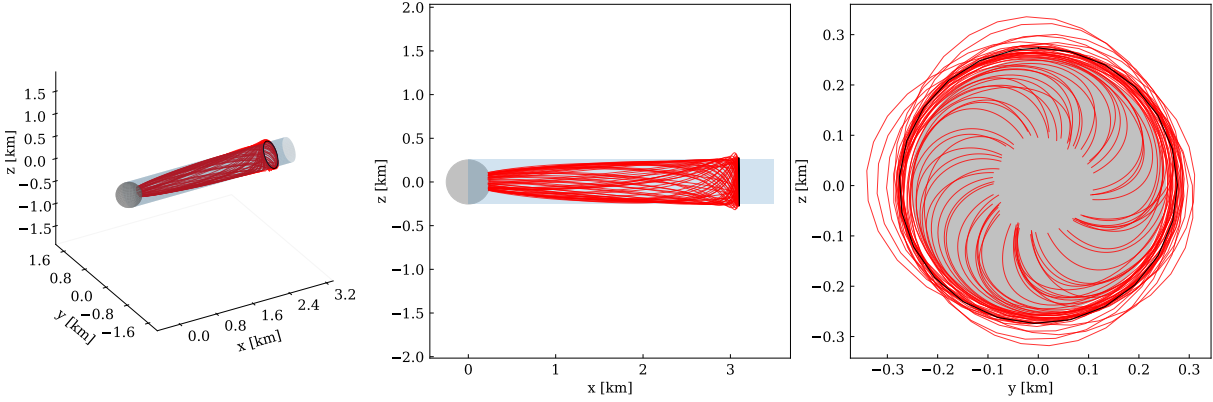


Figure 4.14: Landing trajectories obtained from the deployment velocity sensitivity analysis with $\sigma = 0.1$ (see Eq. (4.3)) for Lander B and asteroid Bennu. The nominal orbit is presented in black and the eclipse shadow is displayed in gray.

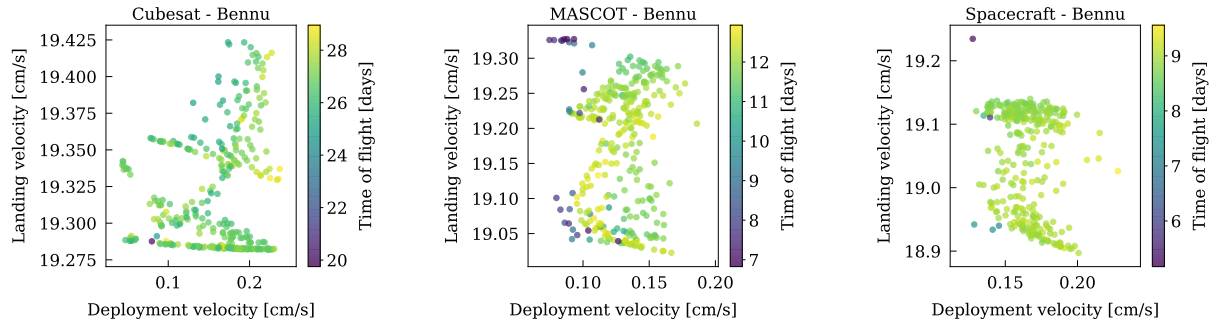


Figure 4.15: Times of flight of landing trajectories as a function of initial and landing velocities obtained from the deployment velocity sensitivity analysis with $\sigma = 0.1$ (see Eq. (4.3)) for the cubesat, MASCOT-type, and spacecraft-type landers.

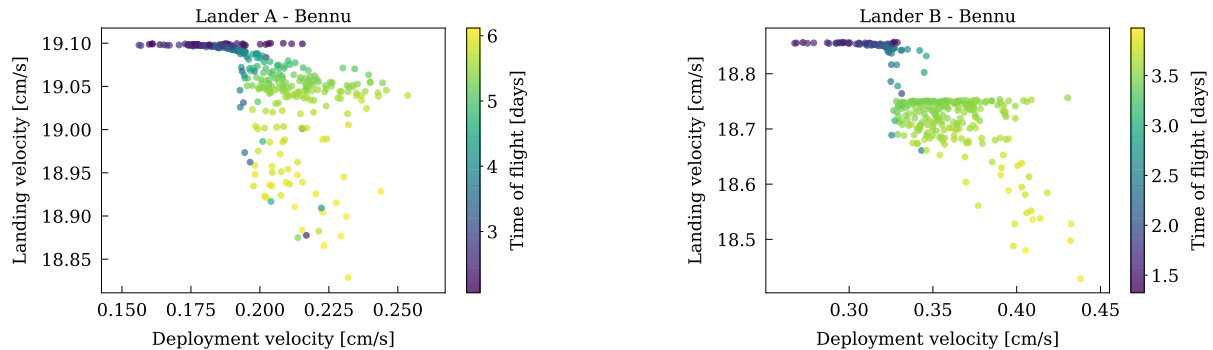


Figure 4.16: Times of flight of landing trajectories as a function of initial and landing velocities obtained from the deployment velocity sensitivity analysis with $\sigma = 0.1$ (see Eq. (4.3)) for the Landers A and B.

Given the robustness of the trajectories presented for the standard deviation value of $\sigma = 0.1$, we test how they respond when significantly increasing the errors. We run the sensitivity analysis again but using a standard deviation of $\sigma = 0.5$, which translates into a mean angle error of deployment velocity around 12° and a mean velocity magnitude error around 33 %. Surprisingly,

we find that even with these large errors, the great majority of trajectories still reach the asteroid. The percentage of the trajectories that reach the asteroid from this new sensitivity analysis can be seen in Table 4.2. Of course, the larger errors mean that we will have larger deviations from

Table 4.2: Percentage of landing trajectories that reach asteroid Bennu, obtained from the deployment velocity sensitivity analysis with $\sigma = 0.5$ (see Eq. (4.3)).

Lander	% that reaches Bennu
Cubesat	93.8 %
MASCOT	99.7 %
Spacecraft	99.7 %
Lander A	99.1 %
Lander B	89.4 %

the nominal landing trajectories. All landers present said larger deviations, and an example of the trajectories that reach the asteroid arising from this sensitivity analysis for Lander B can be seen in Figure 4.17, which offers a direct comparison with Figure 4.14 for the smaller value of standard deviation. We can see the larger deviations clearly by comparing the right-most view in each of the figures, which show the view from the orbit to the asteroid, in the asteroid-Sun direction.

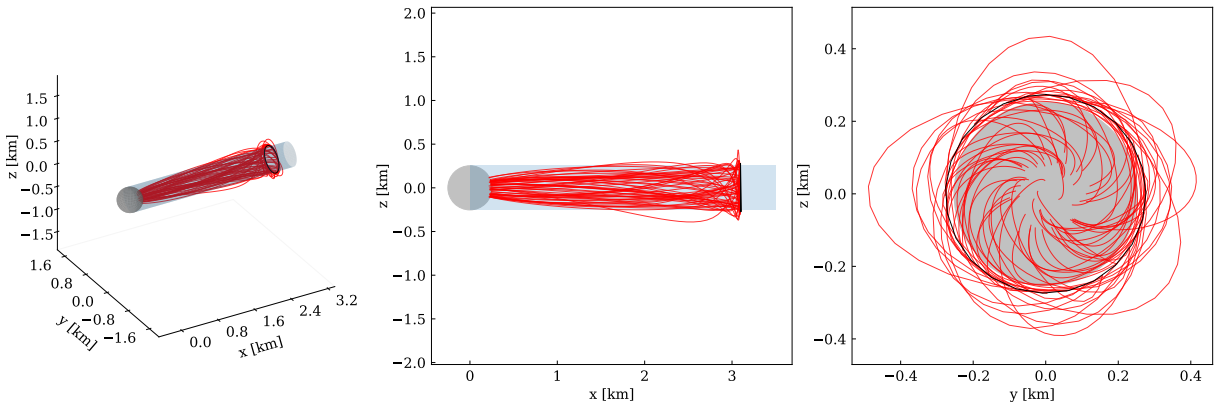


Figure 4.17: Some of the landing trajectories obtained from the deployment velocity sensitivity analysis with $\sigma = 0.5$ (see Eq. (4.3)) for Lander B and asteroid Bennu. The nominal orbit is presented in black and the eclipse shadow is displayed in gray.

Finally, Figures 4.18 to 4.19 show the times of flight as a function of the landing trajectories obtained from this sensitivity analysis. Once again, we see that while the maximum times of flight increase (more significantly due to the larger errors introduced), the minimum times of flight outperform those found using the nominal manifold trajectories, reiterating the indication that an optimization of the deployment conditions obtained from the concept presented in this paper or the use of active control might lead to interesting results. Lastly, the landing velocities remain consistent with the previous simulations.

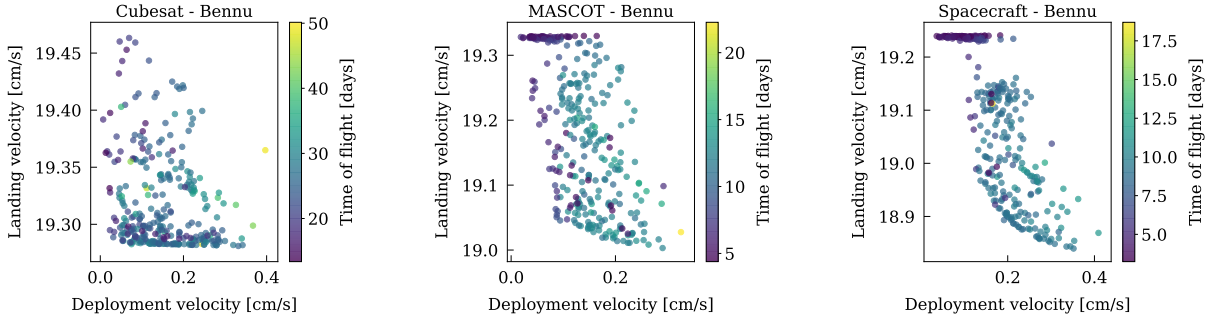


Figure 4.18: Times of flight of landing trajectories as a function of initial and landing velocities obtained from the deployment velocity sensitivity analysis with $\sigma = 0.5$ (see Eq. (4.3)) for the cubesat, MASCOT-type, and spacecraft-type landers.

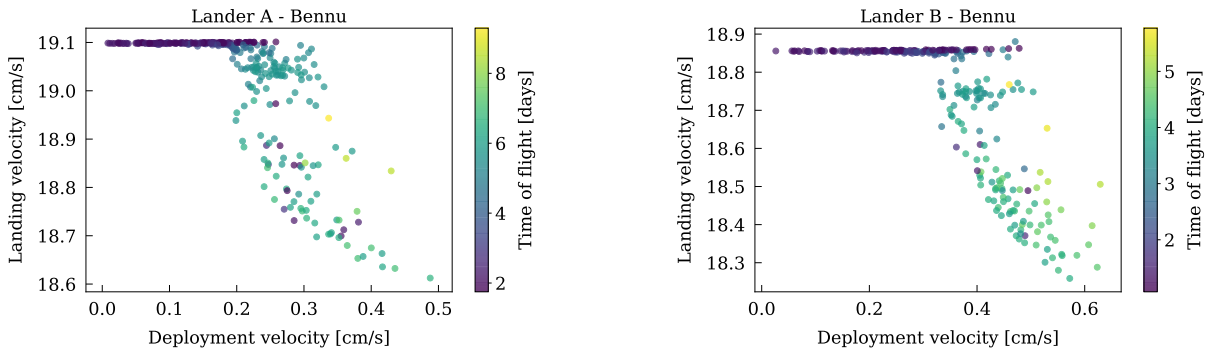


Figure 4.19: Times of flight of landing trajectories as a function of initial and landing velocities obtained from the deployment velocity sensitivity analysis with $\sigma = 0.5$ (see Eq. (4.3)) for the Landers A and B.

4 The hyperbolic manifolds of quasi-periodic terminator orbits

In the same way as we compute the hyperbolic manifolds of the unstable periodic terminator orbits, we can generate the hyperbolic manifolds of their unstable quasi-periodic tori². To do so, we consider quasi-periodic tori associated with periodic terminator orbits close to the L_2 point, at around 90% of the distance between the body and the equilibrium point along the x -axis. From said tori families, of which an example computed for β values associated with the spacecraft SRP values ($\beta = 92.38$ for Bennu) were shown in Figure 4.6, we select the last member of the family before the family stops converging³ – for the spacecraft this corresponds to the torus in Figure 4.6c. For succinctness we consider only asteroid Bennu and the β values associated to the cubesat, MASCOT, Spacecraft, and Lander A.

We find that although not all trajectories intersect the body, due to the tori's extension away from the Sun-asteroid line, a big portion of the unstable manifolds do so, and over a much wider area around the surface of the body. Indeed, for the spacecraft β values at Bennu, we

²a complete formulation for their initialization can be seen in Chapter 6, which is left out from this section for succinctness.

³Note that this happens when the quasi-periodic trajectories get very close to the equilibrium point and the eclipse shadow. Since we want to make use of the L_2 point's manifolds we want the tori to be as close as possible to said point.

can see the unstable manifolds of a quasi-periodic torus close to the L_2 point in Figure 4.20, where we plot only the trajectories that intersect the asteroid, and where the unstable manifolds are represented in light green and the torus is shown in red. A sample landing trajectory is shown in a bold pink line. Although it is hard to distinguish the many different trajectories that lead to the surface, it is clear that they intersect the asteroid in many different locations. This can be seen more clearly in Figure 4.21, where the latitude and longitude of the landing

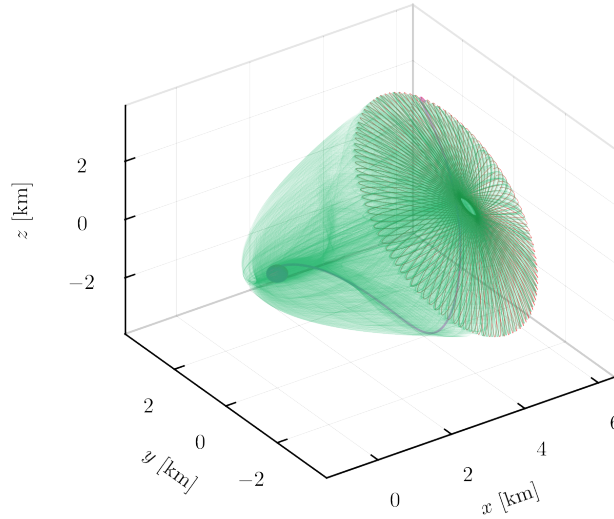


Figure 4.20: Landing trajectories for spacecraft ($\beta = 92.38$) and asteroid Bennu from the Sun-side quasi-periodic terminator torus with $C = 34.421$, $T = 0.200412$. The torus is shown in red and the inner unstable manifolds that reach the asteroid in green. A sample trajectory is shown in pink.

locations on the surface of the asteroid are plotted together with their landing velocity. Note that the latitude is measured from the xy -plane and the longitude's 0° direction coincides with the Anti-Sun direction, whereas 180° longitude points towards the Sun. The landing locations for the terminator orbit's manifolds for the same spacecraft SRP values are also shown using a different colormap for comparison. Although the landing velocities are very close between the solutions (the torus manifolds' velocities are larger by only a few mm/s), the advantage of having a wider array of landing locations to choose from is evident.

Additionally, for completeness, the landing locations at Bennu for the equivalent quasi-periodic tori for the β values associated with the cubesat, MASCOT, and Lander A can be seen in Figures 4.22 and 4.23, where the landing locations from the periodic orbits previously presented for each β value are also shown.

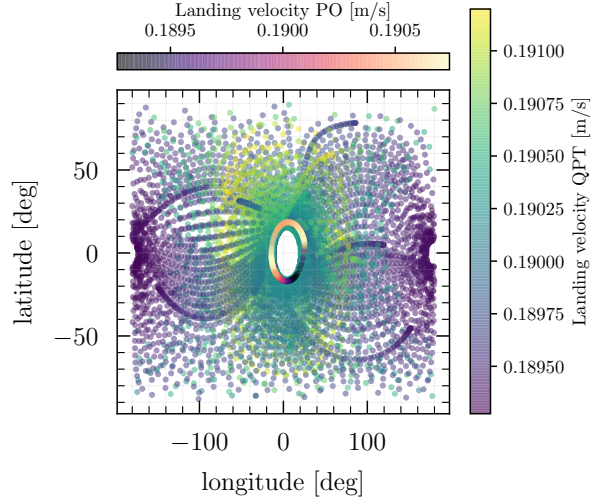


Figure 4.21: The landing locations of the unstable manifold trajectories that intersect the asteroid for spacecraft ($\beta = 92.38$) and asteroid Bennu from the Sun-side quasi-periodic terminator torus with $C = 34.421$, $T = 0.200412$. The landing locations of the periodic terminator's unstable manifolds are also overlayed with a different colormap.

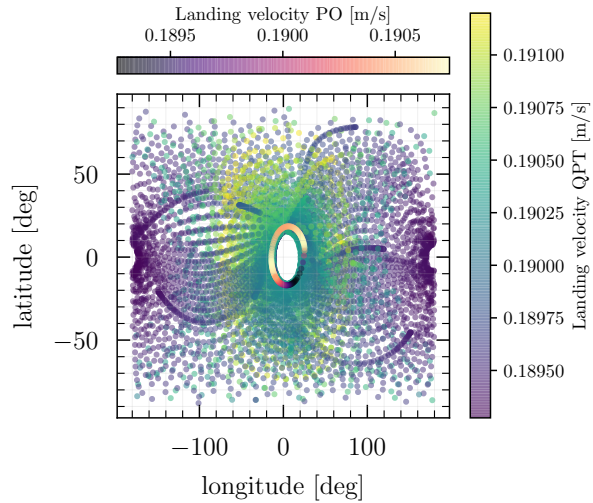


Figure 4.22: Landing locations at asteroid Bennu from the stable manifolds that intersect the asteroid from the terminator quasi-periodic torus for the cubesat lander ($\beta = 18.86$), with $T = 0.66034$, $C = 16.852$, as a function of the ballistic landing velocity. The landing locations of the periodic terminator orbit for the same lander are overlayed with a different colormap.

We note that the same trends observed for the spacecraft are maintained, as is expected. Nevertheless, the trajectories coming from quasi-periodic tori entail much wider areas for the landing locations, with longer times of flight on average, albeit having significantly more non-impacting trajectories.

Finally, it is important to consider that the unstable manifold trajectories that do not reach the asteroid can also be of interest for surface mapping or for other science operations. Looking at the example of such a trajectory in Figure 4.24 for the spacecraft β values at Bennu, we see

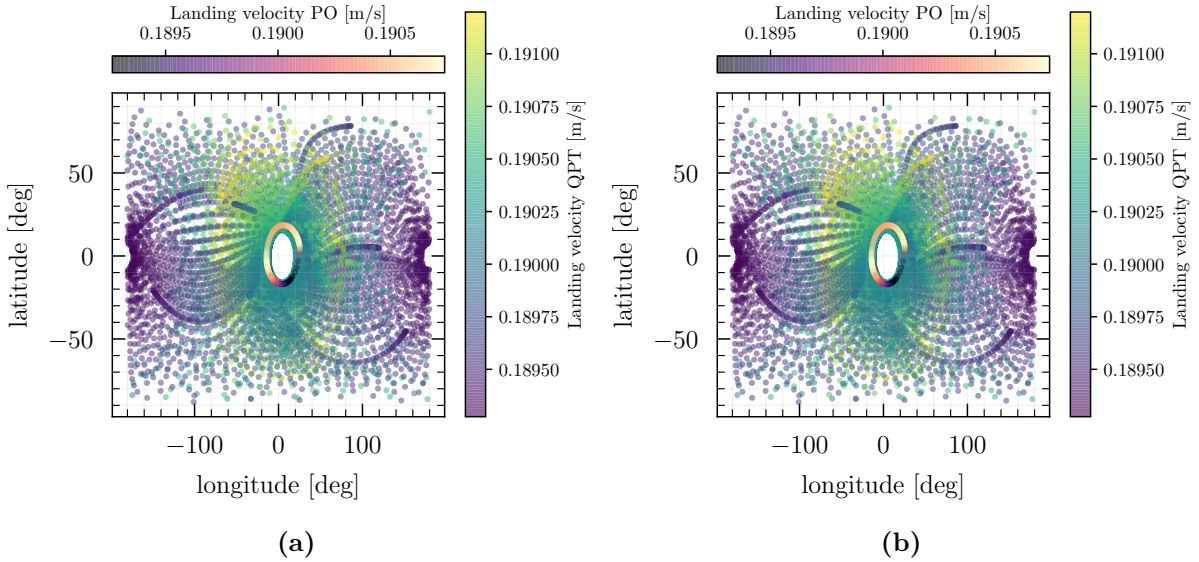


Figure 4.23: Landing locations at asteroid Bennu from the stable manifolds of terminator quasi-periodic tori that intersect the asteroid as a function of the ballistic landing velocity. The landing locations from the periodic terminator orbit for the respective lander are overlayed with a different colormap. (a) MASCOT ($\beta = 58.20$), from torus with $T = 0.28252$, $C = 27.254$; (b) lander A ($\beta = 161.66$), from torus with $T = 0.13169$, $C = 45.526$.

that not only does the trajectory pass on the Sun-lit side of the body two times, but it also almost seems to naturally return to the quasi-periodic torus. This hints at the possibility of designing homoclinic connections from these quasi-periodic terminator orbits, which due to the geometry of the tori considered as well as that of their associated hyperbolic manifolds, they seem especially suited to accommodate.

One way to design homoclinic connections is to make use of Poincaré maps. Note that the hyperbolic manifolds of two-dimensional quasi-periodic tori are three-dimensional manifolds (two dimensions associated with each torus frequency and another associated with the integration time in the hyperbolic direction). As such, at any fixed point in time, they define a two-dimensional torus surface. Likewise, we could argue that by fixing one of the degrees of freedom of the problem by means of a Poincaré map or surface of section, e.g. $x = 0$ with $\dot{x} < 0$, we will have a projection of a two-dimensional torus onto said surface of section. If the two-dimensional surfaces of the stable and unstable manifolds are projected onto the Poincaré section intersect, their intersection defines also a two-dimensional surface, which, potentially, enables an infinite number of homoclinic connections. One can compare these with the intersections of the hyperbolic manifolds of periodic orbits, which are themselves two-dimensional manifolds. Their projections onto the same Poincaré map define one-dimensional curves, which, if they intersect, define only a finite number of connections (unless the two curves are overlapped). This provides a clear advantage in designing connections from quasi-periodic tori. Additionally, because homoclinic connections belong, by definition, to the same manifold, their Jacobi constant will be the same for both the outbound (unstable) and returning (stable) manifolds when in autonomous systems. However, as detailed in [25], because we are considering spatial trajectories

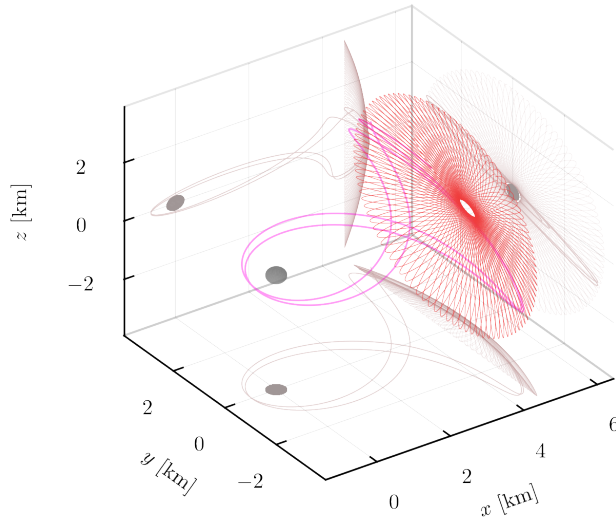


Figure 4.24: Example of an unstable manifold trajectory that does not intersect the asteroid from the quasi-periodic terminator torus associated with the spacecraft ($\beta = 92.38$) at Bennu with $C = 34.421$, $T = 0.200412$.

(instead of planar ones), and because we fix only the variable associated with the Poincaré section and the Jacobi constant, even when their spatial coordinates intersect, this does not guarantee a continuous trajectory that uniquely describes the manifold, as two variables will always be unresolved. Indeed, there will be a (small) velocity discontinuity between the two branches of the connection, which also means that the same intersection in spatial coordinates can correspond to more than one connection.

On another note, the quasi-periodic tori hereby shown are discretized, and as such are represented by trajectories associated with a number of discretization nodes. Nevertheless, note that they represent whole surfaces and the discretization is only necessary for computational reasons. In the same way, although intersections with the Poincaré maps may seem as a collections of curves or points for the same reason, they too represent two-dimensional surfaces. With this in mind, we can analyze the Poincaré map at $x = 0$ associated with the hyperbolic manifolds of the quasi-periodic torus for the β spacecraft values in Figure 4.25. Note that since the stable manifolds are integrated backwards in time and the unstable are integrated forwards, the crossing sign of \dot{x} has to be opposite for each of the integrations to define connections that move in the same direction. Additionally, we don't include the trajectories that impact with the asteroid before reaching the Poincaré section.

Figure 4.25 shows that the Poincaré surfaces corresponding to the hyperbolic manifolds do indeed overlap for a majority of the non-impacting trajectories, which indicates that we can find homoclinic connections by selecting intersections between these surfaces. A more elaborate and accurate method to find these intersections is described in [25]; here, for the sake of simplicity and succinctness, we merely discretize the tori enough so as to find stable and unstable trajectories which are within a specified tolerance (which we set to 0.5 m) in position error from

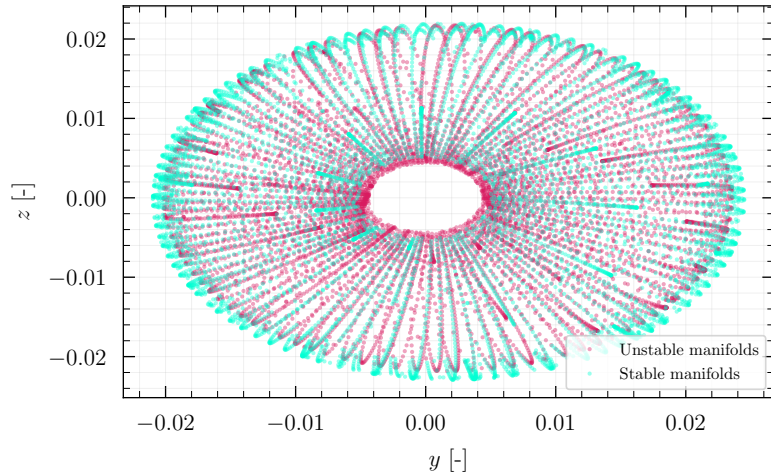


Figure 4.25: Poincaré map at $x = 0$ of the stable and unstable manifolds associated with spacecraft ($\beta = 92.38$) at Bennu, for the manifolds that don't intersect with the asteroid, from the quasi-periodic terminator torus with $C = 34.421$, $T = 0.200412$.

one another at the Poincaré section. This allows us to find the homoclinic connections displayed in Figure 4.26, where in addition to the outbound (unstable) and return (stable) trajectories, we integrate the trajectories for a time T before departing and after arriving, respectively. In a similar way, heteroclinic transfers between tori that have the same value of Jacobi constant are also likely to exist (and could be explored using the methodologies demonstrated in [25] or in [82]), but have not been addressed in this study.

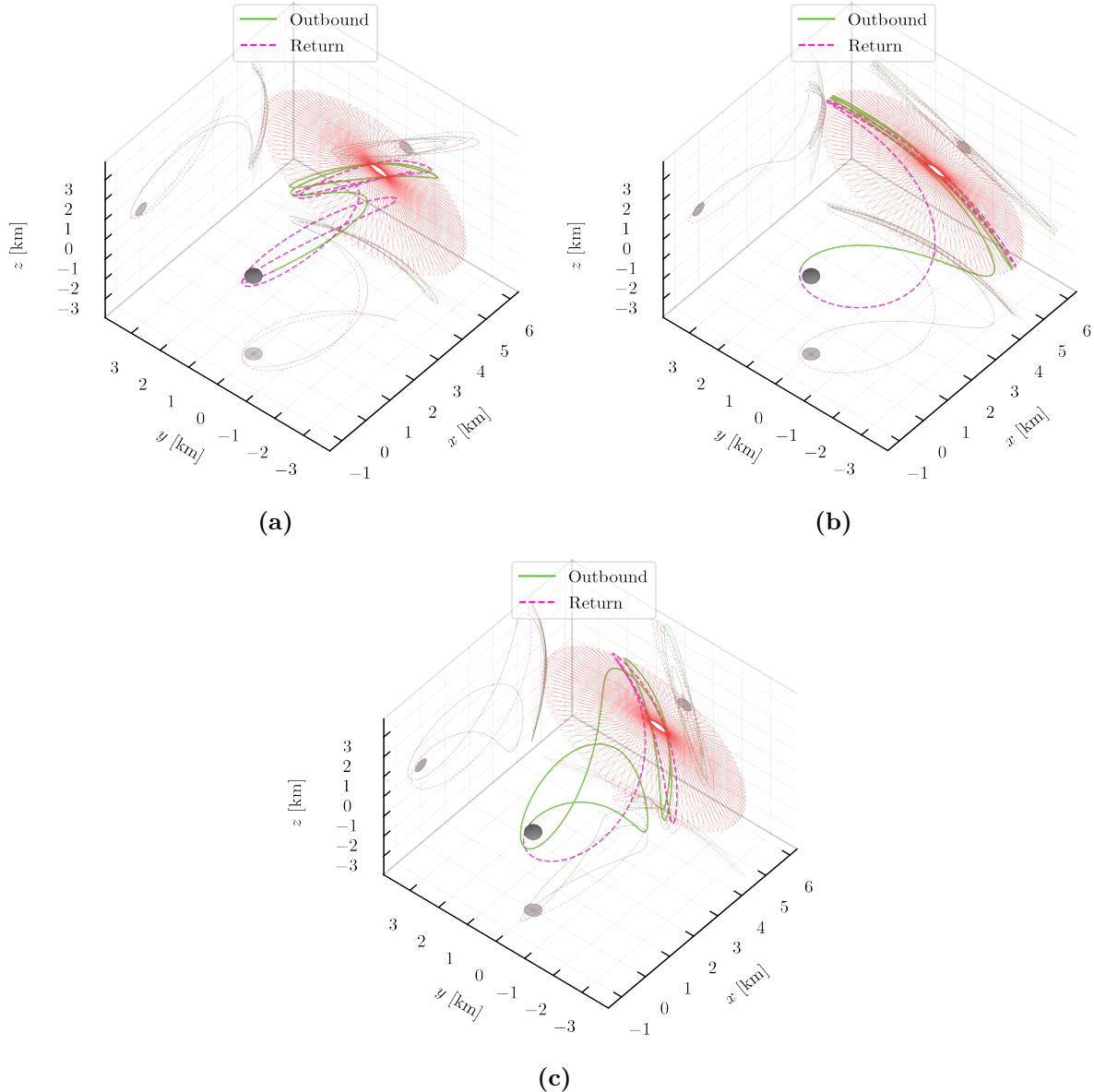


Figure 4.26: Different homoclinic connections for the quasi-periodic terminator torus associated with the spacecraft ($\beta = 92.38$) with $C = 34.421$, $T = 0.200412$ at Bennu. The outbound or unstable manifold trajectories are shown in green and the return or stable manifold trajectories are shown in dashed pink. The torus is shown in red.

5 Conclusions

This chapter has presented applications of numerical [DST](#) methods and trajectory design tools to small-body exploration, which were showcased in the context of the [Augmented Hill Problem \(AHP\)](#). Specifically, we focused on the periodic orbit family that is equivalent to the Halo orbit family of [CR3BP](#), which is often referred to as the terminator family, and the quasi-periodic tori that emanate from these orbits. Both the periodic and quasi-periodic solutions were analyzed for different values of relative [Solar Radiation Pressure \(SRP\)](#) acceleration, which depends on the mass of the small-body and the mass-to-area ratio of the spacecraft being considered. In this frame, the invariant hyperbolic manifolds of these solutions were studied. These are dictated by hyperbolic manifolds of the L_2 point, which are affected by the value of the relative [SRP](#) acceleration. We analyzed the possibility to construct baseline landing trajectories using the unstable manifolds of these solutions. Additionally, we demonstrate how the hyperbolic manifolds of the quasi-periodic terminator tori allow, when selecting trajectories that don't intersect with the body, for the easy design of homoclinic connections.

Chapter 5

The Elliptic-Circular problem and the cislunar environment

In this chapter, a novel dynamical problem is presented, based on the work by Castellà and Jorba [27]. Named the [Elliptic-Circular Restricted Four-Body Problem \(ECR4BP\)](#), or Elliptic-Circular model for short, the problem is especially suited to tackle the dynamics associated with the cislunar environment, as it incorporates both the perturbation posed by the Sun and the eccentricity of the Moon’s orbit. As such, the problem is employed in the frame of NASA’s Lunar Gateway mission in order to find and analyze the dynamical equivalents of the mission’s planned orbit, which belongs to the [Near-Rectilinear Halo Orbit \(NRHO\)](#) family, which was originally computed in the [CR3BP](#). Specifically, we study two resonant synodic or and one resonant sidereal [NRHOs](#), performing numerical continuation from the [CR3BP](#) to the higher-fidelity Elliptic-Circular via the methods presented in the previous chapters. The chapter is divided as follows. Section 1 presents the motivation and frame of this contribution, detailing previous work in trajectory design on the cislunar environment and details on the Lunar Gateway mission. In Section 2, the equations of motion of the Elliptic-Circular are presented, and in Section 3 the numerical continuation procedure of the orbits of interest is formulated, leveraging the schemes previously presented in Chapter 3. Then, Section 4 presents the quasi-periodic tori that arise from these numerical procedures. In Section 5 their stability is studied, and in Section 6 several torus maps associated with these solutions are analyzed. Finally, Section 7 resumes the findings of this study.

1 Cislunar space and the Lunar Gateway mission

Pushed by recently undertaken [44, 110] and planned lunar missions, the interest in accurately modeling the cislunar environment has gained a significant importance for space mission designers. Particularly, NASA’s Artemis program [78] has cemented the relevance of cislunar space and lunar missions for the future of space exploration, be it as the exploration of the Moon or as the staging ground for interplanetary missions. Central to these plans, the NASA-led Lunar Gateway station will be deployed about the Moon in what is known as a [Near-Rectilinear](#)

Halo Orbit (**NRHO**) to serve for science and observation, life support and habitation of visiting astronauts, communications, and as an outpost for future missions. The Gateway's planned orbit type, the **NRHO**, is a sub-family of the Earth-Moon's L₂ Southern Halo orbit family [77, 51] that has been extensively studied due to its relevance in the frame of space exploration. As reported in [31], the **NRHO** sub-family experiences lower perilune altitudes and presents attractive near-stable conditions with respect to the rest of the Halo family, which translates in lower station-keeping costs. Specifically, the targeted orbit for the Lunar Gateway is a 9:2 resonant synodic **NRHO** of the L₂ southern family [77], meaning that a spacecraft along this orbit completes 9 revolutions for every two revolutions of the Earth-Moon-Sun system, where the synodic period of the Earth-Moon-Sun is about 29.5 days. The use of synodic resonant orbits has been shown to be advantageous in the past, particularly regarding eclipse avoidance, as demonstrated in [111, 31, 30].

It is common to study cislunar trajectories in the simplified Earth-Moon dynamical model of the **CR3BP**, where the **NRHO** and Halo families were originally formulated [51]. However, as stated throughout this thesis, the **CR3BP** can be a poor approximation of the real dynamics, which can be particularly true in the case of the cislunar environment. For this reason, studies have been performed where **NRHOs** initially computed in the **CR3BP** are continued into high-fidelity full-ephemeris models and further analyzed in these models, as is the case in [31, 77]. Although multiple techniques exist, this is typically done by applying small velocity corrections (discontinuities) at specific points along the trajectory in order to keep it in the proximity of the baseline **CR3BP** orbit. Although the analyses performed via these techniques are very valuable, one could argue that part of their dynamical information might be lost due to the discontinuities applied, even if very small in magnitude. Moreover, we have no guarantees that the trajectories to which the algorithms converge represent the actual dynamical equivalent of the **CR3BP**'s periodic **NRHOs**.

In order to retain a higher degree of dynamical information and a better dynamical correspondence with respect to the **CR3BP**'s trajectories, we can make use of higher-fidelity dynamical models that allow us to compute the dynamical substitutes of the **CR3BP**'s **NRHOs**. We can do this by using some of the models presented in Chapter 2, such as the periodic Bicircular problem, which incorporates the influence of the Sun's gravity in the dynamics, and has previously been used to analyze periodic and quasi-periodic orbits in the cislunar space [15, 90, 69, 96].

While these works remain very relevant and useful in the design of trajectories around the cislunar space, for the most part, they do not consider a significant perturbation present in the real dynamics of the system: the eccentricity of the Moon's orbit. Aiming to further improve the accuracy of the dynamical systems used to model the cislunar environment, we propose to incorporate this perturbation into our dynamical model, thus generalizing the **BCR4BP** into what we refer to as the **Elliptic-Circular Restricted Four-Body Problem (ECR4BP)**. The **ECR4BP**, or Elliptic-Circular problem, models the Earth and the Moon in elliptical orbits about their barycenter and considers that the Sun moves in a circular orbit about the Earth-Moon's barycenter. The model has been previously shown to describe the motion of a particle near the Earth-Moon's triangular equilibrium points accurately when compared to JPL ephemeris,

as opposed to the CR3BP [27]. This is proven to be particularly significant in terms of the practical stability of solutions, which the authors show the CR3BP and even the Bicircular can over-estimate. Note that, just as the Bicircular, the Elliptic-Circular is not a coherent model. That is, for both models the motion of the massive bodies is not a solution of the Three-Body Problem since the Sun is considered to not affect the motion of the Earth and the Moon. Nevertheless, the model remains a good approximation of the dynamics of a spacecraft subject to the gravitational attraction of all bodies, making it an attractive option for spacecraft mission design. While coherent restricted four-body models such as the Quasi-Bicircular model exist [2], we do not consider them in this thesis. Other restricted four-body problems that should be mentioned include the Hill four-body problem [91] and the BiElliptic problem [3, 29].

In this chapter, we employ the ECR4BP model to study the dynamical equivalents of some of the CR3BP's NRHOs, among them, that planned for the Lunar Gateway. Specifically, we propose to analyze three types of resonant NRHOs in this model: the 9:2 and 4:1 synodic resonant NRHOs, and the 4:1 sidereal resonant NRHO. In addition to the planned Gateway orbit, the two 4:1 resonances are chosen due to their relative proximity to the 9:2 synodic resonance and their consistent stability behavior during continuation to other models [15, 31]. Additionally, while the synodic resonances have been studied before in the Bicircular model, the sidereal resonance has only been analyzed in an ephemeris model [31]. To the best of the author's knowledge, neither has been analyzed in a non-ephemeris high-fidelity dynamical model that incorporates both the perturbation of the Sun and that of the Moon's eccentricity.

2 Equations of motion

The Elliptic-Circular can be seen as a generalization of the Bicircular, the latter of which considers that the primary and secondary move in circular orbits whereas the former considers they move in elliptical orbits. In both models, the third body (in our case, the Sun) moves in a circular orbit about the barycenter of the other two bodies, with all bodies moving in the same orbital plane. As detailed in Chapter 2, the Bicircular model represents a periodic system, characterized by its synodic frequency or period, i.e. the rate at which the relative positions of the Earth-Moon-Sun repeat, which is given by $\Omega_3 = n - n_3$, where n is the mean motion of the primary and secondary and n_3 is the third body's mean motion. The Elliptic-Circular model, however, represents a quasi-periodic system with two (incommensurate) frequencies, one equal to Ω_3 , same as for the Bicircular, and another being the rate of the true anomaly of the two primaries, which is influenced by their eccentricity. Both models use a co-rotating reference frame centered on the barycenter of the primary and such that the x -axis constantly points from the primary to the secondary, the z -axis points in the direction of their mutual orbit's angular momentum vector, and the y -axis completes the orthogonal frame. A representation of each model can be seen in Figure 5.1 in the co-rotating reference frame centered on the barycenter of the primary and secondary. The dashed lines represent the orbits of the primary and secondary in a pseudo-inertial frame at the moment where the rotating and inertial frames coincide to illustrate the differences in the orbits of the primaries between the two models.

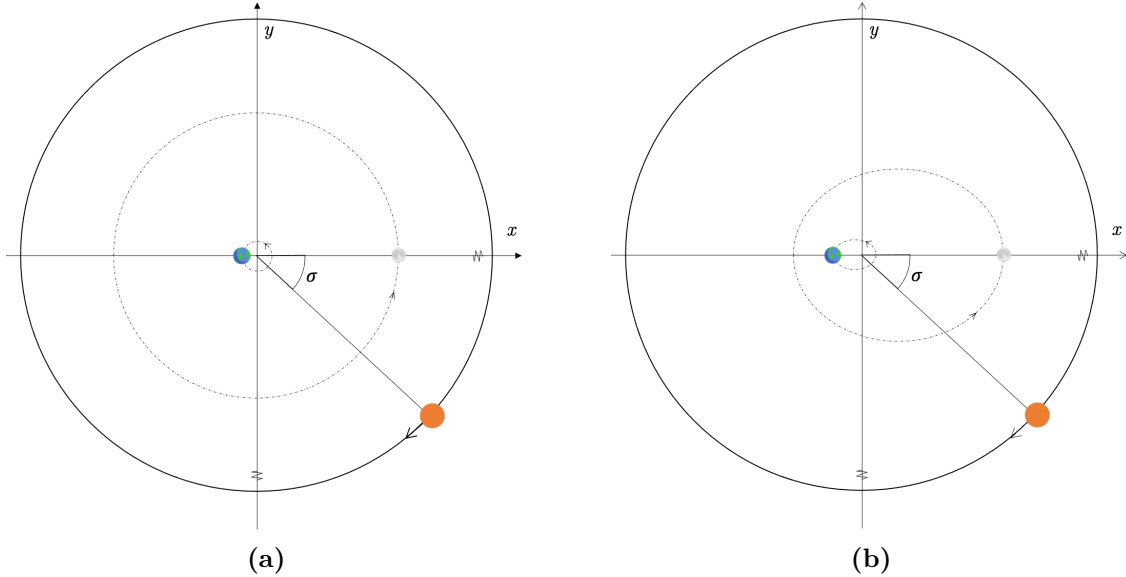


Figure 5.1: Schematic representation of (a) the Bicircular and of (b) the Elliptic-Circular, in their co-rotating frame centered on the Earth-Moon barycenter. The dashed lines represent the orbits of the primary and secondary as viewed from a pseudo-inertial frame at the moment where the rotating and inertial frames coincide. Note that the eccentricity has been exaggerated and the figures are not to scale.

However, since the distance between the two primaries is not constant in the ECR4BP, nor is their angular velocity, we employ the same normalization scheme used in the ER3BP, as presented in Chapter 2. The length unit is set to the distance between the two primaries, which arises from the equations of the two-body problem, and which depends on the value of the true anomaly:

$$l = \frac{a(1-e^2)}{1+e\cos\nu}, \quad (5.1)$$

where a is the semi-major axis of the primary and secondary's orbit, e is their eccentricity, and ν is the true anomaly. In order to compute the time unit, we first compute the time derivative of the true anomaly:

$$\dot{\nu} = \frac{d\nu}{dt} = \frac{(GM)^{1/2}(1+e\cos\nu)^2}{a^{3/2}(1-e^2)^{3/2}}, \quad (5.2)$$

where $M = m_1 + m_2$, m_1 and m_2 are the masses of the primary and secondary, respectively, and G is the gravitational constant. We can now use the use the distance between the two primaries, l , the time derivative of the true anomaly, $\dot{\nu}$, and the sum of the masses of the two primaries, M , to define the units of length, time, and mass as $[LU] = l$, $[TU] = 1/\dot{\nu}$, $[MU] = m_1 + m_2$, respectively. Note that because we are, just like in the ER3BP, using the rate of the true anomaly in the time normalization, our equations of motion will be written (or differentiated) with respect to the true anomaly.

Although the Elliptic-Circular model was, to the best of the author's knowledge, first

mentioned in [27], the equations of motion of the model were not presented in said reference. In order to derive these equations, it is best to start from the derivation of the equations of the ER3BP shown in Chapter 2 and introduce the terms relative to the Sun, which we can directly import from the equations of the Bicircular model. Accordingly, we can write the dimensional acceleration due to the third body's influence as

$$\ddot{\mathbf{r}}_3^* = -\frac{Gm_3^*}{r_3^{*3}} \mathbf{r}_3^* - \frac{Gm_3^*}{a_3^{*3}} \begin{bmatrix} x_3^* \\ y_3^* \\ z_3^* \end{bmatrix}, \quad (5.3)$$

where the superscript \square^* represents dimensional values, μ_3^* is the third body's gravitational parameter, a_3^* is the semi-major axis of the third body's orbit, x_3^* , y_3^* , z_3^* are the position coordinates of the third body in the co-rotating frame, $\mathbf{r}^* = [x^*, y^*, z^*]^T$ is the position-vector of the spacecraft, and $r_3^* = \sqrt{(x^* - x_3^*)^2 + (y^* - y_3^*)^2 + (z^* - z_3^*)^2}$ is the distance between the spacecraft and the third body. Note that the Sun is assumed to be on the same plane as the Earth-Moon system, which means $z_3^* = 0$. Then, using the normalization scheme,

$$\dot{\mathbf{r}}_3^* = \frac{GM}{l^2} \left(-\frac{\mu_3}{r_3^3} \mathbf{r}_3 - \frac{\mu_3}{a_3^3} \begin{bmatrix} x_3 \\ y_3 \\ 0 \end{bmatrix} \right) = \frac{GM}{l^2} \mathbf{r}_3'', \quad (5.4)$$

where \square' denotes differentiation with respect to the true anomaly and \mathbf{r}_3'' is the normalized third-body acceleration. The term $\frac{GM}{l^2}$ simplifies with the other terms coming from the ER3BP normalization (see Eqs. (2.11) to (2.20)), yielding the normalized equations of motion of the ER3BP in the pulsating rotating frame:

$$x'' - 2y' = \frac{\partial \psi}{\partial x}, \quad (5.5a)$$

$$y'' + 2x' = \frac{\partial \psi}{\partial y}, \quad (5.5b)$$

$$z'' = \frac{\partial \psi}{\partial z}, \quad (5.5c)$$

with

$$\psi = \frac{1}{1 + e \cos \nu} \left[\frac{1}{2} (x^2 + y^2 - ez^2 \cos \nu) + \frac{1 - \mu}{r_1} + \frac{\mu}{r_2} + \frac{\mu_3}{r_3} - \frac{\mu_3}{a_3^2} (x_3 x + y_3 y + z_3 z) \right], \quad (5.6)$$

where $r_1 = \sqrt{(x + \mu)^2 + y^2 + z^2}$ and $r_2 = \sqrt{(x - (1 - \mu))^2 + y^2 + z^2}$. We can also write the

equations of motion as

$$x'' - 2y' = \frac{\partial \tilde{\psi}}{\partial x}, \quad (5.7a)$$

$$y'' + 2x' = \frac{\partial \tilde{\psi}}{\partial y}, \quad (5.7b)$$

$$z'' + z = \frac{\partial \tilde{\psi}}{\partial z}, \quad (5.7c)$$

with

$$\tilde{\psi} = \frac{1}{1 + e \cos \nu} \left[\frac{1}{2} (x^2 + y^2 + z^2) + \frac{1 - \mu}{r_1} + \frac{\mu}{r_2} + \frac{\mu_3}{r_3} - \frac{\mu_3}{a_3^3} (x_3 x + y_3 y + z_3 z) \right], \quad (5.8)$$

which can be beneficial when taking partial derivatives, as will be shown in Section 3.1. Note that when setting the eccentricity to zero the equations simplify to the Bicircular case and when setting μ_3 to zero they simplify to the ER3BP model. Due to the normalization used, the primary and secondary are always on the x -axis at $-\mu$ and $1 - \mu$, respectively.

To compute the position of the third body in the pulsating frame we use the same formulation presented previously for the Bicircular:

$$\begin{cases} x_3 = a_3 \cos \sigma = \frac{a_3^*}{l} \cos \sigma, \\ y_3 = -a_3 \sin \sigma = -\frac{a_3^*}{l} \sin \sigma, \\ z_3 = 0, \end{cases} \quad (5.9)$$

where σ is the angular position of the third body in the pulsating frame. Starting from

$$\sigma = (\nu - n_3 t) + \sigma_0, \quad (5.10)$$

we can derive the rate of change of the Sun's angular position with respect to the true anomaly in the pulsating rotating coordinate frame as

$$\sigma' = \frac{d\sigma}{d\nu} = 1 - n_3 / \dot{\nu} = 1 - \frac{n_3 (1 - e^2)^{3/2}}{n (1 + e \cos \nu)^2} \quad (5.11)$$

with $n = \sqrt{GM/a^3}$. Owing to Eq. (5.11), it is found that σ would grow linearly with the true anomaly ν as expected from Eq. (5.10). To enforce periodicity in σ , we find it best to introduce two auxiliary variables, namely $c = \cos \sigma$ and $s = \sin \sigma$. This is done in order for numerical algorithms to identify solutions separated only by a 2π variation on σ as the same solution. Although modulo functions could be used with the same purpose, our implementation allows for derivatives and subsequently dependent equations to behave correctly numerically. Then, obeying to the equations of motion:

$$c' = -s \sigma', \quad (5.12a)$$

$$s' = c \sigma'. \quad (5.12b)$$

The latter may be rewritten in vector form as

$$\boldsymbol{\chi}' = \sigma' \mathbf{J} \boldsymbol{\chi} = \left(1 - \frac{n_3}{n} \frac{(1-e^2)^{3/2}}{(1+e \cos \nu)^2} \right) \mathbf{J} \boldsymbol{\chi}, \quad (5.13)$$

with $\boldsymbol{\chi} = [c, s]^T$ and $\mathbf{J} = \begin{bmatrix} 0 & -1 \\ 1 & 0 \end{bmatrix}$.

By appending Eq. (5.13) to the equations of motion Eq. (5.7) and $\boldsymbol{\chi}$ to the six-dimensional state-vector $[\mathbf{r}^T, \mathbf{v}^T]^T$, we can formulate an eight-dimensional system of first-order ordinary differential equations such that

$$\mathbf{X}' = \mathbf{f}(\mathbf{X}, \boldsymbol{\xi}, \nu,) = \mathbf{f}(\mathbf{X}, \boldsymbol{\xi}, \nu + 2\pi), \quad (5.14)$$

where $\mathbf{X} = [\mathbf{r}^T, \mathbf{v}^T, \boldsymbol{\chi}^T]^T$ and $\boldsymbol{\xi} = [\mu, e, \mu_3]^T$ is a vector of system parameters. In the following, periodic and quasi-periodic orbits are generated by first selecting sidereal and synodic Halo orbits in the CR3BP model of the Earth-Moon system ($\mu = 0.01215$, $e = 0.0$, $\mu_3 = 0.0$). These periodic orbits are later continued into either the ER3BP ($e = 0.0549$, $\mu_3 = 0.0$) or BCR4BP model ($e = 0.0$, $\mu_3 = 328900.55$) by means of homotopy continuation [22, 15, 85], and finally substituted by two-dimensional tori in the Earth-Moon-Sun Elliptic-Circular model via the GMOS algorithm and pseudo-arclength continuation.

3 Numerical continuation

With the goal of finding and studying the dynamical substitutes of NRHOs in the ECR4BP, there are a few possible approaches that can be followed. However, it is important to first understand what these dynamical substitutes will be. Following the explanation in Chapter 3, in a quasi-periodic system such as the ECR4BP, a CR3BP periodic orbit that is non-resonant with any of these perturbations would be replaced by a three-dimensional quasi-periodic torus that incorporates the frequencies of the system's perturbations and the period of the underlying periodic orbit. However, families of three- (and higher) dimensional quasi-periodic tori are harder to compute due to increased computational costs and more complex multi-parameter continuation algorithms [47]. If we choose underlying periodic orbits that are resonant with one of the system's perturbations, the tori become two-dimensional instead of three-dimensional, as one of the torus frequencies will incorporate both the period of the orbit and one of the system's periodic perturbations. As such, the solution envisioned in this study is to choose underlying periodic orbits of the NRHO family that are resonant with one of these perturbations, that is, either synodic resonant orbits (with the Earth-Moon-Sun period) or sidereal resonant orbits (with the Earth-Moon period), which will then produce two-dimensional resonant quasi-periodic tori in the Elliptic-Circular model.

The outset of our analysis are then the CR3BP's $p : q$ resonant orbits, where p is the number of orbital periods and q is the number of either synodic or sidereal months. By design, synodic orbits remain periodic in the Bicircular model, whereas sidereal orbits remain periodic in the

ER3BP. The difference with respect to their **CR3BP** counterparts is that the time-dependent periodic solutions will envision p -revolutions instead of just one in order to equal the q revolutions of either the Bicircular or **ER3BP** system, respectively. A numerical continuation algorithm using homotopy continuation is implemented to compute these synodic and sidereal resonant orbits in their respective systems, while varying their corresponding dynamical parameter (μ_3 for the synodic case and e , the Moon's eccentricity, for the sidereal one), using the formulations presented in Chapter 3. Then the GMOS algorithm described is used to perform a second homotopy continuation along the remaining parameter (e for the synodic case and μ_3 for the sidereal one).

As explained in Chapter 3, both continuation routines can be implemented as **BVPs** of the form $\mathbf{G}(\mathbf{X}_0, \xi) = \mathbf{0}$. Typically, two different algorithms are used, one for obtaining the periodic orbits, and a different algorithm for obtaining quasi-periodic tori. However, we've verified that the GMOS algorithm hereby used to compute quasi-periodic can also be used, successfully, to perform homotopy continuation on periodic orbits, specifically for sidereal and synodic resonant orbits, from the **CR3BP** to the **ER3BP** and from the **CR3BP** to the **BCR4BP**, respectively. When computing resonant periodic orbits, the rotation operator $[R_{-\rho}]$ associated with the GMOS invariance condition (cf. Eq. (3.16)) does not affect \mathbf{X}_1 due to the commensurate nature of the torus' frequencies associated with resonant periodic orbits, which allows us to continue these solutions as well. Additionally, due to the periodicity of these resonant orbits, the invariant circle collapses into a single point, which means we can set N_1 , the number of points along the initial invariant circle, as $N_1 = 1$. Note that this continuation procedure is also effective with non-resonant periodic orbits, as \mathbf{X}_1 will be at the “origin” of an invariant circle, and as such the rotation will have no effect.

Both continuation routines need a reliable initial guess. For the first homotopy continuation, these are obtained by initializing the algorithm with the **CR3BP**'s periodic orbit repeated over p periods, whereas for obtaining the quasi-periodic tori we use the resonant multi-revolution periodic orbit previously obtained in the time-periodic systems, either the **ER3BP** or Bicircular model, to continue along the Sun mass or the eccentricity, respectively.

As detailed in Chapter 3, since we are computing resonant objects in non-autonomous systems, all torus frequencies will be fixed along the continuation procedure. As a consequence, we can effectively exclude them from our vector of unknowns and, subsequently, we will have a one-parameter family of one-dimensional tori for the resonant periodic orbits of the intermediate models (the **ER3BP** and the **BCR4BP**), and a one-parameter-family of two-dimensional tori for the resonant quasi-periodic tori of the Elliptic-Circular. Additionally, whenever we perform continuation on the Sun mass, we use the phase condition associated with θ_1 , and whenever we continue along the Earth-Moon eccentricity, we use the phase condition associated with θ_0 (cf. Eq. (3.23)). Because the **ECR4BP** uses an augmented system and state-vector, we must add two phase constraints to fix the initial angle of the Sun, σ_0 , at either 0 or π as

$$p_c(\mathbf{X}) = c_0 - \cos(\sigma_0), \quad (5.15)$$

$$p_s(\mathbf{X}) = s_0 - \sin(\sigma_0). \quad (5.16)$$

For the parametrizing equation we include the previously introduced pseudo-arclength constraint, including the homotopy parameter in question (either the eccentricity or the Sun mass parameter) in the equation as:

$$q(\mathbf{z}) = \langle \mathbf{z} - \tilde{\mathbf{z}}, \frac{\partial \tilde{\mathbf{z}}}{\partial h} \rangle - \delta h = \frac{1}{N} \sum_{h=1}^{N-1} (\mathbf{X}_0 - \tilde{\mathbf{X}}_0)^T \frac{\partial \tilde{\mathbf{X}}_0}{\partial h} + (\boldsymbol{\xi} - \tilde{\boldsymbol{\xi}}) \frac{\partial \tilde{\boldsymbol{\xi}}}{\partial h} - \delta s = 0, \quad (5.17)$$

where $\mathbf{z} = [\mathbf{X}, \boldsymbol{\xi}]^T$. When the parameter we are continuing along is close to the desired value, we can switch from the pseudo-arclength constraint to a simple forcing equation in order to match said value.

3.1 Partial derivatives with respect to continuation parameters

While the partial of $\partial \mathbf{F}/\partial \mathbf{X}_0$ is explained in [83], the computation of the partials $\partial \mathbf{F}/\partial \varepsilon$ and $\partial \mathbf{F}/\partial e$ for a system like the ECR4BP are not mentioned, noting that ε is the homotopy mass parameter that multiplies μ_3 and varies from zero to one. Additionally, recall that \mathbf{F} refers to GMOS' equations as $\mathbf{F} = [\mathbf{G}, \mathbf{p}, \mathbf{q}]^T$. In order to compute these quantities, we make use of variational equations, integrating the quantities of interest appended to the state-vector of our numerical integrator. We hereby focus specifically on $\partial \mathbf{G}/\partial \boldsymbol{\xi}$, given that the partials of $\mathbf{p}(\mathbf{X}, \boldsymbol{\xi})$ and $q(\mathbf{X}, \boldsymbol{\xi})$ follow from the derivations in [82, 8]. Moreover, note that

$$\frac{\partial}{\partial \boldsymbol{\xi}} ([R_{-\rho}] \mathbf{X}_\tau) = [R_{-\rho}] \frac{\partial \mathbf{X}_\tau}{\partial \boldsymbol{\xi}}, \quad (5.18)$$

since ρ does not depend on any parameter. As for $\frac{\partial \mathbf{X}_\tau}{\partial \boldsymbol{\xi}}$, we must obtain $\boldsymbol{\Theta} = \partial \varphi(\mathbf{X}_0)/\partial \boldsymbol{\xi}$, where $\varphi(\mathbf{X}_0)$ is the flow of the vector field $\mathbf{f} = \mathbf{f}(\mathbf{X}, \boldsymbol{\xi}, \nu)$ at the final state. We can find $\boldsymbol{\Theta}$ by making use of the expression

$$\boldsymbol{\Theta}' = \mathbf{A}\boldsymbol{\Theta} + \mathbf{B}, \quad (5.19)$$

where $\mathbf{A} = \partial \mathbf{f}/\partial \mathbf{X}$ and $\mathbf{B} = \partial \mathbf{f}/\partial \boldsymbol{\xi}$, with initial conditions $\boldsymbol{\Theta}_0 = \mathbf{0}$. Noting that the homotopy mass parameter ε simply multiplies the normalized Sun mass in the equations of motion, the partial $\partial \mathbf{f}/\partial \varepsilon$ can be derived directly from Eqs. (5.7a)-(5.8) as

$$\mathbf{B} = \frac{\partial \mathbf{f}}{\partial \varepsilon} = \frac{1}{1 + e \cos \nu} \mathbf{r}_3'' \quad (5.20)$$

where $\tilde{\psi}$ is defined in Eq. (5.8). Conversely, the partial $\partial \mathbf{f}/\partial e$ can be written as

$$\frac{\partial \mathbf{f}}{\partial e} = -\frac{\cos \nu}{(1 + e \cos \nu)^2} \nabla \tilde{\psi} + \frac{1}{1 + e \cos \nu} \frac{\partial \mathbf{r}_3''}{\partial e}, \quad (5.21)$$

where the dependency of \mathbf{r}_3'' on e comes from the normalization (note that $a_3 = a_3^*/l$ and that r_3 depends on a_3). The derivation of $\frac{\partial \mathbf{r}_3''}{\partial e}$ can be computed by simply writing out the normalized length components relative to the Sun acceleration as function of the dimensional values divided by the length unit, as in Eq. (5.9). Using $\mathbf{g}_{r_3} = \frac{-\mu_3}{r_3^3} \mathbf{r}_3$ and $\mathbf{g}_{a_3} = \frac{-\mu_3}{a_3^3} \mathbf{a}_3$, with

$\mathbf{a}_3 = [c, -s, 0]^T = [x_3, y_3, z_3]^T$, we use the chain rule to write

$$\frac{\partial \mathbf{r}_3''}{\partial e} = \frac{d\mathbf{g}_{r_3}}{d\mathbf{r}_3} \frac{d\mathbf{r}_3}{d\mathbf{a}_3} \frac{d\mathbf{a}_3}{de} + \frac{d\mathbf{g}_{a_3}}{d\mathbf{a}_3} \frac{d\mathbf{a}_3}{de}. \quad (5.22)$$

Both $\frac{d\mathbf{g}_{r_3}}{d\mathbf{r}_3}$ and $\frac{d\mathbf{g}_{a_3}}{d\mathbf{a}_3}$ can be obtained from the expression

$$\frac{d\mathbf{g}_w}{d\mathbf{w}} = -\frac{\mu_3}{w^3} \left[\mathbf{I}_3 - 3\mathbf{w}\mathbf{w}^T \frac{1}{w^2} \right] \quad (5.23)$$

where \mathbf{w} must be replaced with either \mathbf{r}_3 or \mathbf{a}_3 to obtain the respective partial. Additionally, $\frac{d\mathbf{r}_3}{d\mathbf{a}_3} = -\mathbf{I}_3$, and for the last partial we have

$$\frac{d\mathbf{a}_3}{de} = \mathbf{a}_3 \left(\frac{2e}{1-e^2} + \frac{\cos \nu}{1+e \cos \nu} \right). \quad (5.24)$$

The only dependency that cannot be computed explicitly is that of c and s with respect to e . These partial derivatives must be integrated along the trajectory as

$$\frac{dc'}{de} = -s \frac{d\sigma'}{de}, \quad (5.25)$$

$$\frac{ds'}{de} = c \frac{d\sigma'}{de}, \quad (5.26)$$

where $d\sigma'/de$ is obtained directly from Eq. (5.11) as

$$\frac{d\sigma}{de} = \frac{n_3}{n} \left(\frac{3e(1-e^2)^{\frac{1}{2}}}{(1+e \cos \nu)^2} + \frac{2 \cos \nu (1-e^2)^{\frac{3}{2}}}{(1+e \cos \nu)^3} \right). \quad (5.27)$$

3.2 Torus frequencies

As previously mentioned, the torus frequencies can be calculated and known a priori. This is due to the fact that we are computing resonant quasi-periodic tori in a quasi-periodic system that has been recasted as pseudo-periodic. The fundamental torus frequency, ω_0 , is computed from the period of the underlying (multi-revolution) periodic orbits as before

$$\omega_0 = 2\pi/T, \quad (5.28)$$

where T is the normalized period of the underlying periodic orbit. Although the expression for ω_0 remains the same for the two types of resonances, the physical meaning of their torus angles and the expression for the second torus frequency, ω_1 , changes between the synodic and sidereal resonant quasi-periodic tori of the Elliptic-Circular model. These differences will be important when generating the guesses for the initial invariant circles of the different resonant tori.

For synodic resonant tori, the second torus angle, θ_1 , will reflect the true anomaly of the Earth-Moon, due to the additional perturbation imposed by the introduction of their eccentricity. For this reason, ω_1 will be the normalized rate of the true anomaly in the system, which means $\omega_1 = 1$ for all synodic resonances, and, consequently, $\rho = T$, where ρ is the rotation number.

The fundamental torus angle, θ_0 , will reflect the motion of the Sun, where a full rotation over θ_0 corresponds to the integer number of synodic periods that define the resonance, or in other words, $T = qT_{syn}$.

On the other hand, for sidereal resonant tori, since T is resonant with the sidereal period, ω_0 will be $1/q$, e.g. $\omega_0 = 1$ for a 4:1 sidereal resonance but for a 3:2 resonance we would have $\omega_0 = 0.5$. This means that the fundamental torus angle, θ_0 , will reflect the true anomaly of the Earth-Moon and that for a 4:1 and a 3:2 sidereal resonances, a full rotation over θ_0 would correspond to $\Delta\nu = 2\pi$ and $\Delta\nu = 4\pi$, respectively. The second torus angle, θ_1 , will then reflect the Sun angle for the sidereal resonances. However, because the rate of the Sun angle is not constant in the normalized system (recall that the time unit is not constant), we have to integrate the variation of the Sun angle over a full 2π rotation of θ_0 to obtain:

$$\omega_1 = \rho/T = \frac{1}{T} \int_0^{2\pi} \sigma' d\theta_0. \quad (5.29)$$

It follows that, for the sidereal resonant case, ρ will be equivalent to the variation of the Sun angle over one rotation of θ_0 .

4 Dynamical solutions

Using the GMOS algorithm with the multiple shooting implementation, we can produce the dynamical solutions equivalent to the CR3BP's synodic and sidereal resonant periodic orbits of interest in the different dynamical systems. The parameters and constants used can be seen in Table 5.1. Additionally, it is worth noting that while all the resonances studied in this work

Table 5.1: Physical constants and parameters used for the different models. GM refers to the gravitational parameter, R refers to the body's radius, L to the distance or semi-major axis between two bodies. Sources for data: [107, 79, 52].

Parameter	Value
GM Earth [m ³ s ⁻²]	$3.9860044189 \times 10^{14}$
GM Moon [m ³ s ⁻²]	$4.902801076 \times 10^{12}$
GM Sun [m ³ s ⁻²]	$1.32712440018 \times 10^{20}$
L Earth-Moon [km]	384 399
L Sun-Earth [km]	149.5978707×10^6

converge correctly in the full Elliptic-Circular model using the aforementioned algorithm, many of the other synodic and sidereal resonant orbits fail to do so, even after being computed in the intermediate models, i.e. in the Bicircular and ER3BP models. A possible explanation to this phenomenon might be found in [15], where it is referred that convergence issues were also experienced when transitioning the 3:1 synodic resonant NRHO to a high-fidelity ephemeris model by the authors in [31]. The reason put forward relates to the numerical continuation of this orbit and that of the 5:1 synodic resonant NRHO between the CR3BP and the Bicircular, where a bifurcation along the stability curves can be seen at different values of the homotopy

continuation parameter (this is the case for many resonances but extensive testing was not performed). This causes a mismatch in the eigenstructure of the intermediate multi-revolution periodic orbits, which seems to later prevent the numerical continuation to the full Elliptic-Circular model as quasi-periodic tori or good convergence in the ephemeris models. Unlike other resonances, the ones selected in this paper do not present such a bifurcation or mismatch in the continuation to the intermediate models.

4.1 Initial guess generation

As the initial guesses of the quasi-periodic tori continuation procedures, the multi-revolution resonant periodic orbits must first be obtained in the intermediate models, i.e. in the Bicircular and [ER3BP](#) models. To do so, we start from the [CR3BP](#) resonant $p : q$ -type periodic orbits and initialize the continuation procedure by repeating the orbits over p periods of their original [CR3BP](#) trajectories, such that their period will be $T = pT_{\text{res}}$, where T_{res} is the period of the resonant periodic orbits in the [CR3BP](#) model. As mentioned, we also make use of the GMOS algorithm to continue these resonant periodic orbits into the intermediate models. To do so, we set $N_1 = 1$, and, as we are using a multiple shooting implementation, set $N_0 = p$, such that there is only one multiple shooting node per revolution and that each one is placed at the apolune of its orbital revolution. We set a phase constraint with respect to the θ_0 angular coordinate for the continuation along Sun mass parameter ([CR3BP](#) to [BCR4BP](#)) or with respect to θ_1 for the continuation along the eccentricity ([CR3BP](#) to [ER3BP](#)), the two additional phase constraints on the Sun angle, and the pseudo-arclength equation, just as explained in Section 3. The initial resonant periodic [NRHOs](#) in the [CR3BP](#) and the result of this continuation procedure can be seen in Figures 5.2 to 5.4, where the 9:2 synodic, 4:1 synodic and 4:1 sidereal resonant [NRHOs](#) are shown first in the [CR3BP](#) and then in their respective intermediate models, the Bicircular model for the synodic resonances and the [ER3BP](#) for the sidereal resonance. The trajectories are shown in dimensional coordinates in the Earth-Moon rotating reference frame centered on the Moon, where the x -axis points from the Earth to the Moon and the z -axis points in the direction of the angular momentum vector of the Earth-Moon orbits. The projections of each trajectory on the different planes can be seen in grey.

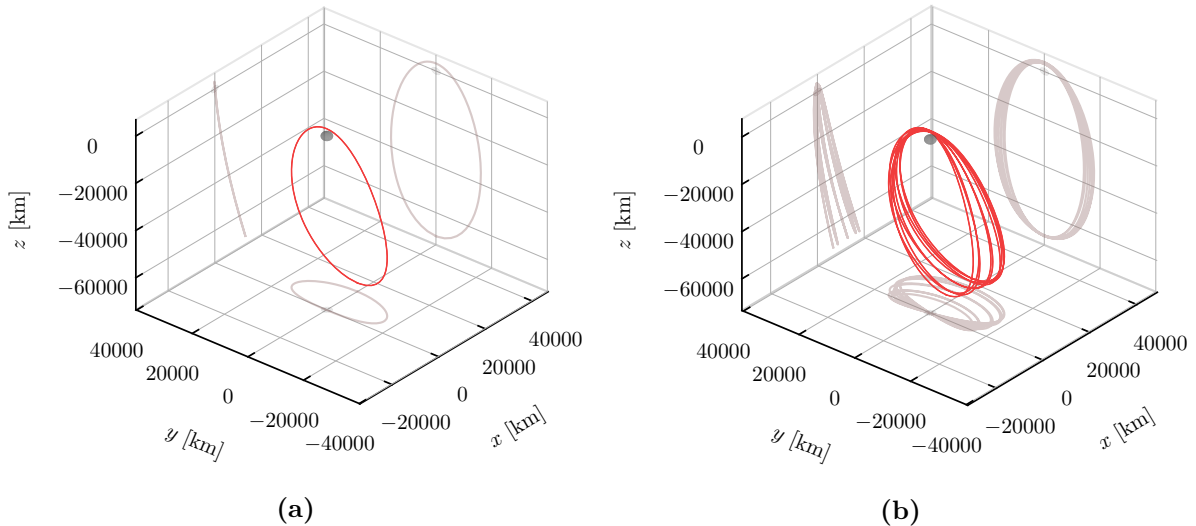


Figure 5.2: The 9:2 synodic resonant NRHO under study, shown in the Earth-Moon rotating frame centered on the Moon in dimensional coordinates: (a) the original periodic orbit computed in the CR3BP and (b) the multi-revolution periodic orbit computed in the Bicircular.

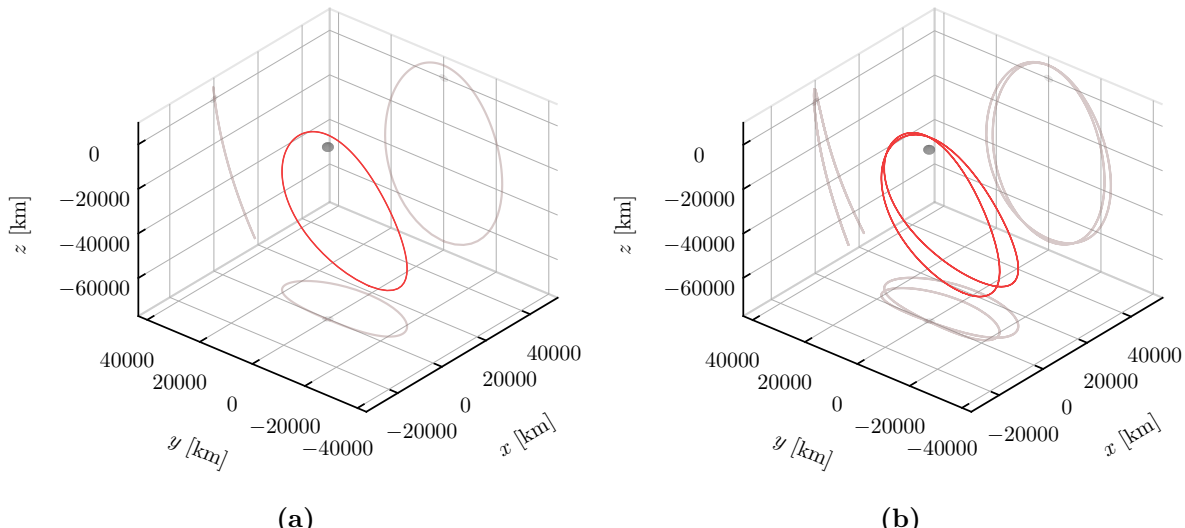


Figure 5.3: The 4:1 synodic resonant NRHO under study, shown in the Earth-Moon rotating frame centered on the Moon in dimensional coordinates: (a) the original periodic orbit computed in the CR3BP and (b) the multi-revolution periodic orbit computed in the Bicircular.

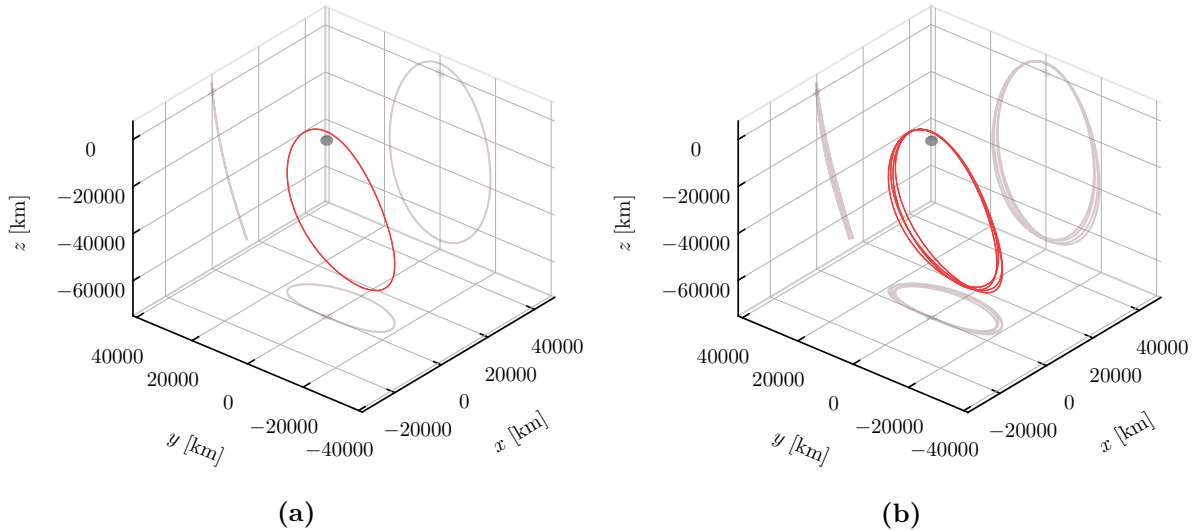


Figure 5.4: The 4:1 sidereal resonant NRHO under study, shown in the Earth-Moon rotating frame centered on the Moon in dimensional coordinates: (a) the original periodic orbit computed in the CR3BP and (b) the multi-revolution periodic orbit computed in the ER3BP.

It is important to point out that all the solutions hereby presented, including the quasi-periodic solutions to be shown, were computed and numerically continued by choosing initial conditions or multiple shooting nodes at apolune points. As shown in [31], NRHOs are highly sensitive to errors and perturbations at perilune, which seems to be caused by strong nonlinearities present around this region [53]. In the same way that these authors advise against applying correction maneuvers around perilune due to the high-sensitivity of said region and instead recommend applying them at apolune, the iterative correction algorithms hereby employed use as initial conditions states that are situated at apolune, thus applying the corrections to these state-vectors at the least sensitive positions along the trajectories. We find that this significantly improves the convergence of the algorithms, which might otherwise fail.

Additionally, it is worth noting that the synodic resonant solutions hereby presented are computed for initial Sun angles equal to zero, i.e. when all bodies are aligned and the Sun is in the positive x -axis. Likewise, the sidereal resonant solutions are computed by setting the initial true anomaly to zero. Nevertheless, note that both intermediate periodic systems, the Bicircular and the ER3BP, present the following symmetries [85, 21]:

$$(x, y, z, \dot{x}, \dot{y}, \dot{z}, \tau) \rightarrow (x, -y, -z, -\dot{x}, \dot{y}, \dot{z}, -\tau), \quad (5.30a)$$

$$(x, y, z, \dot{x}, \dot{y}, \dot{z}, \tau) \rightarrow (x, -y, z, -\dot{x}, \dot{y}, -\dot{z}, -\tau), \quad (5.30b)$$

where τ represents the time-periodic variable of the system, which for the Bicircular is the Sun angle σ and for the ER3BP is the true anomaly ν . This indicates that a sufficient condition for symmetric periodic orbits in these models is that they cross the x -axis or xz -plane perpendicularly at either $\tau = 0$ or $\tau = \pi$. When considering $p : q$ resonant orbits with odd p , the orbit will have completed a non-integer number of revolutions, namely $p/2$, after a time

$q\pi$. Indeed, the different initial angle of zero or π produces two different periodic orbits, which is not the case for even p . Although in this work we focus only on solutions with an initial angle of zero, one could extend these to cover initial angles of π as well.

Moreover, depending on the $p : q$ resonant orbit being computed, one could consider other initial angles separated by a phase of $q2\pi/p$. However, this would lead to the same periodic orbit, simply initialized at a different point along its trajectory. An example would be the 4:1 multi-revolution synodic resonant [NRHO](#) in the Bicircular, which as shown in [15], could be computed with initial Sun angles separated by a phase of approximately $360^\circ/4 = 90^\circ$, which all correspond to the same orbit. Previous authors have presented unique solutions in the Bicircular for different initial Sun angles, but this typically entails small discontinuities in the trajectories [96]. Since we admit a solution as converged when the error vector is below a certain threshold, using the Newton method instead of, for instance, least-squares, our algorithm does not accept these solutions, causing the error vector to plateau and not converge. Nevertheless, as mentioned, the solution space of the trajectories presented in this study could be extended by changing the initial angles of the intermediate periodic models to π , or even to include the discontinuities associated with different angles.

4.2 Quasi-Periodic Tori Continuation

After obtaining the multi-revolutions periodic solutions in the intermediate models, we are in a position to proceed with the numerical continuation towards the Elliptic-Circular model taking these solutions as initial guesses of the quasi-periodic tori. We take the converged solutions of the intermediate models, which are already defined in $N_0 = p$ multiple shooting nodes situated at the apolune of each revolution, and we form the invariant circles at each θ_0 node by repeating each of these states N_1 times. Of course, this means that for the zeroth family member of this numerical continuation, i.e. where $e = 0$ for the synodic resonances or $\epsilon = 0$ for the sidereal resonance, all cartesian coordinates of the initial invariant circle will coincide with the initial state of the underlying multi-revolution resonant periodic orbit. However, as we move along the family they will naturally spread and display the closed curve more clearly. We set the value of N_1 to 50 for higher accuracy but note that it can be set between 30 and 50 (or larger), depending on the resonant trajectories. We find that trajectories with lower perilunes, such as the 9:2 synodic resonant [NRHO](#), typically require a higher number of N_1 nodes to achieve good quadratic convergence and to accurately interpolate points on the surface of the torus, although this is not strictly necessary to find the solutions. This also falls in line with the previous observations about the strong non-linearities present at perilune.

It should be noted that for the initial guess of the first family member, although each multiple shooting node will be comprised of invariant circles that share the same initial position and velocity vectors (since we simply repeated each state N_1 times for each node), the integration of their trajectories will not be equal. In fact, since we are performing continuation along either the Earth-Moon eccentricity for synodic resonant tori or Sun mass parameter for sidereal resonant tori, the θ_1 angular direction of the torus will reflect different quantities, just as mentioned in Section 3.2. Specifically, it will reflect the Earth-Moon true anomaly or the Sun angle,

respectively.

For a synodic resonant torus, each state along the initial invariant circle will have a different value of true anomaly, corresponding to the different values of θ_1 as

$$\nu^{0,j} = 2\pi j/N_1, \quad (5.31)$$

where $j = \{0, 1, \dots, N_1 - 1\}$ and $\nu^{0,j}$ represents the j th value of true anomaly, or, equivalently, of θ_1 , of the initial node $i = 0$ along θ_0 . In the same way, the values of true anomaly for the subsequent nodes will be

$$\nu^{i,j} = Ti/N_0 + 2\pi j/N_1, \quad (5.32)$$

with $i = \{0, 1, \dots, N_0 - 1\}$.

For the initial guess of the first family member of the sidereal resonant tori, we vary θ_1 along with the Sun angle σ , meaning that, for the initial guess, each state along the initial invariant circle will have a different Sun angle

$$\sigma^{0,j} = 2\pi j/N_1. \quad (5.33)$$

However, it should be noted that for sidereal resonant tori we cannot compute the initial guesses for the values of $\sigma^{i,j}$ at the other $N_0 - 1$ nodes in the same way as we do for $\nu^{i,j}$ in the case of synodic resonant tori. The reason for this is that σ does not vary linearly with the true anomaly. Instead, we must first integrate σ' over $\Delta\theta_0 = 2\pi$ and evaluate σ at the N_0 nodes, similarly to how we obtain ω_1 and the rotation number in Eq. (5.29). The values of σ at the first point along each invariant circle will then be

$$\sigma^{i,0} = \int_0^{2\pi i/N_0} \sigma' \Big|_{\sigma=\sigma^{0,0}} d\theta_0, \quad (5.34)$$

where σ' is given by Eq. (5.11). Then,

$$\sigma^{i,j} = \sigma^{i,0} + \sigma^{0,j}. \quad (5.35)$$

Because c and s have been appended to the state-vector of our equations of motion, the values of $\sigma^{i,j}$ are left to vary freely and are corrected at each iteration of the continuation algorithm, constrained only by the multiple shooting equations that enforce continuity at the nodes and the constraint on the initial Sun angle of the initial invariant circle (cf. Eqs. (5.15) and (5.16)). As such, the expression on Eq. (5.35) is used only as an initial guess. Additionally, although σ relates to θ_1 in the case of sidereal tori, we see that they do not necessarily equal each other, as θ_1 varies linearly with θ_0 , which is not the case for σ .

By considering the solution where the homotopy continuation parameter is zero as the first known solution, i.e., by repeating the trajectories coming from the intermediate models over N_1 points, we can take a step along the family tangent direction as described in Eq. (3.32). Then, by means of the GMOS algorithm and the proposed continuation procedure, we continue

the solutions to produce resonant two-dimensional quasi-periodic tori up to an Earth-Moon eccentricity value of $e = 0.0549$ and Sun mass homotopy parameter of $\varepsilon = 1$, corresponding to the actual Sun mass. The results of these continuation procedures can be seen in Figures 5.5 to 5.7, where the initial guesses used, i.e. the multi-revolution periodic orbits from the intermediate models, can be seen on the left and the quasi-periodic tori on the right for comparison. The solutions are plotted in dimensional coordinates in the Earth-Moon rotating frame centered on the Moon, and their projections on the different planes are visible in grey.

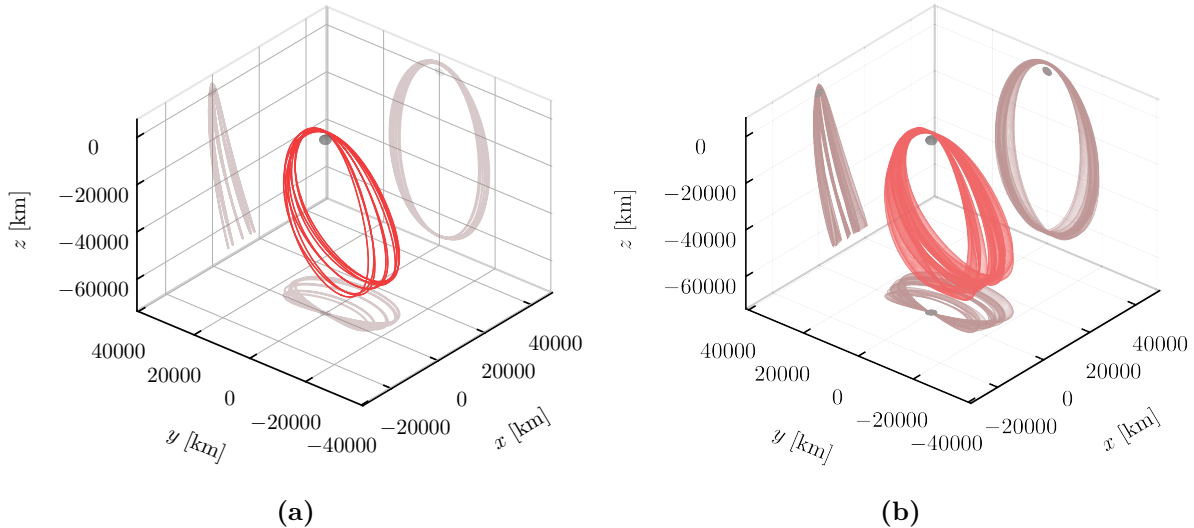


Figure 5.5: (a) The periodic resonant synodic 9:2 NRHO in the Bicircular model and (b) the corresponding quasi-periodic tori of the 9:2 synodic resonant NRHO in the full ECR4BP model for a value of eccentricity $e = 0.0549$.

Additionally, we can also look at the initial invariant circles of the quasi-periodic tori throughout the continuation procedure. This can be seen in Figures 5.8 and 5.9, which display said invariant circles in normalized and dimensional coordinates, respectively. As mentioned earlier, the nodes of the initial invariant circles progressively move away from the point that represents the resonant periodic orbits of the time-periodic intermediate systems as we move along the numerical continuation, which is clearly visible in the figures. Moreover, it is interesting to note that particularly for the case of the 4:1 synodic resonance, the dimensionalization of the position coordinates plotted with respect to the Moon, i.e. where the Moon is at the origin of the frame, deforms the invariant circles of Figure 5.9b when compared to those in normalized coordinates from Figure 5.8b. This is expected due to the previously mentioned values of true anomaly for the different nodes of the invariant circles of the synodic resonant tori (cf. Eqs. (5.31), (5.32)), which affect the value of the length constant, as seen in Eq. (5.1). The deformation is seen mostly along the x -axis, due to varying Earth-Moon distance for different values of true anomaly.

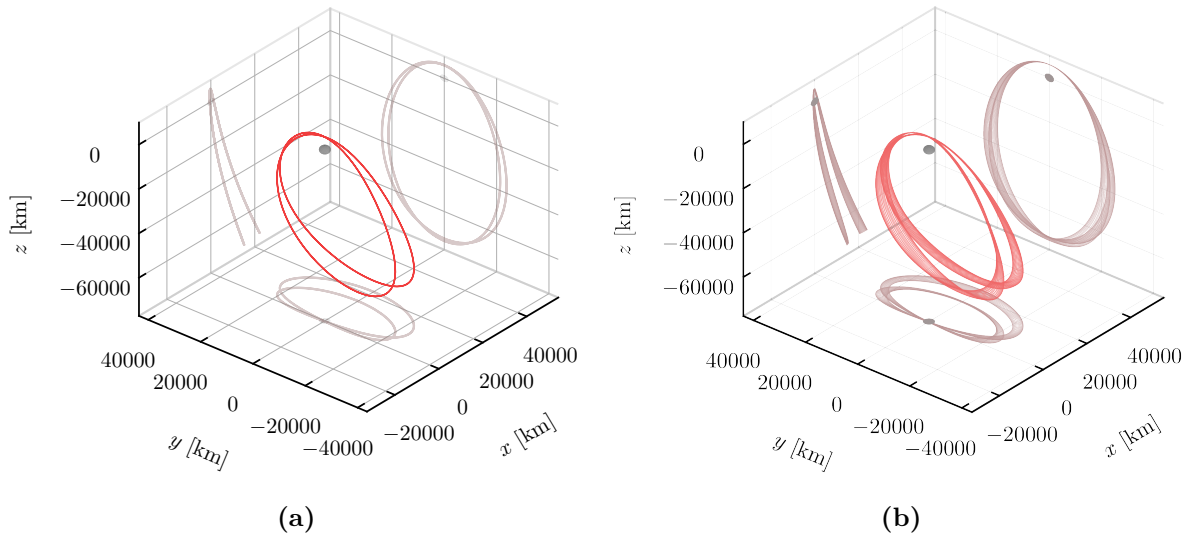


Figure 5.6: (a) The multi-revolution periodic resonant synodic 4:1 NRHO in the BCR4BP model and (b) the corresponding quasi-periodic tori of the 4:1 synodic resonant NRHO in the full ECR4BP model for a value of eccentricity $e = 0.0549$.

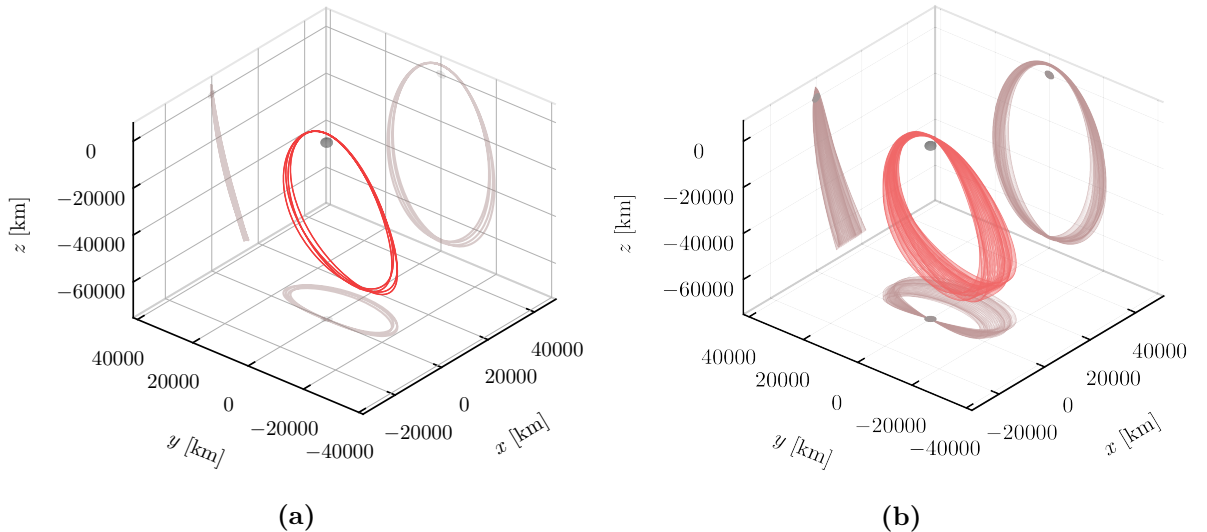


Figure 5.7: (a) The periodic resonant sidereal 4:1 NRHO in the ER3BP model for a value of eccentricity $e = 0.0549$ and (b) the corresponding quasi-periodic tori of the 4:1 sidereal resonant NRHO in the full ECR4BP model for the same value of eccentricity.

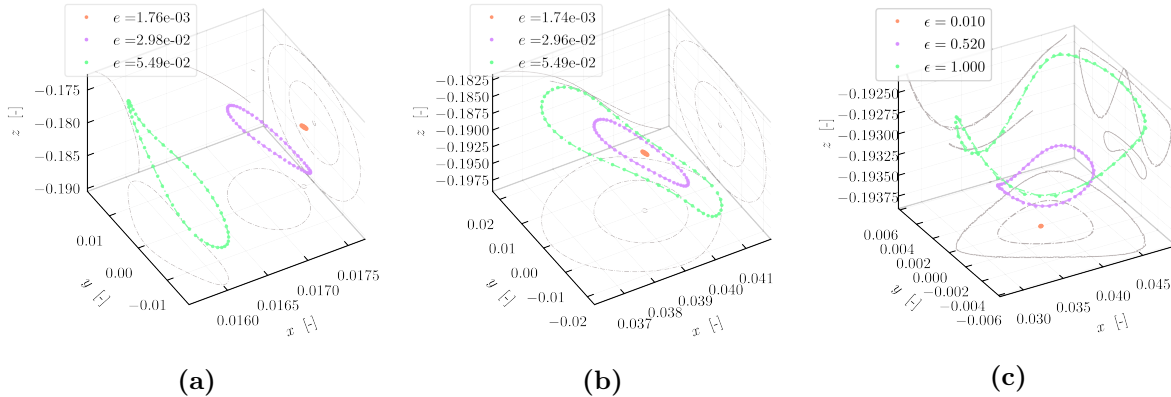


Figure 5.8: The initial invariant circles of the resonant quasi-periodic tori for different family members along the numerical continuation in the ECR4BP, shown in normalized coordinates in co-rotating reference frame centered on the Moon. Initial invariant circles of the (a) 9:2 synodic resonant quasi-periodic NRHO (b) 4:1 synodic resonant quasi-periodic NRHO (c) 4:1 sidereal resonant quasi-periodic NRHO.

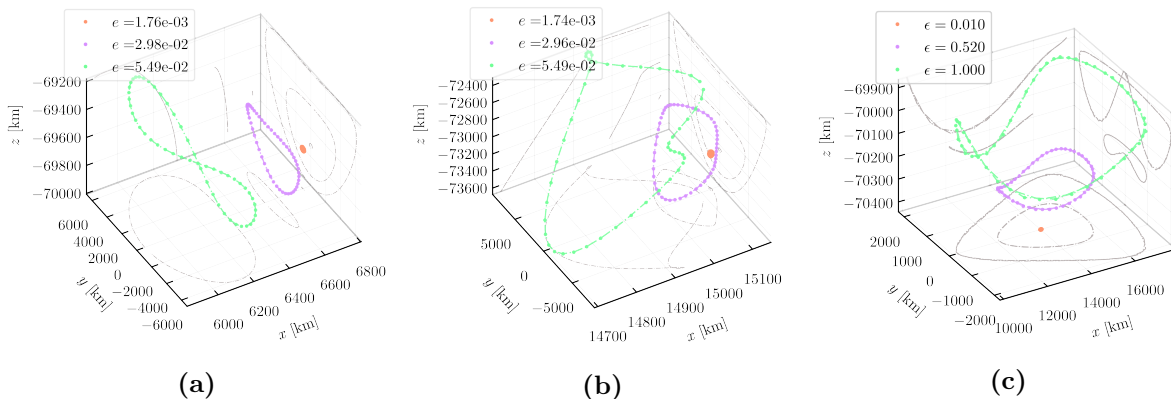


Figure 5.9: The initial invariant circles of quasi-periodic tori for different members along the numerical continuation in the ECR4BP, shown in dimensional coordinates in co-rotating reference frame centered on the Moon. Initial invariant circles of the: (a) 9:2 synodic resonant quasi-periodic NRHO (b) 4:1 synodic resonant quasi-periodic NRHO (c) 4:1 sidereal resonant quasi-periodic NRHO.

Looking at the quasi-periodic tori, we can see that adding the second perturbation to the system translates into a “thickening” of the solution around the periodic resonant **NRHO**. Interestingly, we see that this thickening is most prevalent in the 9:2 synodic and 4:1 sidereal resonant quasi-periodic **NRHOs**. Additionally, when visually comparing the 9:2 synodic resonant **NRHO** to the long-term high-fidelity ephemeris model converged trajectories from literature [77, 31], the quasi-periodic torus shown in Figure 5.5b seems thicker. Of course, even if both solutions have the same starting point – the **NRHO** of the **CR3BP** –, they are computed via different methods. The full-ephemeris solutions are integrated backwards and forwards in time for several years (10 or more) and present velocity discontinuities where correction maneuvers are executed. Even so, the natural quasi-periodic solution hereby presented is integrated for a

much shorter period (less than a year), and it already displays a wider and seemingly thicker visual appearance. This suggests that the quasi-periodic trajectories hereby computed and the converged trajectories obtained in full-ephemeris models might represent different dynamical solutions, although analyses of these quasi-periodic solutions in a full-ephemeris model would be necessary for a more accurate comparison.

5 Stability analysis

In order to better analyze the two-dimensional quasi-periodic tori obtained in the full Elliptic-Circular model, we study the linear stability associated with these dynamical solutions. Although different criteria exist in order to study the stability of dynamical solutions, we choose to analyze the solutions hereby presented using the finite Lyapunov exponents associated with the tori's Floquet matrices (for information on Floquet theory and Lyapunov exponents see [95]). The reason behind this choice of metric is that it normalizes the stability values by the period of the solution. This is convenient due to the long periods introduced with the multi-revolution periodic NRHOs computed in the intermediate models. If another approach was used, such as the norm of the eigenvalues of the state transition matrix, the longer periods of these orbits would make it seem like their stability had significantly decreased with respect to their single-revolution counterparts of the CR3BP. By using Lyapunov exponents we obtain a more accurate interpretation of the changes in stability, as demonstrated by [15] when comparing the stability of the CR3BP resonant NRHOs with the synodic resonant multi-revolutions NRHOs of the Bicircular model. The Lyapunov exponents can be approximated as

$$\phi_i = \Re \left(\frac{\ln \lambda_i}{T} \right), \quad (5.36)$$

where λ_i are the eigenvalues of the state transition matrix after one period, i.e. the monodromy matrix (introduced in Chapter 2), and T is the period of the solution. A solution is considered to be linearly stable if all its Lyapunov exponents are equal to zero. It should be noted that this criteria is formulated for periodic orbits, and that it arises from a limit approximation [95]. Although we do not derive said approximation to employ the Lyapunov exponents in the stability analysis of quasi-periodic solutions, we tacitly use this metric and find that, empirically, it produces consistent results that are congruous with those shown for their underlying periodic orbits. As such, we obtain the eigenvalues associated with the Floquet matrix, \mathbf{B} , of the quasi-periodic tori and use the tori's fundamental period, i.e. one full revolution along θ_0 , which corresponds to the period of the underlying multi-revolution periodic NRHO, to compute their Lyapunov exponents. As explained in [82, 5], the eigenvalues of a quasi-periodic torus' Floquet matrix provide us with linear stability information about the torus, similarly to the monodromy matrices of periodic orbits. The Floquet matrix is computed by assembling a block diagonal of the N_1 monodromy matrices, Φ_i , of each trajectory along the invariant circle, and undoing the

torus rotation by means of the rotation operator, $[R_{-\rho}]$, as

$$\mathbf{B} = [R_{-\rho}] \begin{bmatrix} \Phi_0 & & & \\ & \Phi_1 & & \\ & & \ddots & \\ & & & \Phi_{N_1-1} \end{bmatrix}, \quad (5.37)$$

which will have a dimension of $nN_1 \times nN_1$, where n is the number of state variables. Since the stability of the Sun's position bears no physical meaning, we can focus only on the first six rows and columns of each monodromy matrix. We can then compute the eigenvalues of the Floquet matrix, which will be distributed in concentric circles on the complex plane. Since eigenvalues occur in reciprocal pairs, so will the radii of these circles, i.e. $R_1 = 1/R_2$, where R_1 and R_2 are the radii of reciprocal circles in the complex plane [55]. Due to the six-dimensional state we are considering for the stability analysis of these quasi-periodic tori, we will have six concentric circles, where each is a reciprocal pair of another. We can then either sample each circle to obtain an eigenvalue or simply consider their radius, which will be equal to its intersection with the real axis, in order to obtain the six λ_i necessary for the computation of the Lyapunov exponents. Additionally, we note that because the Elliptic-Circular is non-autonomous, we will not necessarily have a unit radius circle pair, which would be the case for autonomous systems such as the [CR3BP](#).

As mentioned in the beginning of Section 4, Boudad et al. [15] perform the same analysis when translating periodic synodic resonant [NRHOs](#) from the [CR3BP](#) to the Bicircular model, and find that out of the four synodic resonances studied by the authors, the 3:1 and 5:1 synodic resonant [NRHOs](#) present bifurcations along the stability curve of their Lyapunov exponents when plotted against the continuation parameter. These bifurcations, which change the stability of these two [NRHOs](#) from linearly stable to slightly unstable, seem to translate in convergence issues when continuing the solutions to high-fidelity ephemeris models. We verify that the same resonant orbits also experience convergence issues when continuing them into the full Elliptic-Circular model from the Bicircular. Accordingly, the synodic resonances hereby considered (9:2 and 4:1), which as shown in [15] do not present any bifurcations along their stability curve when continuing them from the [CR3BP](#) to the Bicircular model, do not produce convergence issues in their continuation to the full Elliptic-Circular model.

Furthermore, the analysis of the Lyapunov exponents of quasi-periodic solutions as a function of their continuation parameter allows us to verify that the solutions correspond to the actual dynamical equivalents of the [CR3BP](#)'s solutions by ensuring that there are no discontinuities along the family curve.

The evolution of the Lyapunov exponents of each of the resonant quasi-periodic [NRHOs](#) along their continuation parameter can be seen in Figure 5.10. It is interesting to note that, similarly to the cases of the 9:2 and 4:1 synodic resonant [NRHOs](#) of the Bicircular computed in [15], the Lyapunov exponents of their quasi-periodic counter parts remain approximately the same throughout the continuation procedure. Although not visible in Figure 5.10a, a bifurcation along one of the stable (zero) Lyapunov exponent pairs exists from the start of the perturbation,

but does not depart significantly from the zero value (around 0.003 for $e = 0.0549$) and could be the product of numerical errors.

Finally, we verify that no discontinuity exists along the continuation, and that as such, we report the significant result that the resonant quasi-periodic NRHOs hereby computed represent the dynamical substitutes of the CR3BP's resonant NRHOs in the Elliptic-Circular model.

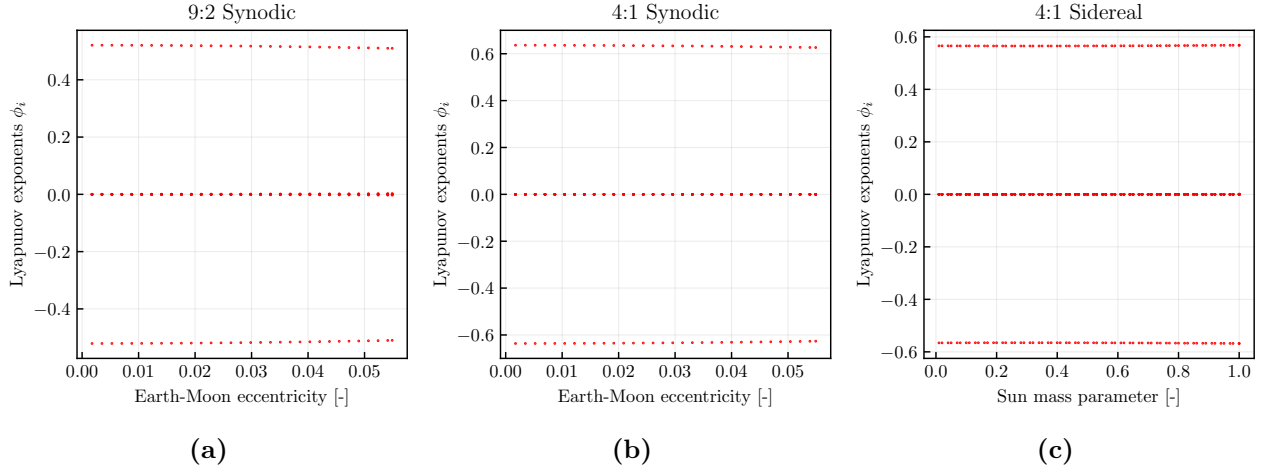


Figure 5.10: Lyapunov exponents plotted against the continuation parameter for each of the quasi-periodic resonant NRHOs during the continuation to the Elliptic-Circular model: (a) 9:2 synodic resonance (b) 4:1 synodic resonance and (c) 4:1 sidereal resonance.

6 Torus maps

In the context of future missions, such as the Lunar Gateway mission, it is relevant to analyze the quasi-periodic solutions hereby presented through a mission analysis lens. To do so, we make use of the two-dimensional torus maps introduced in Chapter 3. As mentioned, these maps allow us to display useful physical information over a representation of the quasi-periodic trajectories, which proves to be a significant tool for mission design and analysis.

Applying this technique to the analysis of the synodic and sidereal resonant quasi-periodic NRHOs, we generate two types of torus maps. For one type, we plot the eclipses, or, more accurately, the Sun disk visibility - where a value of one corresponds to full sunlight, zero to total eclipse, and anything in between to a partial or annular eclipse - using the conic eclipse model and shadow function from [73] for both the Earth and Moon's shadows. A schematic representation of the conic eclipse model used can be seen in Figure 5.11, where R_S represents the Sun radius and R_i is the radius of either the Earth or the Moon. The radii considered for the Earth, Moon, and Sun are $R_E = 6378.137$ km, $R_M = 1737.103$ km, and $R_S = 6.9570 \times 10^5$ km, respectively [68, 107, 79].

For the other type of torus maps, we plot the altitude with respect to the Moon surface. These torus maps can be seen in Figures 5.12 to 5.14.

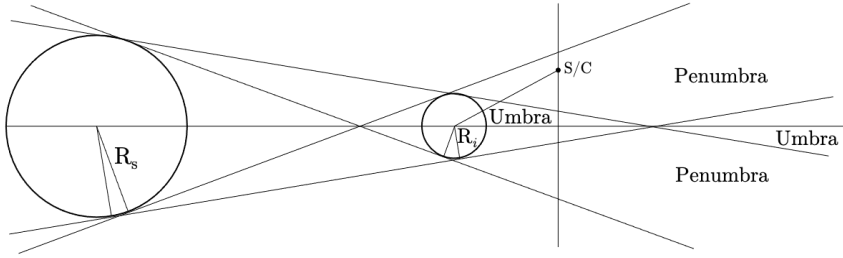


Figure 5.11: Schematic representation of the conic eclipse model used.

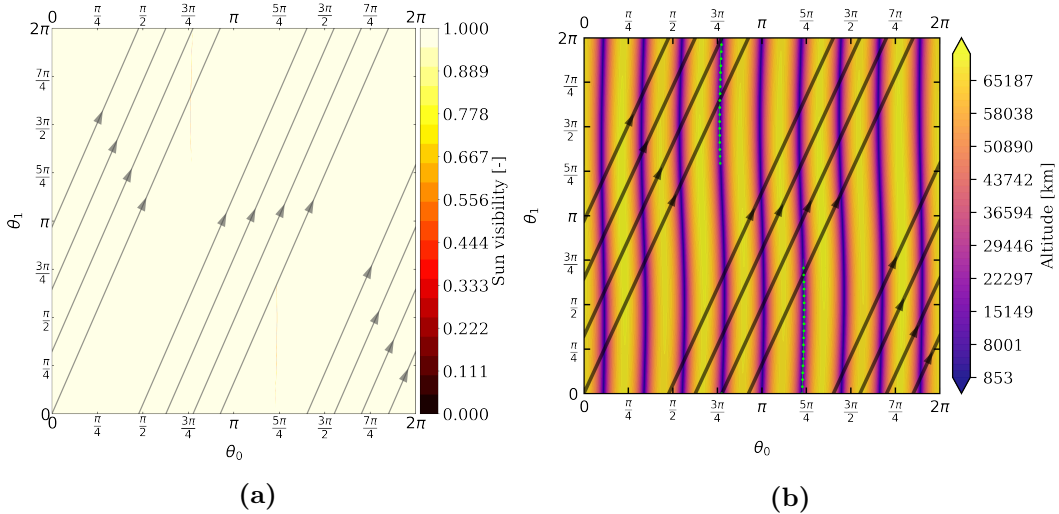


Figure 5.12: Torus maps for the 9:2 synodic resonant quasi-periodic NRHO: (a) eclipse map showing fraction of Sun disk visible (b) altitude with respect to Moon surface with the eclipses overlaid in bright green.

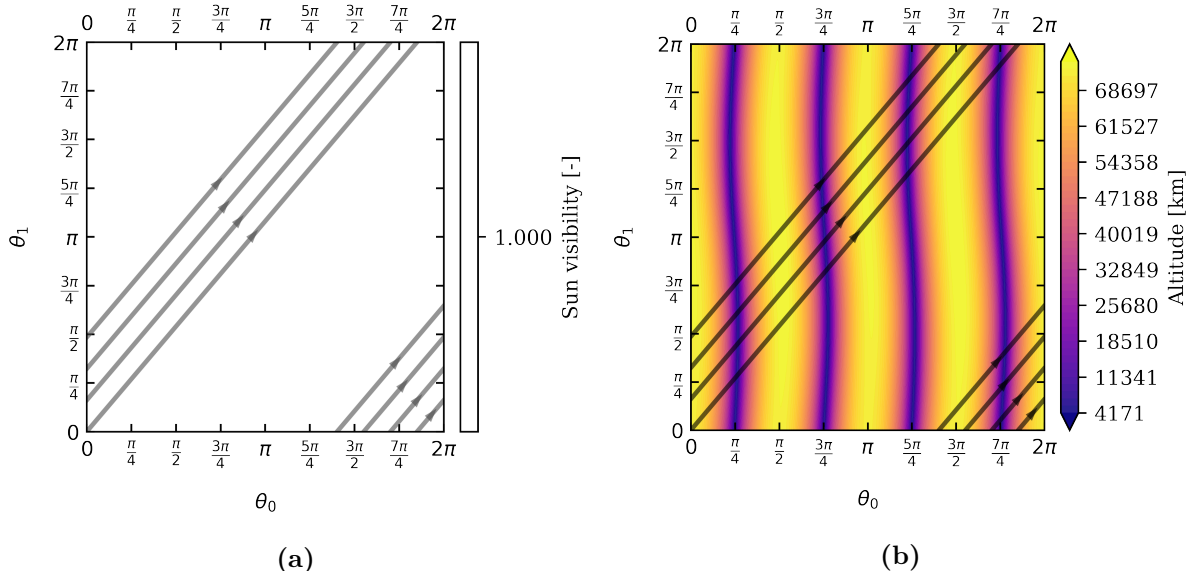


Figure 5.13: Torus maps for the 4:1 synodic resonant quasi-periodic NRHO: (a) eclipse map showing fraction of Sun disk visible (b) altitude with respect to Moon surface.

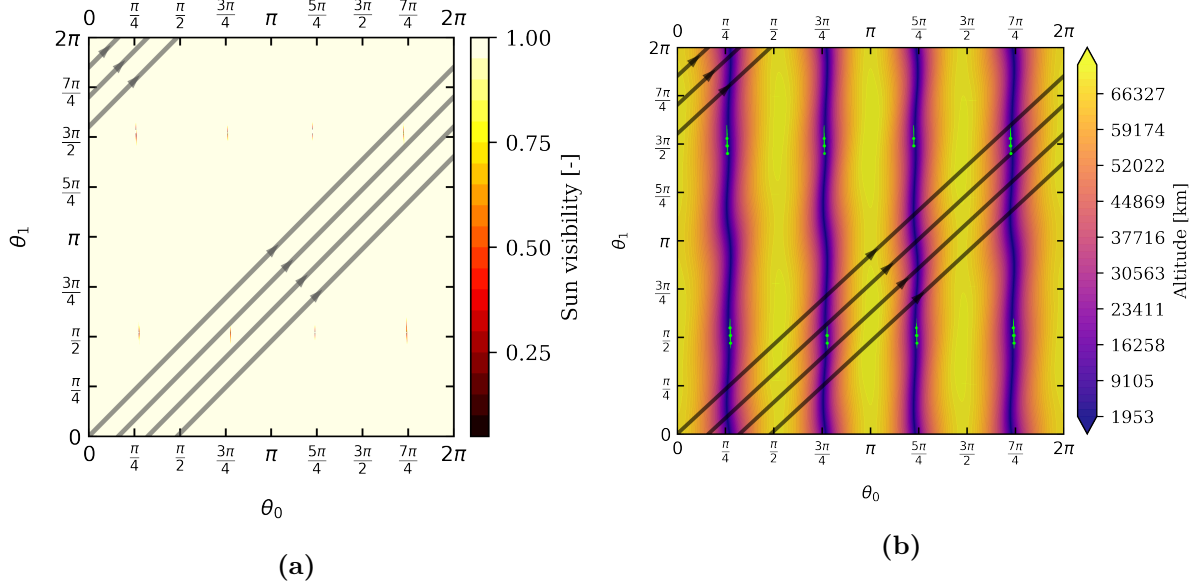


Figure 5.14: Torus maps for the 4:1 sidereal resonant quasi-periodic NRHO: (a) eclipse map showing fraction of Sun disk visible (b) altitude with respect to Moon surface with the eclipses overlayed in bright green.

On the left side of these figures we can see the Sun visibility along the torus surface, whereas the right-hand side of the figures shows the altitude with respect to the Moon surface. These latter altitude torus maps are overlayed with the eclipses shown in bright green dotted lines for better visibility and analysis, albeit now in a single color for any type of eclipse.

By analyzing these figures, we quickly verify that the eclipse avoidance properties of the synodic resonant trajectories are maintained when transitioning to Elliptic-Circular model. The maps for the 9:2 synodic resonant quasi-periodic torus seen in Figure 5.12 present only two small eclipse regions, close to $\theta_0 = 3\pi/4$ and $\theta_0 = 7\pi/4$, which, as expected, coincide with the $z = 0$ crossings and cover only a section of the invariant circle. In fact, it is interesting to note that without any maneuvers, it would be possible to avoid said regions for at least up to three full revolutions of θ_0 , i.e. $3 \times 2\pi$, by choosing appropriate initial conditions for insertion, e.g. the line starting at $\theta_0 = 0$ between $\theta_1 = \pi/2$ and $\theta_1 = 3\pi/4$ approximately. Since this quasi-periodic torus corresponds to a 9:2 synodic resonance, following such a trajectory would enable a spacecraft to avoid any type of eclipse for at least up to $3 \times 2T_{syn}$, approximately 177 days. Eventually, following the same trajectory would lead to crossings with the eclipse region, however, it would be possible to avoid these by performing correction or phasing maneuvers to transfer between two hyper-points of the torus' surface, similarly to how previous work has demonstrated transfers between intersecting tori [48]. We also note that only Moon eclipses are detected for this resonance.

While the 9:2 synodic resonant presents two eclipse regions, we see from Figure 5.13 that the 4:1 synodic resonant quasi-periodic NRHO does not seem to cross any eclipse regions in the Elliptic-Circular model. This is likely be due to the combination of the optimal synodic resonant geometry and the larger perilune radii visible in the 4:1 synodic resonance.

In contrast, the torus maps of the 4:1 sidereal quasi-periodic NRHO seen in Figure 5.14 display four sets of two eclipse regions, spaced approximately by $\pi/4$ along the θ_0 direction and by π along the θ_1 direction. These correspond to the four regions around the perilunes and to opposite sides of the Moon, i.e. around the intersections with the $z = 0$ plane. Because sidereal resonances no longer have such a favorable eclipse avoidance geometry, it is normal to see more eclipse regions for this quasi-periodic torus. Nevertheless, passages through these regions could be minimized by employing the strategies described above. Additionally, as with the 9:2 synodic resonance, only Moon eclipses are detected.

Finally, it should be noted that the Elliptic-Circular model does not take into account the inclination of each of the bodies' orbital planes. Such a consideration would be made when translating these results into a high-fidelity ephemeris model and would likely lead to an even smaller number of eclipse events. Further analyses can be made by means of torus maps, depending on the physical quantities we are interested in representing along the tori. These empower mission designers to choose ideal geometries and conditions for a variety of operations, transfers, or science observations.

7 Conclusions

This chapter has presented and detailed a higher-fidelity dynamical model called the [Elliptic-Circular Restricted Four-Body Problem \(ECR4BP\)](#), which incorporates the eccentricity of the primary and secondary bodies' orbits and a third body in a circular co-planar orbit about their barycenter. Motivated by the model's suitability to study the cislunar environment and by the future exploration of the cislunar space by the Lunar Gateway and associated missions, we have investigated the quasi-periodic structures of the Earth-Moon-Sun system that are the dynamical equivalents to periodic resonant Near-Rectilinear Halo Orbits ([NRHOs](#)) of the [CR3BP](#). We have presented the steps and methods necessary to compute these quasi-periodic tori. Framed by the planned orbits for the Lunar Gateway mission, we have focused on synodic and sidereal resonant orbits, which are resonant with the period of the Earth-Moon-Sun and the period of the Earth-Moon system, respectively. These resonant periodic orbits produce resonant two-dimensional quasi-periodic tori in the [ER3BP](#) model, which can be computed with the numerical continuation routines hereby outlined. We have analyzed these solutions in terms of relevant mission parameters and their possible application to the Lunar Gateway's orbit, such as eclipses events, altitude with respect to the Moon's surface, and the dynamical stability of these quasi-periodic trajectories. We find that the stability of these solutions remains very close to the near-stable behavior presented by their periodic counterparts, although one of the synodic resonances presents a bifurcation along one of its stable eigenpairs during the condition procedure. We also find that the geometry associated with synodic resonances verifies eclipse avoidance properties in the full Elliptic-Circular model, in line with the findings of previous works.

Chapter 6

Connections in the cislunar space

In this chapter, building on the previous formulation of the Elliptic-Circular model, natural connections between Earth-vicinity and the resonant quasi-periodic NRHOs are computed. The chapter is organized as follows. Section 1 presents a brief introduction to the topic of transfer design and interplanetary trajectories, contextualizing the use of the Elliptic-Circular problem as a tool to generate families of solutions that can later be used as initial guesses in full-ephemeris optimization algorithms. Section 2 then presents how these transfers are computed in the Elliptic-Circular model using the hyperbolic invariant manifolds of the previously computed quasi-periodic tori. The results obtained for the transfers in the Elliptic-Circular problem are then presented and analyzed in Section 3. Section 4 formulates the translation of these solutions from the Elliptic-Circular to full-ephemeris models. This is then used in Section 5 to obtain real transfer trajectories computed in a full-ephemeris model via an optimization scheme that corrects the trajectories generated from the initial guesses provided via the Elliptic-Circular's transfers. Finally, Section 6 presents the conclusions and general findings of this chapter.

1 Introduction

Computing and designing transfer trajectories has always been an important activity in the field of space exploration. Accommodating mission requirements into the transfer designs, such as fuel usage (ΔV), type of propulsion, departure dates, time of flight, among many others, often translates into complex multi-variable optimization problems that have been extensively studied in the past, and which stay relevant due to the development of new optimization algorithms and increased computational power [12, 76, 105]. Although highly dependent on the problem, their chaotic high-dimensional nature typically makes it challenging and computationally demanding to systematically obtain families of solutions for varying parameters of the mission design. This is particularly true for what are known as low-energy transfers, which approximate natural connections of the simplified dynamical models and use significantly lower ΔV values. Of course, the lower ΔV represents a trade-off in transfer time, which increases as a consequence. This balance is dictated by mission constraints and requirements. In the frame of the Lunar Gateway

mission, multiple re-supply missions are expected. Because many of these missions will not have tight time of flight constraints and will be looking to maximize the cargo mass, low-energy transfers present a valuable solution for their trajectory design. It is in this frame that the study of high-fidelity non-ephemeris systems – such as the Elliptic-Circular model – can be valuable for trajectory optimization and design. By accommodating the perturbations of the Sun’s gravity and the Moon’s eccentricity, we are able to better approximate the dynamics while providing a sufficiently simple system that allows for said systemic computation of solutions, which can then be passed along as either initial guesses or baseline trajectories to optimization algorithms.

In this chapter, these properties are leveraged to find natural connections between Earth-vicinity and the Moon. Particularly, in the frame of future lunar missions and, more specifically, the Gateway mission, we focus on designing trajectories that arrive at the previously computed resonant quasi-periodic NRHOs of the Elliptic-Circular. In order to find said natural connections we make use of the hyperbolic invariant manifolds of the quasi-periodic tori. Equivalently to the periodic orbit case introduced in Chapter 2, d -dimensional tori possess $(d + 1)$ -dimensional invariant hyperbolic manifolds when their internal eigenstructure includes hyperbolic motion. As seen in Chapter 5, this is indeed the case for the quasi-periodic NRHOs considered, as they all include a pair of non-unitary “eigencircles” ($R \neq 1$), which represent the stable ($R < 1$) and unstable ($R > 1$) hyperbolic directions.

2 Initialization of hyperbolic manifolds

The hyperbolic manifolds of quasi-periodic tori, also known as their whiskers, can be approximated in a similar way as those of periodic orbits. The stability information accessible from the GMOS method can be used to initialize these hyperbolic directions [82]. Specifically, let $\mathbf{v}_0^{S,U}$ be the hyperbolic stable or unstable eigenvectors associated with the torus’ Floquet matrix \mathbf{B} , i.e. representing the hyperbolic directions at $\theta_0 = 0$ (see Eq. (5.37)). Then, we can make use of the matrix $\hat{\mathbf{B}}(t)$, which is defined as

$$\hat{\mathbf{B}}(t) = [R_{-\omega_1 t}] \begin{bmatrix} \Phi_0(t) & & & \\ & \Phi_1(t) & & \\ & & \ddots & \\ & & & \Phi_{N_1-1}(t) \end{bmatrix}, \quad (6.1)$$

where Φ_i are the monodromy matrices of each trajectory along of invariant circle, to propagate the hyperbolic eigenvectors along the θ_0 direction:

$$\mathbf{v}^{S,U}(t) = \hat{\mathbf{B}}(t)\mathbf{v}_0^{S,U}, \quad (6.2)$$

noting that $\hat{\mathbf{B}}(T) = \mathbf{B}$. Discretizing the number of nodes along the θ_0 direction, such that $\mathbf{v}^{S,U}(t_i)$ represent the hyperbolic directions of the torus’ invariant circle at the i th node along

the θ_0 direction, we linearly approximate the initial states of the hyperbolic manifolds as

$$\mathbf{X}_i^{S,U} = \mathbf{X}_i + \varepsilon \frac{\mathbf{v}^{S,U}(t_i)}{\|\mathbf{v}^{S,U}(t_i)\|}, \quad (6.3)$$

where ε is a small perturbation and \mathbf{X}_i is the invariant circle at $\theta_0 = 2\pi i/n_0$ and $t_i = iT/n_0$, where n_0 is the number of discretization nodes and $i = \{0, 1, \dots, n_0 - 1\}$. The eigenvectors in Eq. (6.3) are normalized such that the norm of each individual vector is unitary. Note that in this case, n_0 is different from the N_0 parameter used in GMOS, which also denotes the number of nodes used along the θ_0 direction. However, while GMOS will generally work fine with small values of N_0 (and can even be set as $N_0=1$ for the single shooting implementation), we typically want to use large n_0 values in order to better describe the surface of the hyperbolic manifold. Due to the longer integration times typically used for hyperbolic manifolds, as well as the highly chaotic environments associated with these systems, small n_0 values would provide very sparse solutions, which would not accurately describe the manifold. This is because the hyperbolic manifolds can be parametrized as a torus moving through time $(\boldsymbol{\theta}, \tau) : \mathbb{T}^d \times \mathbb{R}$, where $d = 2$ in the case we are considering. That is, we will no longer integrate the initial invariant circle along the torus as in the GMOS algorithm, but rather integrate a full discretized representation of said torus in time along the hyperbolic directions.

Additionally, note that Eq. (6.1) undoes the rotation of the hyperbolic directions along the torus via the operator $[R_{-\omega_1 t}]$. This is convenient in terms of describing the initial points of the manifold, which, just as in the case for the torus maps, is represented by a regular grid along $\theta_0 = 2\pi i/n_0$ and $\theta_1 = 2\pi k/N_1$, with $k = \{0, 1, \dots, N_1 - 1\}$. However, it means that the discretized torus must also be obtained at a regular grid, using the same procedure as described for the torus maps (see Section 7.2 of Chapter 3). For the values of initial true anomaly associated with the resonant quasi-periodic NRHOs under study, this means that, for the synodic resonant tori:

$$\nu^{i,j} = 2\pi i/n_0, \quad (6.4)$$

and for the sidereal resonant tori:

$$\nu^{i,j} = iT/n_0. \quad (6.5)$$

Recall that for the synodic resonant tori, ν will be representative of θ_1 , while for the sidereal resonant tori it will simply reflect θ_0 (cf. Eqs (5.31) to (5.35)). Since the Sun angle σ is part of the state-vector via c and s , we do not have to enforce any other condition. Even though it reflects θ_1 for the sidereal resonances, its rotation will be undone naturally by the rotation operator $[R_{-\omega_1 t}]$.

3 Transfers in the Elliptic-Circular

Using the previously mentioned formulation, we can integrate the stable invariant manifolds of the three quasi-periodic resonant NRHOs. We set $n_0 = 1800$, set the maximum integration time

to 12 sidereal months and create event functions to detect impacts with the Earth and Moon and, importantly, to detect and record perigees. Additionally, the small perturbation ε is set such that the position variation is approximately 100 km. Then, we filter the results for those with perigees altitudes smaller than 10 000 km and times of flight smaller than approximately 200 days. Note that in order to obtain the real time of flight in dimensional time, we need to integrate $dt/d\nu$ with the true anomaly as

$$\Delta t = \int_{\nu_0}^{\nu_f} \frac{dt}{d\nu} d\nu = \int_{\nu_0}^{\nu_f} \frac{(1 - e^2)^{3/2}}{n(1 + e \cos \nu)^2} d\nu, \quad (6.6)$$

where ν_0 and ν_f are the initial and final true anomaly associated with a transfer, respectively, and $n = \sqrt{G(m_1 + m_2)/a^3}$ with a as the Earth-Moon semi-major axis. Based on this, the families of solutions found for transfers between the Earth and the resonant quasi-periodic NRHOs can be seen in Figures 6.1 to 6.3, which are plotted in Sun-Earth rotating frame, centered on the Earth (x -axis points from the Sun to the Earth at all times, z -axis points in the direction of primaries' angular momentum vector, and the y -axis completes the orthogonal frame). Note that the orbit of the Moon is not visible as it is hidden under the circle of trajectories around the Earth in the center of the plots.

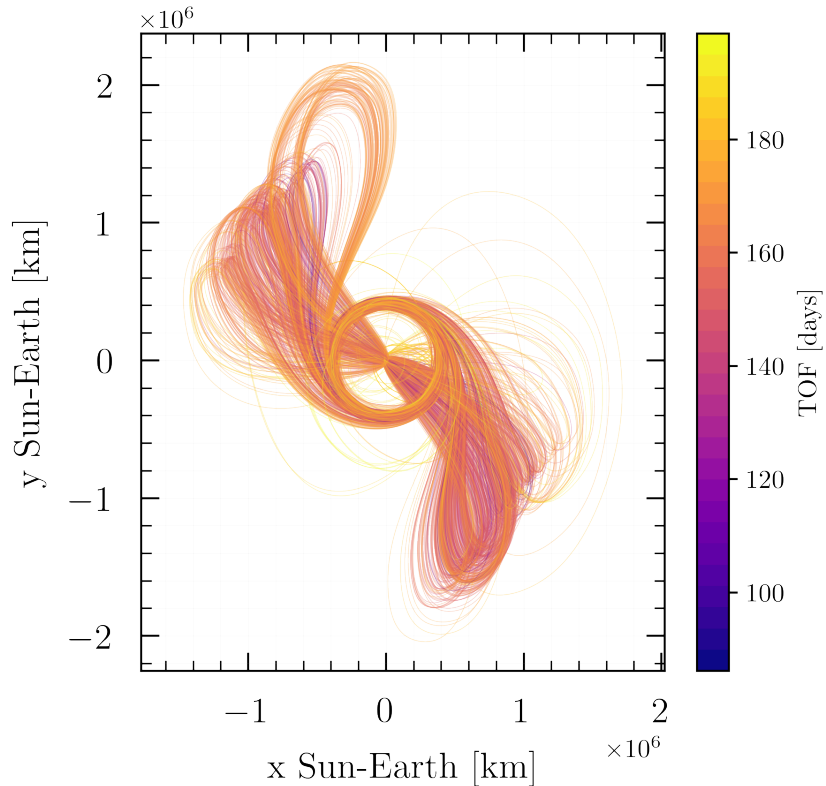


Figure 6.1: Transfers from Earth-vicinity (perigees) to the 9:2 synodic synodic resonant quasi-periodic NRHO.

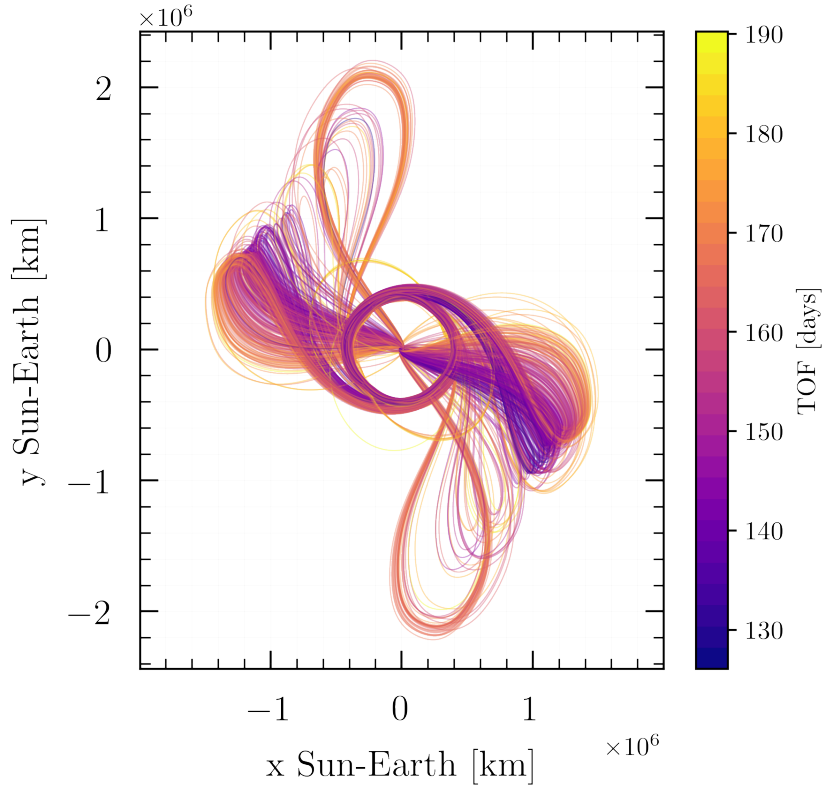


Figure 6.2: Transfers from Earth-vicinity (perigees) to the 4:1 synodic resonant quasi-periodic NRHO.

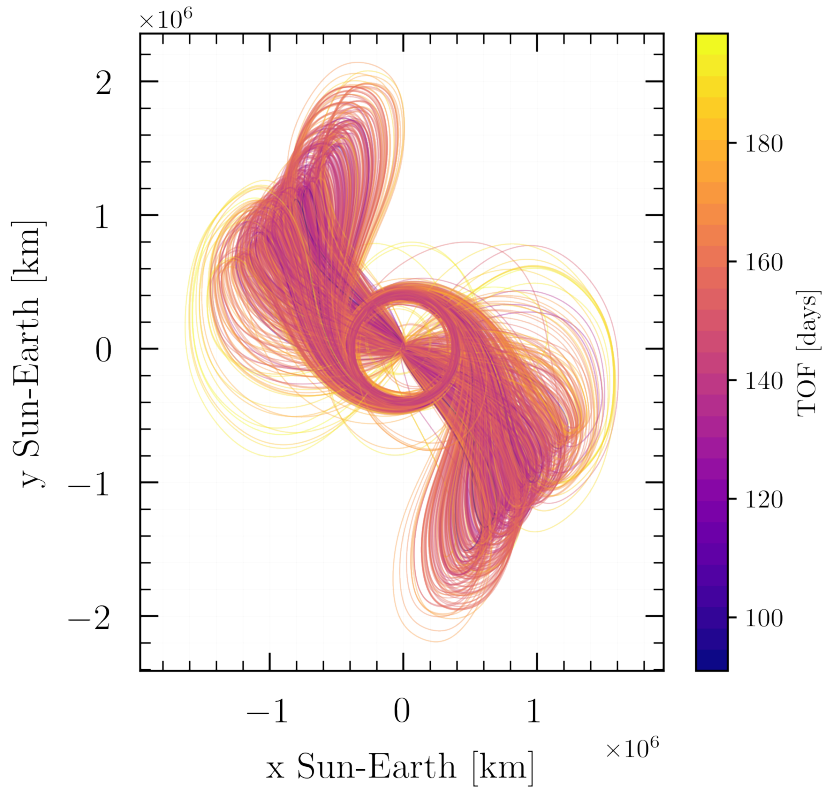


Figure 6.3: Transfers from Earth-vicinity (perigees) to the 4:1 sidereal resonant quasi-periodic NRHO.

We find that the trajectories presented reflect the types of solutions found in previous works in both geometry and average times of flight [87, 86]. Particularly, as observed in [96], the trajectories tend to depart in the directions of quadrants II and IV of the Sun-Earth rotating frame (where the quadrants are numbered in ascending order in the anti-clockwise direction), before arriving at the Moon. We also find that the transfers to the 9:2 synodic resonant torus and to the 4:1 sidereal resonant torus tend to show lower minimum times of flight when compared to the 4:1 synodic resonance, under 100 days versus just under 130 days, respectively. This can be seen more clearly in Figure 6.4, where the times of flight of all the trajectories are plotted against their respective perigee altitude at the point where they depart from Earth-vicinity. It is

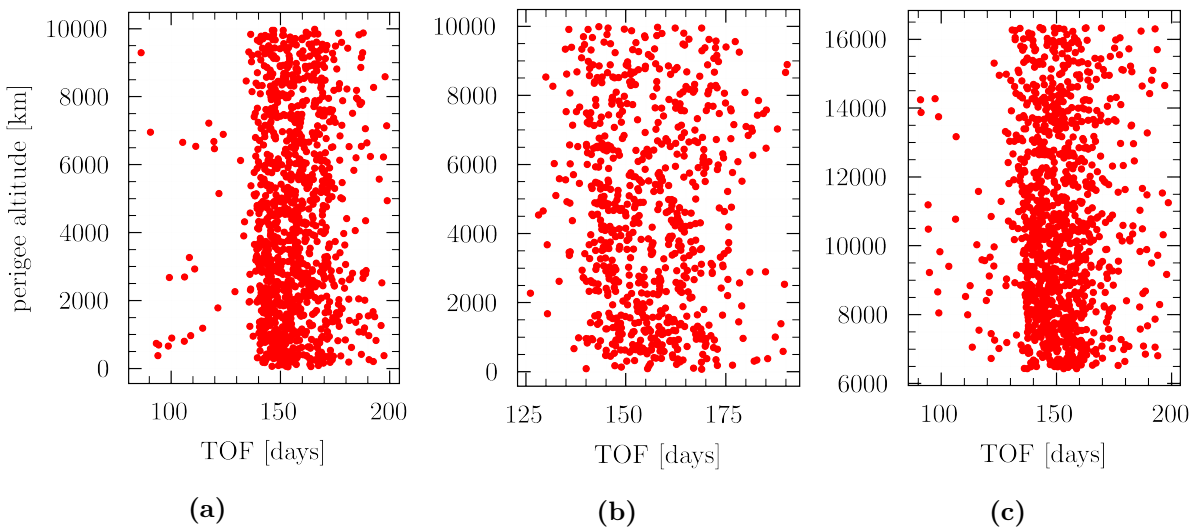


Figure 6.4: Times of flight versus perigee altitudes for the transfers to the quasi-periodic NRHOs: (a) 9:2 synodic resonance (b) 4:1 synodic resonance (c) 4:1 sidereal resonance.

interesting to note that most of the trajectories' time of flight seems to be "centered" around the 150 days mark, or rather seem to have a limit close to the 140 day mark. However, particularly for the 9:2 synodic resonance and for the 4:1 sidereal resonance, we see that several solutions extend towards lower times of flight. Additionally, we see that the perigee altitude does not seem to have a high correlation with the time of flight, meaning that lower perigee altitudes are possible with both longer and shorter times of flight.

In order to better analyze the conditions that lead to the lower times of flight associated with the transfers to each of the tori, we can analyze the arrival conditions at each of the resonant tori. More specifically, we can plot the transfers in the torus's coordinates at the arrival epochs, using similar plots to the previously presented torus maps. The plots seen in Figures 6.5, 6.6, and 6.7 display the time of flight as a function of θ_0 and θ_1 , noting that we clip the colorbar at 145 days in order to see the shorter transfer times more clearly. Additionally, the perilune and apolune locations are marked with blue and red dashed vertical lines, respectively. This allows us to note that the shortest times of flight all occur for trajectories that arrive at perilunes. This is even clearer on the right-hand side of the previous plots, in Figures 6.5b, 6.6b, and 6.7b, where the mean anomaly per orbital revolution is displayed with respect to the torus angle θ_1 .

Note that a value of zero mean anomaly represents the apolune, and a value of π represents the perilune.

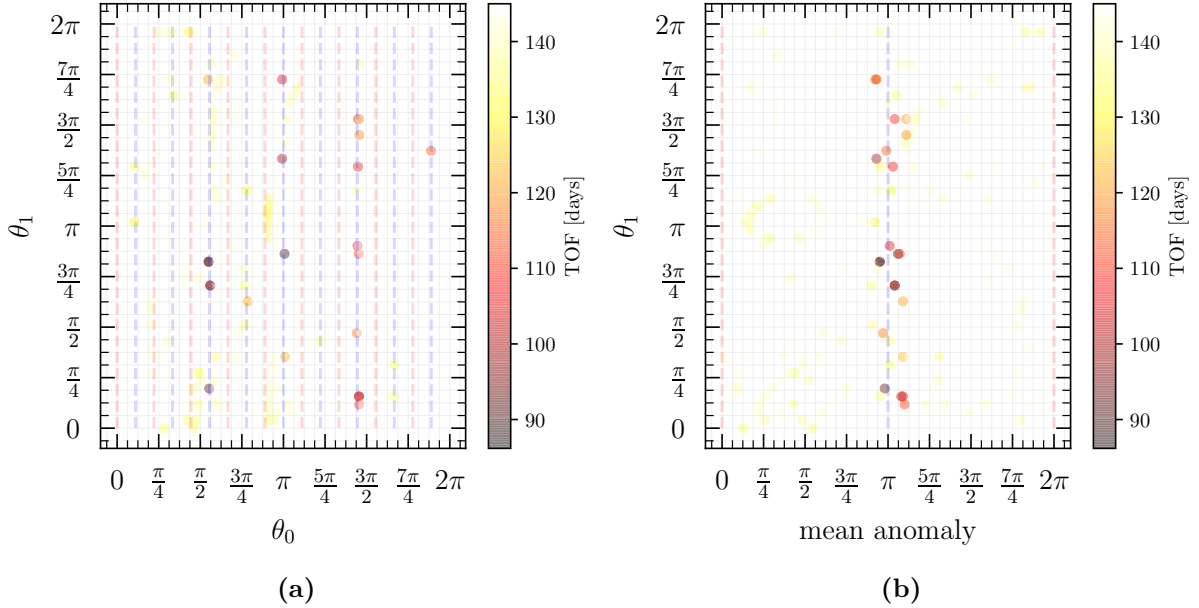


Figure 6.5: Times of flight (under 145 days) associated with the transfers to the 9:2 synodic resonant quasi-periodic NRHO as a function of (a) the torus angles (θ_0, θ_1) and (b) mean anomaly per orbital revolution versus θ_1 . Perilunes and apolunes are represented by blue and red vertical lines, respectively.

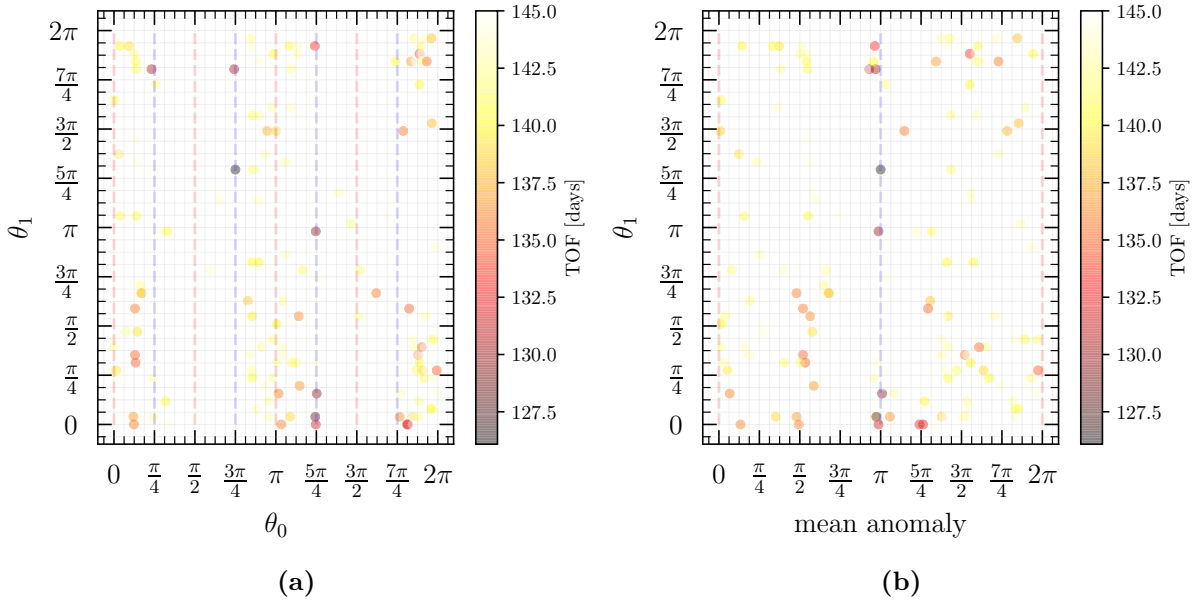


Figure 6.6: Times of flight (under 145 days) associated with the transfers to the 4:1 synodic resonant quasi-periodic NRHO as a function of (a) the torus angles (θ_0, θ_1) and (b) mean anomaly per orbital revolution versus θ_1 . Perilunes and apolunes are represented by blue and red vertical lines, respectively.

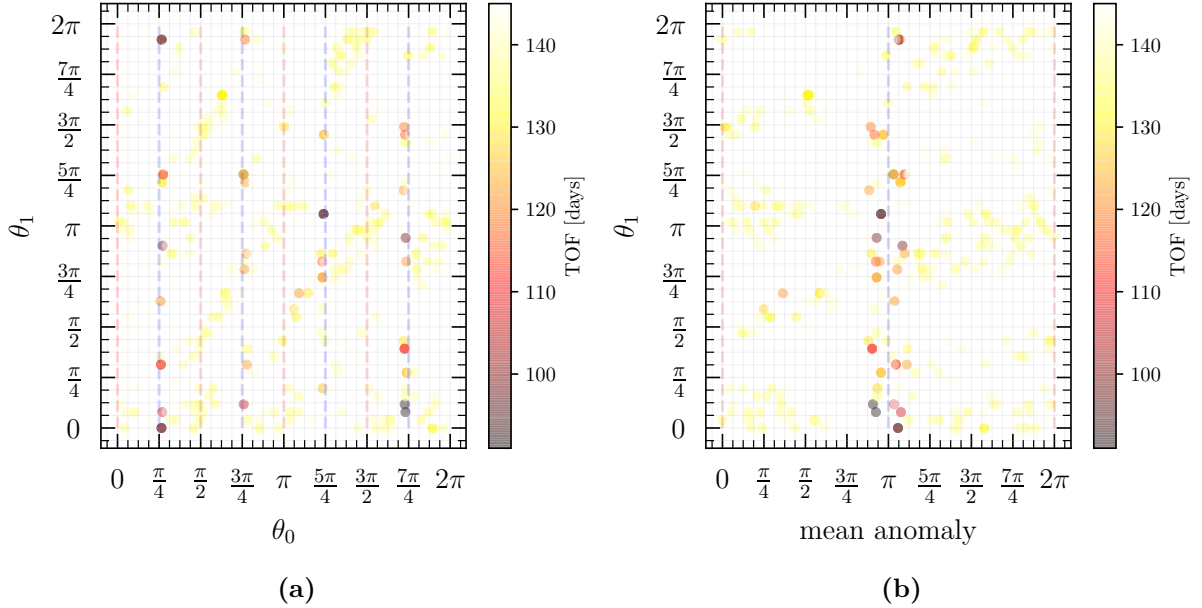


Figure 6.7: Times of flight (under 145 days) associated with the transfers to the 4:1 sidereal resonant quasi-periodic NRHO as a function of (a) the torus angles (θ_0, θ_1) and (b) mean anomaly per orbital revolution versus θ_1 . Perilunes and apolunes are represented by blue and red vertical lines, respectively.

The reason behind this fact likely lies with the high non-linearities that are found around the perilune region of the NRHOs [53], which were referenced in Section 4.1 of Chapter 5. The same mechanism that can be detrimental to the implementation of orbit maintenance maneuvers or correction procedures in numerical algorithms also translates into trajectories that “leave” the quasi-periodic tori faster along their stable hyperbolic manifolds, thanks to the faster dynamics. Moreover, the 9:2 synodic resonant and the 4:1 sidereal resonant tori present lower perilunes when compared with the 4:1 synodic resonance, as evidenced by the torus maps presented in Chapter 5 (see Figures 5.12 to 5.14). It is possible that this is why the 9:2 synodic and 4:1 sidereal resonances presents faster transfers than the 4:1 synodic resonance. Nevertheless, we note that mission requirements may force us to design trajectories that do not arrive at the perilune for safety reasons.

Moreover, the times of flight seen in these figures are mainly used to provide an insight into the problem and to analyze the type of trajectories that they characterize. When designing the final trajectories with full-ephemeris models and optimization algorithms, these times of flight can be used as an initial guess that said algorithms can aim at minimizing. This means that we can use these times of flight as an indication of the duration of these types of trajectories, but that they do not hinder the procedure of obtaining smaller times. Additionally, the main goal is to be able to provide a wide range of transfers opportunities that one can translate to full-ephemeris optimization models. As seen from the number of transfers trajectories showcased in Figures 6.1 to 6.3, this is clearly the case.

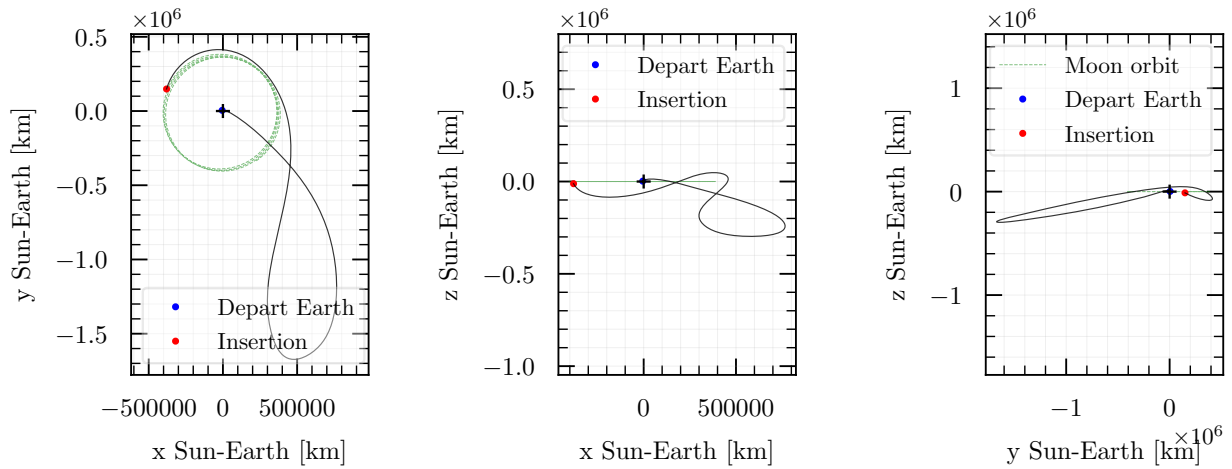


Figure 6.8: Transfer with shortest time of flight from Earth-vicinity (perigee) to the 9:2 synodic resonant quasi-periodic NRHO.

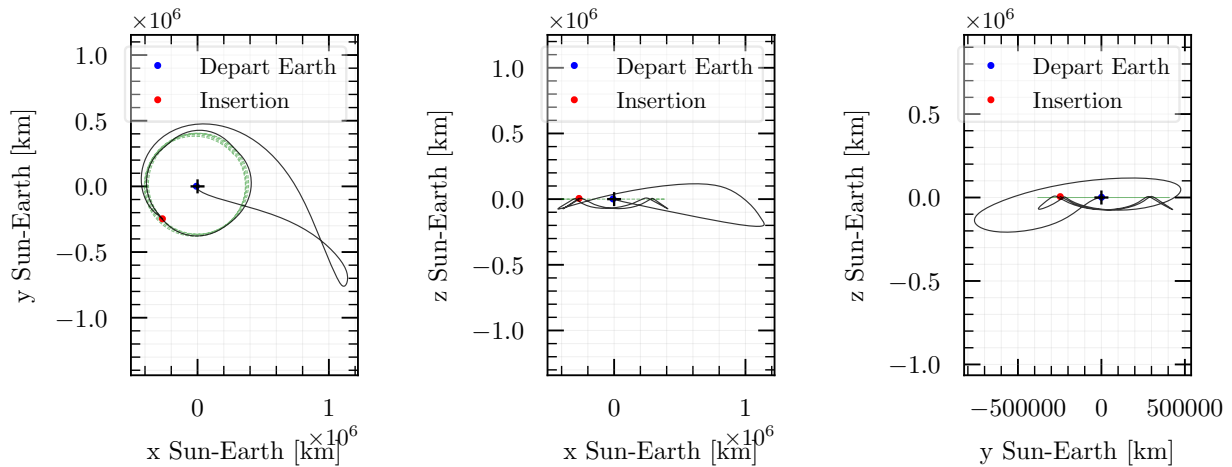


Figure 6.9: Transfer with shortest time of flight from Earth-vicinity (perigee) to the 4:1 synodic resonant quasi-periodic NRHO.

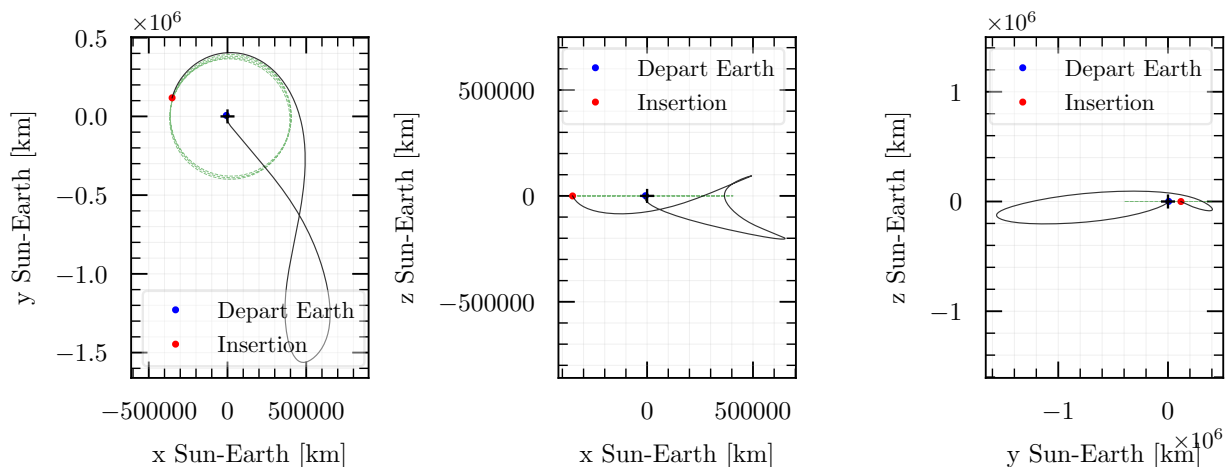


Figure 6.10: Transfer with shortest time of flight from Earth-vicinity (perigee) to the 4:1 sidereal resonant quasi-periodic NRHO.

Finally, the trajectories with shortest times of flight for the previously presented transfers for each of the quasi-periodic tori considered can be seen in Figures 6.8 to 6.10, shown also in the Sun-Earth rotating frame centered on Earth. The Moon’s trajectory during the transfer is shown in a green dashed line. The following section demonstrates how one can translate these transfers to ephemeris models.

4 Translation to ephemeris models

In order to test and optimize the transfer trajectories obtained in a full-ephemeris model, we first need to translate the solutions to adequate reference frames and to real dates. In order to achieve this, we make use of NASA’s NAIF SPICE library, which tracks the real orbits and positions of celestial bodies in the Solar System [1]. Using this, we can obtain the relative geometries of the Earth, Moon, and Sun throughout the time periods for which we want to design transfers and match them with those arising from the precomputed transfers of the Elliptic-Circular. As an example, Figure 6.11a displays the Sun angles obtained from the ephemeris data for the year 2026, and Figure 6.11b shows the correspondence of the Sun angle and the Moon true anomaly as a function of the date for that same year. It is clear, by analyzing Figure 6.11b, that one might

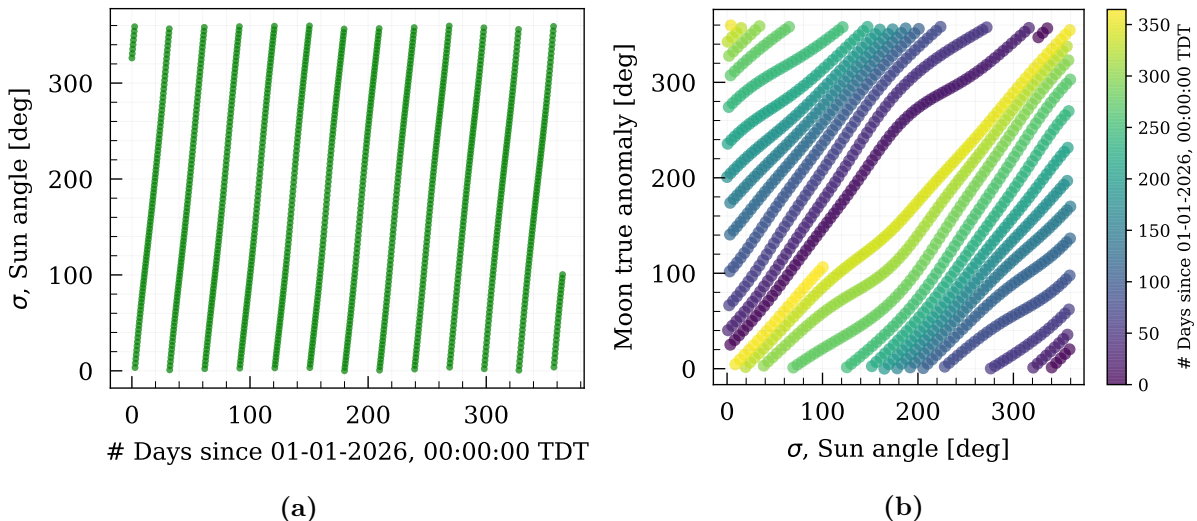


Figure 6.11: Relative geometries of the Earth, Moon, and Sun in the ephemeris files for the year 2026: (a) Sun angle versus date and (b) Sun angle versus Moon true anomaly as function of the date.

not find a date that represents a perfect match for the σ, ν pair coming from the Elliptic-Circular model. This is expected, as the Elliptic-Circular is still a simplification of the real dynamics and the real orbital parameters of the Earth and the Moon actually vary, particularly those associated with the Moon. Nevertheless, minimizing the phase angle difference between both angles should already provide a good enough guess in the full-ephemeris model, and one that should be closer to the real dynamics than something arising from the CR3BP or the Bicircular model.

Additionally, note that in principle we would have to match two pairs of σ, ν angles (or more,

if taking multiple points along the trajectory), corresponding to the departure date from Earth and arrival date to the Moon, which should be spaced apart by a time close to the obtained time of flight. Due to the approximations taken and, particularly, to the variation in the Moon's real rate of true anomaly and orbit eccentricity, this translates into an over-constrained problem for which a solution that meets all conditions (matching both departure and arrival angles, as well as time of flight) is rarely found. To avoid this, it is preferable to select only one pair of angles for which to optimize, either at departure or arrival (or possibly, at half way along the trajectory). After obtaining the date that corresponds to said geometry, one can simply use the time of flight arising from the Elliptic-Circular and either subtract or add that to the converged date to obtain the departure or arrival date, respectively.

In order to find the date that corresponds to the the σ, ν pair, we can formulate the following optimization problem:

$$\min_{t_e \in \Sigma} J(t_e) \quad (6.7)$$

where t_e is the epoch in seconds past the J2000 and J is the cost function

$$J(t_e) = \left(\eta_0(\bar{\sigma}(t_e) - \sigma_{EC})^2 + \eta_1(\bar{\nu}(t_e) - \nu_{EC})^2 \right)^{1/2}, \quad (6.8)$$

where η_i are the weight factors, $\bar{\sigma}(t_e), \bar{\nu}(t_e)$ are the functions that return the Sun angle and Moon true anomaly, respectively, from the SPICE ephemeris at a specific epoch, and σ_{EC}, ν_{EC} are the Sun angle and Moon true anomaly angles coming from the Elliptic-Circular model, respectively.

The inclusion of the weight factors in Eq. (6.8) is common in optimization problems and can also help in targeting the most relevant of the two angles. Although, for this example, we find satisfactory accuracy when using $\eta_0 = 0.5, \eta_1 = 0.5$, it is important to recall how each angle affects and relates to the tori. As was previously mentioned, for synodic resonant tori, the longitudinal torus angle, θ_0 will reflect the Sun angle σ , while for sidereal resonant tori, it will reflect the Moon true anomaly ν . Moreover, it is the angular frequency associated with the fundamental torus direction, ω_0 , that is resonant with either the synodic or the sidereal period. This means that for a synodic resonant torus, all perilunes will happen at specific values of σ – e.g. for the 4:1 resonance they would be separated by approximately $\pi/2$ – but can have any value of ν ; in the same way, for a sidereal resonant torus, the perilunes would correspond to specific values of ν but can have any value of σ . As a consequence, the angular variable associated with θ_0 (σ for the synodic resonances and ν for the sidereal resonances) will typically have a higher impact on the accuracy of the solution for the full-ephemeris model. We find that a good match in terms of both angles is generally found for a particular date (errors with standard deviations below 0.5°) for equal weights. Nevertheless, we note that when a date is found, the time of flight value computed in the Elliptic-Circular is, as mentioned, used to obtain either the corresponding departure or the corresponding arrival date. This means that said corresponding date will generally have a larger error in terms of the aforementioned angles. Although we verify this is indeed the case for the true anomaly, which is tied with the fact that the actual orbital elements of the Moon can vary more significantly throughout its orbit, the errors associated

with the Sun angle remain within acceptable ranges (also below a 0.5° standard deviation).

The optimization problem of Eq. (6.7) can be solved using different algorithms. In this work, we use the readily implemented [Simplicial Homology Global Optimization \(SHGO\)](#) algorithm [34] from Python's Scipy library, which we find produces satisfactory results. Once the dates are known, we are in a position to transform the state-vectors from the Elliptic-Circular frame to one of SPICE's available inertial frames, such as the mean ecliptic and equinox of J2000 (ECLIPJ2000), or the Earth mean equator and equinox of J2000 frame (J2000, also known as ICRF or EME2000).

Let \mathbf{X} be a state-vector in the Elliptic-Circular rotating frame centered on Earth in dimensional coordinates. Then, the invertible transformation from the Elliptic-Circular to the ECLIPJ2000 holds [4]:

$$\mathbf{Y} = \begin{bmatrix} \mathbf{R}_I^R & \mathbf{0} \\ \mathbf{R}_I^R[\tilde{\boldsymbol{\Omega}}] & \mathbf{R}_I^R \end{bmatrix} \mathbf{X}. \quad (6.9)$$

\mathbf{R}_I^R is the 3×3 rotation matrix from the Elliptic-Circular's rotating frame to the ECLIPJ2000 inertial frame

$$\mathbf{R}_I^R = \left[\frac{\mathbf{r}_m}{r_m}, \frac{\mathbf{h}_m \times \mathbf{r}_m}{\|\mathbf{h}_m \times \mathbf{r}_m\|}, \frac{\mathbf{h}_m}{h_m} \right], \quad (6.10)$$

where \mathbf{r}_m is the Moon's position vector as seen from the Earth in the ECLIPJ2000, $\mathbf{h}_m = \mathbf{r}_m \times \mathbf{v}_m$ is the Moon's specific angular momentum, and \mathbf{v}_m is the Moon's velocity as seen from the Earth in the same frame. The matrix $[\tilde{\boldsymbol{\Omega}}]$ in Eq. (6.9) represents the cross product in matrix form associated with the Moon's angular frequency vector, $\boldsymbol{\Omega} = [\Omega_x, \Omega_y, \Omega_z]^T$:

$$[\tilde{\boldsymbol{\Omega}}] = \begin{bmatrix} 0 & -\Omega_z & \Omega_y \\ \Omega_z & 0 & -\Omega_x \\ -\Omega_y & \Omega_x & 0 \end{bmatrix}, \quad (6.11)$$

noting that $\boldsymbol{\Omega}$ can be obtained directly from SPICE via

$$\boldsymbol{\Omega} = \frac{\mathbf{r}_m \times \mathbf{v}_m}{r_m^2}, \quad (6.12)$$

and is written as $\boldsymbol{\Omega} = [0, 0, \Omega]^T$.

Finally, it is important to mention that although $\mathbf{X} = [\mathbf{r}_{EC}; \mathbf{v}_{EC}]^T$ is the dimensional state of the spacecraft in the Earth-centered Elliptic-Circular, when considering the arrival states around the Moon, we compute \mathbf{r}_{EC} considering the distance between Earth and the Moon as the real distance obtained from SPICE:

$$x_{EC} = r_m + x_{EC/m}, \quad (6.13)$$

where x_{EC} is the x -coordinate of \mathbf{r}_{EC} in the Earth-centered Elliptic-Circular and $x_{EC/m}$ is the spacecraft's x -coordinate in the Moon-centered Elliptic-Circular.

5 Transfers in the ephemeris models

In order to test the initial guesses generated from the aforementioned algorithms, we use a simple Earth-centered n-body model with point masses, taking into account the Earth, the Moon, and the Sun. We can write the acceleration, $\ddot{\mathbf{r}}$, in the Earth-centered inertial frame (e.g. ECLIPJ2000) as

$$\ddot{\mathbf{r}} = -\mu_e \frac{\mathbf{r}}{r^3} - \mu_m \left(\frac{\mathbf{r}_{sc/m}}{r_{sc/m}^3} + \frac{\mathbf{r}_m}{r_m^3} \right) - \mu_s \left(\frac{\mathbf{r}_{sc/s}}{r_{sc/s}^3} + \frac{\mathbf{r}_s}{r_s^3} \right), \quad (6.14)$$

where \mathbf{r} is the position vector, μ_e, μ_m, μ_s are, respectively, the gravitational parameters of the Earth, Moon, and Sun, $\mathbf{r}_{sc/m}, \mathbf{r}_{sc/s}$ are the spacecraft's position with respect to the Moon and the Sun, respectively, and \mathbf{r}_s is the Sun's position with respect to the Earth.

Using this ephemeris model, a few trajectories have been obtained by means of an optimization routine from Airbus Defence and Space that takes the initial guesses generated from the Elliptic-Circular after the aforementioned transformation procedure. Two examples of said trajectories can be seen in Figures 6.12 and 6.13, representing transfers to the 9:2 synodic resonant quasi-periodic torus. Figures 6.12a and 6.13a show the trajectories in the Sun-Earth rotating frame, with the converged trajectory in red. The initial guesses provided to the optimization algorithm are displayed in dashed lines and are integrated backwards from the final state and forwards from the initial state. The original Elliptic-Circular trajectory is also overlayed on top in blue. Figures 6.12b and 6.13b show the trajectories in the ECLIPJ2000 frame.

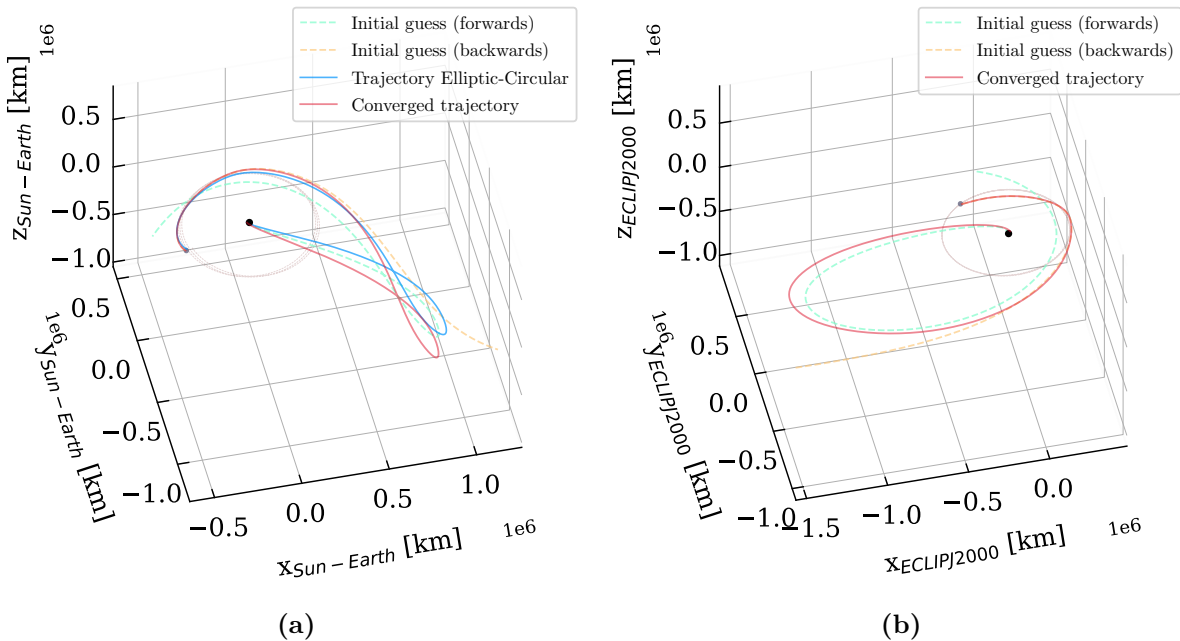


Figure 6.12: Example of transfer trajectory to the 9:2 synodic resonant quasi-periodic NRHO departing from Earth on 11-Apr-2032 13:33:15.93 (TDB) and duration of 88.47 days: (a) shown in Sun-Earth rotating frame; (b) shown in ECLIPJ2000 frame. The converged trajectory entails a total ΔV of 14.75 m/s.

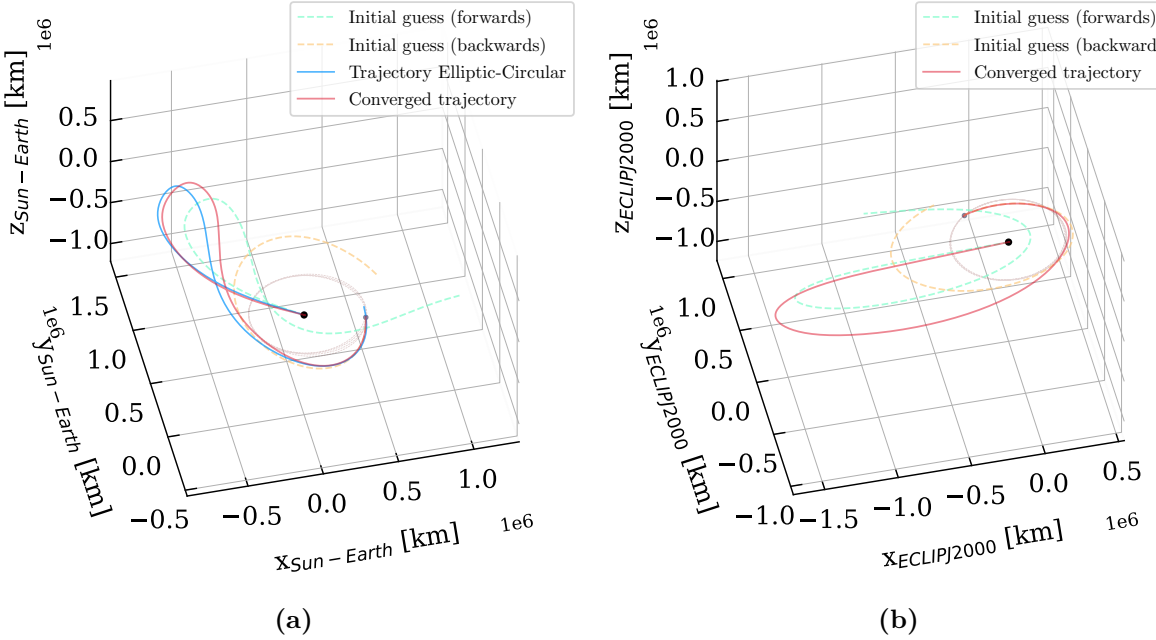


Figure 6.13: Example of transfer trajectory to the 9:2 synodic resonant quasi-periodic NRHO departing from Earth on 28-Oct-2030 19:02:50.75 (TDB) and duration of 100.61 days: (a) shown in Sun-Earth rotating frame; (b) shown in ECLIPJ2000 frame. The converged trajectory entails a total ΔV of 17.37 m/s.

A few points are noted from these trajectories. Firstly, we can see that the initial guesses, which are integrated in the ephemeris model without any correction, diverge from both the nominal Elliptic-Circular trajectory and from the converged trajectory. This is expected as we are only taking two points – at the initial and final states – and the differences in the dynamics will naturally cause an uncorrected trajectory to diverge. We also note that this is more significant in the portion of the trajectory that remains close to the Moon (at arrival), as the spacecraft remains longer in its proximity, meaning it will be more sensitive to its perturbations, and as the real rate of true anomaly and eccentricity of the Moon vary more significantly throughout its orbit. As such, the trajectories that are integrated backwards from the final state (at arrival to the Moon) tend to be more perturbed and diverge more significantly.

Secondly, note that only two states are being used in this optimization. This is due to the fact that the optimization routine used was not built specifically for this type of application. Indeed, when transitioning trajectories from simplified models to full-ephemeris ones, it is more common to make use of multiple shooting corrector algorithms that slowly correct each segment of the trajectory to create continuity in position and time via non-linear optimization routines like SNOPT [38, 20]. The algorithm used treats the problem differently and rather integrates the initial and final trajectories to find a common patch point. It also has flexibility on the departure and arrival conditions and applies a correction ΔV at Earth-departure and at the patch point. Although this is not the best approach for our problem formulation, it is interesting to see that the algorithm still manages to converge on transfer trajectories using the guesses created from the Elliptic-Circular transfers.

The converged transfer shown in Figure 6.12 entails a total ΔV of 14.75 m/s for a time of flight of 88.47 days – versus to the time of flight of 86.18 days estimated in the Elliptic-Circular model – whereas the converged transfer shown in Figure 6.13 entails a total ΔV of 17.37 m/s for a time of flight of 100.61 days – versus to the time of flight of 98.61 days estimated in the Elliptic-Circular model. We see that both converged trajectories have approximately a two-day difference in time of flight with respect to the nominal guess coming from the Elliptic-Circular model. Finally, we note that adapting the optimization algorithm to use a more common multiple shooting corrector routine should yield lower ΔV values. This is a work in progress.

6 Conclusions

This chapter has presented low-energy cislunar transfers between the Earth-vicinity and three types of resonant quasi-periodic NRHOs. Using the Elliptic-Circular model and the 9:2 synodic, 4:1 synodic, and 4:1 sidereal resonant quasi-periodic tori thereby computed and previously presented, we first make use of the tori’s hyperbolic manifolds to find natural connections between Earth-vicinity and these dynamical objects. We verify that the approach allows us to generate families of solutions that have, on average, transfer times between 90 and 200 days, centered around the 150 day mark. The shorter times of flight (<100 days) are found for the 9:2 synodic and 4:1 sidereal tori, which have lower perilunes, and specifically for trajectories that arrive around the perilune region of the tori. These trajectories are then translated to an ephemeris model by matching the geometry of the Elliptic-Circular problem to their real positions known via ephemeris files, which allows to us to find corresponding departure and arrival dates. Using a two-point optimizer algorithm from Airbus Defence and Space that patches the trajectories from the final and initial states at a mid-point, we obtain corresponding transfers in a real-ephemeris model. Although the optimization algorithm is not particularly adapted to treat this type of problem, the trajectories found maintain low ΔV values (below 20 m/s) that follow trajectories close to those found in the Elliptic-Circular model.

Chapter 7

Conclusions and future work

This thesis work has investigated and elaborated on the models and tools necessary to design trajectories in strongly perturbed environments. With space missions seeking higher scientific-value targets in innovative and bolder mission designs, the traditional methods and models that have been used in the past for designing their trajectories can often overlook interesting design scenarios, require higher operational maintenance, and lack the dynamical insight that can, among others, allow us to generate families of solutions. This is due to the fact that these missions often take place in highly-perturbed systems, which can be affected by a variety of perturbations such as the small mass of the main body, irregular gravity fields, presence of additional bodies, ellipticity of their orbits, among others. In this frame, we have formulated dynamical models and techniques that allow us to incorporate the main perturbations associated with these environments into the trajectory design solutions.

In particular, after an initial introduction to the necessary background theory, contributions to the computation of quasi-periodic tori have been presented in Chapter 3. The subject of quasi-periodic motion is heavily explored throughout this work, and forms the basis for the incorporation of perturbations into the higher-fidelity representation of dynamical solutions. We have shown how the modifications implemented to the algorithms can improve their computational efficiency and their robustness, and presented an example of these using the Mars-Phobos system and [JAXA’s MMX mission](#).

Using the notions previously presented, we explored the dynamical environment around small bodies, which is heavily perturbed by [Solar Radiation Pressure \(SRP\)](#), using the formulation of the [Augmented Hill Problem \(AHP\)](#) in Chapter 4. The formulation used also includes eclipses, which are often not incorporated into the dynamical models used to study these systems. We analyzed invariant manifold structures associated with this problem, and noted that the hyperbolic manifolds of the L₂ equilibrium point are heavily influenced by [SRP](#). Using periodic and quasi-periodic tori belonging to what is known as the terminator or Halo family, we generated baseline landing trajectories to the surface of small bodies via the hyperbolic unstable manifolds of the tori. For this, multiple “landers” with different mass-to-area ratios were considered, as well as asteroids Bennu and Ryugu, as example scenarios. We also showed that the quasi-periodic tori considered are specially suited for the design of homoclinic connections and presented several examples of these trajectories.

We then moved onto an analysis of the cislunar space in Chapter 5, where we presented a novel dynamical model that includes the presence of the Sun and the ellipticity of the Moon’s orbit. Using this model, which we call the Elliptic-Circular, we investigated the dynamical substitutes or the Lunar Gateway’s planned orbits, which become two-dimensional resonant quasi-periodic tori. After demonstrating how to formulate and continue these solutions, we analyzed them in terms of stability, eclipse avoidance properties, and overall geometry. We verified that the tori approximately retain these properties when compared to their formulation in simpler models such as the [Circular Restricted Three-Body Problem \(CR3BP\)](#).

Finally, we have used the resonant quasi-periodic tori computed for the Lunar Gateway to generate transfer trajectories from Earth-vicinity to the tori in Chapter 6 via their stable hyperbolic manifolds. These trajectories were first presented and analyzed in the Elliptic-Circular model, and then their transformation to ephemeris models was addressed. We verified that the procedure allows for the formulation of large numbers of transfer trajectories that can then be used to initialize optimization algorithms in the real ephemeris, thereby enabling the generation of families of low-energy transfer trajectories.

In spite of the work developed, there are areas of work that would benefit from further exploration, as well as valuable research topics that have arisen from the studies hereby presented. These are listed below:

- With regards to the numerical computation of quasi-periodic tori, the use of sparse matrix libraries, such as those existing in Python and Matlab, could provide computational improvements, particularly when dealing with larger-dimension matrices, as those in the PDE(DFT) method or as those arising from the computation of three-dimensional tori. On this last aspect, the implementation of multi-parameter continuation for the numerical continuation of families of three-dimensional quasi-periodic tori would be a valuable direction of work that would allow us to increase the number of perturbations to a system and to cover an even larger region of the solution phase space.
- Although we have presented applications of trajectory design to small-body exploration, the subject can be further explored in the directions proposed by this thesis. Specifically, the subject of binary asteroids, which is framed by ESA’s Hera mission, was one of the applications of this work that did not materialize due to finite time resources. Indeed, their study is especially suited to be tackled by the means proposed in this thesis, such as the use of higher-fidelity models as the Elliptic-Circular or the Bicircular with [SRP](#), and even including higher-fidelity gravitational models, using quasi-periodic tori for the trajectories of spacecraft. Although higher-fidelity gravity models were not extensively used in this work, they can easily be treated as another periodic perturbation to the dynamics and addressed in the same way as the other periodic perturbation presented. Additionally, we note that the computation of quasi-periodic tori when considering [SRP](#) and, particularly, eclipses, should be given more attention in the future. We have found that numerical procedures need to be adjusted for the dynamical discontinuity created by the eclipses (when the quasi-periodic trajectories cross these regions), which seem to isolate solutions

in the phase space and make it difficult to find the directions of continuation.

- Finally, the work arising from the formulation of the Elliptic-Circular model would benefit from a study and comparison about its accuracy when compared to other dynamical models. This would allow to quantify the fidelity of these models with respect to the real-ephemeris. Furthermore, the correction and continuation of the quasi-periodic tori found in the Elliptic-Circular model to real-ephemeris models would be extremely valuable and would provide a direct comparison with the solutions that have been continued from the CR3BP to the real-ephemeris models. Additionally, a more extensive analysis on the families of transfer solutions that are found in the ephemeris model (by means of, e.g. multiple shooting optimization), and that come from the Elliptic-Circular's trajectories would further our understanding of these connections and their main characteristics.

Bibliography

- [1] Charles H. Acton. “Ancillary data services of NASA’s navigation and Ancillary Information Facility”. *Planetary and Space Science* 44.1 SPEC. ISS. (1996), pp. 65–70. doi: [10.1016/0032-0633\(95\)00107-7](https://doi.org/10.1016/0032-0633(95)00107-7) (cit. on p. 106).
- [2] M A Andreu. “The quasi-bicircular problem”. PhD thesis. 1998 (cit. on p. 74).
- [3] Nima Assadian and Seid H. Pourtakdoust. “On the quasi-equilibria of the BiElliptic four-body problem with non-coplanar motion of primaries”. *Acta Astronautica* 66.1-2 (2010), pp. 45–58. doi: [10.1016/j.actaastro.2009.05.014](https://doi.org/10.1016/j.actaastro.2009.05.014) (cit. on p. 74).
- [4] Nicola Baresi. “Transition of two-dimensional quasi-periodic invariant tori in the real-ephemeris model of the Earth-Moon system”. *Modeling and Optimization in Space Engineering (In Press)* (cit. on p. 108).
- [5] Nicola Baresi. “Spacecraft Formation Flight on Quasi-periodic Invariant Tori”. PhD thesis. University of Colorado Boulder, 2017, p. 180 (cit. on pp. 25, 42, 91).
- [6] Nicola Baresi, Diogene Alessandro Dei Tos, Hitoshi Ikeda, and Yasuhiro Kawakatsu. “Orbit design and maintenance in the elliptical Hill problem with applications to the Phobos sample return mission MMX”. *International Astronautical Congress (IAC)*. Washington, D.C., USA, 2019 (cit. on pp. 4, 45).
- [7] Nicola Baresi and Yasuhiro Kawakatsu. “Quasi-periodic Motion around Phobos : Applications to the Martian Moons eXploration (MMX)”. *32nd International Symposium on Space Technology and Science*. Fukui, Japan, 2019 (cit. on pp. 43, 44).
- [8] Nicola Baresi, Zubin P. Olikara, and Daniel J. Scheeres. “Fully numerical methods for continuing families of quasi-periodic invariant tori in astrodynamics”. *Journal of the Astronautical Sciences* 65.2 (2018), pp. 157–182. doi: [10.1007/s40295-017-0124-6](https://doi.org/10.1007/s40295-017-0124-6) (cit. on pp. 3, 4, 28, 29, 31, 32, 34, 36, 80).
- [9] Nicola Baresi, Daniel J. Scheeres, and Hanspeter Schaub. “Bounded relative orbits about asteroids for formation flying and applications”. *Acta Astronautica* 123 (2016), pp. 364–375. doi: [10.1016/j.actaastro.2015.12.033](https://doi.org/10.1016/j.actaastro.2015.12.033) (cit. on p. 4).
- [10] O. S. Barnouin, M. G. Daly, E. E. Palmer, R. W. Gaskell, J. R. Weirich, C. L. Johnson, et al. “Shape of (101955) Bennu indicative of a rubble pile with internal stiffness”. *Nature Geoscience* 12.4 (2019), pp. 247–252. doi: [10.1038/s41561-019-0330-x](https://doi.org/10.1038/s41561-019-0330-x) (cit. on p. 57).
- [11] Mark Beckman and Leigh Janes. “Finding acceptable james webb space telescope mission orbits from a fixed ariane flight profile”. *AIAA/AAS Astrodynamics Specialist Conference*. San Diego (CA), USA, 2005 (cit. on p. 2).
- [12] John T. Betts. “A Survey of Numerical Methods for Trajectory Optimization”. *Journal of Guidance, Control, and Dynamics* 21.2 (1998), pp. 193–207. doi: <https://doi.org/10.2514/2.4231> (cit. on p. 97).
- [13] John T. Betts. *Practical Methods for Optimal Control and Estimation Using Nonlinear Programming*. 2010 (cit. on pp. 34, 39, 42).
- [14] William H. Blume. “Deep Impact mission design”. *Space Science Reviews* 117.1-2 (2005), pp. 23–42. doi: [10.1007/s11214-005-3386-4](https://doi.org/10.1007/s11214-005-3386-4) (cit. on p. 1).
- [15] Kenza K. Boudad, Kathleen C. Howell, and Diane C. Davis. “Dynamics of synodic resonant near rectilinear halo orbits in the bicircular four-body problem”. *Advances in Space Research* 66.9 (2020), pp. 2194–2214. doi: [10.1016/j.asr.2020.07.044](https://doi.org/10.1016/j.asr.2020.07.044) (cit. on pp. 4, 73, 74, 78, 82, 86, 91, 92).
- [16] Stephen B. Broschart, Gregory Lantoine, and Daniel J. Grebow. “Quasi-terminator orbits near primitive bodies”. *Celestial Mechanics and Dynamical Astronomy* 120.2 (2014), pp. 195–215. doi: [10.1007/s10569-014-9574-3](https://doi.org/10.1007/s10569-014-9574-3) (cit. on pp. 4, 53, 54).

Bibliography

- [17] Stephen B. Broschart and Benjamin F. Villac. “Identification of non-chaotic terminator orbits near 6489 golevka”. *Advances in the Astronautical Sciences* 134. September (2009), pp. 861–880. doi: [10.13140/2.1.1246.8484](https://doi.org/10.13140/2.1.1246.8484) (cit. on p. 52).
- [18] R. Broucke. “Stability of periodic orbits in the elliptic, restricted three-body problem”. *AIAA Journal* 7.6 (1969), pp. 1003–1009. doi: [10.2514/3.5267](https://doi.org/10.2514/3.5267) (cit. on p. 22).
- [19] California Polytechnic State University. *CubeSat Design Specification, Rev. 13*. Tech. rep. 2014 (cit. on p. 57).
- [20] S Campagnola, N Ozaki, Y Sugimoto, CH Yam, H Chen, Y Kawabata, et al. “Low-thrust trajectory design and operations of PROCYON, the first deep-space micro-spacecraft.” *25th International Symposium on Space Flight Dynamics*. Munich, Germany, 2015. doi: [10.2307/j.ctv2jtxrhd.18](https://doi.org/10.2307/j.ctv2jtxrhd.18) (cit. on p. 110).
- [21] Stefano Campagnola, Martin Lot, and Paul Newton. “Subregions of motion and elliptic halo orbits in the elliptic restricted three-body problem”. *Advances in the Astronautical Sciences* 130 PART 2 (2008), pp. 1541–1555 (cit. on pp. 15, 85).
- [22] Stefano Campagnola, Chit Hong Yam, Yuichi Tsuda, Ogawa Naoko, and Yasuhiro Kawakatsu. “Mission analysis for the Martian Moons Explorer (MMX) mission”. *Acta Astronautica* 146 (2018), pp. 409–417. doi: [10.1016/j.actaastro.2018.03.024](https://doi.org/10.1016/j.actaastro.2018.03.024) (cit. on p. 78).
- [23] Elisabet Canalias, Gerard Gomez, M. Marcote, and Josep J. Masdemont. *Assessment of mission design including utilization of libration points and weak stability boundaries*. Tech. rep. ESA 18142/04/NL/MV, 2004 (cit. on p. 22).
- [24] Elisabet Canalias, Laurence Lorda, Thierry Martin, Julien Laurent-Varin, Jean Charles, and Yuya Mimasu. “Trajectory analysis for the Phobos proximity phase of the MMX mission”. *26th International Symposium on Spaceflight Dynamics*. 2017, pp. 1–9 (cit. on p. 42).
- [25] Elisabet Canalias Vila. “Contributions to Libration Orbit Mission Design using Hyperbolic Invariant Manifolds”. PhD thesis. Universitat Politècnica de Catalunya, 2007, p. 203 (cit. on pp. 4, 9, 67–69).
- [26] Enric Castellà and Àngel Jorba. “On the vertical families of two-dimensional tori near the triangular points of the bicircular problem”. *Celestial Mechanics and Dynamical Astronomy* 76.1 (2000), pp. 35–54. doi: [10.1023/A:1008321605028](https://doi.org/10.1023/A:1008321605028) (cit. on p. 15).
- [27] Enric Castellà and Àngel Jorba. “The lagrangian points of the real Earth-Moon system”. *International Conference on Differential Equations*. Hassel, Belgium, 2003, pp. 3–12 (cit. on pp. 5, 72, 74, 76).
- [28] Onur Çelik, Nicola Baresi, Ronald Louis Ballouz, Kazunori Ogawa, Koji Wada, and Yasuhiro Kawakatsu. “Ballistic deployment from quasi-satellite orbits around Phobos under realistic dynamical and surface environment constraints”. *Planetary and Space Science* 178. January (2019). doi: [10.1016/j.pss.2019.06.010](https://doi.org/10.1016/j.pss.2019.06.010) (cit. on p. 57).
- [29] A. Chakraborty and A. Narayan. “BiElliptic Restricted Four Body Problem”. *Few-Body Systems* 60.1 (2019). doi: [10.1007/s00601-018-1472-x](https://doi.org/10.1007/s00601-018-1472-x) (cit. on p. 74).
- [30] Takuya Chikazawa, Nicola Baresi, Stefano Campagnola, Naoya Ozaki, and Yasuhiro Kawakatsu. “Minimizing eclipses via synodic resonant orbits with applications to EQUULEUS and MMX”. *Acta Astronautica* 180 (2021), pp. 679–692. doi: [10.1016/j.actaastro.2020.12.028](https://doi.org/10.1016/j.actaastro.2020.12.028) (cit. on p. 73).
- [31] Diane C. Davis, Sagar A. Bhatt, Kathleen C. Howell, Jiann Woei Jang, Ryan J. Whitley, Fred D. Clark, et al. “Orbit maintenance and navigation of human spacecraft at cislunar near rectilinear halo orbits”. *Advances in the Astronautical Sciences* 160 (2017), pp. 2257–2276 (cit. on pp. 4, 73, 74, 82, 85, 90).
- [32] E. J. Doedel, R. C. Paffenroth, H. B. Keller, D. J. Dichmann, J. Galán-Vioque, and A. Vanderbauwhede. “Computation of periodic solutions of conservative systems with application to the 3-body problem”. *International Journal of Bifurcation and Chaos in Applied Sciences and Engineering* 13.6 (2003), pp. 1353–1381. doi: [10.1142/S0218127403007291](https://doi.org/10.1142/S0218127403007291) (cit. on pp. 20, 21, 38, 39).
- [33] E. J. Doedel, V. A. Romanov, R. C. Paffenroth, H. B. Keller, D. J. Dichmann, J. Galán-Vioque, et al. “Elemental periodic orbits associated with the libration points in the Circular Restricted 3-Body Problem”. *International Journal of Bifurcation and Chaos* 17.8 (2007), pp. 2625–2677. doi: [10.1142/S0218127407018671](https://doi.org/10.1142/S0218127407018671) (cit. on p. 20).
- [34] Stefan C. Endres, Carl Sandrock, and Walter W. Focke. “A simplicial homology algorithm for Lipschitz optimisation”. *Journal of Global Optimization* 72.2 (2018), pp. 181–217. doi: [10.1007/s10898-018-0645-y](https://doi.org/10.1007/s10898-018-0645-y) (cit. on p. 108).
- [35] Robert W Farquhar and David W Dunham. “A new trajectory for Exploring the Earth’s Geomagnetic Tail”. *Journal of Guidance and Control* 4.2 (1980), pp. 192–196 (cit. on p. 2).

- [36] Fabio Ferrari and Michèle Lavagna. “Ballistic landing design on binary asteroids: The AIM case study”. *Advances in Space Research* 62.8 (2018), pp. 2245–2260. DOI: [10.1016/j.asr.2017.11.033](https://doi.org/10.1016/j.asr.2017.11.033) (cit. on pp. 4, 57).
- [37] Daniel García Yáñez, Daniel J. Scheeres, and Colin R. McInnes. “On the a and g families of orbits in the Hill problem with solar radiation pressure and their application to asteroid orbiters”. *Celestial Mechanics and Dynamical Astronomy* 121.4 (2015), pp. 365–384. DOI: [10.1007/s10569-015-9604-9](https://doi.org/10.1007/s10569-015-9604-9) (cit. on p. 18).
- [38] Philip E. Gill, Walter Murray, and Michael A. Saunders. “SNOPT: An SQP algorithm for large-scale constrained optimization”. *SIAM Review* 47.1 (2005), pp. 99–131. DOI: [10.1137/S0036144504446096](https://doi.org/10.1137/S0036144504446096) (cit. on p. 110).
- [39] Karl Heinz Glassmeier, Hermann Boehnhardt, Detlef Koschny, Ekkehard Kührt, and Ingo Richter. “The Rosetta mission: Flying towards the origin of the solar system”. *Space Science Reviews* 128.1-4 (2007), pp. 1–21. DOI: [10.1007/s11214-006-9140-8](https://doi.org/10.1007/s11214-006-9140-8) (cit. on p. 1).
- [40] Hannah R Goldberg, Ozgur Karatekin, Birgit Ritter, Alain Herique, Paolo Tortora, Claudiu Prioroc, et al. “The Juventas CubeSat in Support of ESA’s Hera Mission to the Asteroid Didymos”. *33rd Annual AIAA/USU Conference on Small Satellites* (2019) (cit. on p. 53).
- [41] G. Gómez, J. Masdemont, and C. Simó. “Lissajous orbits around halo orbits”. *Advances in the Astronautical Sciences* 95 PART 1 (1997), pp. 117–134 (cit. on p. 3).
- [42] G. Gómez and J. M. Mondelo. “The dynamics around the collinear equilibrium points of the RTBP”. *Physica D: Nonlinear Phenomena* 157.4 (2001), pp. 283–321. DOI: [10.1016/S0167-2789\(01\)00312-8](https://doi.org/10.1016/S0167-2789(01)00312-8) (cit. on pp. 3, 28, 32).
- [43] G. Gómez, C. Simó, J. Llibre, and R. Martínez. *Dynamics and mission design near libration points - Vol. II fundamentals: the case of the triangular libration points*. Vol. 3. World Scientific, 2001 (cit. on pp. 4, 16).
- [44] Jitendra Nath Goswami and Mylswamy Annadurai. “Chandrayaan-1 mission to the Moon”. *Acta Astronautica* 63.11-12 (2008), pp. 1215–1220. DOI: [10.1016/j.actaastro.2008.05.013](https://doi.org/10.1016/j.actaastro.2008.05.013) (cit. on p. 72).
- [45] À Haro and R. De La Llave. “A parameterization method for the computation of invariant tori and their whiskers in quasi-periodic maps: Numerical algorithms”. *Discrete and Continuous Dynamical Systems - Series B* 6.6 (2006), pp. 1261–1300. DOI: [10.3934/dcdsb.2006.6.1261](https://doi.org/10.3934/dcdsb.2006.6.1261) (cit. on p. 3).
- [46] Martin Hechler and Jordi Cobos. “Herschel, Planck and GAIA Orbit Design”. *7th International Conference on Libration Point Orbits and Application*. 2002 (cit. on p. 2).
- [47] Michael E. Henderson. “Multiple parameter continuation: Computing implicitly defined k-manifolds”. *International Journal of Bifurcation and Chaos in Applied Sciences and Engineering* 12.3 (2002), pp. 451–476. DOI: [10.1142/S0218127402004498](https://doi.org/10.1142/S0218127402004498) (cit. on pp. 36, 78).
- [48] Damennick B Henry and Daniel J Scheeres. “Transfers between intersecting quasi-periodic tori”. *AIAA SciTech Forum*. Orlando, Florida, 2020, pp. 1–17 (cit. on p. 95).
- [49] E. Herrera-Sucarrat, P. L. Palmer, and R. M. Roberts. “Asteroid observation and landing trajectories using invariant manifolds”. *Journal of Guidance, Control, and Dynamics* 37.3 (2014), pp. 907–920. DOI: [10.2514/1.59594](https://doi.org/10.2514/1.59594) (cit. on pp. 4, 57).
- [50] K. C. Howell. “Three-dimensional, periodic, ‘halo’ orbits”. *Celestial Mechanics* 32 (1984), pp. 53–71 (cit. on p. 19).
- [51] K. C. Howell and J. V. Breakwell. “Almost rectilinear halo orbits”. *Celestial Mechanics* 32.1 (1984), pp. 29–52. DOI: [10.1007/BF01358402](https://doi.org/10.1007/BF01358402) (cit. on pp. 5, 73).
- [52] IAU Division Working Group. *Numerical Standards for Fundamental Astronomy - Astronomical Constants : Current Best Estimates (CBEs)*. Last accessed: 2022-08-01; https://iau-a3.gitlab.io/NSFA/NSFA_cbe.html. 2022 (cit. on p. 82).
- [53] Erica L Jenson and Daniel J Scheeres. “Semianalytical Measures of Nonlinearity Based on Tensor Eigenpairs”. *AAS/AIAA Astrodynamics Specialist Conference* (2021), pp. 1–17 (cit. on pp. 85, 104).
- [54] Steven G Johnson. *Notes on FFT-based differentiation*. MIT Applied Mathematics, 2011 (cit. on p. 32).
- [55] À Jorba and J. Villanueva. “On the Persistence of Lower Dimensional Invariant Tori under Quasi-Periodic Perturbations”. *Journal of Nonlinear Science* 7.5 (1997), pp. 427–473. DOI: [10.1007/s003329900036](https://doi.org/10.1007/s003329900036) (cit. on pp. 3, 24, 25, 28, 34, 92).
- [56] Àngel Jorba and Josep Masdemont. “Dynamics in the center manifold of the collinear points of the restricted three body problem”. *Physica D: Nonlinear Phenomena* 132.1-2 (1999), pp. 189–213. DOI: [10.1016/S0167-2789\(99\)00042-1](https://doi.org/10.1016/S0167-2789(99)00042-1) (cit. on p. 3).

- [57] Ángel Jorba and Estrella Olmedo. “On the computation of reducible invariant tori on a parallel computer”. *SIAM Journal on Applied Dynamical Systems* 8.4 (2009), pp. 1382–1404. DOI: [10.1137/080724563](https://doi.org/10.1137/080724563) (cit. on p. 3).
- [58] Marc Jorba-Cuscó, Ariadna Farrés, and Ángel Jorba. “Two periodic models for the Earth-Moon system”. *Frontiers in Applied Mathematics and Statistics* 4.July (2018), pp. 1–14. DOI: [10.3389/fams.2018.00032](https://doi.org/10.3389/fams.2018.00032) (cit. on pp. 4, 15).
- [59] Yasuhiro Kawakatsu, Kiyoshi Kuramoto, T. Usui, Hitoshi Ikeda, N. Ozaki, Nicola Baresi, et al. “Mission Design of Martian Moons eXploration (MMX)”. *69th International Astronautical Congress (IAC)*. Bremen, Germany, 2018 (cit. on pp. 1, 42).
- [60] Wang Sang Koon, Martin W. Lo, Jerrold E. Marsden, and Shane D. Ross. *Dynamical Systems, the Three-Body Problem and Space Mission Design*. 2011 (cit. on pp. 22, 23).
- [61] Wang Sang Koon, Lo Martin W, Jerrold E. Marsden, and Shane D. Ross. “Heteroclinic connections between periodic orbits and resonance transitions in celestial mechanics”. *Chaos* 10.2 (2000), pp. 427–461. DOI: [10.1063/1.166509](https://doi.org/10.1063/1.166509) (cit. on p. 3).
- [62] D. S. Lauretta, S. S. Balram-Knutson, E. Beshore, W. V. Boynton, C. Drouet d’Aubigny, D. N. DellaGiustina, et al. “OSIRIS-REx: Sample Return from Asteroid (101955) Bennu”. *Space Science Reviews* 212.1-2 (2017), pp. 925–984. DOI: [10.1007/s11214-017-0405-1](https://doi.org/10.1007/s11214-017-0405-1). arXiv: [1702.06981](https://arxiv.org/abs/1702.06981) (cit. on p. 1).
- [63] D. S. Lauretta, D. N. DellaGiustina, C. A. Bennett, D. R. Golish, K. J. Becker, S. S. Balram-Knutson, et al. “The unexpected surface of asteroid (101955) Bennu”. *Nature* 568.7750 (2019), pp. 55–60. DOI: [10.1038/s41586-019-1033-6](https://doi.org/10.1038/s41586-019-1033-6) (cit. on pp. 50, 57).
- [64] Harold F. Levison, Catherine B. Olkin, Keith S. Noll, Simone Marchi, James F. Bell, Edward Bierhaus, et al. “Lucy mission to the Trojan asteroids: Science goals”. *Planetary Science Journal* 2.5 (2021), p. 171. DOI: [10.3847/PSJ/abf840](https://doi.org/10.3847/PSJ/abf840) (cit. on p. 51).
- [65] Rafael de la Llave. “A tutorial on KAM theory” (2001), pp. 175–292. DOI: [10.1090/pspum/069/1858536](https://doi.org/10.1090/pspum/069/1858536) (cit. on p. 26).
- [66] Martin W. Lo, Bobby G. Williams, Williard E. Bollman, Dongsuk Han, Yungsun Hahn, Julia L. Bell, et al. “Genesis mission design”. *AIAA/AAS Astrodynamics Specialist Conference and Exhibit* 49.1 (1998), pp. 1–12. DOI: [10.1007/bf03546342](https://doi.org/10.1007/bf03546342) (cit. on pp. 2, 22).
- [67] L. G. Luk’yanov. “Energy conservation in the restricted elliptical three-body problem”. *Astronomy Reports* 49.12 (2005), pp. 1018–1027. DOI: [10.1134/1.2139818](https://doi.org/10.1134/1.2139818) (cit. on pp. 14, 15).
- [68] E. E. Mamajek, A. Prsa, G. Torres, P. Harmanec, M. Asplund, P. D. Bennett, et al. “IAU 2015 Resolution B3 on Recommended Nominal Conversion Constants for Selected Solar and Planetary Properties” (2015), pp. 1–6. arXiv: [1510.07674](https://arxiv.org/abs/1510.07674) (cit. on p. 93).
- [69] Brian McCarthy and Kathleen C. Howell. “Characterization of Families of Low-Energy Transfers to Cislunar Four-Body Quasi-Periodic Orbits”. *AIAA SciTech Forum*. San Diego, California, 2022, pp. 1–17. DOI: [10.2514/6.2022-1889](https://doi.org/10.2514/6.2022-1889) (cit. on pp. 4, 73).
- [70] Colin R. McInnes. *Solar Sailing - Technology, Dynamics and Mission Applications*. Springer-Verlag Berlin Heidelberg, 1999. DOI: [10.1017/CBO9781107415324.004](https://doi.org/10.1017/CBO9781107415324.004). arXiv: [arXiv:1011.1669v3](https://arxiv.org/abs/1011.1669v3) (cit. on p. 18).
- [71] K.R. Meyer, G. R. Hall, and D. Offin. *Introduction to Hamiltonian Dynamical Systems and the N-Body Problem*. 2nd. Vol. 90. Springer, 2010. DOI: [10.2307/3615195](https://doi.org/10.2307/3615195) (cit. on p. 20).
- [72] Patrick Michel, Michael Kueppers, Holger Sierks, Ian Carnelli, Andy F. Cheng, Karim Mellab, et al. “European component of the AIDA mission to a binary asteroid: Characterization and interpretation of the impact of the DART mission”. *Advances in Space Research* 62.8 (2018), pp. 2261–2272. DOI: [10.1016/j.asr.2017.12.020](https://doi.org/10.1016/j.asr.2017.12.020) (cit. on pp. 1, 51).
- [73] Oliver Montenbruck and Eberhard Gill. *Satellite Orbits - Models, Methods, and Applications*. Springer, Berlin, Heidelberg, 2000, pp. 10–11. DOI: <https://doi.org/10.1007/978-3-642-58351-3> (cit. on pp. 22, 93).
- [74] T. Morota, S. Sugita, Y. Cho, M. Kanamaru, E. Tatsumi, N. Sakatani, et al. “Sample collection from asteroid (162173) Ryugu by Hayabusa2: Implications for surface evolution”. *Science* 368.6491 (2020), pp. 654–659. DOI: [10.1126/science.aaz6306](https://doi.org/10.1126/science.aaz6306) (cit. on p. 50).
- [75] F. J. Muñoz-Almaraz, E. Freire, J. Galán, E. Doedel, and A. Vanderbauwhede. “Continuation of periodic orbits in conservative and Hamiltonian systems”. *Physica D: Nonlinear Phenomena* 181.1-2 (2003), pp. 1–38. DOI: [10.1016/S0167-2789\(03\)00097-6](https://doi.org/10.1016/S0167-2789(03)00097-6) (cit. on p. 38).

- [76] D R Myatt, V M Becerra, S J Nasuto, and J M Bishop. *Global Optimization Tools for Mission Analysis and Design*. Tech. rep. ESA ACT Technical report 18138/04/NL/MV, 2004 (cit. on p. 97).
- [77] NASA. “White Paper : Gateway Destination Orbit Model : A Continuous 15 Year NRHO Reference Trajectory” (2019) (cit. on pp. 1, 73, 90).
- [78] NASA. *NASA’s Lunar Exploration Program Overview*. Tech. rep. September. 2020, p. 74 (cit. on pp. 1, 72).
- [79] NASA/JPL. *Astrodynamic Parameters - Solar System Dynamics*. Last accessed: 2022-08-01; https://ssd.jpl.nasa.gov/astro_par.html. 2022 (cit. on pp. 82, 93).
- [80] David Y. Oh, Dan Goebel, Bill Hart, Gregory Lantoine, John Steven Snyder, and Whiffen. “Development of the Psyche Mission for NASA’s Discovery Program”. *International Electric Propulsion Conference* (2019), p. 153 (cit. on p. 51).
- [81] Z. P. Olikara and D. J. Scheeres. “Computing Families of Quasi-Periodic Tori in Autonomous Hamiltonian Systems”. *EUROMECH Nonlinear Dynamics Conference* July (2011), pp. 24–29 (cit. on pp. 25, 32).
- [82] Zubin P. Olikara. “Computation Of Quasi-Periodic Tori And Heteroclinic Connections In Astrodynamics Using Collocation Techniques”. PhD thesis. University of Colorado Boulder, 2016, p. 113 (cit. on pp. 3, 19, 29, 33, 34, 36, 38, 69, 80, 91, 98).
- [83] Zubin P. Olikara and Daniel J. Scheeres. “Numerical method for computing quasi-periodic orbits and their stability in the restricted three-body problem”. *Advances in the Astronautical Sciences* 145 (2012), pp. 911–930 (cit. on pp. 3, 28, 31, 37, 80).
- [84] Zubin P. Olikara and Daniel J. Scheeres. “Mapping connections between planar sun-earth-moon libration point orbits”. *Advances in the Astronautical Sciences* 160 (2017), pp. 1645–1663 (cit. on pp. 4, 36).
- [85] Kenta Oshima. “Continuation and stationkeeping analyses on planar retrograde periodic orbits around the Earth”. *Advances in Space Research* 69.5 (2022), pp. 2210–2222. DOI: [10.1016/j.asr.2021.12.020](https://doi.org/10.1016/j.asr.2021.12.020) (cit. on pp. 78, 85).
- [86] Jeffrey S. Parker. “Targeting low-energy ballistic lunar transfers”. *Journal of the Astronautical Sciences* 58.3 PART 1 (2011), pp. 311–334. DOI: [10.1007/bf03321173](https://doi.org/10.1007/bf03321173) (cit. on p. 102).
- [87] Nathan L. Parrish, Ethan Kayser, Matthew J. Bolliger, Michael R. Thompson, Jeffrey S. Parker, Bradley W. Cheetham, et al. “Ballistic lunar transfers to near rectilinear halo orbit: Operational considerations”. *AIAA Scitech 2020 Forum* 1 PartF (2020), pp. 1–19. DOI: [10.2514/6.2020-1466](https://doi.org/10.2514/6.2020-1466) (cit. on p. 102).
- [88] F Renk and M Landgraf. “Gaia: Trajectory Design with Tightening Constraints”. *24th International Symposium on Space Flight Mechanics*. 2014. DOI: [10.1093/oseo/instance.00168128](https://doi.org/10.1093/oseo/instance.00168128) (cit. on p. 2).
- [89] Andrew S. Rivkin, Nancy L. Chabot, Angela M. Stickle, Cristina A. Thomas, Derek C. Richardson, Olivier Barnouin, et al. “The double asteroid redirection test (DART): Planetary defense investigations and requirements”. *Planetary Science Journal* 2.5 (2021), p. 173. DOI: [10.3847/PSJ/ac063e](https://doi.org/10.3847/PSJ/ac063e) (cit. on pp. 1, 51).
- [90] José J. Rosales, Àngel Jorba, and Marc Jorba-Cuscó. “Families of Halo-like invariant tori around L2 in the Earth-Moon Bicircular Problem”. *Celestial Mechanics and Dynamical Astronomy* 133.4 (2021), pp. 1–30. DOI: [10.1007/s10569-021-10012-0](https://doi.org/10.1007/s10569-021-10012-0) (cit. on pp. 4, 73).
- [91] D. J. Scheeres. “The Restricted Hill Four-Body Problem with Applications to the Earth-Moon-Sun System”. *Celestial Mechanics and Dynamical Astronomy* 70.2 (1998), pp. 75–98. DOI: [10.1023/A:1026498608950](https://doi.org/10.1023/A:1026498608950) (cit. on pp. 4, 74).
- [92] D. J. Scheeres and J. Bellerose. “The Restricted Hill Full 4-Body problem: Application to spacecraft motion about binary asteroids”. *Dynamical Systems* 20.1 (2005), pp. 23–44. DOI: [10.1080/1468936042000281321](https://doi.org/10.1080/1468936042000281321) (cit. on p. 4).
- [93] D J Scheeres, J W McMahon, E B Bierhaus, J Wood, C M Hartzell, P Hayne, et al. “Janus: A NASA SIMPLEx mission to explore two NEO Binary Asteroids”. *51st Lunar and Planetary Science Conference*. 2020 (cit. on p. 51).
- [94] D J Scheeres and Aaron J Rosengren. “Design, Dynamics and Stability of the OSIRIS-REx Sun-Terminator Orbits”. *Advances in the Astronautical Sciences*. January. 2013, pp. 1–20 (cit. on pp. 4, 53).
- [95] Daniel J. Scheeres. *Orbital Motion in Strongly Perturbed Environments*. 2012. DOI: [10.1007/978-3-642-03256-1](https://doi.org/10.1007/978-3-642-03256-1) (cit. on pp. 4, 11, 18, 19, 22, 43, 44, 91).
- [96] Stephen T Scheuerle and Kathleen C Howell. “Characteristics and Analysis of Families of Low-Energy Ballistic Lunar Transfers”. *AAS/AIAA Astrodynamics Specialist Conference*. Big Sky, Montana (Virtual), 2021, pp. 1–20 (cit. on pp. 4, 73, 86, 102).

Bibliography

- [97] R. Seydel. *Practical Bifurcation and Stability Analysis*. Third. Vol. 5. Springer Science & Business Media, 2009. doi: [10.1007/978-0-387-75847-3](https://doi.org/10.1007/978-0-387-75847-3) (cit. on pp. 19, 21, 36).
- [98] Stefania Soldini and Yuichi Tsuda. “Assessing the Hazard Posed by Ryugu Ejecta Dynamics on Hayabusa2 Spacecraft”. *26th International Symposium of Space Flight Dynamics* (2017), pp. 1–11 (cit. on p. 57).
- [99] Andrew J. Sommese and Charles W. Wampler. *The Numerical Solution of Systems of Polynomials - Arising in Engineering and Science*. World Scientific, 2005 (cit. on p. 30).
- [100] Victor Szebehely. *Theory of orbits*. Academic Press Inc., 1967. doi: [10.1016/0016-0032\(67\)90217-7](https://doi.org/10.1016/0016-0032(67)90217-7) (cit. on pp. 9, 12).
- [101] Simon Tardivel and Daniel J. Scheeres. “Ballistic deployment of science packages on binary asteroids”. *Journal of Guidance, Control, and Dynamics* 36.3 (2013), pp. 700–709. doi: [10.2514/1.59106](https://doi.org/10.2514/1.59106) (cit. on pp. 4, 18, 57).
- [102] Yuichi Tsuda, Takanao Saiki, Fuyuto Terui, Satoru Nakazawa, Makoto Yoshikawa, and Sei ichiro Watanabe. “Hayabusa2 mission status: Landing, roving and cratering on asteroid Ryugu”. *Acta Astronautica* 171 (2020), pp. 42–54. doi: [10.1016/j.actaastro.2020.02.035](https://doi.org/10.1016/j.actaastro.2020.02.035) (cit. on p. 1).
- [103] Stephan Ulamec, Jens Biele, Pierre W. Bousquet, Philippe Gaudon, Koen Geurts, Tra Mi Ho, et al. “Landing on small bodies: From the rosetta lander to MASCOT and beyond”. *Acta Astronautica* 93 (2014), pp. 460–466. doi: [10.1016/j.actaastro.2013.02.007](https://doi.org/10.1016/j.actaastro.2013.02.007) (cit. on p. 57).
- [104] Daniel Villegas-Pinto, Stefania Soldini, Yuichi Tsuda, and Jeannette Heiligers. “Temporary Capture of Asteroid Ejecta into Periodic Orbits: Application to JAXA’s Hayabusa2 Impact Event”. *AIAA Scitech 2020 Forum*. 2020. doi: [10.2514/6.2020-0221](https://doi.org/10.2514/6.2020-0221) (cit. on pp. 18, 52).
- [105] Tamás Vinkó, Dario Izzo, and Claudio Bombardelli. “Benchmarking different global optimisation techniques for preliminary space trajectory design”. *58th International Astronautical Congress (IAC)* 6.September (2007), pp. 4181–4190 (cit. on p. 97).
- [106] Robert A. Werner. “Spherical harmonic coefficients for the potential of a constant-density polyhedron”. *Computers and Geosciences* 23.10 (1997), pp. 1071–1077. doi: [10.1016/S0098-3004\(97\)00110-6](https://doi.org/10.1016/S0098-3004(97)00110-6) (cit. on p. 18).
- [107] Mark A. Wieczorek, Bradley L. Jolliff, Amir Khan, Matthew E. Pritchard, Benjamin P. Weiss, James G. Williams, et al. “The constitution and structure of the Lunar interior”. *Reviews in Mineralogy and Geochemistry* 60 (2006), pp. 221–364. doi: [10.2138/rmg.2006.60.3](https://doi.org/10.2138/rmg.2006.60.3) (cit. on pp. 82, 93).
- [108] Daniel García Yáñez, Joan Pau Sanchez Cuartielles, and Colin R. McInnes. “Alternating orbiter strategy for asteroid exploration”. *Journal of Guidance, Control, and Dynamics* 38.2 (2015), pp. 280–291. doi: [10.2514/1.G000562](https://doi.org/10.2514/1.G000562) (cit. on p. 51).
- [109] M. Yoshikawa, A. Tsuchiyama, A. Fujiwara, and J. Kawaguchi. “Hayabusa sample return mission”. *Asteroids IV* (2015) (cit. on p. 1).
- [110] Changyi Zhou, Yingzhuo Jia, Jianzhong Liu, Huijun Li, Yu Fan, Zhanlan Zhang, et al. “Scientific objectives and payloads of the lunar sample return mission—Chang’E-5”. *Advances in Space Research* 69.1 (2022), pp. 823–836. doi: [10.1016/j.asr.2021.09.001](https://doi.org/10.1016/j.asr.2021.09.001) (cit. on p. 72).
- [111] Emily M. Zimovan, Kathleen C. Howell, and Diane C. Davis. “Near rectilinear halo orbits and their application in cis-lunar space”. *3rd IAA Conference on Dynamics and Control of Space Systems*. Moscow, Russia, 2017 (cit. on pp. 4, 73).



ABSTRACT

KEYWORDS

trajectory design, perturbed systems, dynamical systems theory, quasi-periodic, cislunar, small bodies